Title
Growth and Evolution of Electromagnetic Ion Cyclotron Waves in the Presence of Multiple Ion Species in the Earth's Magnetosphere

Author
Lee, Justin H

Publication Date
2014

Peer reviewed|Thesis/dissertation

UNIVERSITY OF CALIFORNIA

Los Angeles

Growth and Evolution of Electromagnetic Ion Cyclotron Waves in the Presence of Multiple Ion Species in the Earth's Magnetosphere

A dissertation submitted in partial satisfaction

of the requirements for the degree

Doctor of Philosophy in Geophysics and Space Physics

by

Justin Hao Lee

2014

ABSTRACT OF THE DISSERTATION

Growth and Evolution of Electromagnetic Ion Cyclotron Waves in the Presence of Multiple Ion Species in the Earth's Magnetosphere

by

Justin Hao Lee

Doctor of Philosophy in Geophysics and Space Physics

University of California, Los Angeles, 2014

Professor Vassilis Angelopoulos, Chair

Electromagnetic ion cyclotron (EMIC) waves are generated by a fundamental plasma instability and interact with multiple particle populations in the Earth's magnetosphere. This dissertation describes the application of spacecraft data and linear theory of electromagnetic waves to investigating the evolution of EMIC wave properties in the presence of multiple magnetospheric ion species. In particular, the role of the low-energy heavy ion species on the wave properties is explored. A case study describes spacecraft measurements of EMIC wave activity, the multiple ion species (hot protons, cold protons, and cold He^{+}) present during the wave activity, and the methods for performing thorough characterization and analysis of the wave observations. I show that the observed wave characteristics are not typical of such waves as established from linear cold plasma theory. By using the full range of the observations and applying them to modeling of

linear wave growth, I then show that wave properties evolve in the presence of sufficient free energy (low density hot protons), high density cold protons, and warm He^+ (~10 eV). Parametric study of linear wave growth using the observed multiple ion properties as a reference point implies that EMIC waves evolve due to these warm plasma effects of the heavier ion species, and may also evolve due to non-local generation and propagation. This motivates a global multi-spacecraft magnetospheric study of the dominant cold/warm ions (H^+, He^+, and O^+) to establish their typical properties (composition, densities, and temperatures) at different magnetospheric locations and to determine where such cold/warm ions can lead to similar evolution of warm plasma EMIC waves assuming the hot proton free energy is available. I then apply these results to successfully explain typical growth rates and properties of EMIC waves observed in each MLT sector. The results show how our findings on cold/warm ion properties can be used in future studies of EMIC wave generation and properties, including the effect of the waves on scattering of relativistic radiation belt electrons, cold ion heating, and hot ion precipitation to the ionosphere resulting in the proton aurora.

The dissertation of Justin Hao Lee is approved.

Christopher T. Russell

Richard M. Thorne

Vassilis Angelopoulos, Committee Chair

University of California, Los Angeles

2014

Dedicated in the memory of

Dr. S.-K. Chao,

Professor C.-H. Lee,

and

Lăolao

TABLE OF CONTENTS

LIST OF FIGURES

LIST OF TABLES

ACKNOWLEDGEMENTS

There are many people who made my graduate studies and this research project possible. My advisor, Vassilis Angelopoulos, has been supportive but has also always challenged me to work harder. Vassilis has also managed to always make time for his research group and students. Our weekly meetings as a group and then another time one-on-one are chances to discuss research progress broadly and also in finer detail. The one-on-one "lessons" have echoed my past experience studying piano K–12, in which weekly lessons were also important for reinforcing fundamentals and at the same time ensuring new progress was steadily made. My discussions with Vassilis have helped me reconnect with and further develop many facets of my interests, including the importance of the ionosphere for magnetospheric processes and vice versa, instrument development, and data analysis techniques. Robert McPherron and Christopher Russell have provided their candid feedback and suggestions on my research and also important lessons learned in Geology 3814. Bob and Prof Russell have encouraged me to broaden my perspective and think more about how the many phenomena occurring in planetary magnetospheres are related. They have also pushed me to understand the fundamental principles of spacecraft instruments and their measurements as well as data analysis techniques. Richard Thorne and Lunjin Chen have shown me the importance of theory in driving advancement of research and its role in determining directions for future experimentation. I have had numerous stimulating discussions with Richard and Lunjin on wave-particle interactions and the fruits of those discussions are inserted throughout the chapters presented in this thesis. I am lucky to have had a thesis committee made up of members whose combined breadth of knowledge is seemingly infinite. I also acknowledge helpful discussions on space physics concepts with Raymond Walker. Many discussions with other UCLA research and engineering staff (Xu-Zhi

Zhou, Drew Turner, Andrei Runov, Ryan Caron, and Adam Kellerman) and other graduate students (special thanks to Jiang Liu, Christine Gabrielse-Lin, Xiaojia Zhang, and Shan-shan Li) have also made my graduate school experience memorable and I look forward to future opportunities for collaboration.

I have also met and collaborated with numerous people while working in industry. I thank Simon Liu for his continued support of my decisions to further my education and career. John Halpine has also provided guidance and encouraged me to pursue and develop my interests through collaborations with other scientists and engineers. Through such collaborations I have been fortunate enough to participate in several nanosatellite flight experiments. Taking part in the flight experiment cycle from concept to operations would not have been possible without the support of David Hinkley and Edward Simburger. I thank James Clemmons for providing me an early opportunity to work on analysis of particle and wave data from measurements made by the GEODESIC sounding rocket. My interest in wave-particle interactions and many exciting discussions stemmed from this early project, including discussions with David Knudsen from University of Calgary who shared with me his enthusiasm for ionospheric research and his first-hand accounts of the rocket launch. Hallway conversations with Bern Blake and Joe Fennell have provided me with additional historical perspective on experimental space research and inspired me to tell a good story about the observations. I have enjoyed discussions with Colby Lemon and Tamitha Skov and look forward to working on future projects with them.

Completing my graduate studies was without a doubt also owing to the love and support of family and friends. In particular, my mother and father, my brother, Jason, and sister, Ya Ting have been especially supportive. I thank my cousin Ning Chao for being a good listener and providing straightforward advice. My other aunts, uncles, and cousins have also been important

sources of humor and encouragement. I thank Cindy Tseng for overlapping orbits with me again, accompanying me on this journey, and for all the priceless moments; I look forward to when we learn another four hands piece. I also thank the Tseng and Chang families. Lastly, as I noted on an earlier page, this thesis is dedicated to three family members who all passed away before I could complete it. My uncle, Dr. S.-K. Chao, enjoyed sharing stories about when he was also a UCLA graduate student. He reminded me to keep a sense of humor even during difficult times. My earliest memory of my grandfather, Professor C.-H. Lee, was being in his engineering lab, where he first showed me how to solder. My grandmother, whom we all called Lăolao, always encouraged us to further our education even though she never had the chance to do so herself.

I acknowledge NASA THEMIS contract NAS5-02099 and the THEMIS team for productive group meetings and discussions. Many people have contributed to making data available for application to the research discussed in this dissertation. I specifically acknowledge Charles Carlson and James McFadden for use of the ESA data, Davin Larson and Robert Lin for use of SST data, John Bonnell and Forrest Mozer for use of EFI data, Karl-Heinz Glassmeier, Uli Auster and Wolfgang Baumjohann for the use of FGM data provided under the lead of the Technical University of Braunschweig and with financial support through the German Ministry for Economy and Technology and the German Center for Aviation and Space (DLR) under contract 50 OC 0302, and the THEMIS software team (in particular: Jim Lewis, Jim McTiernan, Pat Cruce, and Aaron Flores) for providing constant enhancements to the THEMIS data analysis software (TDAS). I acknowledge useful discussions with Chris Chaston and Olivier Le Contel on wave analysis and the usage of wavpol.pro. I acknowledge the Goddard Space Flight Center/Space Physics Data Facility (GSFC/SPDF) OMNIWeb interface at http://omniweb.gsfc.nasa.gov for providing the OMNI data, the Space Weather Prediction Center,

Boulder, CO, National Oceanic and Atmospheric Administration (NOAA), US Dept. of Commerce for providing the geomagnetic K-indices data, and the World Data Center for Geomagnetism, Kyoto University in Kyoto, Japan for providing the Kyoto Dst index data.

Chapter 2 is a version of Lee, J. H., L. Chen, V. Angelopoulos, and R. M. Thorne (2012), THEMIS observations and modeling of multiple ion species and EMIC waves: Implications for a vanishing He^+ stop band, J. Geophys. Res., 117, A06204, doi:10.1029/2012JA017539.

Chapter 3 is a version of Lee, J. H., and V. Angelopoulos (2014), On the presence and properties of cold ions near Earth's equatorial magnetosphere, J. Geophys. Res. Space Physics, 119, 1749–1770, doi:10.1002/2013JA019305.

Chapter 4 is a version of my review on equatorial low-energy plasma populations that was motivated by the presentations and discussions at the ISSI Workshop on Plasma Sources of Solar System Magnetospheres. I acknowledge Michel Blanc, Emma Bunce, Charles "Rick" Chappell, Andrew Nagy, Hermann Opgenoorth, James Slavin, and the International Space Science Institute in Bern, Switzerland for planning the workshop and inviting me to present my research there. I enjoyed discussions with numerous people during and following this workshop, including Rick Chappell, Mats André, Daniel Welling, Chih-Ping Wang, Masaki Fujimoto, and Iannis Dandouras. I look forward to additional discussions as we work towards combining our reviews into a book.

Chapter 5 is a version of Lee, J. H., and V. Angelopoulos (2014), Observations and modeling of EMIC wave properties as function of local time in the presence of multiple ion species, J. Geophys. Res. Space Physics, (to be submitted).

Financial support for this dissertation and graduate student research assistantship was provided by NASA contract NAS5-02099.

VITA

2001 – 2005	Bachelor of Science in Atmospheric, Oceanic, and Environmental Sciences (Major) and East Asian Languages and Cultures (Minor) University of California, Los Angeles, California, USA.
2006 –	Research Associate Affiliated with The Aerospace Corporation, El Segundo, California, USA.
2007 – 2010	Master of Science in Geophysics and Space Physics University of California, Los Angeles, California, USA.
2011 – 2014	Graduate Student Researcher Department of Earth, Planetary, and Space Sciences University of California, Los Angeles, California, USA.

SELECTED PUBLICATIONS AND PRESENTATIONS

Lee, J. H., J. H. Clemmons, V. Angelopoulos, and D. J. Knudsen (2008), Automated identification of field-aligned electron bursts from GEODESIC sounding rocket data, Abstract SA33B-1637 presented at 2008 Fall Meeting, AGU, San Francisco, Calif., 15–19 Dec.

Lee, J. H., J. H. Clemmons, V. Angelopoulos, R. F. Pfaff, D. D. Wallis, and D. J. Knudsen (2009), Application of the Alfvén-assisted precipitation model to field-aligned electron bursts, Abstract SA23A-1464 presented at 2009 Fall Meeting, AGU, San Francisco, Calif., 14–18 Dec.

Lee, J. H., L. Chen, V. Angelopoulos, and R. M. Thorne (2012), THEMIS observations and modeling of multiple ion species and EMIC waves: Implications for a vanishing He^+ stop band, J. Geophys. Res, 117, A06204, doi:/10.1029/2012JA017539.

Lee, J. H., and V. Angelopoulos (2012), Occurrence of low-energy ions near the magnetic equator and their role in the EMIC instability, Abstract SM31B-2293 presented at 2012 Fall Meeting, AGU, San Francisco, Calif., 3–7 Dec.

Lee, J. H. (2013), Cold ions in the inner magnetosphere, invited presentation at the ISSI Workshop on Plasma Sources of Solar System Magnetospheres, International Space Science Institute, Bern, Switzerland, 23–27 Sep.

Lee, J. H., and V. Angelopoulos (2013), New statistics on low-energy ion composition and properties near the equatorial magnetosphere and their relation to EMIC wave characteristics, Abstract SM43A-2265 presented at 2013 Fall Meeting, AGU, San Francisco, Calif., 9–13 Dec.

Lee, J. H., and V. Angelopoulos (2014), On the presence and properties of cold ions near Earth's equatorial magnetosphere, J. Geophys. Res. Space Physics, 119, 1749–1770, doi:/10.1002/2013JA019305.

Lee, J. H. and V. Angelopoulos (2014), Observations and modeling of EMIC waves as function of local time in the presence of multiple ion species, J. Geophys. Res. Space Physics, (to be submitted).

CHAPTER 1

Introduction

1.1 EMIC waves in the Earth's magnetosphere

Space-based observations of electromagnetic ion cyclotron (EMIC) waves by Earth-orbiting spacecraft have revealed a number of defining features of the low-frequency plasma emissions that match those determined through extensive theoretical work [e.g., *Smith and Brice*, 1964; *Cornwall*, 1965; *Kennel and Petschek*, 1966; *Gendrin*, 1968; *Barfield and Coleman*, 1970; *Thorne and Kennel*, 1971; *Barfield and McPherron*, 1972; *Young et al*., 1981; *Fraser and McPherron*, 1982; *Gomberoff and Neira*, 1983]. These left-hand polarized waves experience excitation through cyclotron resonance with anisotropic ($T_{\perp} > T_{\parallel}$) energetic protons near the magnetic equator and often emit power in separate frequency bands, usually with clear band gaps or "stop bands" at the local gyrofrequencies of He^+ and O^+.

Past case studies that combine spacecraft data and theory have focused on the processes through which the wave emissions are excited and the characteristics of multiple ion species, in particular the low-energy ions, that support or suppress this excitation [e.g., *Mauk and McPherron*, 1980; *Young et al*., 1981; *Roux et al*., 1982]. *Young et al*. [1981] analyzed wave and particle data and showed intense EMIC wave emissions were arranged around the local He^+ gyrofrequency (f_{He+}) when the ion composition instrument had also detected the presence of low-energy (< ~100 eV) He^+. These pathfinder observations of in situ wave-particle interactions motivated additional theoretical work, e.g., *Gendrin and Roux* [1980], who studied through

linear cold plasma theory the effects of increasing cold He^+ abundance and the subsequent interaction of the cold He^+ with the waves.

The likelihood of EMIC waves leading to rapid scattering and loss of relativistic (E > 1.6 MeV) radiation belt electrons during magnetic storm main phase [*Thorne and Kennel*, 1971] has also seen recent experimental investigation [e.g., *Meredith et al*., 2003]. In particular, the role of the low-energy or cold He^+ presence during generation of EMIC waves during magnetic storms has continued to receive special attention since the waves tend to possess more power below f_{He+} [*Chen et al*., 2009; *Fraser et al*., 2010]. Furthermore, recent observational evidence of waves emitted near f_{He+} and even across the cold plasma theory He^+ stop band suggests that the minimum resonant energy for wave-particle interaction by anomalous Doppler-shift with relativistic radiation belt electrons could be significantly reduced [*Ukhorskiy et al*., 2010], rendering EMIC waves an important mechanism for losses of a broad distribution of high-energy electrons. This interaction of EMIC waves with relativistic electrons has been investigated by noting the condition for the anomalous Doppler shifted cyclotron resonance, i.e,

$$\boldsymbol{\omega - k_{\parallel} v_{\parallel} = \Omega_e / \gamma},$$

where ω is the wave frequency, $k_{\parallel}$ is the parallel wave number, $v_{\parallel}$ is the parallel drift speed of relativistic electrons, Ω_e is the electron cyclotron frequency, and γ is the relativistic mass enhancement factor. This resonance condition can be expressed primarily as a relationship between the minimum resonant parallel electron energy and $k_{\parallel}$ (adapted from *Chen et al*. [2011]), i.e.,

$$\boldsymbol{E^e_{res\parallel} = \left(\left[\frac{\Omega_e^2}{c^2 k_{\parallel}^2} + 1 \right]^{1/2} - 1 \right) E_o},$$

where c is the speed of light and E_o is the electron rest mass (~0.5 MeV). In the cold plasma approximation, waves emitted below f_{He+} are undamped at large $k_{\parallel}$ and the minimum resonant

energy of these energetic electrons could be near 0.5 MeV. If the intense EMIC waves seen during magnetic storms occur in a plasma with properties consistent with this cold plasma approximation, rapid scattering of radiation belt electrons could potentially occur over a broad energy range [*Ukhorskiy et al*., 2010; *Gary et al*., 2012]. It has thus been predicted that a necessary condition for scattering of 0.5 MeV ≤ E ≤ few MeV electrons is the presence of a cold (~1 eV) and dense (~0.2n_{tot}) He^+ component even though it has also been recognized that heating of the low-energy He^+ significantly changes the frequencies where EMIC waves are unstable, resulting in damping of waves emitted below f_{He+} in precisely the range of $k_{||}$ important for scattering of < few MeV electrons [*Gary et al*., 2012]. It is therefore important to determine the presence and compositional properties of low-energy He^+ as a fundamental step towards further testing of these theoretical predictions.

The importance of the compositional properties of multiple ion species has been corroborated by additional theoretical studies by *Silin et al*., [2010] and *Chen et al*., [2011]; the authors have discussed the properties of EMIC waves as predicted through parametric studies of the kinetic (and warm plasma) dispersion relation including the effects of low-energy He^+ that has been moderately heated. These studies suggest that linear cold plasma theory does not adequately describe the wave characteristics as the wave dispersion and unstable frequencies are modified substantially near f_{He+} by the hot proton anisotropy and low-energy heavy ion temperature and density. In particular, *Chen et al*. [2011] showed that for a certain range of plasma compositional properties, the cold plasma stop band near f_{He+} may vanish, and waves near f_{He+} may be unstable. The studies by *Silin et al*., [2010] and *Chen et al*., [2011] focused on how this evolution of the wave properties near f_{He+} affects evaluation of electron scattering energies associated with EMIC waves; the authors showed that using the cold plasma description

of EMIC waves can result in erroneous estimates of the minimum resonant energy of electrons. *Chen et al*. [2011] concluded that the class of EMIC waves that do not have a cold He^+ stop band can only resonate with electrons > a few MeV due to catastrophic damping that occurs at larger $k_{||}$. Furthermore, they demonstrated that even when there is a He^+ stop band, the warm plasma effects of the low-energy He^+ and energetic protons can significantly alter the wave properties at frequencies just below f_{He+}, also limiting the unstable range of wave frequencies to low $k_{||}$, which again limits the range of electron energies that can be affected by EMIC waves to much higher energies. Sub-MeV electrons cannot be scattered by such warm plasma EMIC waves. Thus, it is important to understand the origin of and establish the conditions for the growth of EMIC waves near and even across the He^+ stop band and also whether warm plasma effects are evident in spacecraft observations. The conclusions by *Silin et al*. [2010] and *Chen et al*. [2011] imply that the properties of the multiple ion species in the magnetospheric plasma must be carefully considered when evaluating relativistic electron scattering by EMIC waves. Their theoretical predictions still await tests to new, high-resolution observational data, as it is currently debated whether warm plasma effects are important for in situ EMIC wave studies [e.g., *Mauk*, 2013, and references therein].

The above theoretical works continue to improve definition and provide additional understanding of EMIC waves and the plasma properties that result in wave excitation or damping. In recent years, a number of observational studies on interactions of various electromagnetic waves and particles in the equatorial magnetosphere fueled by the launch of the THEMIS (Time History of Events and Macroscale Interactions during Substorms) mission [*Angelopoulos*, 2008] have also been carried out using state-of-the-art, comprehensive instrumentation [e.g., *Usanova et al*., 2008; *Li et al*., 2010]. In particular, burst-mode

observations (particle and wave data captures at the highest rate possible for short intervals, triggered by ambient, local conditions) by the THEMIS spacecraft now open up the possibility of high-quality studies of EMIC waves, their growth, their saturation, and their effects on particles. But even with the most advanced instrumentation, there remain significant hurdles to improving our understanding of EMIC wave generation and properties. Several aspects of magnetospheric EMIC wave occurrence rates and properties as determined by numerous spacecraft studies continue to be mysterious and could be directly related to the compositional properties of the magnetospheric plasma that remains largely unknown.

1.2 Puzzling aspects of magnetospheric EMIC wave properties

Several authors have described some of the puzzling aspects of EMIC wave occurrence rates and properties in the Earth's magnetosphere. Recently, *Min et al*. [2012] and *Usanova et al*. [2012] discussed EMIC waves observed throughout the equatorial magnetosphere during quiet geomagnetic conditions from the first few years of operation of the THEMIS mission. They found that EMIC wave occurrence rates peaked at large geocentric distances ($L > 8\ R_E$) regardless of MLT, with highest occurrence rates observed near the dayside magnetopause and along the flanks. *Usanova et al*. [2012] suggested that magnetospheric compression increased the temperature anisotropy of the hot protons that excite EMIC waves, thereby enhancing the occurrence of the waves at these locations. Although not discussed in these studies, it is expected that the occurrence rates of EMIC waves at these locations should also depend on the existence of cooler ions. An EMIC wave study of both the hot proton anisotropy and the cold ions that lower the instability threshold is needed to characterize EMIC wave generation. Although *Usanova et al*. [2012] did not discriminate for the different bands of EMIC waves or their

spectral properties, which provide additional hints about the cold plasma conditions supporting the wave activity, *Usanova et al*. [2013], using Cluster II data did examine whether EMIC wave activity was related to the presence of dense plasmaspheric plumes. The latter study revealed only a weak relationship between plume and EMIC wave occurrence, again suggesting that the dominant factor in enhancing EMIC waves was the solar wind dynamic pressure. *Keika et al*. [2013], on the other hand, examined Active Magnetospheric Particle Tracer Explorers program/Charge Composition Explorer (AMPTE/CCE) data to show that waves occurring at smaller geocentric distances are correlated with increased geomagnetic activity, consistent with times of contracted plasmasphere radius to near geosynchronous distance, a sunward surge of the storm-time plume, and injection of hot plasma sheet ions. This storm-time reconfiguration of the inner magnetosphere creates special conditions for EMIC wave generation along the dusk side that can extend from near or within 6 R_E to the outer dayside magnetosphere. *Keika et al*. [2013] also showed that waves below f_{He+} tended to occur more often during such conditions but did not provide further information on the polarization properties or particle distributions during these same times.

Anderson et al. [1992a, 1992b] also analyzed the AMPTE/CCE dataset during mostly quiet geomagnetic conditions and described the occurrence rates and polarization properties of EMIC waves. In this analysis they showed that EMIC waves occurred mostly in the outer magnetosphere with occurrence rates that increased with increasing L-shell, similar to the radial distribution and occurrence rates described by *Usanova et al*. [2012]. But in their analysis of the polarization properties, *Anderson et al*. [1992b] noticed primarily linear waves in the outer dawn magnetosphere that contradicted expectations that EMIC waves should be mostly left-hand polarized. The authors suggested that the linear polarization was due to oblique propagation or

multiple reflections of waves propagating through the growth region. *Horne and Thorne* [1994] performed modeling using a range of plasma parameters to interpret the results by *Anderson et al*. [1992b] and concluded that low thermal (i.e., low-energy) plasma densities were the most important factor controlling the properties of dawn sector EMIC waves. An alternate explanation was given by *Denton et al*. [1992], who suggested the waves were actually a loss-cone-driven mode that could be generated at oblique angles with linear polarization by a hot proton distribution with a large loss cone-like feature; but *Denton et al*. [1996] remarked that the loss-cone-driven mode was not likely to occur since such large loss cone features are not seen in hot proton distributions around the dayside outer magnetosphere.

Using THEMIS data from a quiet time interval, similar to that utilized for the *Usanova et al.* [2012] analysis, *Min et al*. [2012] studied EMIC wave occurrence rates, wave polarization properties, and provided some supporting information about the ambient magnetospheric plasma populations. *Min et al*. [2012] found that the typical wave polarization in the dawn trough was linear or right-handed, similar to what was described by *Anderson et al*. [1992b]. They also observed more linear waves around noon and showed that left-handed waves occur more often in the afternoon, though there was also some evidence of right-handed waves at large geocentric distances in the afternoon. Because of the atypical polarization features of the waves, the authors discussed the importance of cold ion species for the wave spectral properties, especially the He^+ abundance for the crossover frequency where wave polarization changes occur. But without in situ information on cold ion composition they examined ion abundance ratios and wave growth modeling from different spacecraft and observation periods and only qualitatively addressed how such ion composition could explain the wave spectral properties observed. *Min et al*. [2012] showed that the strange polarization properties of dawn EMIC waves in the THEMIS dataset

correlated well with a lower total plasma density inferred from the spacecraft potential, consistent with the modeling performed by *Horne and Thorne* [1994]. *Min et al.* [2012] used the total plasma density as a proxy for the low-energy plasma densities since the relative abundance of individual cold or warm ion species, important for determining EMIC wave growth and properties, was not available. Thus, although the wave characteristics found in *Min et al*. [2012] are in broad agreement with expectations from *Horne and Thorne's* [1994] modeling, further information on the multiple ion species is needed to fully understand EMIC wave generation, and the wave properties and propagation at large geocentric distances. This is particularly so since the plasma composition used in *Horne and Thorne's* [1994] modeling was from near geosynchronous orbit and thus biased towards plasmaspheric composition (for which the cold proton component dominates).

Discussion of cold heavy ions and their effects on EMIC wave growth and properties also appeared in recent 2.5-D simulation work. *Omidi et al*. [2013] showed the influence of cold O^+ (~11 eV) on the propagation of EMIC waves in a dipole magnetic field with a homogeneous plasma containing hot (keV) protons, cold (~1 eV) protons, and cold O^+. They showed how varying the abundance of cold O^+ affects wave propagation: waves generated at the magnetic equator in O^+ concentrations of 7% or less propagated to the ionosphere, whereas moderate increases in concentration to ~15% led to confinement in latitude; waves were damped near the equator for O^+ concentrations greater than 30%. The authors showed a second effect involving the hot proton density: in the presence of moderate O^+ concentration, EMIC waves were confined to regions along the field line where hot proton density was above 1% of the background density, but in the absence of O^+ the waves propagated to regions where hot proton density was below 1%. They suggested further investigation of linear and nonlinear effects of

EMIC waves using plasma profiles that are inhomogeneous along the field line is needed, as the role of multiple ion species and their spatial variation in EMIC wave generation and evolution is still not understood.

The above observations and modeling work have a common link in that they all recognize the importance of the low-energy ions in affecting various aspects of the wave generation and properties. This begs the question of why a detailed examination of the presence and properties of the low-energy ions has not been made.

1.3 Measurements of the low-energy ions

It is known that the presence of multiple low-energy ion species in the magnetospheric plasma can produce major changes in the properties of EMIC waves. Because of positive spacecraft charging in sunlight, however, it is also well known that much of the time the low-energy ion compositional properties are difficult or impossible to measure experimentally. This determination of the ambient state of cold plasma of the magnetosphere has continued to be problematic but is essential to characterize the effects of the cold ions' partial densities and temperatures on the growth, dispersion, propagation, and properties of EMIC waves. Recently, *André and Cully* [2012] reviewed numerous methods to detect the presence of low-energy ions. Of those methods, one is of particular interest for EMIC wave studies. During sporadic intervals of convection or ULF waves, the plasma bulk flow velocity can be substantially increased and accelerate the ambient low-energy ions above the positive spacecraft potential energy. At these times, particle instruments have the opportunity to directly measure the low-energy ions. It has been shown in the past that by assuming a common flow velocity for the multiple low-energy ion species, we can deduce estimates of the properties of multiple ion species from model ion

distributions fitted to the particle data [e.g., *Chen and Moore*, 2004]. Because convection and ULF waves are common in the Earth's magnetosphere, applying such a method could potentially provide not only the presence but also the properties of multiple low-energy ion species throughout the magnetosphere. This information on the low-energy ions in a global sense could then be applied to explain observations of typical EMIC waves as well as the wave properties and be used to determine if the warm plasma effects described in the theoretical works noted above are pervasive throughout the Earth's magnetosphere.

1.4 Format of the dissertation

A common theme in past in situ EMIC wave studies is the lack of good modeling of the observed EMIC wave properties due to a dearth of information on the low-energy ion compositional properties—including the heavy ion partial densities and temperatures—that are all too critical for wave growth, dispersion, and propagation.

In Chapter 2, I describe THEMIS observations of multiple ion species, including composition, made possible by a convection flow and concurrent EMIC wave activity that motivated detailed modeling of the observations in the context of linear warm plasma theory. The modeling agreed with the observations and showed that EMIC wave properties can evolve from the cold plasma description following marginal heating of a low-density and low-energy He^+ component in the presence of a high-density, cold proton component and the low-density hot proton free energy needed to drive the waves unstable. This result motivated a parametric study of the effects of low-energy He^+ density and temperature on the growth and dispersion of magnetospheric EMIC waves. The results of the parametric study suggested a range of He^+

density and temperature values that could support the evolution of warm plasma EMIC waves throughout the Earth's magnetosphere.

In Chapter 3, motivated by the improved modeling and interpretation of EMIC wave observations that were a direct result of obtaining more detailed characteristics of the multiple ion species compositional properties, I describe a THEMIS multi-spacecraft study of the multiple low-energy ion species designed to explore the typical properties of these low-energy plasma populations that are needed to determine where such properties could influence magnetospheric EMIC waves due to warm plasma effects. In the process I reveal the spatial distributions of occurrence rates, abundance, and temperatures of the dominant cold and warm ions (H^+, He^+, and O^+) near the Earth's equatorial magnetosphere, as well as insights into the sources and transport pathways of those ions. I also show that the temperatures of the low-energy ions were warmest at pre-midnight, and all three species' partial densities and temperatures varied significantly with geocentric distance and magnetic local time.

In Chapter 4, I review other spacecraft observations of the occurrence rates, properties, and transport of low-energy plasma populations near the equator in light of the results presented in Chapter 3. Through the course of this review, I show that the combined observations imply that a diffusion of plasma from the ionosphere and the solar wind is responsible for populating the equatorial magnetosphere with low-energy plasma. I suggest that future multi-spacecraft missions are needed to characterize such a diffusion process but that further knowledge on the low-energy plasma populations can be gained now by multi-instrument measurements of both the particles and waves, since together they can be used as a diagnostic of the plasma properties, including composition.

In Chapter 5, armed with the knowledge from the results in preceding chapters, I revisit some of the EMIC wave topics described in previous studies and present case studies of EMIC waves observed in each MLT sector, composition information either measured in situ or inferred from the findings described in Chapter 3, and modeling using the full dispersion relation for parallel-propagating EMIC waves. The four prototypical EMIC wave intervals chosen have wave spectral properties similar to those found in the recent global survey of EMIC waves from THEMIS [*Min et al*., 2012]. I explain the MLT-dependence of EMIC wave properties and the peculiar wave characteristics noted in the past as entirely due to the compositional properties of the background plasma.

In Chapter 6, I summarize and conclude my dissertation and provide directions for future work on obtaining more knowledge on magnetospheric EMIC wave generation, properties, propagation, as well as the effects of the waves on scattering of radiation belt particles. Future advances on these topics can only be accomplished by also carefully considering the presence and properties of multiple ion species.

CHAPTER 2

Spacecraft observations and modeling of electromagnetic ion cyclotron waves in the presence of multiple ion species

2.1 Introduction

Observations of left-hand polarized electromagnetic ion cyclotron (EMIC) waves with significant wave power across f_{He+} are presented in this chapter. Concurrent field and particle measurements reveal pitch-angle scattering of the energetic ions during the interval of maximum wave power. The observations suggest the presence of multiple low-energy ion species (H^+, He^+) during this same time, below the sum of spacecraft potential and minimum energy of the ion instrument (i.e., < ~20 eV). Fortuitously, immediately following the most intense wave activity, the ambient plasma flow velocity became sufficiently large such that the low-energy ions could be accelerated into the energy range of the particle instrument. Thus, two low-energy ion components are revealed in the particle measurements at energies consistent with cold protons and He^+. Maxwellian fits provide approximations of these low-energy ion species component densities and temperatures. The linear dispersion relation of parallel propagating EMIC waves for the observed conditions shows a vanishing cold plasma He^+ stop band, consistent with the wave measurements during this interval.

These results provide the first observational evidence of the importance of the low-energy ion species densities and temperatures in controlling linear wave growth near and across the heavy ion stop bands in warm plasma theory. The observations enable the first detailed

examination of the observed plasma properties giving rise to waves within the cold plasma He^+ stop band. Although signatures of low-energy He^+ are clear in initial observations of the ion distributions, it is demonstrated that due to the combination of hot proton anisotropy and low-density and non-zero temperature of the He^+ component, EMIC wave instability can occur within the frequency band that usually corresponds to the He^+ stop band under the cold plasma approximation. The modeling and observations agree well and parametric study of the linear dispersion relation further elucidates the range of He^+ densities and temperatures that support unstable EMIC waves without a heavy ion stop band as well as additional wave instabilities associated with warm plasma effects.

2.2 Instruments and Data

The observations discussed within this study draw on various data products from the THEMIS mission [*Angelopoulos*, 2008]. The magnetic field data all originate from the fluxgate magnetometer (FGM) [*Auster et al*., 2008]; spin-averaged (0.33 Samples/s) and low-resolution (4 Samples/s) FGM data types are used. The low-resolution magnetometer data provides three-dimensions of the ambient magnetic field from DC to 2 Hz Nyquist frequency. Details about the wave spectral analysis, including the transform methods used to produce the wave dynamic power spectrograms, are given in the section describing wave observations; a more detailed description also appears in Appendix A. Three-dimensional particle data measured by the electrostatic analyzer (ESA) [*McFadden et al*., 2008] are also used. The spacecraft potential-derived plasma density (Ne_SCpot) data originated from measurements made by the electric field instrument (EFI) [*Bonnell et al*., 2008]. Only data from THEMIS probe A (TH-A) are presented in this study.

2.3 Observational methods

During the interval of interest TH-A was in the pre-midnight sector at a radial distance near geosynchronous orbit. To establish the background magnetic field that is used to define the field-aligned coordinate (FAC) system, the spin-averaged FGM data is low-pass filtered using a 600-point (30 minute) sliding window. The low-resolution FGM data (4 S/s) is then transformed into the FAC system (Z along the average field, X perpendicular to Z in the direction of Earth, and Y completing the orthogonal system) prior to performing any spectral analysis. The various types of ESA data are also transformed into and presented in FAC when applicable. Any additional data processing is described further in its respective section and a more detailed discussion of methods appears in Appendix A.

2.3.1 Waves and their characterization

EMIC wave observations made by TH-A during the time interval from 10:49:30 to 11:10:30 UT are summarized in Figure 2.1 in a stack plot showing the wave dynamic power spectrograms along the average magnetic field (plotted as total magnetic field power spectral density along Z as defined in the FAC system and labeled P_{tot}, with units of nT^2/Hz) produced using both fast Fourier (Figure 2.1a) and Morlet wavelet (Figure 2.1b) transform methods; degree of polarization (P^2) (Figure 2.1c); wave normal angle (θ) (Figure 2.1d); ellipticity (e) (Figure 2.1e); ESA ion (Ni_ESA), ESA electron (Ne_ESA) and spacecraft potential-derived (Ne_SCpot) densities (Figure 2.1f); and the computed DC magnetic field (Figure 2.1g). Local f_{H+} and f_{He+} are also superposed on each of the panels. The dynamic spectrogram produced via the fast Fourier

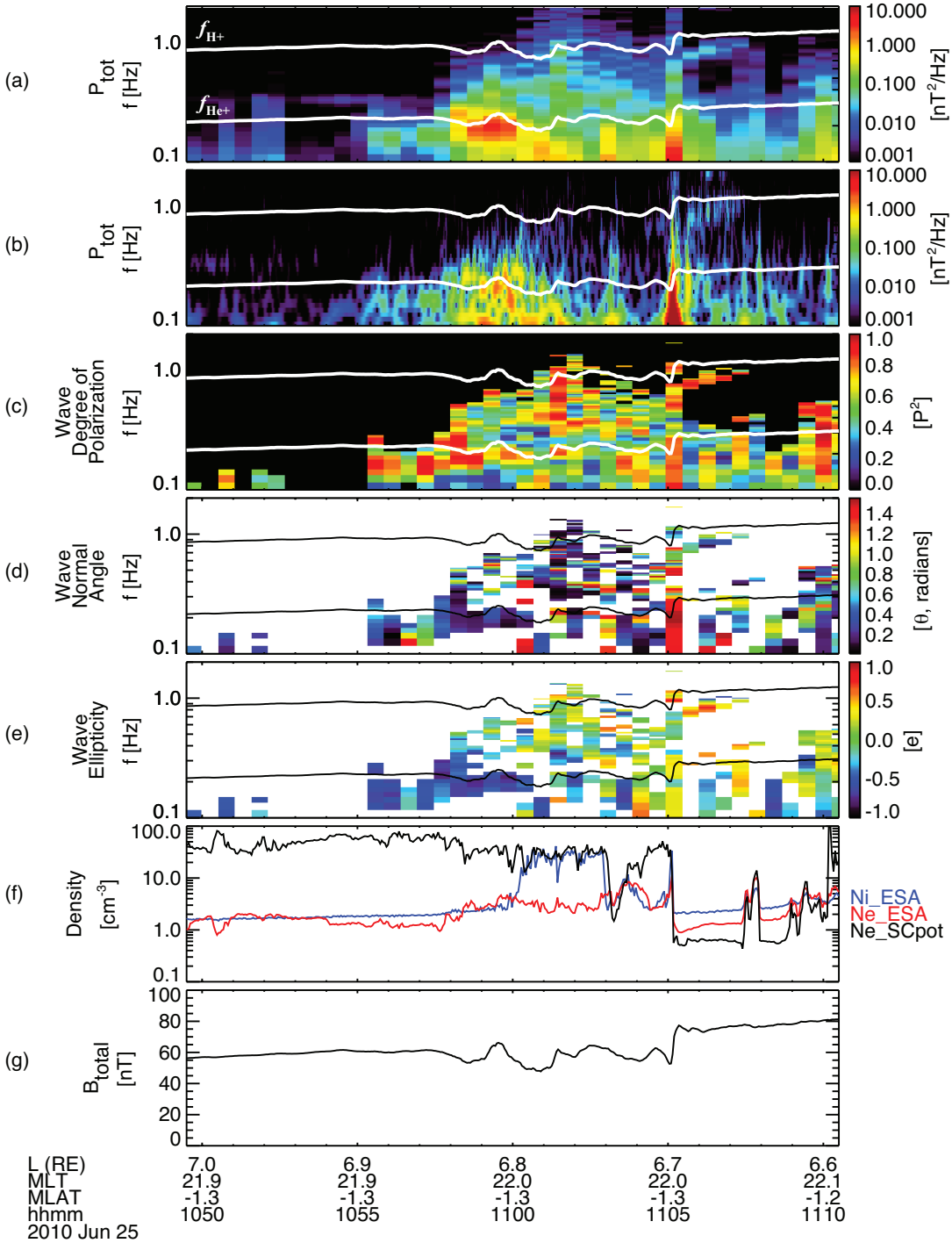

Figure 2.1: Stack plot summarizing the wave observations, spectral analysis results, approximate plasma densities and the computed background magnetic field.

transform (FFT) method in Figure 2.1a uses an FFT window of 256 points and a slide time of 128 points. Figures 2.1c–2.1e are products of the spectral matrix produced using the FFT method. Dynamic spectrograms produced using both FFT and Morlet wavelet transform (MWT) methods suggest that either one can be used for wave spectral analysis in this case; the results will remain similar.

I use the procedures defined by *Samson and Olson* [1980] and *Means* [1972] for wave spectral analysis and characterization. The procedures include calculation of the wave degree of polarization, where $P^2 > \sim 0.70$ indicates a coherent wave, wave normal angle (θ) and ellipticity (e), which describe the wave's propagation angle with respect to B_z and the rotation sense of its perturbation vector, respectively. Values for θ range from 0 to $\pi/2$, for which a wave with $\theta = 0$ propagates purely parallel to the field and a wave with $\theta = \pi/2$ propagates perpendicular to the field. Values for e range between −1 to +1, where $e \approx -1$ indicates a left-hand polarized wave, $e = 0$ indicates linear polarization and $e \approx +1$ indicates a right-hand polarized wave. Moderate masking (using the NaN flag) is applied to the spectral analysis results to facilitate interpretation: cells with wave power < 0.01 nT^2/Hz are masked when plotting P^2, and cells with $P^2 < 0.5$ are masked when plotting θ and e. The masking eliminates much of the remaining spacecraft spin tones or harmonics from the plots and clears away some, though not all of the extraneous measurement noise.

Wave observations can be partially characterized using the aforementioned spectral analysis tools. Between 10:55 and 11:02 UT, a series of peaks in wave power between 1 and 10 nT^2/Hz close to f_{He+} are visible in both Figure 2.1a and Figure 2.1b. I note that signatures of a magnetic field dipolarization are also observed at about 11:05 UT, visible in Figure 2.1g as well as in the accompanying panels. Within the interval prior to the dipolarization, which is the

interval of interest in this chapter, there are two shorter intervals, from 10:57:50 to 10:58:40 UT and from 11:00 to 11:01 UT, when total wave power is significant, coherent, and present right below and across f_{He+} without a clear cold plasma stop band. I focus my attention on the waves during these two short intervals. It is clear that the highly polarized waves are propagating primarily parallel to the field ($\theta \approx 0$) and have left-handed rotation ($e < 0$), both attributes matching those of EMIC waves. Since the waves emitted power both below and above f_{He+}, however, the question arises whether the waves can be characterized as He^+ band waves, proton band waves, or both, strictly in the context of cold plasma theory. (I note that the selected FFT spectral resolution is 0.002 Hz and frequency averaging has been avoided in order to avoid wave power overlap.)

Whereas in the cold plasma approximation clear stop bands appear near each heavy ion gyrofrequency and left-hand polarized waves cannot exist within the stop bands, the approximation is an oversimplification. To better address this concern, I consult measurements of the plasma and particles and show that the waves indeed should exhibit signatures that differ from the familiar cold plasma case.

Before closing this section, however, I point out that the differences in ion (Ni_ESA) and electron (Ne_ESA) densities in Figure 2.1f are purely instrumental and have to do with the spacecraft positive charging that repels ions up to an energy comparable to the spacecraft potential, whereas electron densities suffer in part from photoelectrons (but can be avoided by a good measure of the spacecraft potential from the electric field instrument) and in part from cold (~1 eV) ambient electrons that cannot be distinguished well from the photoelectrons at very low energies. The spacecraft potential-determined density (Ne_SCpot), however, is not affected by missing the cold populations and can thus approximate the total plasma density quite well. It is

evident that Ne_SCpot agrees with Ni_ESA between 11:00 and 11:03UT while before that interval the ion ESA underestimates the total ion density. I will come back to this point later in this chapter.

2.3.2 Particle observations and ion species separation during plasma flows

Data from the ESA instrument during the EMIC wave event are shown in Figure 2.2 (the wave power spectrum is shown in Figure 2.2a for reference). The ESA instrument measures ions (energy per charge without mass discrimination) from ~6–7 eV up to 25 keV and electrons from ~6–7 eV to 30 keV. The remaining panels in Figure 2.2 show the ion flow velocities in the FAC system (Figure 2.2b), energy-time spectrograms for ions (Figure 2.2c) and electrons (Figure 2.2d), and two pitch-angle spectrograms for energies: 5 to 500 eV (Figure 2e) and (Figure 2.2f) 10 to 25 keV. Key features during the time interval appear from 10:58 to 11:00 UT and 11:00 to 11:03 UT.

The time interval 10:58–11:00 UT corresponds to the period of maximum wave power. Looking at Figure 2.2f just before this interval, there is strong pitch angle anisotropy of the > 10 keV ions (assumed protons), with more energy flux perpendicular to the background field. During this maximum wave power interval, the perpendicular energy flux intensifies but is also accompanied by enhanced energy flux parallel and anti-parallel to the field. I interpret the increase in parallel and anti-parallel energy flux as due to strong pitch-angle scattering caused by cyclotron resonant scattering. The cyclotron resonant energy of energetic protons generally ranges from a few keV up to 10's of keV [e.g., *Gendrin and Roux*, 1980; *Chen et al*., 2010], which agrees well with the observations.

The second time interval, 11:00–11:03 UT, displays less wave power, but shows the onset of a plasma flow in Figure 2.2b, in v_y, peaking at about 80 km/s just before 11:02 UT. This

flow also coincides in the ESA ion spectra, Figure 2.2c, as two energy flux peaks at energies less than 200 eV. The flow is also evident as flow anisotropy of low-energy ions in Figure 2.2e as an energy flux concentrated perpendicular to the field. The pitch angle distribution of energetic ions shown in Figure 2.2f isotropizes during this interval of fast flow. The double peak in the energy flux enhancement visible in Figure 2.2c between 11:00 and 11:03 UT requires additional explanation.

As mentioned before, the THEMIS ion ESA does not measure plasma composition. A straightforward calculation using the observed $|v_y|$ and proton, He^+ and O^+ masses, however, allows the prediction of the ion kinetic energies if present during the fast flow. Cold protons carried by a fast flow of 80 km/s have a kinetic energy of $(0.5m_pv^2) \sim 30$ eV, whereas He^+ will have an energy ($0.5m_{He+}v^2 = 2m_pv^2$) of 120 eV. Figure 2.3 shows a zoomed interval from 10:59:40 to 11:04:20 UT when the ESA also recorded particle burst-mode data. The white traces superposed on Figures 2.3c, 2.3d, and 2.3e are the kinetic energy solutions for protons, He^+, and O^+ if present during the fast flow. With the exception of Figure 2.3e, the traces match the detected ion energy enhancements closely thus implying the presence of cold protons and He^+ in significant densities. Any notable densities of O^+ would result in an additional peak above that of He^+; I therefore conclude that the plasma does not contain much O^+ at this time.

At this point, recall that in Figure 2.1f the spacecraft potential-determined density, Ne_SCpot, agreed quite well with the ESA ion density, Ni_ESA, during the 11:00–11:03 UT interval, precisely the time when the low-energy ions were measureable by the ESA instrument due to their flow velocity that enabled their energy to exceed the electro-static repulsion from

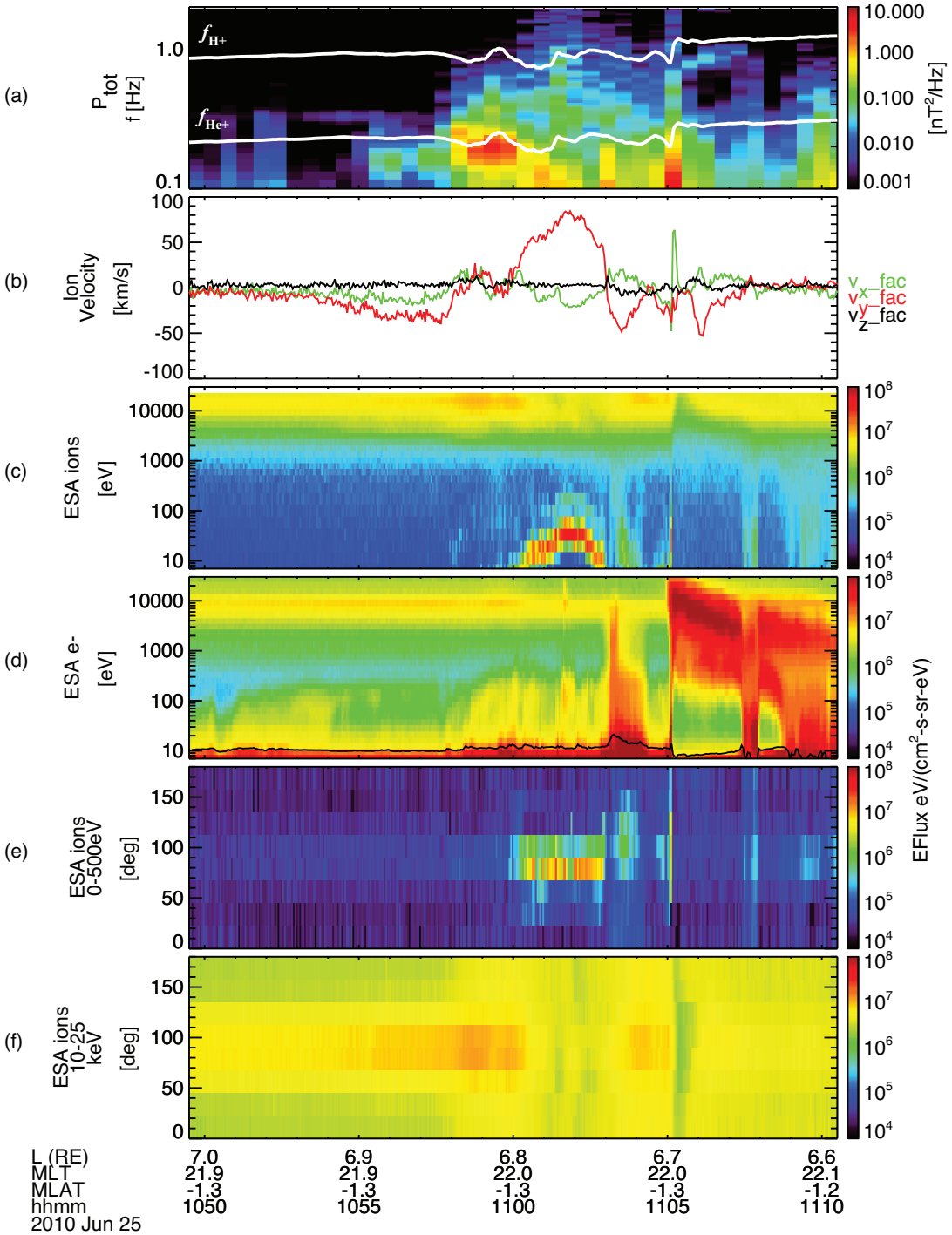

Figure 2.2: Stack plot summarizing the ESA observations during the interval of wave activity.

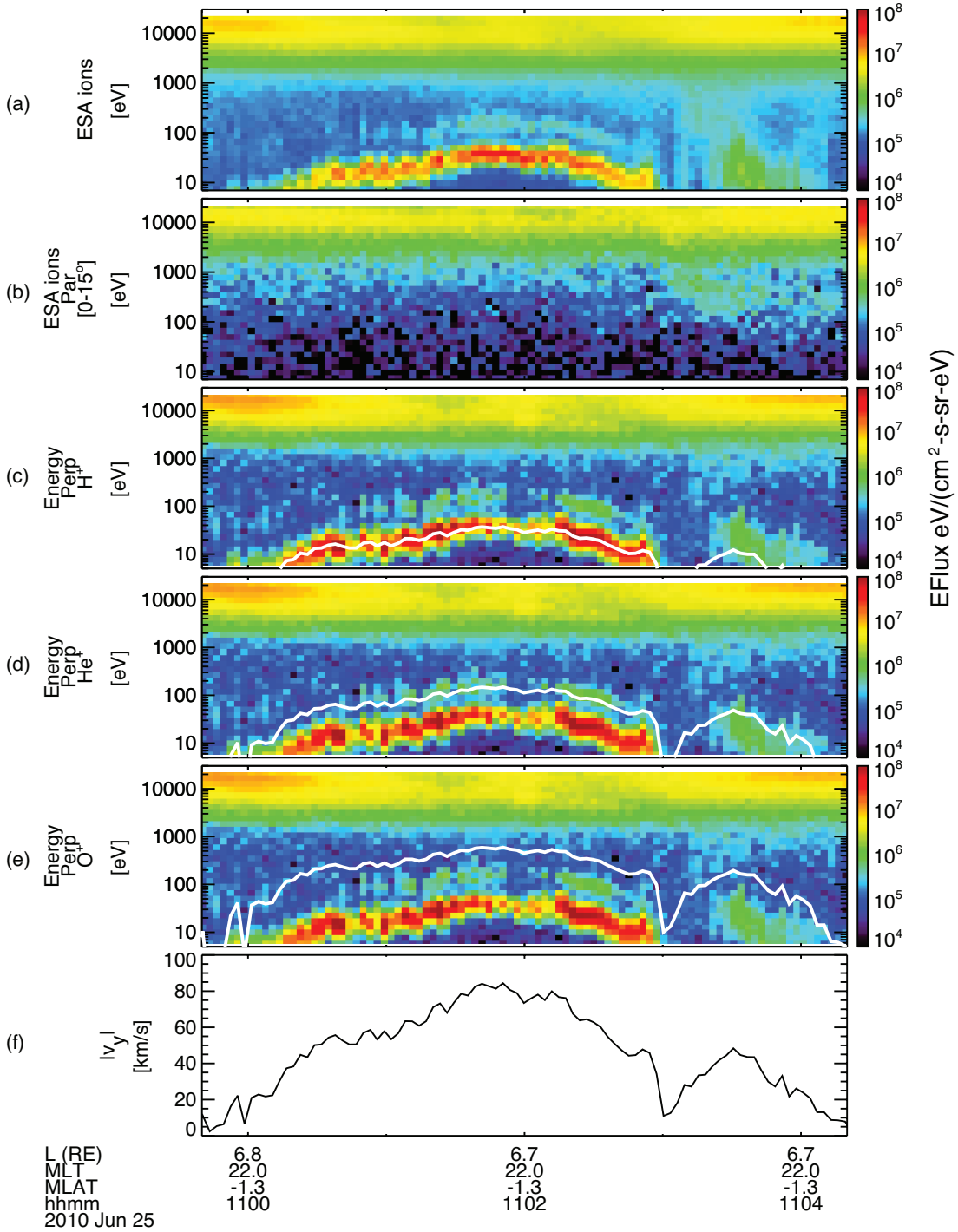

Figure 2.3: Stack plot showing the kinetic energy solutions of the cold ions detected during the fast plasma flow using $|v_y|$.

the positively-charged spacecraft. This suggests that Ne_SCpot is a good measure of the plasma density. But the fact that Ne_SCpot was actually larger than the ESA-determined density from both ions and electrons, and had a relatively large range from 20 to 80 cm^{-3} around the time of the wave activity suggests that the dominant part of the plasma is missed by the ESA instrument prior to the flow interval, and therefore primarily consists of cold plasma with energy below the sum of the spacecraft potential and the minimum ESA energy, i.e., < ~11 + ~7 = ~18 eV at 10:59 UT. The spacecraft potential has been superposed on the electron energy-time spectrogram (Figure 2.2d) as a solid black line.

The realization that multiple plasma species exist during the wave activity encourages a determination of the characteristics of each species by examining their observed phase space densities (PSD) to derive partial densities and temperatures. In Figure 2.4, 2-D cuts of the observed three-dimensional ion distribution functions, averaged over 18-second time intervals, are shown in the B-V coordinate system, where B is along the magnetic field direction and V contains the average velocity vector perpendicular to the field during the interval. Specifically, Figure 2.4a shows the hot proton anisotropy from 10:58:26–10:58:44 UT, i.e., when the peak wave growth was seen, and Figure 2.4b shows the two cold ion energy flux enhancements from 11:02:01–11:02:19 UT. Though it would have been ideal that the PSD contours are calculated over the same time interval, the cold ions were not in motion during the time of strong pitch angle anisotropy of the hot protons and eluded measurement by the ESA; it is assumed based on inference from the earlier discussion regarding Ne_SCpot that the cold ion distributions were also present during the interval of hot proton anisotropy. It is evident in Figure 2.4a that the hot protons are anisotropic, with more PSD distributed perpendicular (V_V) to the field than along

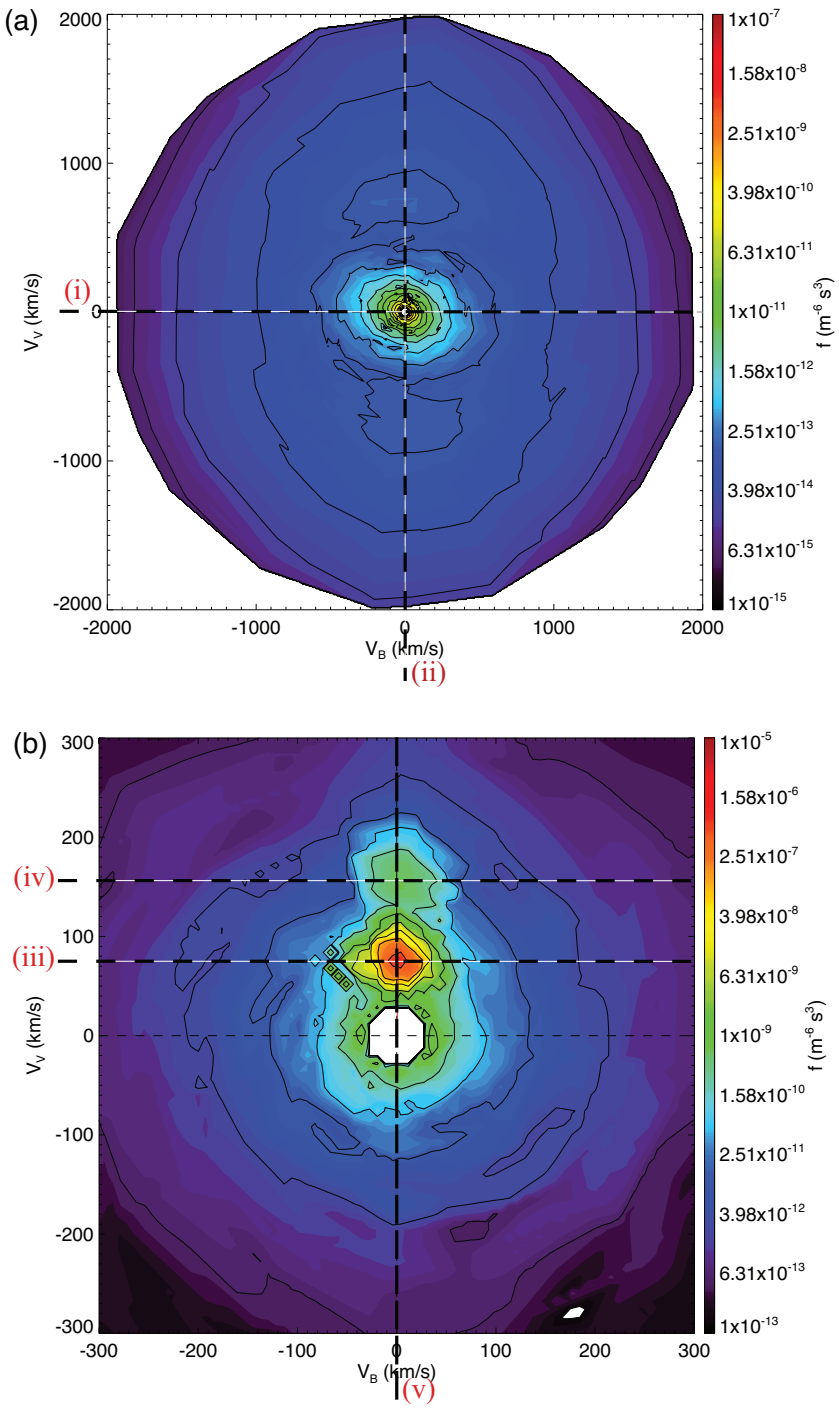

Figure 1.4: Observed phase space densities of (a) the full ion distribution function over the time interval 10:58:26–10:58:44 UT and (b) cold ions below 500 eV over the time interval 11:02:01–11:02:19 UT. The anisotropic energetic ions with velocities greater than 800 km/s in Figure 2.4a are assumed protons. The cold ions present within the fast plasma flow, indicated by the long horizontal dashed lines, are (iii) protons and (iv) He^+ and are re-plotted separately in Figure 2.5; the long vertical dashed line (v) denotes the cut along the perpendicular direction.

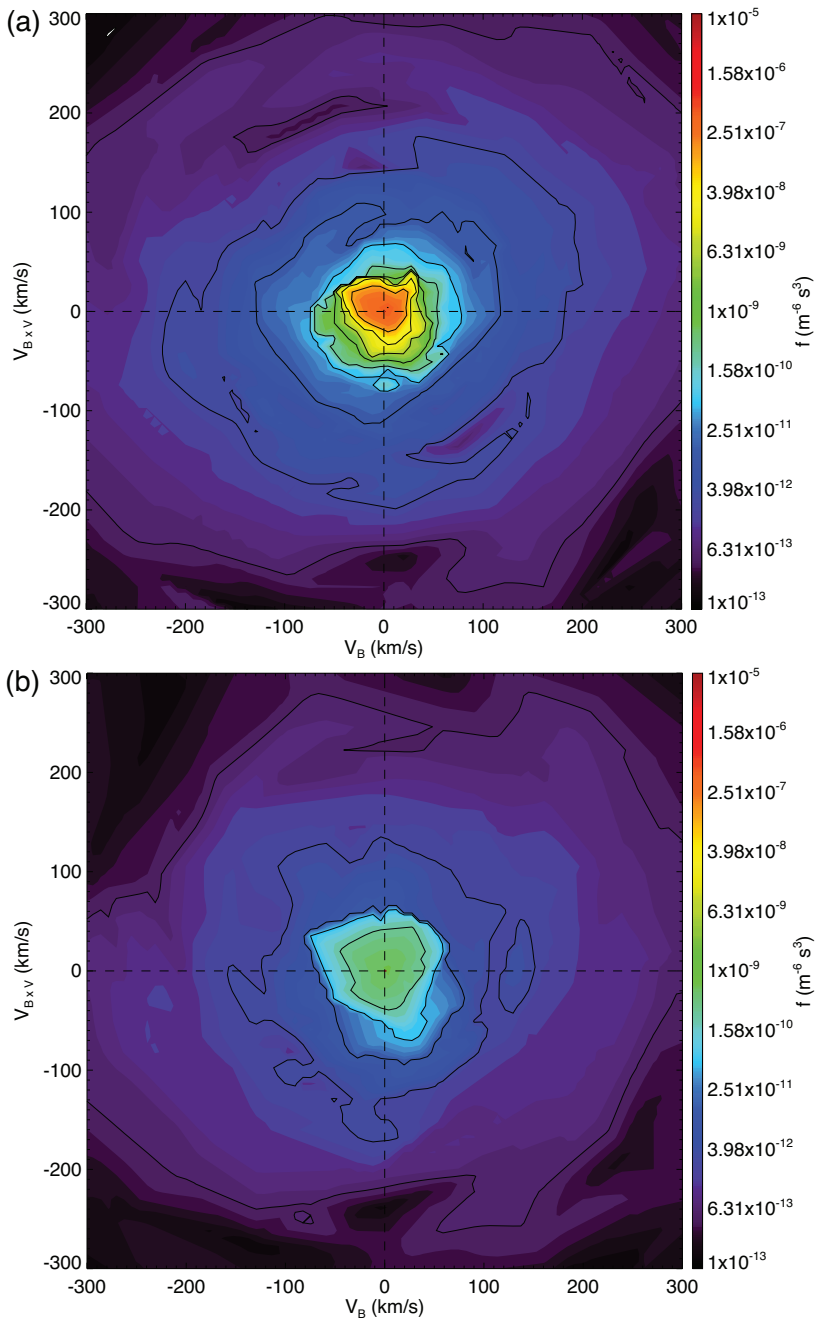

Figure 2.5: Observed phase space densities of the cold ions with the velocity space origins shifted using the offsets shown by the long horizontal dashed lines at (iii) 85 km/s and (iv) 155 km/s in Figure 2.4 over the time interval from 11:02:01 to 11:02:19 UT: (a) cold protons and (b) cold He^{+}.

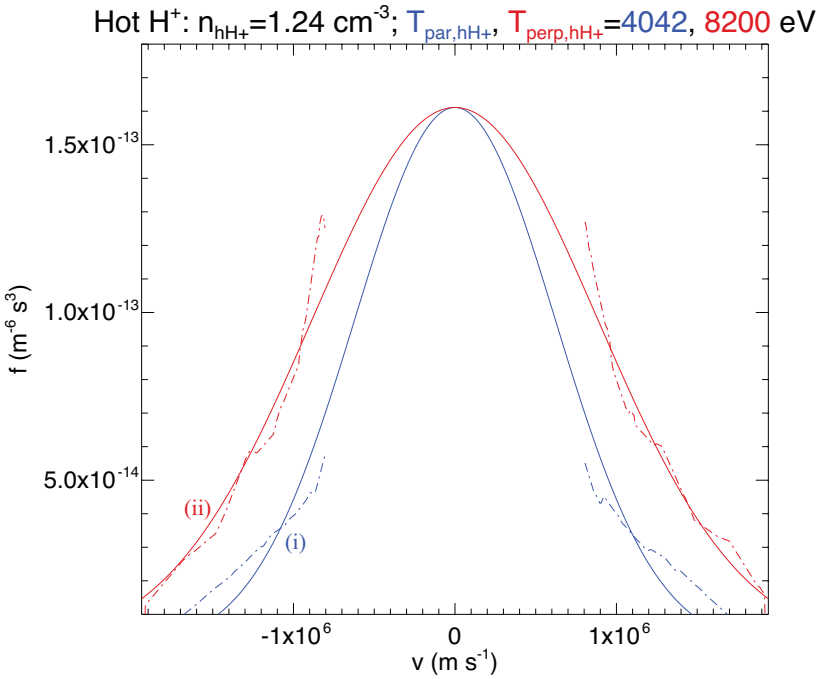

Figure 2.6: Bi-Maxwellian distribution (blue and red solid lines) fitted to the observed PSD cross-sections (blue and red dash-dotted lines) of hot protons shown by the dashed lines in Figure 2.4 (i) along the field, plotted in blue, and (ii) perpendicular to the field, plotted in red. The bi-Maxwellian distribution is fitted to the observed PSD of protons with energies greater than 3 keV (800 km/s).

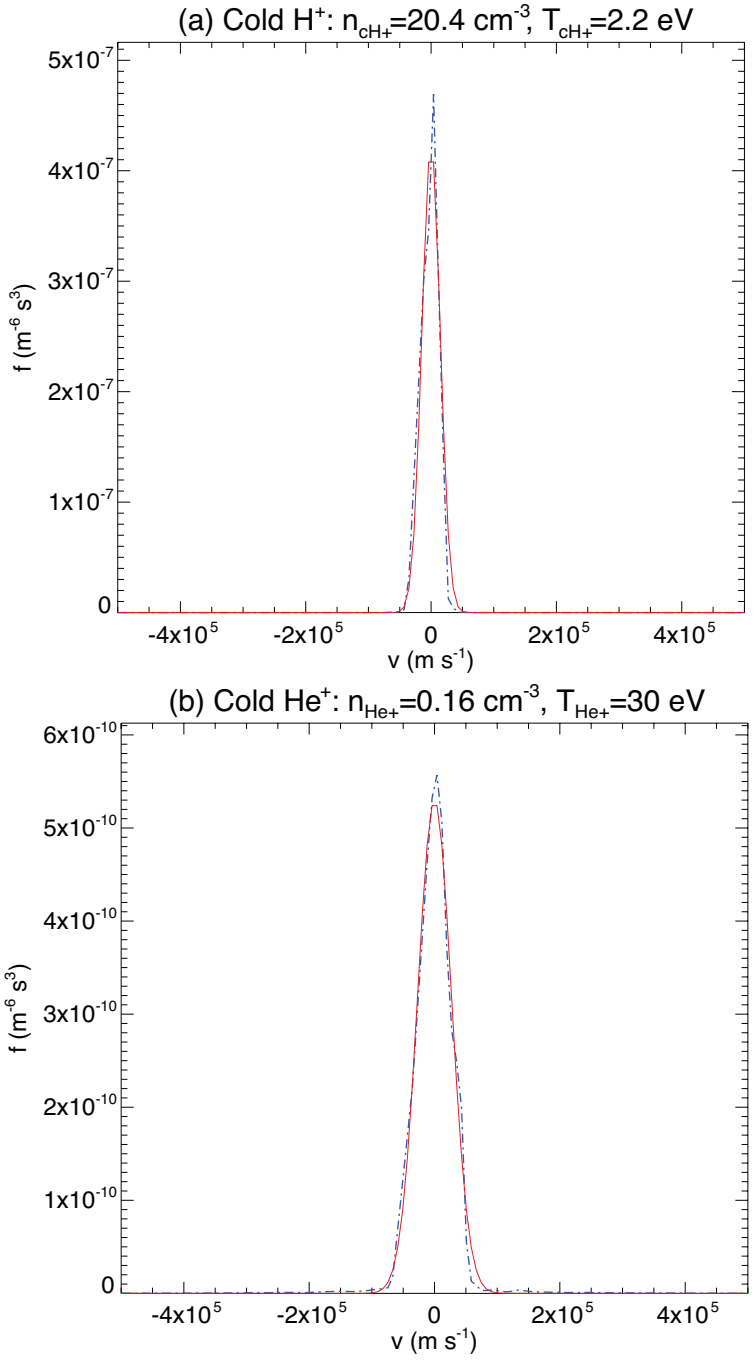

Figure 2.7: Maxwellian distributions (solid red lines) fitted to the PSD cross-sections (dash-dotted blue lines) of (a) cold protons and (b) cold He^+ as shown in Figure 2.5. Both ion species are assumed isotropic.

(V_B) it. I mark the two directions (parallel and perpendicular) with lines (i) and (ii) to remind the reader that I will perform 1D cuts of this distribution along these lines later, for modeling. By comparison to the hot ions, the cold ions, seen in Figure 4b are isotropic. The PSD of the cold ions can be analyzed separately by obtaining 2D velocity space cuts along the plane normal to the B-V plane that contain the dashed lines (iii) for cold protons, at 85 km/s, and (iv) for cold He^+, at 155 km/s. Additionally, the perpendicular cut for both ions is denoted by a vertical dashed line (v). The PSD is then recalculated for each cold ion distribution. Note that the white hexagonal core that is surrounded by residual PSD (noise) at the lowest velocities is not real. In Figure 2.5, the individual PSD of cold protons (Figure 2.5a) and He^+ (Figure 2.5b) are shown, representing planar cuts intersecting the B-V plane along lines (iii) and (iv) in Figure 2.4.

To obtain the density and temperature of each ion species, I fit the observed PSD with Maxwellian distributions. This is achieved using a least squares fitting method. A single bi-Maxwellian distribution is used for fitting of the hot proton distribution due to the clear temperature anisotropy that was seen in Figure 2.4a. I note that fitting of the anisotropic hot protons is achieved by excluding the PSD of ions with kinetic energies less than about 3 keV (800 km/s), which are seen to peak near the origin in Figure 2.4a. This kinetic energy cut-off was determined by considering that hot protons with energies from a few keV to tens of keV make up the expected resonant particle distribution. Fits with this kinetic energy cut-off shifted to ~2 and ~5 keV (600 and 1000 km/s, respectively) were also performed and yielded similar fitting results that also indicated clear temperature anisotropy of the hot proton distribution. I use the 3-keV energy cut-off to avoid including cooler particles in the fitting, and to ensure that the fitting captures the previously noted energy range of resonant particles. The hot proton anisotropy, $A_{hH+} = T_{perp,hH+}/T_{par,hH+} - 1$, where $T_{perp,hH+}$ and $T_{par,hH+}$ are the perpendicular and parallel temperature

of the hot protons, was about 1.03 for the fitting that excluded PSD of ions <3 keV (Figure 2.6). On the other hand, the roughly isotropic cold proton and He^+ distributions are fitted with Maxwellian distributions, as shown in Figures 2.7a and 2.7b. The densities and temperatures of each ion species as obtained through the fitting are summarized in Table 2.1, along with other relevant parameters that help define the plasma environment during the interval of wave observations. The drift velocities are set to zero during the fitting of the various Maxwellian distributions to the PSD data.

2.4 Linear theory

The dispersion relation for parallel propagating EMIC waves and the various cases presented in this section follow the methodology described by *Chen et al*. [2011]; products are obtained using the wave dispersion relation in dimensionless form [following *Swanson*, 1989] and incorporate the plasma dispersion function as defined by *Fried and Conte* [1961]. Only the solutions to the parallel propagating case are shown due to general acceptance that wave growth is most rapid for parallel waves [e.g., *Kennel and Petschek*, 1966]. Numerical solution of the dispersion relation using the observed plasma parameters indeed demonstrates the presence of an unstable wave mode that can propagate across Ω_{He+}. My results extend previously explored conditions for the unstable wave mode to very low-densities of the warm He^+ plasma component (where "warm" indicates ~few eV < T_{He+} < 100 eV to distinguish He^+ from a typical cold plasma of $T \approx 1$ eV). To better understand the effects that warm He^+ density and temperature have on the propagation of the unstable wave mode, that component's density and temperature are alternately varied. Additionally, results of parametric study of the relationship of warm He^+ characteristics to EMIC wave instability due to warm plasma effects are presented.

Table 2.1: A summary of the space plasma environment parameters as observed by TH-A on 25 June 2010.[a]

Species	Hot protons	Cold protons	Warm He^+	Cold electrons
n_s (cm^{-3})	1.24	20.4	0.16	21.8
$T_{par,s}$ (eV)	4042	2.2	30	1
$T_{perp,s}$ (eV)	8200	2.2	30	1

[a]The number densities and temperatures of the hot and cold protons and warm He^+ are approximate values obtained from least squares fitting of Maxwellian distributions to the observed PSD. The cold electron component's density is based on the sum of all ion components and ensures charge neutrality. B_o = 60 nT; n_{total} = 21.8 cm^{-3}.

2.4.1 Modeling using observed plasma parameters

Numerical solutions to the dispersion relation for parallel-propagating EMIC waves are shown in Figures 2.8a and 2.8b showing the real (ω_r) and imaginary (ω_i) wave frequencies (normalized to the proton gyrofrequency, Ω_{H+}) as a function of normalized wave number, kc/ω_{pH+}, where c is the speed of light and ω_{pH+} is the plasma frequency of protons; ω_i is also referred to as the wave growth rate, with the range of positive values corresponding to wave growth. The results are consistent with the observations of maximum wave power detected very near f_{He+}. The dispersion relation is obtained in a homogeneous plasma containing cold electrons, cold protons with a Maxwellian distribution, warm He^+ with a Maxwellian distribution and hot anisotropic protons with a bi-Maxwellian distribution. The thin black solid lines in Figure 2.8a show, for reference, the cold plasma dispersion relation, i.e., the case with n_{He+} = 0.16 cm^{-3} and all particle species temperatures set to be cold. The familiar banded structure is clear, with a narrow stop band starting at and ending just above Ω_{He+}, where the stop band is between Ω_{He+} and the cut-off frequency ($\Omega_{He+} < \omega < \omega_{co}$), labeled ω_{co} and denoted with a thin black dashed line. The thick red solid line in Figure 2.8a shows the solution obtained by considering all the temperatures of the multiple ion species as estimated through the fitting; it shows that the wave mode can indeed

propagate across Ω_{He+}. This mode possesses maximum growth rate just under Ω_{He+} (Figure 2.8b), but has positive growth rates over a frequency range including Ω_{He+} as well as above it.

I now note that the observed plasma parameters applied to solving the dispersion relation shed new light on previous results obtained by *Chen et al*. [2011]. In previous work, the unstable mode caused by the hot proton anisotropy ($n_{hH+} > 7.5$ %; $T_{par,hH+} > 25$ keV; $A_{hH+} > 1.3$) that propagates across Ω_{He+} is produced under the primary condition of sufficiently high He^+ temperature ($T_{He+} > 100$ eV) and lower density ($n_{He+} < 4\%$). The present study probes the low He^+ density condition at a He^+ temperature at least a factor of 3 lower than this previously presented nominal case. It is also shown here that the unstable mode also occurs in a high-density, cold plasma ($n_{total} \sim 20$ cm^{-3}; $\omega_{pe}/|\Omega_e| \sim 20$) with hot proton temperature anisotropy ($n_{hH+} \sim 5\%$; $T_{par,hH+} \sim 4$ keV; $A_{hH+} \sim 1$), but with very low densities of warm He^+ ($n_{He+} < 1\%$; $T_{He+} \sim 30$ eV). The new results refine the low-density warm He^+ condition and show that the unstable mode occurs within plasma containing much cooler He^+ and that the instability threshold may be exceeded due to a combination of the heavy ion's density and minimum temperature. To explore the density dependence of the unstable mode, the He^+ density is varied while keeping all other parameters unchanged. Although *Chen et al*. [2011] have noted temperature variation of He^+ as having a smaller effect on the dispersion relation, He^+ temperature is also varied separately to compare alongside the effects of the density variation.

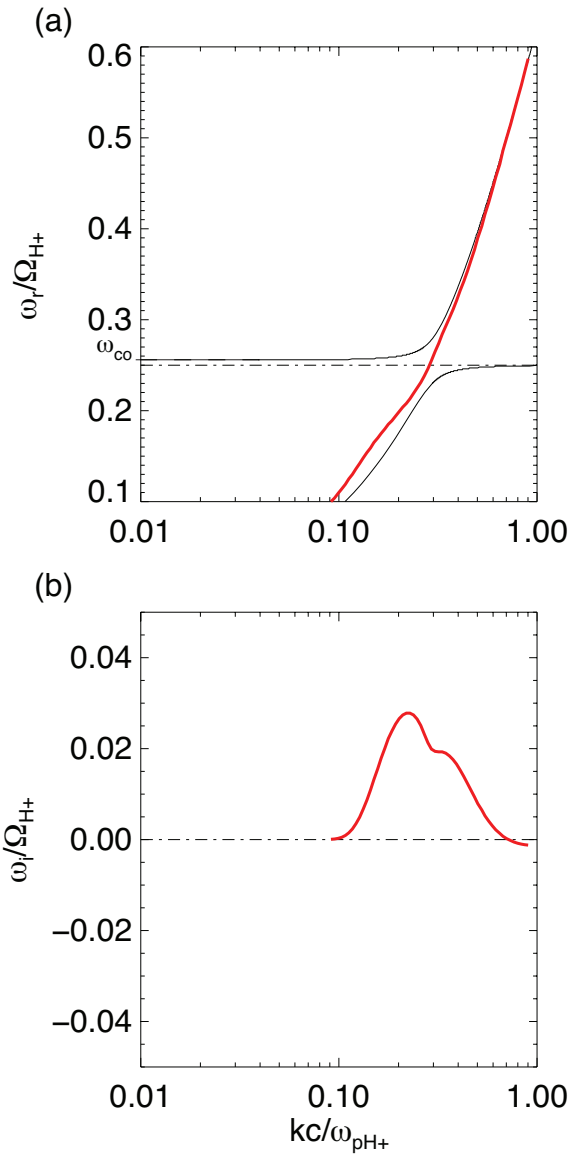

Figure 2.8: The dispersion relation for parallel propagating EMIC waves using the observed plasma parameters that shows (a) the relation between ω_r and k and (b) corresponding ω_i. Black horizontal dash-dotted lines in (a) and (b) denote Ω_{He+} and $\omega_i = 0$, respectively. With all particle species' temperatures set to be cold and $n_{He+} = 0.16\text{cm}^{-3}$, the cold plasma dispersion relation is plotted using thin black solid lines. The cut-off frequency, ω_{co}, is shown in (a) with thin black dashed lines and labeled along the left vertical axis.

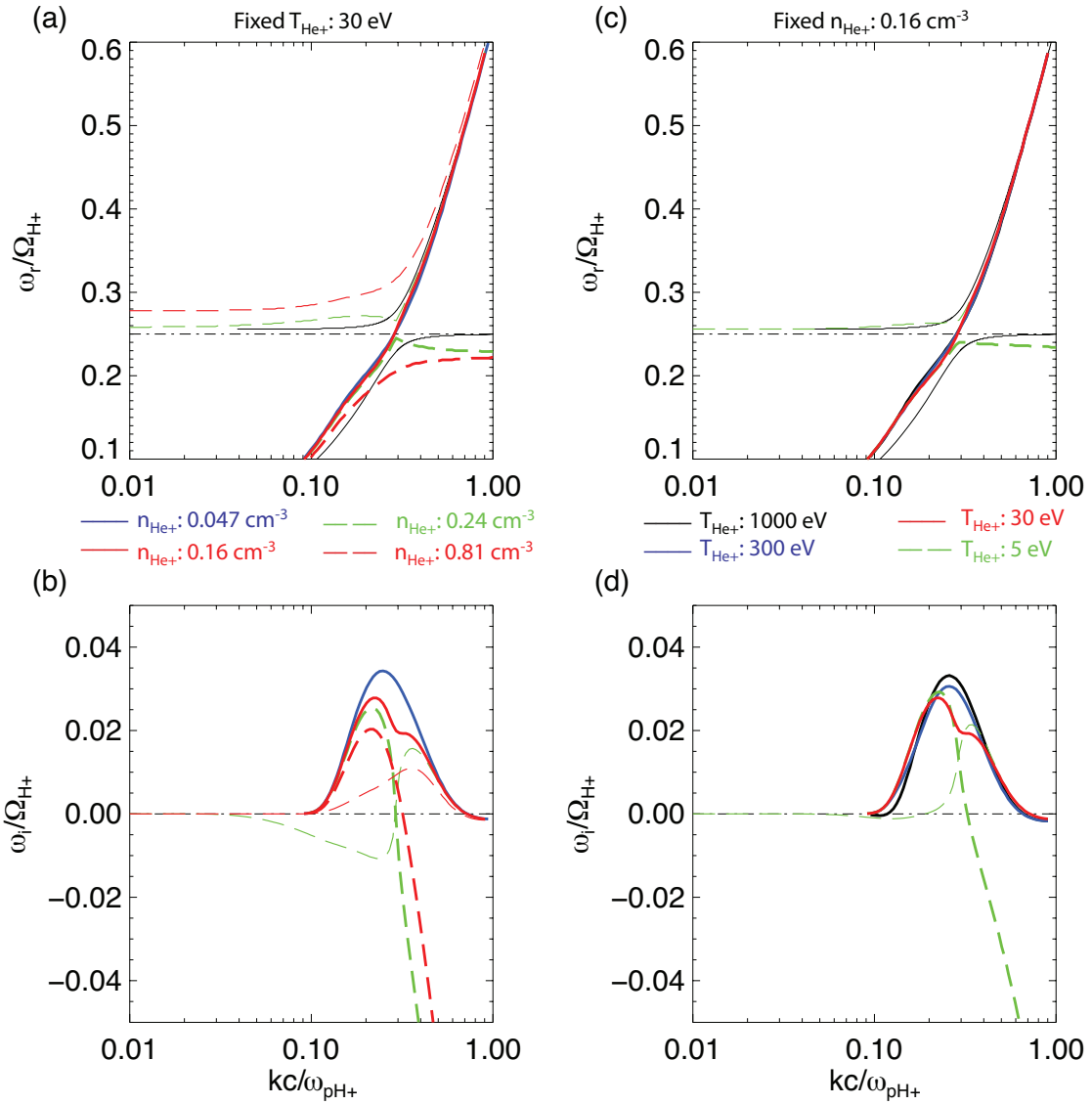

Figure 2.9: Several EMIC wave dispersion relation cases under Ω_{H+} obtained while varying He^+ density and temperature. (a) The relation between ω_r and k while varying warm He^+ density at fixed temperature (T_{He+} = 30 eV) and (b) corresponding ω_i. (c) The relation between ω_r and k while varying He^+ temperature at fixed density (n_{He+} = 0.16 cm^{-3}) and (d) corresponding ω_i. Thin black dash-dotted horizontal lines in (a) and (b) indicate Ω_{He+} and ω_i = 0, respectively; again, thin black solid lines represent the cold plasma dispersion relation for n_{He+} = 0.16 cm^{-3} with all particle species' temperatures set to be cold. (a to d) Long dashed lines represent the cases for which a He^+ stop band exists, where thick long dashed lines show ω_r and ω_i as a function of k for the He^+ band ($\omega < \Omega_{He+}$) and thin long dashed lines designate the relations for the proton band ($\Omega_{He+} < \omega < \Omega_{H+}$); thick solid lines represent the cases for no stop band, where thick red solid lines represent the observed case. Only the noted He^+ characteristics are varied; the remaining plasma parameters remain the same as the observed case, summarized in Table 2.1.

2.4.2 Variation of He^+ density and temperature

The role of warm He^+ characteristics on the unstable wave mode that propagates across Ω_{He+} can be explored numerically to better understand the contribution of density and temperature to the wave mode's generation. The EMIC wave dispersion relation at different He^+ densities is presented in Figures 2.9a and 2.9b. The observed case is plotted using thick red solid lines. It is clear that as He^+ density increases above the observed value (long dashed lines), the dispersion relation reverts back to resembling the cold plasma case. The stop band grows wider with elevated He^+ density, as more He^+ is available to damp the waves. This process of wave damping and subsequent He^+ heating has received much attention in the past [e.g., *Young et al*., 1981]. I also note that in the cases in which the wave modes split into two frequency bands, the waves have larger growth rates at wave frequencies below Ω_{He+}.

He^+ temperature variations indeed also affect the generation and propagation of the unstable mode, as previously noted. Traces of the dispersion relation at different He^+ temperatures are presented in Figures 2.9c and 2.9d for fixed density. It is apparent that if the He^+ temperature drops to 5 eV (green dashed lines), the dispersion relation splits into two separate modes, suggesting that He^+ that has been heated even slightly (e.g., above 5 eV for n_{He+} ~ 0.7%) can still play a role in generation of the unstable wave mode across the He^+ gyrofrequency. Even if the He^+ stop band appears again when He^+ temperature drops below the threshold for the single unstable EMIC wave mode, warm plasma effects continue to affect dispersion for wave numbers at ω_r near Ω_{He+}, specifically, catastrophic damping occurs at high wave numbers, which was previously noted by *Chen et al*. [2011] to place severe limits on the scattering energies of electrons. As He^+ temperature increases above the observed temperature to 300 eV (thick blue solid line) and 1000 eV (thick black solid line), the single unstable wave

mode becomes more defined and the maximum growth rate increases; the range of wave frequencies with positive growth rate narrows slightly.

In summary, I find that it is the combination of warm He^+ density and temperature that contributes to the occurrence of the single unstable wave mode. Very low density of He^+ leads to increased instability and larger deviation from the cold plasma dispersion relation. Conversely, high He^+ component densities result in damping of EMIC waves with ω_r near Ω_{He+}. Although the observed temperature is lower than the nominal case presented by *Chen et al.* [2011], the temperature is still warmer than that of typical plasmaspheric cold ions of a few eV. The fact that an extended temperature range leads to instability of a single, crossing mode suggests a possible mode evolution: cold heavy ions enable initial wave growth but it is not until moderate heating of those ions occurs that the waves can extend over a broad frequency range and resonate with an energy range of both hot ions and relativistic electrons that differs significantly from the cold plasma approximation.

2.4.3 Parametric study of warm He^+ effects on EMIC wave growth

An extended study of the specific cases presented in Figure 2.9 is undertaken to obtain a larger picture of the relationship of the warm He^+ parameter variability to EMIC wave instability. A wide range of parameters are studied by varying twenty increments of n_{He+}/n_{cH+}, from 0.0008 to 0.25, at twenty increments of T_{He+}, from 0.001 to 1 keV; the remaining ion components' parameters remained fixed and the cold electron component density was varied only to maintain charge neutrality. The 400 cases are visualized in Figures 2.10a and 2.10(b) as two contour plots that show the peak ω_i for each case (Figure 2.10a) and ($\omega_r - \Omega_{He+}$) where the peak ω_i occurs

(Figure 2.10b); cases with $\omega_i/\Omega_{H+} < 0.001$ are masked in both plots. The cases from Figure 2.9 are superposed as symbols on the contour plots.

The contours of peak ω_i, Figure 2.10a, show a few trends. The density dependence of peak ω_i is immediately apparent: increasing n_{He+}/n_{cH+} at any T_{He+} results in decreasing peak ω_i; for $T_{He+} < 0.02$ keV, peak ω_i decreases monotonically with increasing n_{He+}/n_{cH+}; for $T_{He+} > 0.02$ keV, peak ω_i also decreases with increasing n_{He+}/n_{cH+} but evolves in a less organized manner, e.g., sudden drop-offs in peak ω_i occur for $T_{He+} > 0.1$ keV as n_{He+}/n_{cH+} increases above 0.02. Additional trends can be seen when examining for temperature influences on peak ω_i at a given n_{He+}/n_{cH+}: the first trend is present only at $n_{He+}/n_{cH+} < 0.002$, as increasing T_{He+} leads to increasing peak ω_i; an opposite trend is present at n_{He+}/n_{cH+}, > 0.05, where increasing T_{He+} leads to decreasing peak ω_i; and, for $0.002 < n_{He+}/n_{cH+} < 0.05$, variations of T_{He+} can lead to both increasing and decreasing peak ω_i. An example of the last trend can be seen at $n_{He+}/n_{cH+} = 0.008$ and also in Figures 2.9c and 2.9d: as T_{He+} is increased incrementally from 0.001 to 1 keV, peak ω_i starts out near 0.03, decreases towards 0.02 and then increases towards 0.04.

Additional trends surface when examining the value of $(\omega_r - \Omega_{He+})$ where peak ω_i occurs, Figure 2.10b. For any T_{He+}, increasing n_{He+}/n_{cH+} results in peak ω_i occurring at larger deviations from Ω_{He+} (i.e., $|\omega_r - \Omega_{He+}|$ increases). For $0.0008 < n_{He+}/n_{cH+} < 0.01$, increasing T_{He+} leads to decreasing $|\omega_r - \Omega_{He+}|$, with higher T_{He+} leading to peak ω_i occurring at ω_r very near Ω_{He+} (i.e., $(\omega_r - \Omega_{He+}) \sim 0$). For $n_{He+}/n_{cH+} > 0.01$, peak growth is confined to $(\omega_r - \Omega_{He+}) < 0$, even for increasing T_{He+}. Again, $T_{He+} \sim 0.02$ keV appears to be an important temperature. For $0.002 < n_{He+}/n_{cH+} < 0.05$, the temperature is seen to separate two distinct behaviors of the $(\omega_r - \Omega_{He+})$

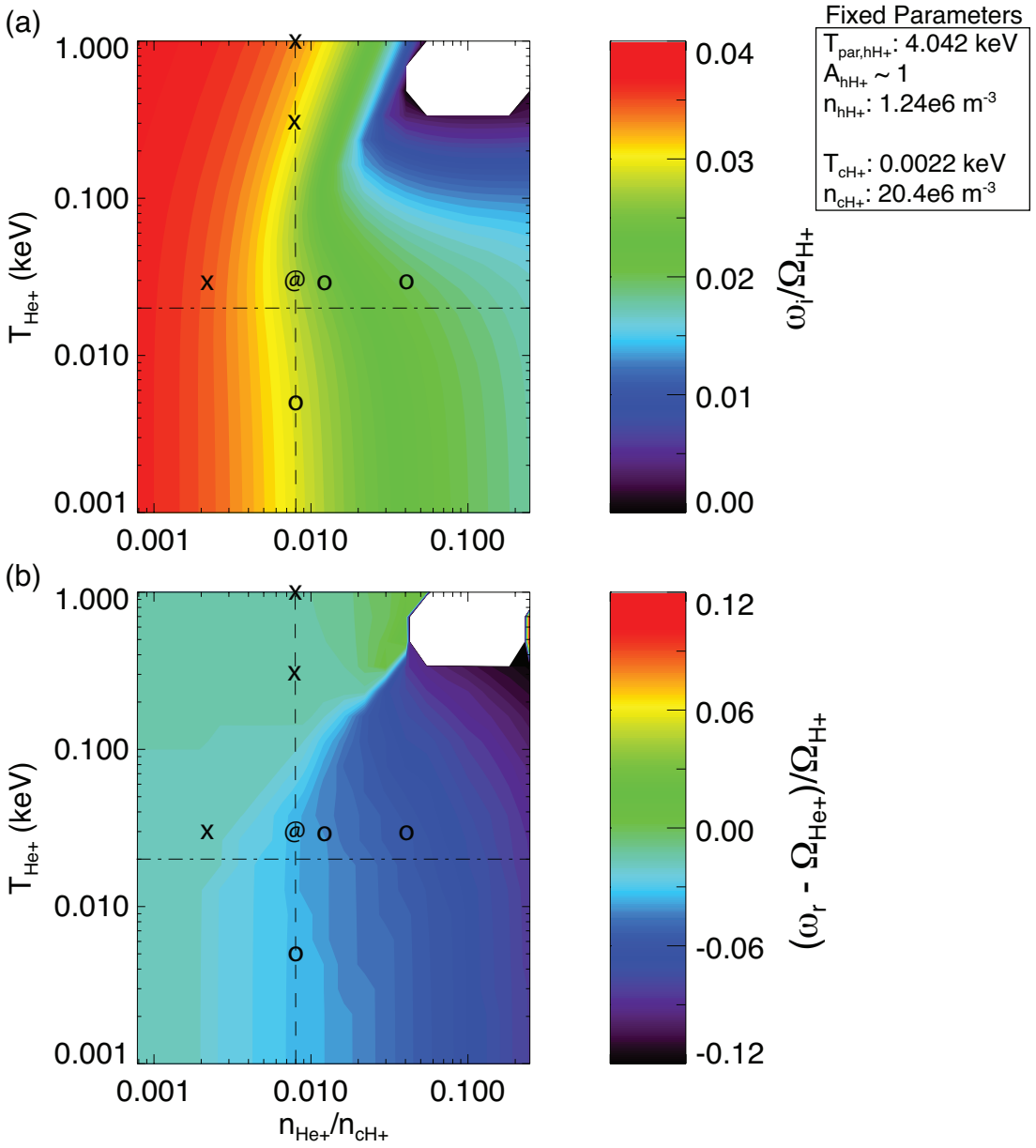

Figure 2.10: Contours of (a) peak ω_i and (b) ($\omega_r - \Omega_{He+}$) where peak growth rate occurs for 20 different n_{He+} at 20 different T_{He+}. Symbols @, x, and o designate the cases presented in Figure 2.9: @ indicates the observed case, "x" indicates the cases without a He^+ stop band, and "o" indicates the cases for which a He^+ stop band exists. Horizontal dash-dotted lines designate T_{He+} = 0.02 keV and vertical dashed lines designate n_{He+}/n_{cH+} = 0.008 (n_{He+} = 0.16 cm^{-3}).

contours; for T_{He+} < 0.02 keV, ($\omega_r - \Omega_{He+}$) < 0 and remains nearly the same at any given density; this changes significantly as heating to T_{He+} > 0.02 keV occurs, with ($\omega_r - \Omega_{He+}$) ~ 0 and eventually positive at higher temperatures.

Results of the parametric study reemphasize significant points brought up in previous sections. I find that the effects of heavy ion characteristics in the presence of hot proton anisotropy on EMIC wave instability are strongly coupled to density changes but are also influenced by changes in temperature. In particular, the changes in peak ω_i and ($\omega_r - \Omega_{He+}$) as T_{He+} increases above 0.02 keV for $0.002 < n_{He+}/n_{cH+} < 0.05$ supports the suggestion in section 2.4.2 of an EMIC wave mode evolution that occurs only when He^+ is heated above a critical temperature.

2.5 Discussion and conclusions

Although the observations and modeling results agree well, the clear signatures of wave power crossing over f_{He+} could have a different explanation, which I explore and refute here. The possibility exists that in the presence of parallel flows the waves are Doppler-shifted into the range of the local gyrofrequency. Close inspection of the ion velocity moments in Figure 2.2b shows that v_z also shows a small but finite flow velocity of a few km/s. The peak flows in v_z occur in the time interval 10:58–11:00 UT, coincident with the dominant wave power and signatures of f_{He+} crossover. The flows in v_z, however, are exceedingly small and certainly less than 10 km/s. From the angular real frequency of the dispersion relation at peak power I obtain $\omega_r \approx 0.24$ rads/s, with $\Omega_{He+} = 0.25$ rads/s. From the dispersion relation, for $\omega_r = 0.24$ rads/s, $kc/\omega_{pH+} \approx 0.3$, which corresponds to $k = k_z = 5.265\text{e}{-3}$ km^{-1}. A plasma flow with $v_z = 10$ km/s may then cause a Doppler-shift $\Delta\omega_r \approx 0.0526$ rads/s, bringing the peak power waves across the local gyrofrequency and into the stop band. Larger or smaller gains in frequency can be observed for different flow speeds. Whereas minor plasma flows in v_z can Doppler-shift f_{actual} closer to the He^+ stop band, the wave emissions observed from 11:00–11:01 UT, which also show wave power just under and through f_{He+}, cannot be explained in this way. Moreover, flows on the order

of a few km/s are very near the random noise value of the ESA instrument (and consistent with statistical fluctuations of the hot plasma thermal velocity of several hundreds of km/s). I therefore suggest that though this possibility of a Doppler-shift is not out of the question, it is not the most likely explanation of the observed, persistent presence of wave power within the He^+ stop band.

I would also like to point out that the technique I have used to determine the plasma composition during the EMIC wave observations could be applied towards future cases. As discussed earlier, the positive spacecraft potential repels the majority of the ambient cold ions under steady conditions. Flows associated with ULF waves and convection, however, may allow sampling of these cold ion populations. Some preliminary limits for use of this plasma composition technique have been determined using the measured spacecraft potential and ion flow velocities. In the absence of flows ($v = 0$) and a spacecraft potential < 12 V (+ ~7 eV ion ESA minimum energy), protons with thermal velocities $v_{th} = (k_B T/m_p)^{-1/2} \approx 41.5$ km/s or larger ($T_{H+} > 18$ eV) can be sampled. A flow velocity > 60 km/s ($0.5 m_p v^2 \sim 19$ eV) at 11:02 UT allowed for clear sampling of the cold proton species ($T_{H+} \sim 2.2$ eV); the spacecraft potential was near 11 V at this time such that protons with energies > 11 + ~7 eV = 18 eV were within the minimum energy threshold and could be discerned by the ion ESA. This suggests that for flow velocities > 60 km/s and a spacecraft potential < 12 V, even 0 eV particles may be sampled by the ion ESA. The limits for sampling of the additional heavy ion species He^+ and O^+ can be determined using the straightforward methodology discussed above. Conditions matching these initial limits are easily satisfied throughout the magnetosphere, allowing for the application of this technique towards determining the composition of the equatorial magnetosphere as well as clarifying the conditions for EMIC wave growth.

In summary, a unique observation of EMIC waves by TH-A has been presented in this chapter. Fortuitous observations of the cold ions that were likely present throughout the period of wave growth were made by taking advantage of an enhanced flow period just shortly after the peak EMIC wave power was observed. Using a numerical solution of the linear warm plasma dispersion relation I found that the unstable EMIC wave mode obtained from parameters consistent with observations has maximum growth rate just below Ω_{He+}, is unstable from below Ω_{He+} and without a stop band at Ω_{He+} and thus does not fit the typical characteristics of the cold plasma dispersion relation. The results provide the first observational evidence of a class of EMIC waves predicted by warm plasma theory that can be unstable within a cold plasma stop band. As recent theoretical work has already shown, EMIC waves that do not have a cold plasma stop band(s) are severely damped at high wave number and, thus, can only interact with high-energy electrons > a few MeV. If we take the maximum wave number of the observed case where the wave mode was undamped and compute the minimum resonant energy of relativistic electrons from

$$E_{res\parallel}^{e} = \left(\left[\frac{\Omega_e^2}{c^2 k_\parallel^2} + 1 \right]^{1/2} - 1 \right) E_o,$$

we obtain an estimate near 3 MeV, which lies within the energy range discussed by *Chen et al*. [2011]. It remains to be determined experimentally where this class of EMIC waves occurs and the conditions of the magnetospheric plasma that support their generation. If these waves are a common occurrence, their existence will significantly alter predictions of their influence on high-energy electron scattering.

Parametric study of the density and temperature of warm He^+ further illustrated the competition between various ion plasma species and the influences of the heavy ion's characteristics on EMIC wave instability, reiterating the importance of considering individual

ions' attributes to more accurately characterize EMIC waves. The realization that a multi-species plasma containing low densities of warm He^+ can engender EMIC waves that are not damped at the heavy ion's gyrofrequency has implications for theories seeking to quantify the effects the waves have on related processes, such as ion heating and losses of high-energy electrons. Investigation of additional wave and particle observations can provide more accurate maps of heavy ion density and temperature in the magnetosphere and the corresponding effects on EMIC waves, even when cold plasma and composition measurements are impossible or hard to make.

CHAPTER 3

Global multi-spacecraft study of magnetospheric cold and warm ion species

3.1 Introduction

Obtaining the occurrence rates and properties of cold (T_s < hundreds of eV) or low-energy (E_s < 1 keV) ions is a challenge using in-situ measurements from spacecraft observing the charged particle environment of Earth as well as of other planets. Even with time-of-flight ion mass spectrometers, high time- and energy-resolution particle instruments, and techniques to temporarily lower the floating potential of sunlit spacecraft, observation of such ions remains difficult due to spacecraft positive charging by solar ultraviolet radiation that overwhelms the negative charge deposited by ambient thermal electrons [e.g., *Olsen*, 1982; *André and Cully*, 2012, and references therein]. Yet, the observation and characterization of low-energy plasmas in space is still important. They influence processes such as the growth and evolution of EMIC (electromagnetic ion cyclotron) waves, may slow down magnetic reconnection at the dayside [*André and Cully*, 2012; *Walsh et al*., 2013], and enhance magnetic reconnection at the nightside [*Brambles et al*., 2011; *Lotko*, 2007]. As a result, there is considerable interest in observing them and understanding their involvement in physics of coexisting phenomena. At Earth, cold ions are observed over a broad range of states and altitudes. Sounding rockets and satellites probe the ionosphere and observe such ions thanks to the motion of the vehicle in relation to the ion velocity peak. Spacecraft at higher altitudes have provided such observations throughout the

magnetosphere over a range of geocentric distances and magnetic latitudes, again thanks to the motion of these ions along or across the magnetic field with sufficient velocity for the ion energy to exceed the spacecraft potential. With such a variety of vehicles providing ample opportunities for sampling of cold ions, one would have expected that detailed knowledge on such ions now exists. This, however, is not the case.

Previous work on cold ions using spacecraft data sometimes took advantage of ULF (ultralow frequency) waves or other drivers of bulk plasma flow that accelerated the low-energy plasmas, so they could be observed by particle instruments. This natural occurrence allows for detection of cold ions without use of an ion mass spectrometer or neutralizing spacecraft charging. *Kokubun et al*. [1977] investigated signatures of particle flux modulations by ULF waves using OGO 5 (Orbiting Geophysical Observatory 5) data, concluding that these modulations were due to plasma motion related to the waves. Only the modulation of the ion density was examined; compositional properties were not inferred. Advances in particle detectors have extended the lower energy range of such instruments to a few eV while also increasing the energy resolution, making it possible to study cases when ULF waves make cold ions (~1 eV) visible above the spacecraft potential [*Lennartsson and Shelley*, 1986; *Fuselier et al*., 1989; *Klumpar et al.*, 1990]. *Hirahara et al*. [2004] described observations of multiple ion species (H^+, He^+ and O^+) during Pc5 ULF waves using magnetic field and particle data from the GEOTAIL spacecraft. Observations during perigee (9 R_E) showed that cold ions could be observed near the magnetic equator and, in particular, the plasma sheet where they could match the partial density of the hot (few keV) ions. Around the same time, *Chen and Moore* [2004, 2006] used Polar TIDE (thermal ion dynamics experiment) data [*Moore et al*., 1995] during periods of plasma flows to also obtain limited samples of low-energy ions and their properties, and to study their

occurrence in the dayside magnetosphere between ~5 and 9 R_E. They showed that TIDE data could be used to provide approximations of the partial densities and temperatures of multiple ion species with temperatures of ~1–100 eV if a common plasma flow speed was assumed for observations made during the flows; they noted that this was an additional product of the prime TIDE mission to obtain ion composition as a time-of-flight ion mass spectrometer. In their latter study on low-energy ion occurrence, they showed that there was a greater than 50% chance of observing such ions near the afternoon magnetopause, near the same local time where other authors reported spacecraft observations of detached plasma or plasmaspheric drainage plumes [e.g., *Chappell*, 1974; *Carpenter et al*., 1993; *Moldwin et al*., 2004; *Darrouzet et al*., 2008, 2009].

More recently, *André and Cully* [2012] reviewed numerous methods to detect low-energy ions. They also presented their statistical results obtained using such techniques, including a new detection method that identifies intervals in electric field data when a spacecraft wake electric field forms due to the presence of cold ions [e.g., *Engwall et al*., 2009]. Though the spacecraft wake method cannot provide ion composition, *André and Cully* [2012] applied it in combination with other techniques towards detection of low-energy ions during a sample of dayside magnetopause crossings. They showed the ions to be present 50–70% of the time but were not detectable by standard, body-mounted particle instruments due to the ions' very low temperature. In particular, they discussed cold ion occurrence in the context of dayside reconnection, in which the cold ions play an important role, slowing down the reconnection rate due to their effect on decreasing the local Alfvén speed. Dayside reconnection rate is related to plasma β: reconnection-driven flows or jets are less frequent at times when magnetospheric plasma β was significantly lower than solar wind β due to the presence of cold magnetospheric ions

[*McFadden et al*., 2008b; *Phan et al*., 2013]. Another statistical study of dayside magnetopause crossings and observations of reconnection jets showed decreased jet speeds were observed more often when the observed total plasma density indicated the presence of a plasmaspheric plume near the magnetopause [*Walsh et al*., 2013].

Low-energy ions are also important for the generation and properties of electromagnetic ion cyclotron (EMIC) waves. As described in Chapter 2, satellite observations of multiple ion species were obtained around the same time that unusual, He^+ band EMIC waves without a stop band at f_{He+} were detected. The cold ion species were accelerated into the energy range of the plasma instrument by a convection flow. Thanks to that flow, estimation of the ion species densities and temperatures was possible and it was shown that a low-density component of cool He^+ (tens of eV), concurrent with hot proton anisotropy were the reason for the peculiar EMIC wave characteristics that enabled propagation across the traditionally forbidden He^+ stop band. It was shown that moderate heating of He^+ (few to tens of eV) leads to a change in EMIC wave characteristics relative to cold plasma theory and the inclusion of warm plasma effects was needed to fully characterize the waves. This relationship between heavy ion temperature and EMIC wave growth has seen previous theoretical inquiry using a range of assumed plasma parameters [e.g., *Gomberoff et al*., 1996; *Silin et al*., 2011; *Chen et al*., 2011, 2013; *Gary et al*., 2012]. Clear differences between cold and warm plasma EMIC waves emerged in all these modeling studies but it remains unknown whether magnetospheric EMIC waves occur more often in one or both regimes due to low observational data availability on magnetospheric cold ion species and their properties. A characterization of the cold ions throughout the magnetosphere can enable better understanding of EMIC wave generation and comparisons with wave observations that are dependent on the temperature of various ion species present during

the wave activity. Further investigation may determine if the natural plasma environment in Earth's magnetosphere supports global evolution of warm plasma EMIC waves, particularly in the He^+ band. As described in Chapter 1, the importance of when and where cold ions participate in EMIC wave generation and growth is that therein also lies the answer to a longstanding question: to what extent can EMIC waves lead to losses of a significant population of energetic (0.5 MeV $\leq E \leq$ few MeV) electrons by pitch angle scattering [*Thorne and Kennel*, 1971; *Ukhorskiy et al*., 2010; *Gary et al*., 2012] and where does such scattering occur? But in order to explore the occurrence of warm plasma EMIC waves, plasma observations should accompany the wave observations. Though determining the multiple ion species that render EMIC waves unstable in arbitrary situations proves difficult even with state-of-the-art particle instruments, a statistical study of intervals with ULF waves or plasma flows occurring throughout the magnetosphere may yield observations of cold ions, including in nominal locations of EMIC wave activity. Such observations can then characterize the typical environment properties and support studies on the effects of cold ion temperature and abundance on EMIC wave generation and growth.

A common theme in the above topics is the importance of characterizing the low-energy plasma environment and in particular the multiple ion species occurrence rates, densities, and temperatures. The past assumptions on cold ion abundance for wave studies were a result of limited knowledge on such ions, with plasma composition measurements at energies below hundreds of eV being rare, particularly near Earth's equatorial magnetosphere beyond geosynchronous orbit. The equatorial magnetosphere is a source region for EMIC waves [*Loto'aniu et al*., 2005] and also a region best sampled by the low inclination orbits of the THEMIS satellites. The THEMIS satellites also often cross the dayside magnetopause,

supporting sampling of cold ions near nominal locations for dayside reconnection. Although the satellites do not carry plasma composition instruments, by using the full range of the instruments available to us there are ways to not only deduce the presence of cold ions, but also explore their occurrence rates, spatial distribution, activity dependence, and other properties. I undertake this task using past methods and new refinements. The THEMIS satellites extend past investigations of these cooler ions to the outer (>9 R_E) dayside/nightside magnetosphere and flanks, providing opportunities to expand previous knowledge on low-energy plasma populations, their sources, as well as their transport.

3.2 Instruments and Data

I leverage various data sets from the THEMIS mission for this study. Computation of the particle moments and omnidirectional energy flux utilize three-dimensional particle data from the ion and electron electrostatic analyzers (IESA and EESA) [*McFadden et al*., 2008a] and the solid state telescopes for ions and electrons (SSTI and SSTE) [cf. *Ni et al*., 2011]; the IESA measures energy per charge without mass discrimination such that all ion species are assumed protons, a point I discuss later in this chapter. High time resolution "fast-survey" (~3-sec samples, with increased angle and energy resolution) particle data is available about half of each orbit prior to 2013 and is the main data type for the ion detection methods I describe in section 3. I combine the IESA and SSTI moments so that a wider energy range of ions is used for computation of the three components ($v_{i,x}$, $v_{i,y}$, and $v_{i,z}$) of the ion velocity vector, as well as for subsequent computation of the perpendicular and parallel ion velocity components only ($v_{i,perp}$ and $v_{i,par}$). Due to the presence of the intense radiation in the outer Van Allen belt, there are times when penetrating electrons contaminate the particle data. I remove instrumental noise resulting from

penetrating electron radiation before performing analysis of the particle data and exclude intervals when the total particle flux in the >0.5 MeV electron SST channel exceeds 1e+7 particles/cm^2 to avoid false identification of low-energy ions. I also remove the sun contamination from the ion SST instrument measurements. Dayside orbit intervals with magnetosheath or solar wind plasma observations are identified and excluded from further analysis by noting if the 15–25 keV EESA particle fluxes decrease at the same time the ~100–200 eV fluxes increase or if $v_{i,x}$ exceeds 100 km/s in the anti-sunward direction at all dayside locations (X-GSM > 0 R_E) when the geocentric distance is also larger than 7 R_E.

Measurements of the spacecraft floating potential (Φ_{SC}) by the electric field instrument (EFI) [*Bonnell et al*., 2008] are used for computation of a minimum velocity threshold (v_{min}) for detection of cold ions and are also combined with EESA moment data to provide estimates of the total plasma density (N_SCpot). N_SCpot data can approximate the total plasma density generally to within a factor of two [e.g., *Mozer*, 1973; *Pedersen et al*., 1998, 2008] and I use it to infer the approximate plasma density distribution near the equatorial magnetosphere. I note that N_SCpot data is available on full orbit intervals but only use data obtained at the same time the ion detection methods are applied (fast-survey intervals only).

Measurements of the ambient magnetic field by the fluxgate magnetometer (FGM) [*Auster et al*., 2008] are needed for determining $v_{i,perp}$ and $v_{i,par}$. Transformation of the IESA and SSTI velocity moments to a field-aligned coordinate (FAC) system (defined with Z parallel to the mean magnetic field, X normal to Z in the plane containing the Earthward direction, and Y completing the right-handed, orthogonal coordinate system) is followed by computation of $v_{i,par}$ and $v_{i,perp}$. $v_{i,perp}$ is obtained by computing the summed magnitude of the IESA and SSTI velocity vectors and subtracting the field-aligned component.

Data from the three inner THEMIS spacecraft (TH-A, TH-D, and TH-E) are combined in this study. I use all fast-survey data intervals from 28 January 2008 to 1 May 2013 and refer to these combined intervals as "the entire time period".

3.3 Methods

3.3.1 Detecting fluxes of low-energy ions

The IESA measures the ambient ions continuously each orbit. At times, low-energy ions (E_s < 1 keV) can be identified by eye in fast-survey energy-time spectrograms and resemble the particle flux signatures below 1 keV in Figure 3.1a. I identify time intervals when the IESA observes enhanced energy fluxes associated with the presence of cooler ions using the absolute energy flux method (AFM) criteria below:

1. Compute an energy-dependent 10^{th} percentile of the IESA energy fluxes over a 30-minute sliding interval and use it as a background energy flux.
2. Verify the average counts quantity in the 5–120 eV range exceeds 30 at each time step. Also verify that the median of the computed 10^{th} percentile in the 5–120 eV energy range is above zero to ensure sufficient background exists for comparison with the observed energy fluxes.
3. Compute the mean energy flux from 5–120 eV for both the observed and background energy fluxes and compare the ratio of the two quantities. Test all intervals for times when the ratio of observed to background fluxes is greater than a factor of two.

Cold, dense ions present during flows can occur over short, dynamic intervals and exceed the background energy flux. There are also times when there are no noticeable flows, yet low-

energy ion fluxes are still observed. If low-energy ion fluxes are present in the absence of flows, it suggests the observed ions are warm enough to exceed the minimum energy threshold for detection by the IESA. All time intervals when the AFM criteria are satisfied appear as black symbols in Figure 3.1c. An explanation of my selection of the 5–120 eV energy range for detecting low-energy ions is given in the next section.

3.3.2 Low-energy ion properties during flows

3.3.2.1 Detection of flows

As discussed by *Lee et al*. [2012], Φ_{SC} is often tens of Volts during sunlit orbit portions and is an energy threshold that cold ions must exceed for observation by the IESA. *Lee et al*. [2012] also described the process of converting the sum of Φ_{SC} and the minimum energy of the IESA into a minimum velocity threshold for detection of cold ions; this relation is shown in equation (1):

$$\frac{1}{2} m v_{\min}^2 = e\Phi_{SC} + IESA_{\min} \qquad (1)$$

In this relation m is the mass of protons, $v_{\min}$ is the minimum velocity threshold, e is charge, Φ_{SC} is the observed spacecraft floating potential, and $IESA_{\min}$ is the mid-point of the lowest energy bin of the IESA instrument (~6.5 eV); I define $IESA_{\min}$ in this way to ensure the peak of the ion velocity distribution is greater than the lowest energy limit of the IESA to support better estimation of cold ion density and temperature when obtaining the individual ion properties (described in section 3.2.3). Creation of a time series variable, $v_{\min}$, allows for automated detection of $v_{i,perp} > v_{\min}$ intervals throughout the entire time period. This $v_{\min}$ criterion may be satisfied by flows associated with convection or ULF waves; saving the combined ion velocity moments during such times provides the location, direction, and magnitude of such flows

throughout the equatorial magnetosphere. Time intervals that satisfy the criterion appear in Figure 3.1c as blue symbols. I also note the v_{min} criterion can be satisfied by the contribution of enhanced drifts of hot ions when cold ions do not dominate the total ion density or in locations near the plasmasphere where convection is unable to overcome co-rotation, topics I will come back to later.

3.3.2.2 Detecting ion fluxes during flows

The absolute energy flux method (AFM) criteria described in section 3.1 are also applied during flows associated with convection or waves to determine the presence of cold ions at the same time such flows are observed. While enhanced hot ion drifts can contribute to $v_{i,perp}$ and trigger the v_{min} criterion, if low-energy ion fluxes satisfying the AFM criteria are absent, the time interval is excluded from further analysis. Requiring that the v_{min} and AFM criteria be met simultaneously singles out the times when the observed IESA fluxes below 120 eV exceed the background due to acceleration of low-energy ions above the spacecraft potential energy. In addition, due to higher occurrence of enhanced low-energy ion fluxes in the same locations of enhanced hot ion drifts in the deep inner magnetosphere ($L<6\ R_E$) I require that the measured total ion density (Ni_ESA+SST) matches the total inferred plasma density from the spacecraft potential (N_SCpot) to within a factor of 2 to ensure that the enhanced particle fluxes are actually consistent with the presence of cold ions; locations where this requirement is not met are excluded from my statistics. The 5–120 eV energy range is chosen because cold protons (~1 eV) accelerated by plasma flows within Earth's magnetosphere have typical energy flux peaks in the 10–40 eV range (median $v_{i,perp}$ during $v_{i,perp} > v_{min}$ ~ 45–90 km/s) and peak less often above 120 eV ($v_{i,perp} > 150$ km/s); v_{min} during $v_{i,perp} > v_{min}$ events was 40–70 km/s (Φ_{SC} ~ 4–20 Volts). Therefore, low-energy ion fluxes observed within this energy range during flows are a general

indicator for the presence of cooler protons, including those that have been moderately heated. Protons are assumed the most common cold ion species, so detecting times when particle fluxes in the 5–120 eV energy range exceed the flux background indicate the presence of low-energy protons and serves as a proxy for determining the presence of additional heavy ions. But in the absence of low-energy protons and presence of higher speed flows, this method may overlook the presence of warm He^+ or O^+, since their energy flux peaks could occur outside of the 5–120 eV range. The times when low-energy ion fluxes exceed the AFM criteria at the same time $v_{i,perp} > v_{min}$ are shown as red symbols in Figure 1c; such intervals are then examined for possible ion species separation.

3.3.2.3 Species separation for composition and properties

If particle fluxes satisfying the AFM criteria are also detected during flows, the observed omnidirectional energy fluxes during these candidate times are further analyzed using an automated fitting routine to detect and estimate the properties of multiple ion species. *Lee et al*. [2012] used THEMIS IESA data to observe multiple ion species during a convection flow, showing that energy flux peaks separated according to ion mass number could be seen in both the omnidirectional and perpendicular particle fluxes. Others have also discussed similar observations using other spacecraft data [e.g., *Hirahara et al*., 2004; *Chen and Moore*, 2004]. Ion species separation in particle flux data contains clues on ion composition. I examine all such candidate events to extract the ion composition and estimated properties by performing a multi-component fit with the sum of three flowing Maxwellian distribution functions to a 1-D cut of the observed ion distribution function. Similar to the procedure described by *Chen and Moore*

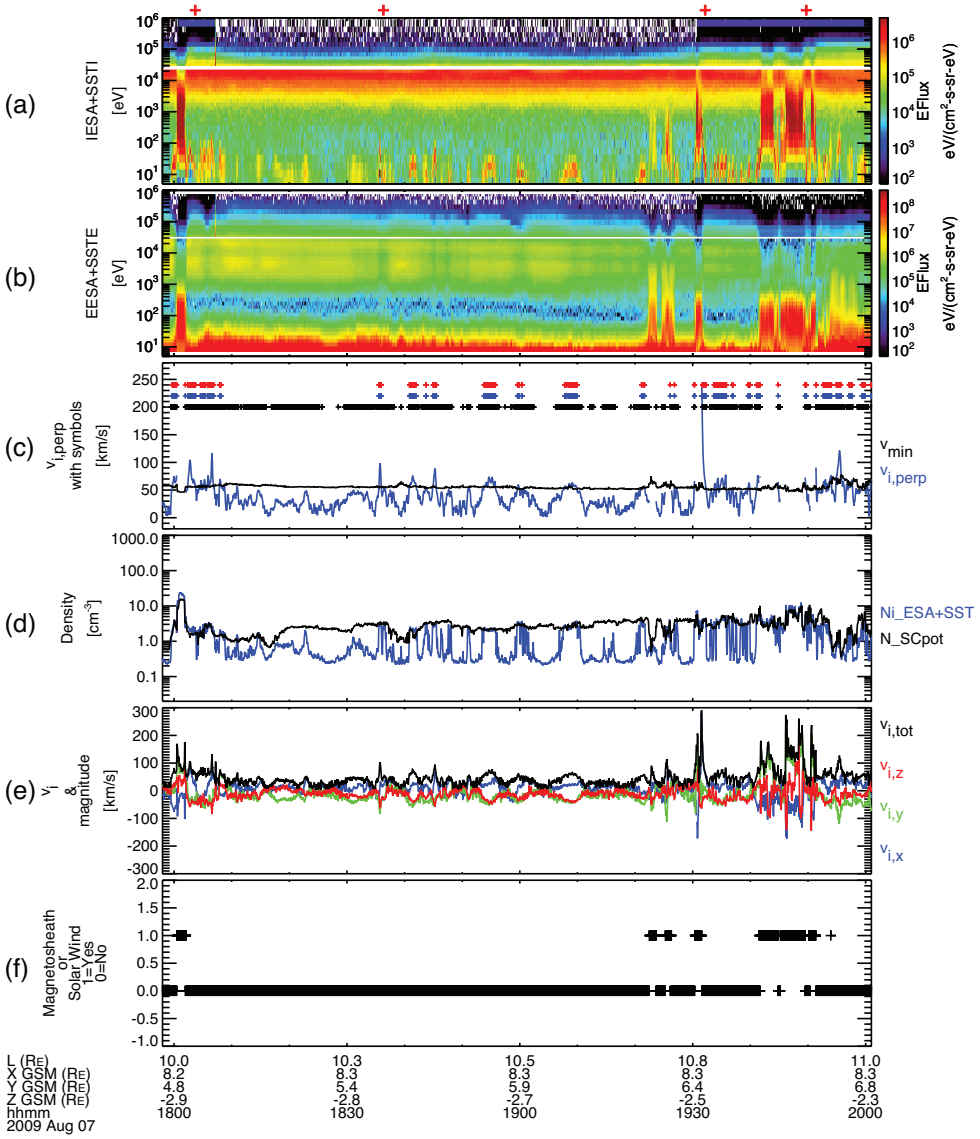

Figure 3.1: The application of all low-energy ion identification techniques and the combined magnetosheath and solar wind plasma exclusion to observations on 7 August 2009 by TH-E. (a) Combined omnidirectional IESA and SSTI energy flux; (b) combined omnidirectional EESA and SSTE energy flux; (c) $v_{i,perp}$ intervals when the ion identification methods are applied and colored symbols indicating when (black) the absolute energy flux method identified low-energy ion fluxes, (blue) $v_{i,perp} > v_{min}$, and (red) low-energy ion fluxes are seen the same time as $v_{i,perp} > v_{min}$; (d) observed plasma density products, (black) the total plasma density inferred from the spacecraft potential, N_SCpot, and (blue) the ion density computed from the IESA and SSTI combined moments, Ni_ESA+SST; (e) three components of the observed ion velocity in GSM coordinates and its magnitude; and (f) time intervals when TH-E observes magnetosheath or solar wind plasma. Four red plus symbols in Figure 1a (top) indicate times for which fits to the 1-D ion distribution function are shown in Figure 2 as examples. Descriptions of the low-energy ion identification methods indicated by the colored symbols in Figure 1c are described in the section 3.

[2004], I used the Levenberg-Marquardt least squares fitting method (e.g., *Moré* [1978]; *Markwardt*, 2009) and developed an automated fitting routine to obtain the best fit parameters for observations satisfying the flow and AFM criteria discussed above. To limit the fitting to cooler ion species (T_s < 1000 eV), the routine first fits the hot (E > 1 keV) ion component, assumed protons, with a single flowing Maxwellian and subtracts it from the observed ion distribution function. Although hot particles are known to have a high-energy tail and are better modeled by a kappa distribution, I do not attempt this in my study since I focus on the low-energy ion components and a single flowing Maxwellian fit to the hot ion component sufficiently models this component at energies below 20 keV. Following subtraction of the hot ion component, the remaining IESA fluxes are fitted using the summed flowing Maxwellians; each flowing Maxwellian has two free parameters, n_s and T_s, in which s indicates the dominant ion species (H^+, He^+ or O^+), a total of six free parameters. Also included is the observed $v_{\mathrm{i,perp}}$, providing a fixed parameter for the bulk plasma flow velocity that predicts peaks in energy flux should exist near multiples of observed $v_{\mathrm{i,perp}}$ after conversion into perpendicular kinetic energy, i.e., for $v_{\mathrm{i,perp}}$ ~ 80 km/s, protons have an energy flux peak near $0.5 m_p v_{\mathrm{i,perp}}^2$ ~ 30 eV, while He^+ would have a peak near $0.5 m_{He^+} v_{\mathrm{i,perp}}^2 = 2 m_p v_{\mathrm{i,perp}}^2$ ~ 120 eV [*Lee et al*., 2012]. This fixed bulk velocity parameter constrains the model; if observed energy fluxes do not fit the common bulk velocity assumption, the best-fit model deviates from the observations and obtained parameters are excluded from the statistics. In addition to the bulk velocity constraint, fitting outputs for ion number density are limited to the 0.01–100 cm^{-3} range and ion temperature to the 0–1000 eV range. Any fitting results obtained outside these ranges are filtered out when combining the obtained properties for statistics.

3.3.3 Application of methods to spacecraft observations

On 7 August 2009, TH-E passed through the afternoon sector near the magnetopause and observed multiple low-energy ion flux signatures that are likely observations of plasmaspheric plumes or filaments, visible in Figure 3.1a. This interval also shows observation of magnetosheath plasma, visible in Figure 3.1b by noting the large increase in electron fluxes between ~20 and 200 eV with simultaneous decrease in fluxes between ~10 and 25 keV; magnetosheath intervals are indicated with symbols equaling one in Figure 3.1f. Flows of $v_{i,perp} > v_{min}$ (blue symbols in Figure 3.1c) coincide with many of the ion flux enhancements (red symbols in Figure 3.1c) and Ni_ESA+SST matches well with N_SCpot during these same times (Figure 3.1d); assuming quasi-neutrality, the matching of densities suggests that the ion instruments are observing nearly all the ion species present in the ambient plasma. The three components of the ion velocity vector show that during the intervals of $v_{i,perp} > v_{min}$, the flows tend to point sunwards ($+v_{i,x}$ and $-v_{i,y}$), consistent with magnetospheric convection. The four red plus symbols on top of Figure 3.1a (top) indicate times selected for demonstration of the automated fitting routine performance.

Figures 3.2a–3.2d shows four examples of automated fits to 1-D cuts of the omnidirectional IESA energy fluxes observed by TH-E on 7 August 2009 between 18 and 20 UT (indicated by the red plus symbols in Figure 3.1a (top)); the flux peak energies predicted by the common bulk velocity assumption are superposed as vertical dashed lines (labeled E_{H+}, E_{He+}, and E_{O+}) on each plot and show good agreement with the actual energies where flux peaks are seen. The fit to the hot ion component has been subtracted from the total energy flux in each of the

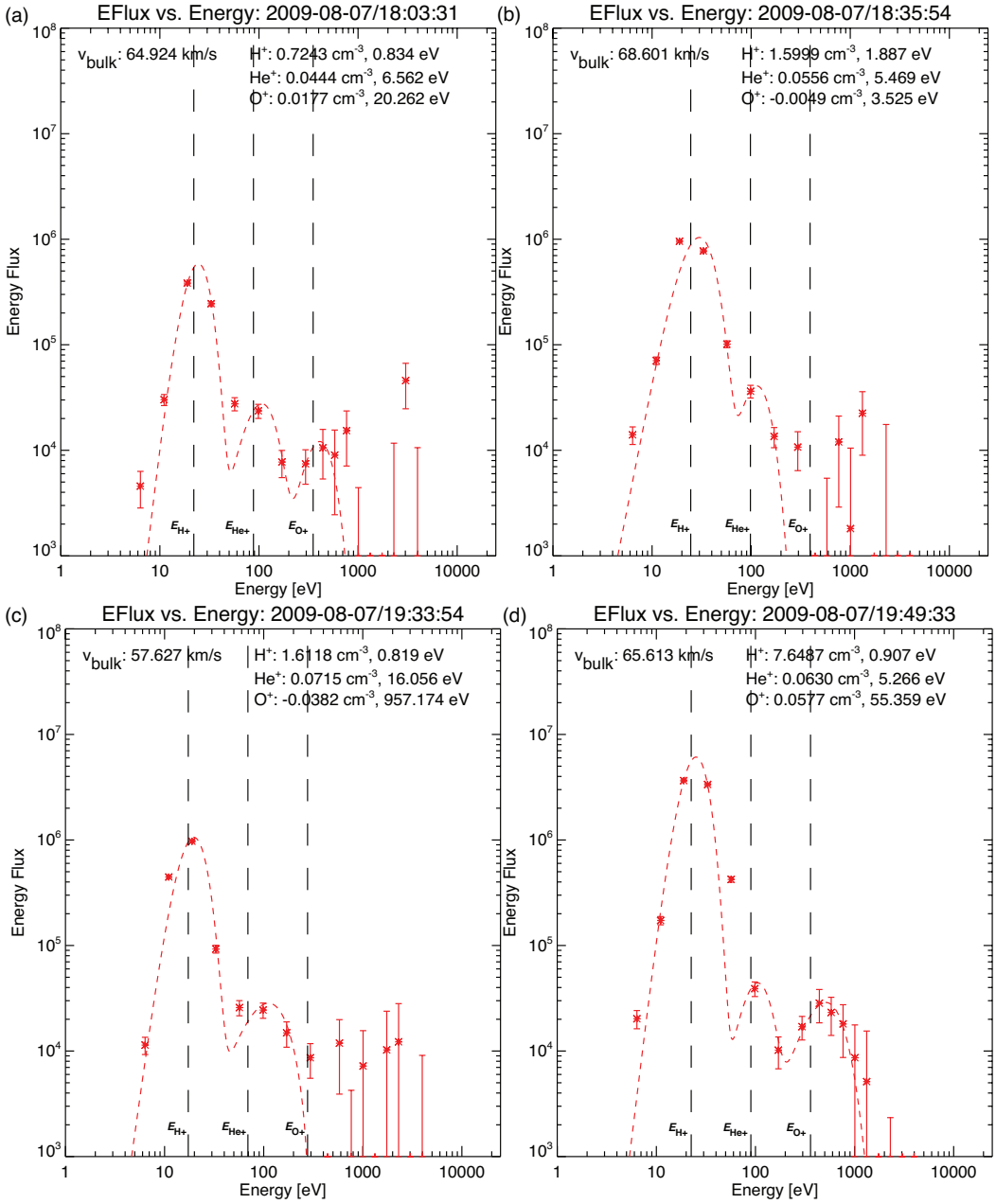

Figure 3.2: Fits to 1-D cuts of the observed ion distribution function with the sum of three flowing Maxwellians after subtraction of the hot proton component at the four times indicated by the red plus symbols in Figure 3.1a (top).

plots. In Figures 3.2b and 3.2c, flux peaks at E_{O+} are not seen because there is likely too little O^+ at these times. The fitting captures the apparent absence of O^+ in these cases, with the fitting results indicating $n_{O+} < 0$ for both. The fitting results for O^+ are excluded for these two intervals, consistent with the exclusion criteria described in section 3.2.3. In all four cases, H^+ has the highest density and coldest temperature. He^+ is warmer but less dense. O^+ is the warmest but is the least dense. The combined results using this fitting method during all candidate events throughout the entire time period are described in section 3.4. Further descriptions of the multiple methods described in this section are located in Appendix A.

3.4 Statistics

The statistical results are projected onto the XY-GSM (geocentric solar magnetospheric) coordinate plane with four concentric dotted circles plotted at 4, 6, 8, and 10 R_E. Dayside observations (events seen at X-GSM > 0 R_E) are normalized to the nominal magnetopause that is plotted with a solid line. I use an empirical magnetopause model [i.e., *Petrinec et al*., 1991; *Petrinec and Russell*, 1993] with median P_{dyn} (~1.31 nPa) and B_z (~0.096 nT) obtained from the Goddard Space Flight Center/Space Physics Data Facility (GSFC/SPDF) OMNIWeb interface during valid THEMIS data intervals to compute the nominal magnetopause shape and normalize events observed on the dayside in relation to this nominal magnetopause. The normalization is performed for each dayside event by taking the P_{dyn} and B_z values during each event and computing the predicted magnetopause stand-off distance at the subsolar point for that event, taking the ratio of the event's magnetopause stand-off distance to the nominal magnetopause stand-off distance, and then dividing the event's X-GSM position by that ratio, thereby shifting the event's position in reference to the nominal magnetopause position.

3.4.1 Occurrence of warm ions

Low-energy ion fluxes are sometimes observed in IESA data even without large flows and I refer to them as warm ions. Enhanced low-energy ion fluxes observed at the same time as flows consistent with convection or ULF waves are referred to as cold, flowing ions. Shown in Figure 3.3 are the locations where cold or warm ion fluxes satisfying the AFM criteria are identified, with a description of each panel given in the figure caption. Locations with less than thirty events are given a NaN flag and appear as white space on the plots. I note that because the subtraction of the cold, flowing ion events (Figure 3.3b) from the combined cold and warm ion flux events (Figure 3.3a) reveals a similar distribution of events in Figure 3.3c (excluding the NaN regions that are carried through in the subtraction), I normalized the total number of cold or warm ion flux events in 3a to the total valid fast-survey intervals shown in Figure 3.4b to obtain the normalized occurrence rate of warm ions (Figure 3.3d). The normalized occurrence rate is also presented as a bar plot (Figure 3.3e).

There is an enhancement in occurrence (~30–40%) of warm ions at geocentric distances smaller than 6 R_E that appears to wrap around the nightside of Earth, with occurrence decreasing after passing counterclockwise by dawn; the occurrence of these ions reaches a minimum on the dayside and appears to match the occurrence characteristics of the oxygen torus as determined by other spacecraft [e.g., *Nosé et al*., 2011, and references therein]. Beyond 6 R_E there is a global drop in occurrence rate. This drop starts at 6 and stops at ~8 R_E on the dayside, whereas it continues beyond that geocentric distance monotonically on the nightside. At L>8 R_E there is more MLT-dependence in the observed occurrence rates, with higher occurrence of the warm ions on the entire dayside from 8 R_E to near the nominal magnetopause (~10–15%), peaking in the afternoon sector beyond 10 R_E (>20%). Warm ion fluxes are also seen at the dawn and dusk

flanks (>10%), perhaps due to Kelvin-Helmholtz instability that may mix the warm magnetosheath plasma into the magnetospheric plasma [*Otto and Nykyri*, 2003]. The occurrence of the warm ions on the nightside beyond 8 R_E is ~10% or less and continues to decrease to below 5% beyond 10 R_E. Multiple heating mechanisms may contribute to the observed occurrence of warm ions in these locations [*Keika et al*., 2013a, and references therein] and I expect wave-particle interactions to be partly responsible for certain enhancements. The higher occurrence of warm ions at larger geocentric distances in the afternoon sector may be related to the higher occurrence of EMIC waves in this location [e.g., *Usanova et al*., 2012] that could heat these ions to high enough temperatures so they can be seen without large flows [e.g., *Zhang et al*., 2010, 2011]. Equatorial noise (magnetosonic waves) [*Russell et al.,* 1970] may also heat ions at geocentric distances smaller than 6 R_E and could contribute to the observed increased occurrence of warm ions there [*Olsen et al*., 1987].

3.4.2 Ion flow characteristics

The flow events observed are likely associated with magnetospheric convection and ULF waves but should also include a contribution from the diamagnetic drift that is energy dependent and thus predominantly due to the hot ion component of the distributions. Figure 3.4 shows the total number of $v_{i,perp} > v_{min}$ flow events recorded (Figure 3.4a), the total number of valid fast-survey intervals (Figure 3.4b), the median $v_{i,perp}$ flow vectors over all valid velocity moment intervals (Figure 3.4c), and the normalized occurrence rate of $v_{i,perp} > v_{min}$ flow events (Figure 3.4d). The normalized occurrence rate is computed by dividing the flow events in Figure 3.4a by the number of valid observation intervals (Figure 3.4b). As shown in Figures 3.4a–3.4d the largest number of flow events appears on the nightside at geocentric distances beyond 8 R_E with

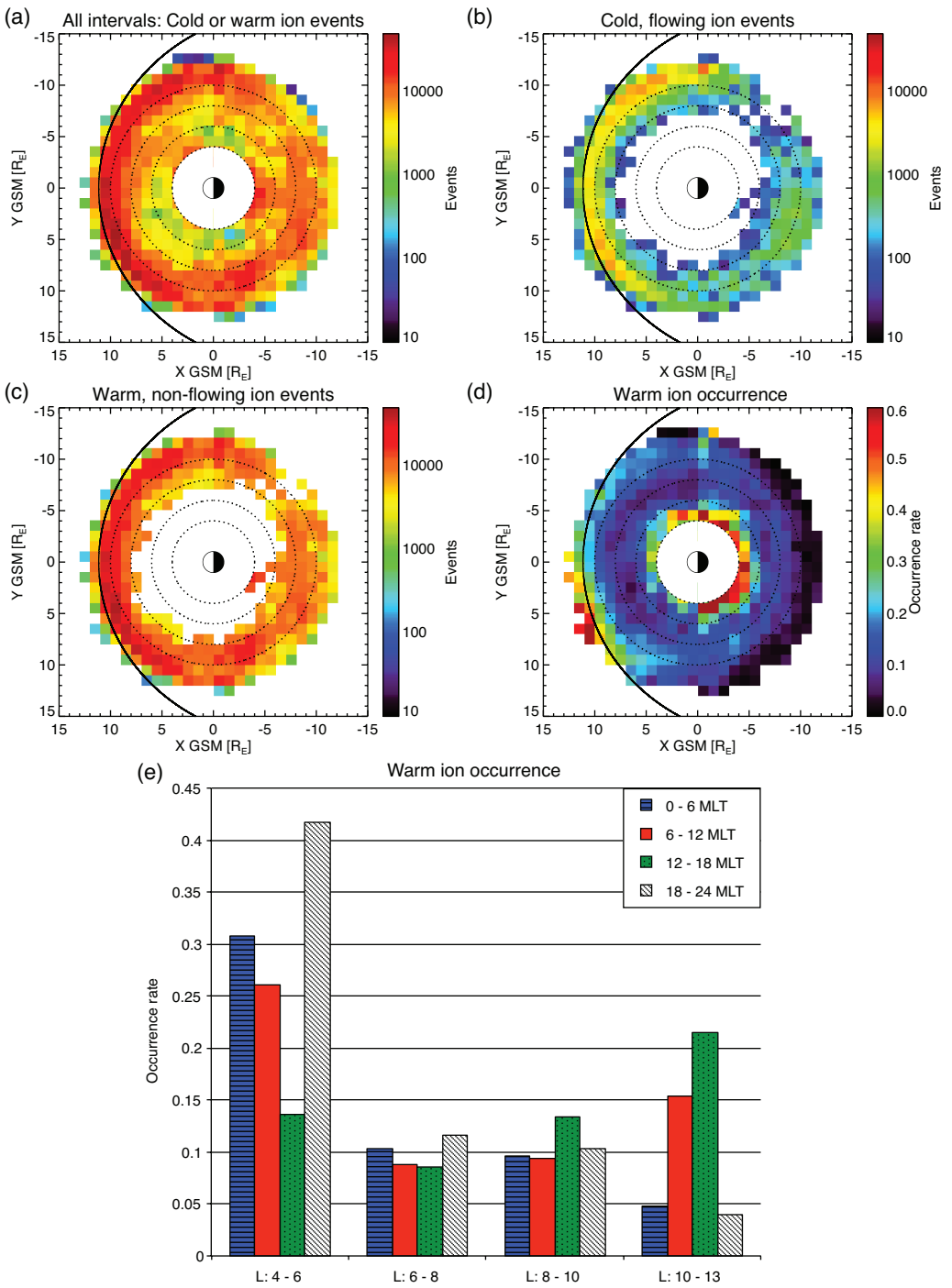

Figure 3.3: Locations where the absolute energy flux (AFM) method identified (a) cold or warm ion fluxes at all valid times; (b) cold, flowing ion events (AFM and v_{min} satisfied simultaneously); (c) the remaining events after subtraction of cold, flowing ion events; and the normalized occurrence rate of warm ions (d) projected onto the equatorial plane and (e) as a bar plot. Each event is a single 3-second fast-survey interval.

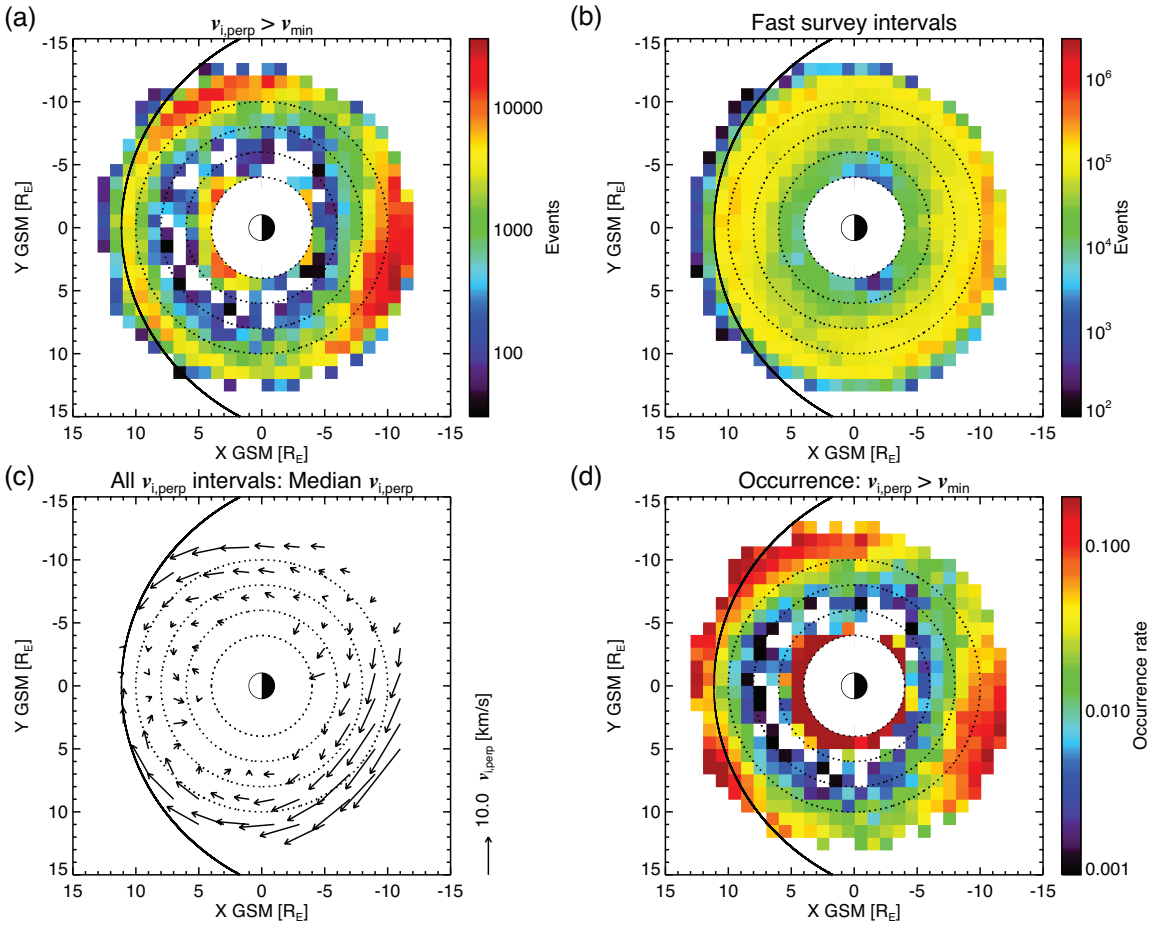

Figure 3.4: The (a) number of events when $v_{i,perp} > v_{min}$, (b) number of fast-survey observation intervals, (c) median $v_{i,perp}$ flow vectors computed from median $v_{i,x}$ and $v_{i,y}$, and (d) normalized occurrence rate of $v_{i,perp} > v_{min}$. Each event is a single 3 s fast-survey interval.

occurrence rates for $v_{i,perp} > v_{min}$ reaching 10–20%. Another peak in occurrence rate around 5–15% is seen at the outer dayside near the magnetopause that wraps around the flanks. There is yet another peak in occurrence rate at distances smaller than 6 R_E; I note that the majority of these flows are due to $v_{i,perp} > v_{min}$ being satisfied by enhanced hot ion (likely ring current) drifts and not due to bulk plasma flows caused by convection or waves. There is asymmetry in the dayside and nightside observations, with more flows closer to the Earth on the nightside than on

the dayside, most dayside flows occurring nearer the nominal magnetopause, and increased flow occurrence along the dawn side versus dusk. I attribute the asymmetry in the occurrence of flows at the dawn flank to convection but note that they could also be related to enhanced Pc3 ULF waves that occur near the outer magnetosphere along the dawn side [e.g., *Anderson et al*., 1990; *Engebretson et al*., 1991]. The valid events (high-flow) distribution likely reflects the preponderance of fast flows due to tail activity at the nightside, magnetopause boundary layer waves (driven by pressure pulses or surface waves) at the dayside, and the increased presence of upstream drivers in quasi-parallel shock conditions due to the nominal IMF (interplanetary magnetic field) orientation at the pre-noon sector. Despite there being fewer events in the pre-dawn sector, coverage of the magnetosphere from the 6–12 R_E range is fair, with few bins with less than thirty events, shown as white; geocentric distances beyond 8 R_E have the best coverage and I base my main conclusions regarding cold ions on observations obtained in this geocentric distance range.

The median $v_{i,perp}$ vectors in Figure 3.4c were computed from all valid velocity moment intervals, using the combined observed ion velocity moments from the IESA and SSTI using all the observations in each 2 x 2 R_E bin, with a minimum of 50,000 valid intervals (about 42 hours) per vector. The results show flow speeds on the order of ~10–25 km/s, which would seem small at first. But the similarity of the flow vectors from nearby cells increases the confidence in my statistics. The existence of multiple ion species in the Earth's magnetosphere, of which the cooler components begin to dominate the total ion density at smaller geocentric distances, reducing the total flow velocity, can explain this flow pattern. In various locations the cooler ions (few eV to few keV) and more energetic ions (>few keV) have been predicted to have nearly opposite directions of travel [*Kavanagh et al*., 1968]; a merging of cooler and energetic ions on the

dayside has also been suggested using spacecraft data [e.g., *Chappell et al*., 2008]. I see such trends near noon, where the vectors indicate flow speeds below 10 km/s and imply that particle transport is stagnant there, a competition between eastward and westward convection. The second stagnation point at post-midnight near the inner edge of the plasma sheet (~8 R_E) is more likely a result of the superposition of cold and hot ion component drifts that cancel each other out when studied using the median of the combined IESA and SSTI velocity moments over an extended time period. A similar trend appears at that MLT at larger geocentric distances; the stagnation can be attributed to the superposition of the **E** × **B** drift of ions Earthward (due to the cross-tail electric field) and the diamagnetic drift of ions predominantly towards dusk [e.g., *Angelopoulos et al.* 1993]. The observation of these low flow speeds suggests that the contribution of cold and hot ions to the total ion density is comparable near these locations. I will discuss this topic further in section 3.5.

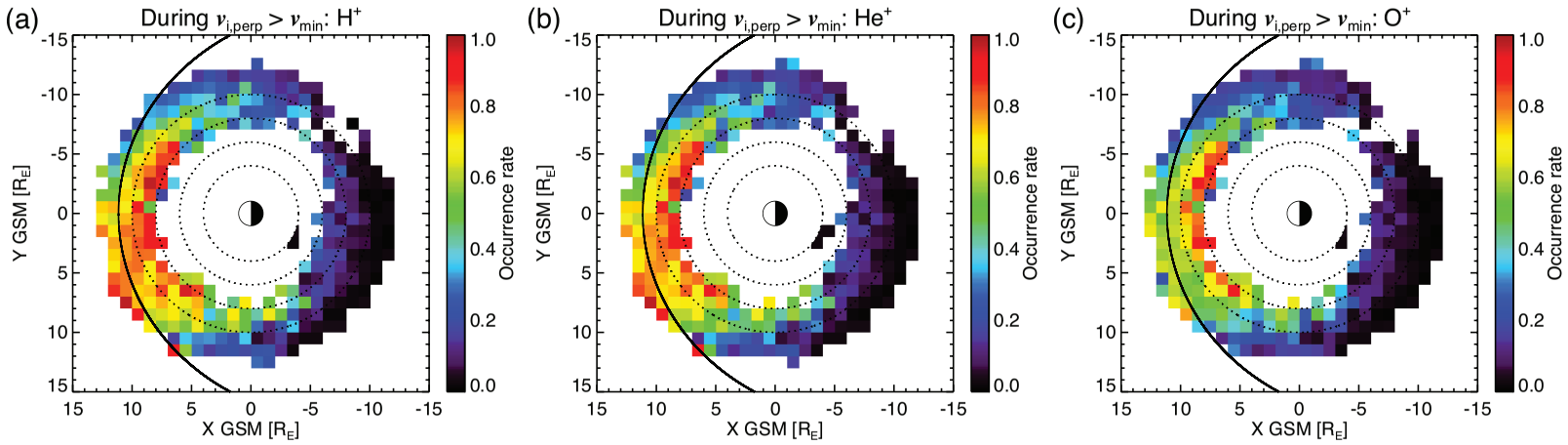

Figure 3.5: A summary of the locations where (a) H^+, (b) He^+, and (c) O^+ are identified normalized to the number of valid $v_{i,perp} > v_{min}$ events (Figure 3.4a).

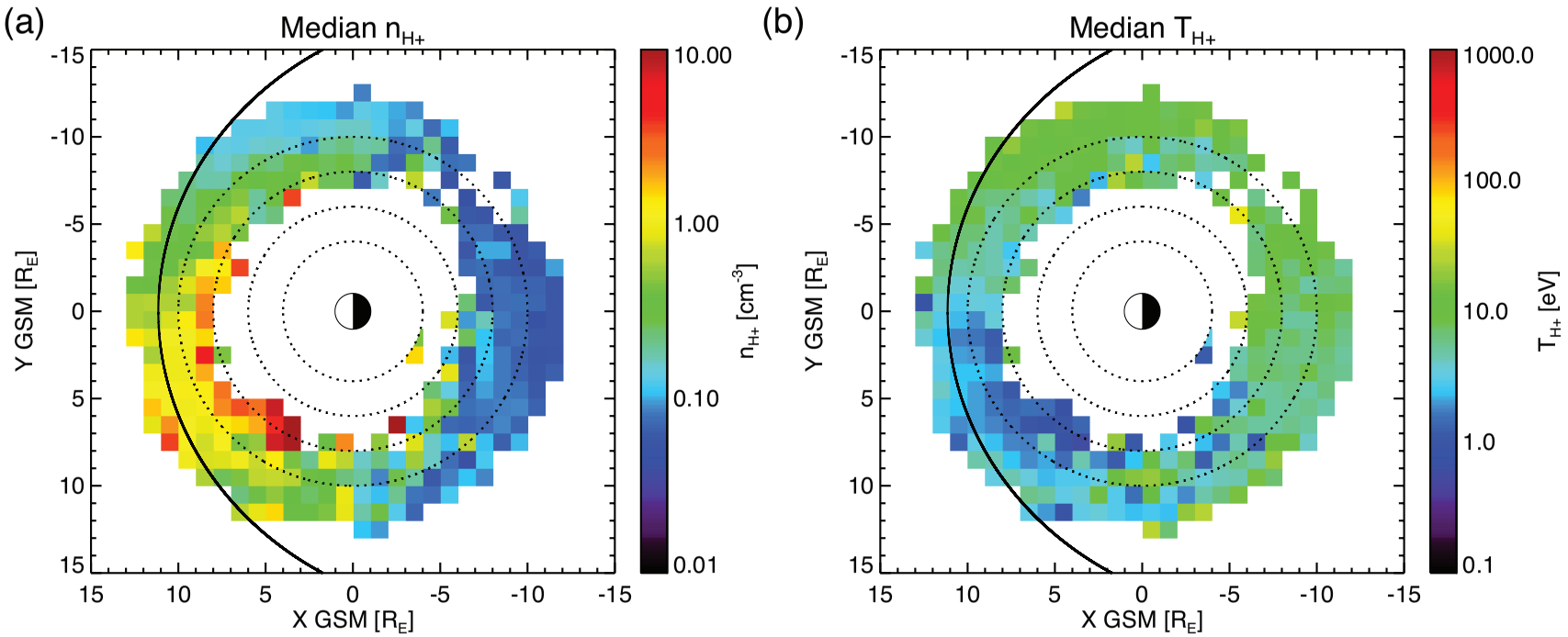

Figure 3.6: H^+ median (a) density and (b) temperature.

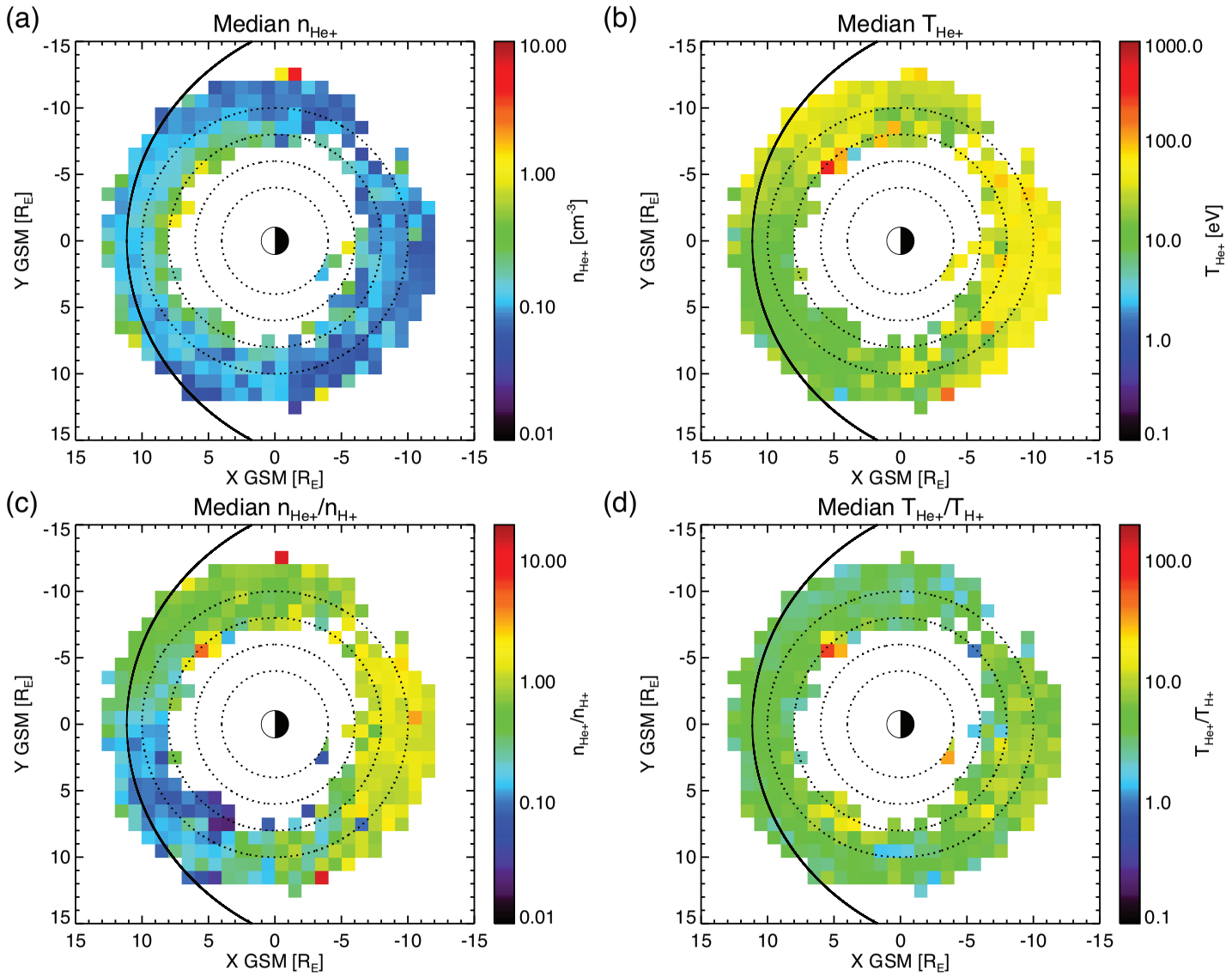

Figure 3.7: (a) He^+ median density, (b) He^+ median temperature, (c) ratio of median He^+ density to median H^+ density, and (d) ratio of median He^+ temperature to median H^+ temperature.

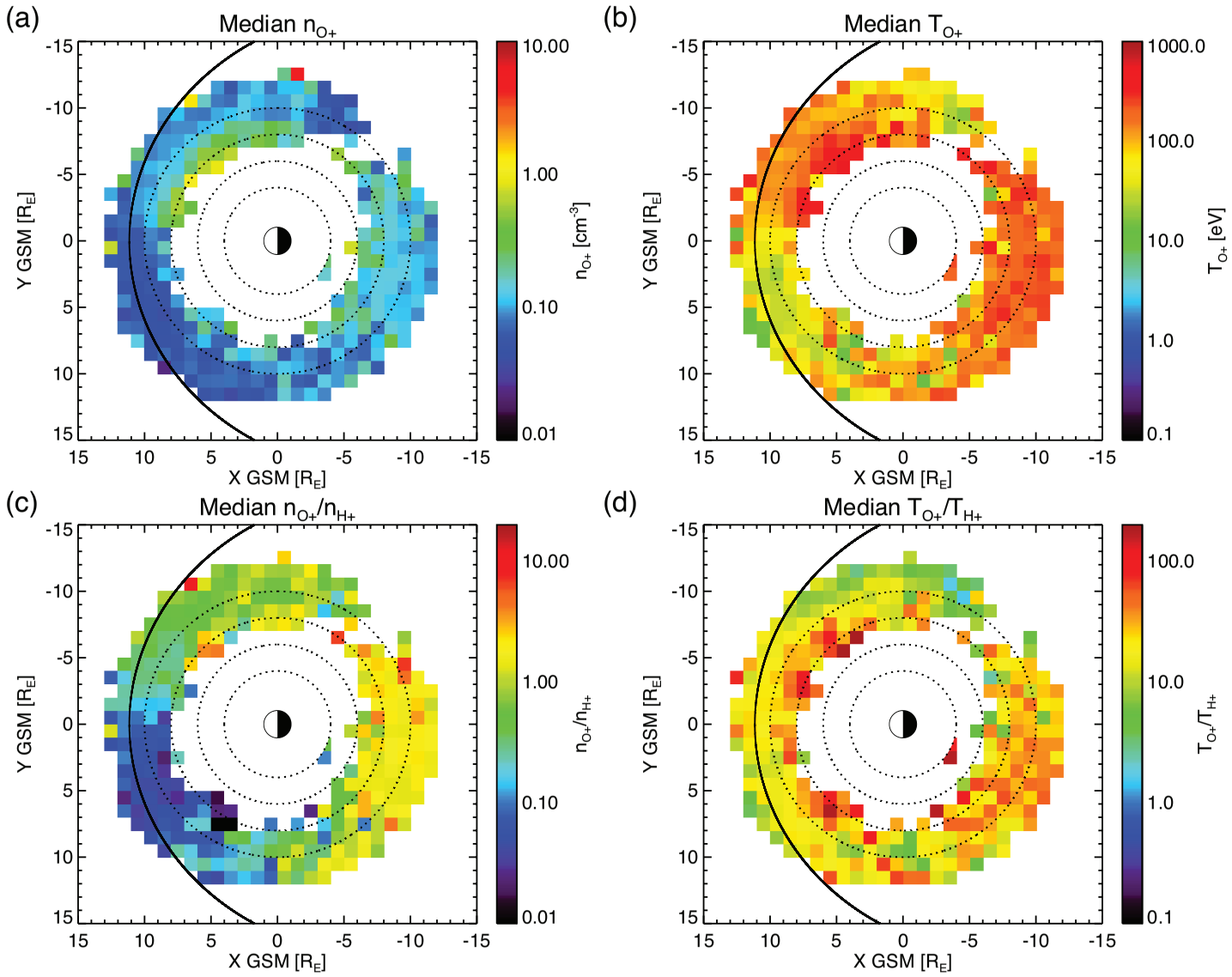

Figure 3.8: (a) O^+ median density, (b) O^+ median temperature, (c) ratio of median O^+ density to median H^+ density, and (d) ratio of median O^+ temperature to median H^+ temperature.

3.4.3 Cold ion composition and properties

Figure 3.5 shows a summary of the occurrence rates for all three dominant cold ion species (Figure 3.5a: H^+, Figure 3.5b: He^+, and Figure 3.5c: O^+) normalized to the total number of $v_{i,perp} > v_{min}$ flow events. The ion species occurrence is normalized by taking the ratio of individual ion species events to the total number of flow events seen in Figure 3.4a and shows the relative occurrence of times the fitting routine identifies the presence of each ion species from peaks in ion energy flux during the flows. As noted in section 3.2.2, I find that the majority of flows at L<~6 R_E in Figure 3.4 are not consistent with convection or waves and are therefore not considered in the occurrence rates shown in Figure 3.5. All three species are identified most often in the afternoon magnetosphere, though their properties show clear differences. The additional plots (Figures 3.6–3.8) show the ion density and temperature as a function of geocentric distance and local time and are described in the subsections below. The ion properties appear in two columns, with all density products on the left column and temperatures on the right column. The ion properties shown in these figures are all median values with the standard deviation in each spatial bin below one order of magnitude. I present the results using the median method because the average method shows similar trends but with larger scatter.

3.4.3.1 Protons

Protons are the most abundant cold ion species I identify on the dayside. Figure 3.5a shows the spatial distribution of the occurrence rate for protons. Figures 3.6a and 3.6b shows the proton density and temperature as function of geocentric distance and local time. Proton temperature is appropriately described as cold in the afternoon sector, but exceeds a few eV and approaches tens of eV in all other local time sectors. The proton density is highest in the post-noon/dusk sector near the outer plasmasphere and plume regions. It is higher in general on the dayside

relative to the nightside by about a factor of ten. I note that a comparison to the *Sheeley et al*. [2001] plasmasphere and plasma trough density models was performed to check for plasmaspheric-like density trends in the median proton density. The median proton density was below the model plasmasphere density throughout the spatial grid. The median proton density did exceed the trough model density in the afternoon sector and suggests refilling of the plasma trough during quiet times with plasmaspheric material.

3.4.3.2 Helium ions

The relative occurrence rate of He^+, shown in Figure 3.5b, resembles that of the protons. The He^+ properties also resemble those of protons, with higher density on the dayside and lower temperature within the afternoon sector, Figures 3.7a and 3.7b. Median densities are greater than 0.1 cm^{-3} at all dayside locations and the post-noon/dusk sector where the plume forms. Only at large geocentric distances (>8 R_E) at the nightside, dawn, and dusk sectors is the density below 0.1 cm^{-3}. T_{He+} is a few eV to ~10 eV in the outer plasmasphere and afternoon plume regions. From there it ranges from a few tens of eV to ~100 eV from dusk through midnight and dawn to noon. There is a tendency of the temperature to increase with proximity to Earth at all MLTs.

Also shown are ratios of the He^+ properties relative to the proton properties, Figures 3.7c and 3.7d. The density ratio n_{He+}/n_{H+} is near 0.1 from 12–14 MLT, near 0.5 from 06–12 MLT and ≥1.0 on the nightside. The temperature ratio T_{He+}/T_{H+} is almost always greater than 1, and approaches 10 on the entire nightside. In addition, even though the occurrence is low at L<6 R_E (Figure 3.5b), He^+ appears quite warm there, with T_{He+}/T_{H+} near or exceeding 10. This feature appears near the locations where I see enhanced occurrence of warm ion fluxes consistent with the location of the warm ion torus (Figure 3.3).

3.4.3.3 Oxygen ions

The relative occurrence rate of O^+ resembles that of protons and He^+ but with lower occurrence overall, as seen in Figure 3.5c. Evident in Figure 3.5 and by comparing Figures 3.8a and 3.8b with Figure 3.7, of the three dominant cold ion species O^+ is the least abundant on the dayside, is observed less often but has high relative abundance on the nightside, and is the warmest of the three dominant cold ion species. There are obvious differences in O^+ properties when compared to those of protons and He^+. Although T_{O+} is lower in the afternoon sector, it is not observed with a higher density than protons there. Instead, O^+ density appears higher than protons on the nightside. O^+ density is a factor of 2 lower than protons at dawn and noon. O^+ temperature is in the tens of eV range at the afternoon sector and 5–10 times higher in the morning and evening sectors. This suggests preferential heating of O^+ may occur in these locations. Like for He^+, there is a tendency for O^+ temperature to also increase with proximity to Earth at all MLTs.

The ratios of O^+ properties to proton properties are shown in Figures 3.8c and 3.8d. The density ratio n_{O+}/n_{H+} is less than 0.1 from 12–14 MLT, near 0.5 from 06–12 MLT, and greater than 1 on the nightside. T_{O+}/T_{H+} is always greater than 1 and ranges from ~10–100 in all locations except for at dawn at L>8 R_E where it is ~1–10. The observation that the density ratios of cold O^+ and He^+ to H^+ are either near or greater than 1 on the nightside suggest a mass dependent acceleration/heating of cold ions in the nightside magnetosphere. The nightside cold ions likely originate from a nightside ionospheric source, a topic that has been discussed in the context of mass loading of the tail [e.g., *Brambles et al*., 2011; *Yu and Ridley*, 2013, and references therein] but their occurrence near the magnetic equator on the nightside has not been studied extensively with spacecraft observations due to observational limitations [*Engwall et al*., 2009].

3.4.4 Plasma density, flows, and cold ions and their activity dependence

I relate the $v_{i,perp}$ vectors, median of the inferred total plasma density, $v_{i,perp} > v_{min}$ events, and cold ion occurrence rate to geomagnetic activity. The comparison is made by splitting the observations by the median Kp index over the entire time period (28 January 2008 to 1 May 2013), to below and above Kp = 1; I do not perform further classification by Kp index due to lower data availability on flows and cold ion occurrence at higher Kp. Combined, these observations are relevant to past studies on the plasmasphere and observations of strong dayside to nightside plasmasphere asymmetry that varies with geomagnetic activity. Shown in Figure 3.9 are the median $v_{i,perp}$ vectors (Figures 3.9a and 3.9e); median of the total plasma density inferred from the spacecraft potential (Figures 3.9b and 3.9f); the number of $v_{i,perp} > v_{min}$ events (Figures 3.9c and 3.9g); and cold, flowing ion occurrence during the $v_{i,perp} > v_{min}$ events (Figures 3.9d and 3.9h). The two rows are for Kp ≤ 1 (Figures 3.9a–3.9d) and Kp > 1 (Figures 3.9e–3.9h). Again, if events at L<6 R_E satisfied both the AFM and v_{min} criteria but Ni_ESA+SST was not within a factor of 2 of N_SCpot, they were excluded from the statistics of cold, flowing ions (Figures 3.9d and 3.9h).

The ion flow vectors in Figures 3.9a and 3.9e display overall trends in agreement with Figure 3.4c but with larger flow speeds for the dataset Kp > 1, consistent with enhanced convection during intervals of higher geomagnetic activity. Larger vectors also appear at smaller geocentric distances for higher Kp, consistent with enhanced convection overcoming co-rotation at smaller geocentric distances, leading to the contraction of the plasmasphere.

I extended the *Sheeley et al*. [2001] plasmaspheric density profile to the maximum geocentric distance of my observations (about 13 R_E) to enable a comparison between

plasmaspheric densities predicted by the model to the median of N_SCpot throughout the spatial grid to show the distribution of plasmaspheric density and its Kp-dependence (Figures 3.9b and 3.9f). Locations where the median of N_SCpot fell below the model density value are indicated with diamonds. I note that this comparison between N_SCpot and the *Sheeley et al*. [2001] model is preliminary and a future study on plasmaspheric density using the full N_SCpot data set will be pursued to enable a more detailed investigation into plasmaspheric density, its structure, and variability. For now, the median of N_SCpot is used to infer the distribution of total plasma density in the magnetosphere and the diamonds are superposed to show the locations where this density falls below levels representative of the plasmasphere. These diamonds help inform the reader on the location of the cold ions and their features relative to the plasmaspheric model and the observed locations of the plasmasphere in my database.

At low Kp, the diamonds in Figure 3.9b reveal a shape that is roughly symmetric with respect to the terminator. Diamonds appear out near 8 R_E at dusk in comparison to ~5 R_E at dawn and carve out a shape representing the quiescent plasmasphere, capturing the bulge at dusk where convection and co-rotation drifts oppose each other and cause the equipotentials to expand outwards from Earth.

At higher Kp, there are global changes in the distribution of median N_SCpot and the diamonds, Figure 3.9f. It is clear that the diamonds are now observed at smaller geocentric distances globally, especially along the dawn side, where diamonds appear close to ~4 R_E between 0 and 8 MLT. At dusk the diamonds occurring near or above 6 R_E are also reduced but there remains a narrow region from ~13–16 MLT in the afternoon sector where densities still exceed the *Sheeley et al*. [2001] model. The shift in occurrence of diamonds to smaller geocentric distances is consistent with a contraction of the plasmasphere during active times that

follows an increase in convection strength, while the persistence of enhanced density in the afternoon sector is consistent with formation of the plasmaspheric plume that has been observed during higher geomagnetic activity. It is evident that the plasmasphere is more contracted for higher Kp, in agreement with the contraction of the region of increased average flow, Figures 3.9c and 3.9g.

During low Kp, most flow events (Figure 3.9c) are near the dayside magnetopause and the occurrence rate of cold ions during these flow events (Figure 3.9d) is high (>50%) throughout the dayside, including the morning sector, with evidence of higher (>80%) occurrence in the afternoon sector. During higher Kp intervals, the flows (Figure 3.9g) occur more often throughout the magnetosphere, especially at smaller geocentric distances, and enable additional sampling of cold ions. But in contrast, Figure 3.9h shows the occurrence of cold ions in the morning sector falls to below 50% at larger geocentric distances while the occurrence rate in the afternoon sector remains high. There is also a drop in the occurrence of cold ions at both flanks during higher Kp. This trend supports previous work that described the expansion or refilling of the plasmasphere throughout the quiet time dayside possibly out to the magnetopause on a timescale of a day or less, while increasing geomagnetic activity results in loss of dayside plasmasphere ions due to the effects of enhanced convection [e.g., *Chappell*, 1972; *Horwitz et al*., 1984; *Goldstein and Sandel*, 2005]. My results also suggest dayside cold ions, presumably of plasmaspheric origin, appear more often near the dayside magnetopause during low geomagnetic activity that would accompany extended periods of northward IMF. In addition, I show their occurrence at dawn falls during higher geomagnetic activity, likely due to increased convection that would follow periods of southward IMF, but still remains high (~80%) near 10–16 MLT.

Both of these effects seen in the cold ion occurrence rate are consistent with increased geomagnetic activity and convection [e.g., *Borovsky and Denton*, 2008; *Walsh et al*., 2013].

3.5 Discussion

3.5.1 Equatorial ion transport

3.5.1.1 Cold ion flow pattern

On the nightside, hot (a few to tens of keV) magnetospheric ions convecting earthward are diverted close to Earth towards dusk on their approach due to the increased importance of gradient-curvature drifts relative to convection and co-rotation drifts; their approximate paths are in agreement with the plots of $v_{i,perp}$ vectors shown in Figures 3.4c, 3.9a, 3.9e, and 3.10a. Lower energy ions (E_s ~ 10 eV to 3 keV) are not sufficiently energetic for their gradient-curvature drifts to overcome co-rotation, are deflected near dusk, and drift around dawn, forming a warm plasma cloak draping over the plasmasphere and flowing out towards the dayside magnetopause [*Chappell et al*., 2008].

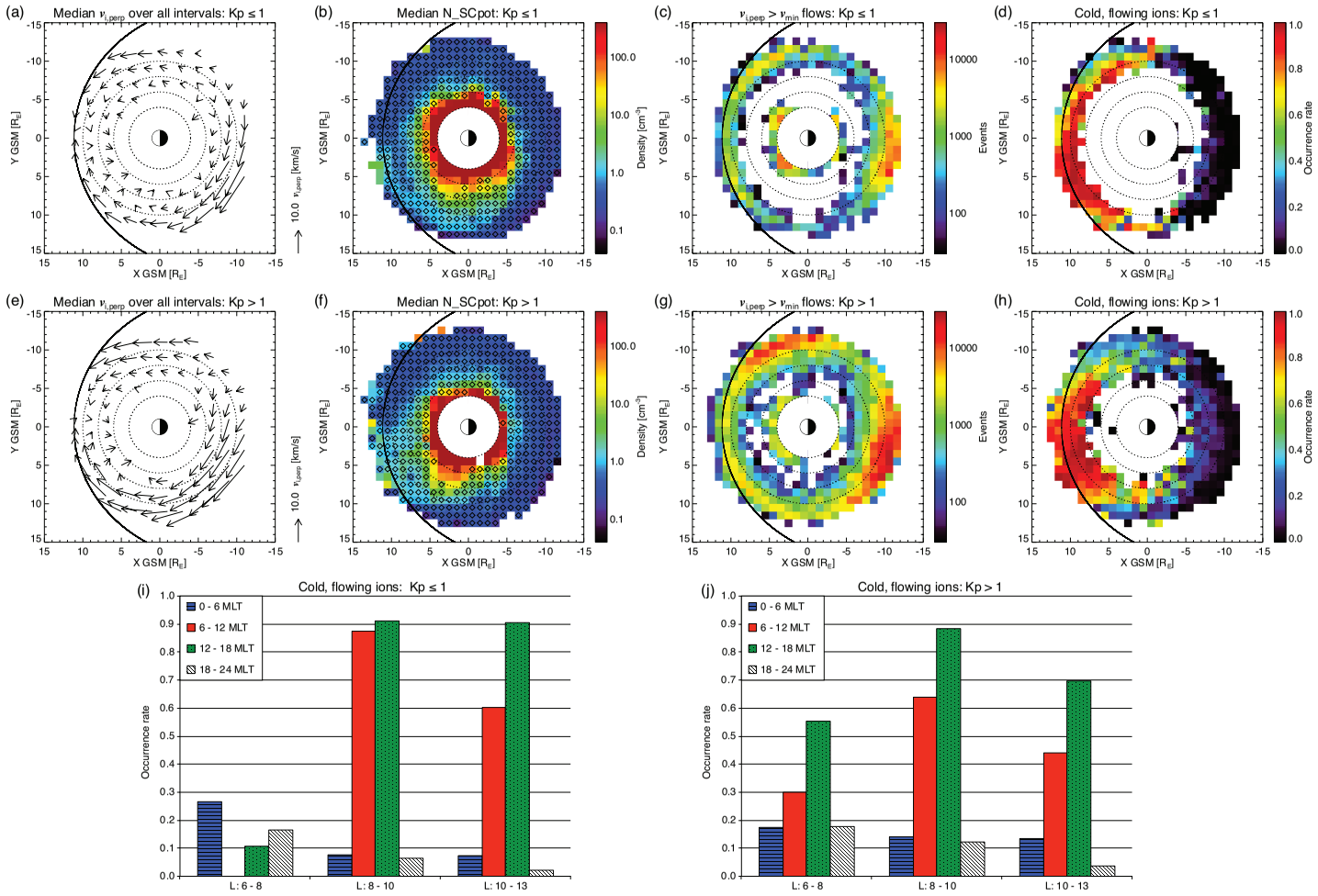

Figure 3.9: (a) and (e): median $v_{i,perp}$ vectors, (b) and (f): median total plasma density inferred from the spacecraft potential (N_SCpot), (c) and (g): number of $v_{i,perp} > v_{min}$ flow events, and (d) and (h): occurrence rate of cold, flowing ions for (a)–(d) Kp ≤ 1 and (e)–(h) Kp > 1. The diamond symbols superposed on (b) and (f) indicate the locations where the median total plasma density falls below the plasmaspheric density model by *Sheeley et al*. [2001]. Also shown are the occurrence rates of cold, flowing ions for (i) Kp ≤ 1 and (j) Kp > 1 presented as bar plots.

The warm ions I observe on the nightside are likely components of that warm plasma cloak. From the properties of protons, He^+, and O^+ at the nightside (Figures 3.6–3.8), it is apparent that these ions are present from the pre-midnight sector, through midnight, and appear cut off just after dusk near 20 MLT at geocentric distances larger than ~6 R_E, where I notice a change in ion species density and temperature.

Based on the equatorial drift paths of cold particles [*Kavanagh et al*., 1968], a boundary between closed (plasmasphere) versus open (magnetosphere) drift paths was predicted to exist on the dusk side. I see signatures of such a boundary near dusk in Figures 3.6–3.8, appearing most clearly in the plots of median ion temperature. In these figures I see that all cold ions sampled after 20 MLT at geocentric distances near 8 R_E are warmer than those sampled prior to that local time. This temperature trend continues counterclockwise, wrapping around dawn and ending just before noon where ion temperatures cool down again, possibly due to expansion of field lines at the dayside or due to turbulent mixing with cooler plasmaspheric ions [*Borovsky and Denton*, 2008]. I also see a sliver of warmer ions occurring beyond 10 R_E along the dusk side. These trends in ion temperature can be further understood by inferring the ion flow pattern in my data using the full velocity moments during $v_{i,perp} > v_{min}$ flow events and the expected diamagnetic drift contribution to those moments from the hot plasma.

In the two-fluid approximation, the total particle drift for each species includes the contributions of electric field and diamagnetic drifts [e.g., *Chen*, 1984; *Angelopoulos et al*., 1993]. In Figure 3.10a, the flow vectors computed during $v_{i,perp} > v_{min}$ events show flows being diverted on the nightside near 03 MLT at geocentric distances larger than 7 R_E towards dusk and is in agreement with past observations and modeling [*Angelopoulos et al*., 1993]. In contrast, the flow vectors through dawn are smaller, but point in nearly a straight line towards the sun. But

because the computed flow vectors include the contribution of diamagnetic drifts that depend on the plasma pressure that in turn relates to particle energy, their inclusion in the flow vectors distorts the flow pattern that describes transport of the low-energy, cooler particles. To study the flow pattern that better captures the transport of cold ions by convection and co-rotation, I recall previous work by *Angelopoulos et al*. [1993], in which the average ion velocity vectors computed from particle measurements by the AMPTE/IRM (Ion Release Module) spacecraft were compared to drift paths of hot ions computed using an empirical geomagnetic field model and average ion density to show the ion flow pattern in the quiet-time central plasma sheet. There was qualitative agreement between the observations and model outputs, showing the model captured both the flow magnitude and direction that was actually observed.

I perform a similar computation for geocentric distances larger than 6 R_E in the inner magnetosphere using the *Tsyganenko* [1989] (T89) geomagnetic field model for simplicity (with Kp = 1), with a dipole tilt equal to zero to further study the flow pattern during times of $v_{i,perp} > v_{min}$. I use the $v_{i,perp} > v_{min}$ database because these are the flows that allowed us to identify the occurrence and properties of cold ions. To compute the model diamagnetic drift as a function of geocentric distance and MLT I first compute the currents (using a distance of 3 R_E for the spatial derivatives of the magnetic field) and use the median of observed Ni_ESA+SST over the entire time period to approximate the ion density. I note that using the median Ni_ESA+SST is appropriate since the contribution of cold ions is included in the ion density determined from measurements by the IESA since the cold ion energy is above the spacecraft potential.

Noting that the total measured ion flux $n_t v_t$ is a combination of cold/warm ions that are too low in energy to contribute to the diamagnetic current, $n_{c,w} v_{c,w}$, and hot ions that are the dominant contributors to the diamagnetic current but are not affected significantly by convection,

$n_h v_h$, it holds: $n_t v_t = n_{c,w} v_{c,w} + n_h v_h$, or $v_t = (n_{c,w}/n_t) v_{c,w} + (n_h/n_t) v_h = (n_{c,w}/n_t) v_{c,w} + (n_h/n_t) \cdot J_D/(n_h \cdot e) = (n_{c,w}/n_t) v_{c,w} + J_D/(n_t \cdot e)$, where I have replaced the hot ion velocity with its estimate from the diamagnetic current, J_D (assuming electrons are too cold to contribute to that current). My estimate of the diamagnetic current contribution to the ion velocity measurement comes from T89: $J_{D,T89}/(n_h \cdot e)$. Substituting, I get: $v_t = (n_{c,w}/n_t) v_{c,w} + J_{D,T89}/(n_t \cdot e)$, where the last term is my estimate of the diamagnetic current contribution to the total ion velocity. When cold/warm ions are present they dominate the ion density, $n_{c,w} \sim n_t$, resulting in $v_{c,w} \sim v_t - J_{D,T89}/(n_t \cdot e)$. Thus, by subtracting the diamagnetic current contribution $v_{D,T89} \sim J_{D,T89}/(n_t \cdot e)$, shown in Figure 10b, from the total ion velocity represented by the median $v_{i,perp}$ vectors during $v_{i,perp} > v_{min}$ intervals (Figure 3.10a), the flow vectors that remain should be primarily related to **E** × **B** drift, the dominant contributor to the cold/warm ion flow (Figure 3.10c). A comparison between Figure 3.10a and 3.10c shows a shift in the location where flows are diverted from dawn towards pre-midnight: while the combined flows are diverted near 03 MLT towards dusk in Figure 3.10a, representing the average momentum transport of cold and hot ions, Figure 3.10c shows the modified flows (representative of cold and warm ions) to instead be diverted near 20 MLT towards midnight then dawn, representing the dominant mass/species transport. This modified flow pattern coincides well with the trends in ion species temperature, suggesting that the cold/warm ions on the nightside are a contiguous population that is not energetic enough to be affected by diamagnetic drift and instead flows primarily around midnight to the dawn side or through dusk outside of the plasmasphere due to co-rotation and the global convection electric field. The trends in cold ion properties and the modified flow pattern agree well with descriptions of the warm plasma cloak [*Chappell et al*., 2008, and references therein] and earlier predictions of cold particle transport near the magnetic equator [*Kavanagh et al*., 1968]. The predicted cold ion flow

pattern, individual ion densities, and their temperatures draw further attention to the sources of cold ions seen near the equatorial magnetosphere and how their transport and population of the near-Earth magnetosphere varies with geomagnetic activity.

3.5.1.2 Sources and Transport

Two dominant sources for ionospheric cold ions are at the dayside cusp and also at the nightside, pre-midnight oval mainly during active times. There is also one major source of cold ions in the solar wind that also populates the dayside. These sources populate different locations of the magnetosphere with cold ions depending on the level of geomagnetic activity that results from changes in IMF.

At the dayside there is entry of solar wind at the LLBL (low-latitude boundary layer) during northward IMF [e.g., *Li et al.*, 2009, *Øieroset et al*., 2008]. At the same time there is outflow from the cusp and an expanded plasmasphere. The combination of the solar wind and cusp ion sources should result in a thicker LLBL that is filled with solar wind and cusp plasma that is adjacent to a dense, expanded plasmasphere. Waves occurring within the LLBL could provide a mechanism for mixing of expanded plasmaspheric ions in with LLBL plasma and could be why during $Kp \leq 1$ (likely representing conditions of northward IMF) I observe a wider swath of ions around the magnetopause. But during predominantly southward IMF ($Kp > 1$) the cold ions are more concentrated near the plasmaspheric plume region in the afternoon that suggests a forcing of cold ions outwards towards the magnetopause, leading to their escape from the magnetosphere (compare Figures 3.9d and 3.9h). The sunward ion transport should be enhanced during southward IMF conditions because the LLBL is likely thinner, dayside

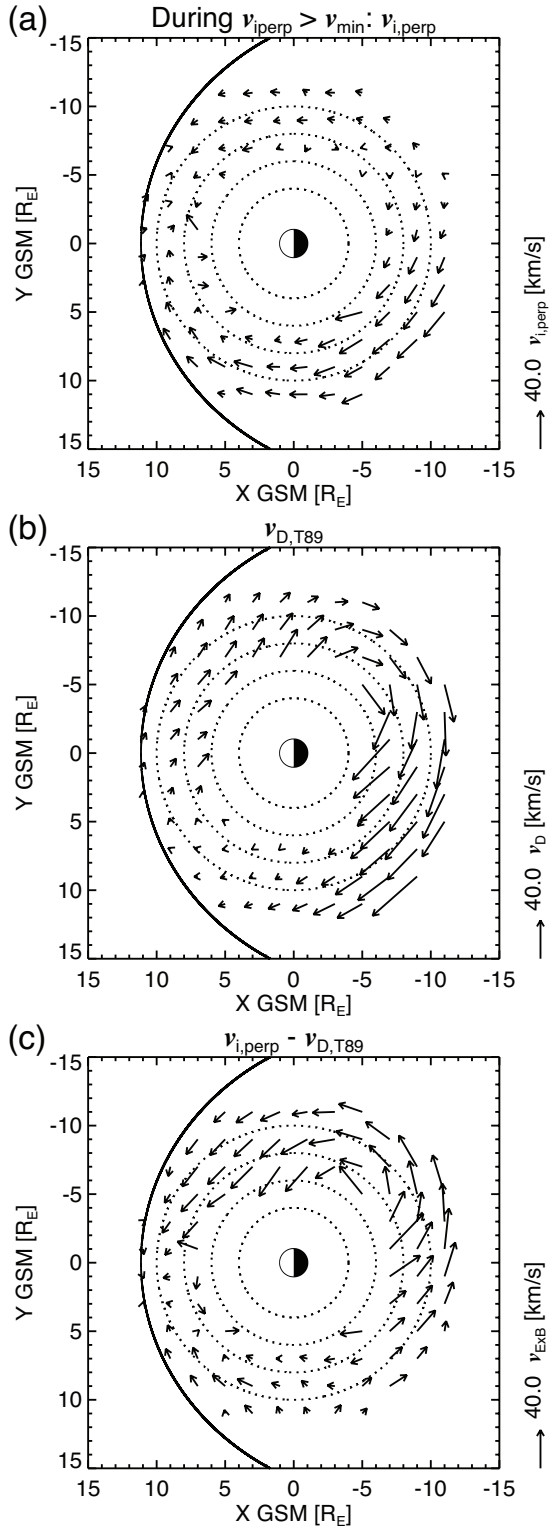

Figure 3.10: (a) $v_{i,perp}$ vectors during $v_{i,perp} > v_{min}$ events, (b) diamagnetic drifts ($v_{D,T89}$) computed using the magnetic field model by *Tsyganenko* [1989] and the median of observed IESA and SSTI combined ion density (Ni_ESA+SST), and (c) the predicted v_{ExB} flow pattern for cooler ions after subtraction of the $v_{D,T89}$ component from $v_{i,perp}$.

reconnection creates a demand for sunward transport, and the sunward convection due to the enhanced magnetospheric electric field is also enhanced. As *Walsh et al*. [2013] showed, every time there is reconnection some portion of the magnetosphere is sucked out; this sunward transport of plasma has also been termed the sunward surge of the plasmasphere [*Goldstein and Sandel*, 2005, and references therein] and has been observed to coincide strongly with an increase in magnitude of southward IMF. My observations suggest that enhanced electric fields (and more vigorous convection) accompanying higher Kp transport ions out towards the magnetopause more rapidly during active times. By noting the presence of larger flow vectors both at smaller L and in a global sense in the comparison between Figures 3.9a and 3.9e, I also expect that the dayside ions flow through faster along the convection paths shown in Figure 3.10c during higher Kp.

Transport of cold ions at the nightside, where the cold ions originate from the nightside oval, is predicted to stagnate around pre-midnight (Figure 3.10c). This gives them enough time to get accelerated and heated by injections that occur both at quiet times (less frequently) and at active times. EMIC and other low-frequency waves are another heating source that can contribute to the increased temperature trend around pre-midnight; in particular He^+ band EMIC waves are damped by O^+ at the ionosphere (and H^+ band waves are damped by He^+) [*R. M. Thorne*, personal communication, May 13, 2014]. Such a mass-dependent heating mechanism at the topside ionosphere has indeed been observed in the past [e.g., *Moore et al*., 1986, and references therein]. Interestingly, the ion temperature does not increase significantly along the streamlines from pre-midnight through dusk. Therefore I expect the dusk/pre-midnight sector to be the dominant region of cold ion heating, possibly due to the presence of EMIC waves excited by injected, energetic ions there. These warm ions originating at the dusk/pre-midnight sector are

expected to drift around the plasmasphere as the streamlines dictate in Figure 3.10c (both along dawn and dusk, depending on their initial location).

As noted above, the dawn warm ions I observe are part of the warm plasma cloak. The dusk warm ions cannot make it through the plasmasphere but flow along the dusk plasmapause out towards the magnetopause. During lower Kp, the expanded plasmasphere causes the dusk warm ions to flow out at larger geocentric distances (~7 R_E and larger). But during higher Kp, the contraction of both the plasmasphere and the high-speed flow lines suggests these warm ions could flow along the plasmapause at much smaller geocentric distances (~7 R_E or less). In addition to the warm ions flowing along the dusk boundary and the cold plasmasphere inside the boundary, in this same region there are injected ions (hot plasma sheet) that take the paths along dusk shown in Figure 3.4c (also Figures 3.9a and 3.9e). The injected ions are the free energy source for EMIC waves and their drift paths show why EMIC waves are predominant along dusk [e.g., *Anderson et al*., 1992; *Min et al*., 2012; *Usanova et al*., 2012; *Keika et al*., 2013b]. But the waves at dusk could be further influenced by the sliver of warm ions that drift through from pre-midnight and should differ from the waves at noon (cold ions from solar wind and cusp). Further studies of the waves occurring in these regions as well as along dawn should reveal differences in the wave properties.

The properties of cold ions discussed in this chapter can find broader applications in understanding cold or warm particle source and loss processes, and modeling the contributions and effects of waves to acceleration, heating, and loss of energetic particles in the Earth's magnetosphere.

3.6 Conclusions

I have presented numerous features of cold ion occurrence and properties near Earth's equatorial magnetosphere and discuss the results in relation to multiple magnetospheric ion populations, their sources, and transport. My principal conclusions are listed below.

1. In the absence of flows, warm ions are seen over ~10% of the time near the equatorial magnetosphere at all local times, with slight enhancements to >10% along the dusk and dawn flanks, and another enhancement (~15%) near the magnetopause that is higher in the afternoon sector (>20%). At distances less than 6 R_E the warm ions are most enhanced on the nightside, wrap around the dawn side, and have lowest occurrence in the afternoon sector. During flows, cold ions are seen most frequently on the dayside in the late morning to afternoon sector (~60–90%) and the location of peak occurrence changes with geomagnetic activity; occurrence is high along the entire dayside near the magnetopause for $Kp \leq 1$ and peaks more in the late morning to afternoon for $Kp > 1$.
2. The cold ion species are predominant in the afternoon at a few eV (protons) to tens of eV (He^+ and O^+), though the heavy ions are less dense than protons by a factor of 10 or more.
3. The relative density of cold He^+ and O^+ increases near midnight, where they become denser than protons, with density ratios for both heavy ions exceeding 1.0.
4. All nightside cold ions are quite warm, having temperatures from near 10 eV (protons), tens of eV (He^+), to hundreds of eV (O^+). They wrap around both the dusk and dawn sides, with the dawn warm ions consistent with previous descriptions of the warm plasma cloak.

5. The $v_{i,perp}$ vectors during $v_{i,perp} > v_{min}$ events shows ion flows are diverted before dawn towards the dusk side. The strongest flows passing through dusk include the contribution of the diamagnetic drifts associated with hot ions. A subtraction of the model diamagnetic drift component from the $v_{i,perp}$ vectors results in a flow pattern that depicts the combined convection and co-rotation drifts of cooler particles. This modeled cold particle flow pattern overlaps well with the trends in cold ion species temperature to suggest transport of cold magnetospheric ions that wraps around the dawn side, again consistent with descriptions of the warm plasma cloak and with past modeling of cold particle transport.

More sampling of cold ion properties at small geocentric distances and high latitudes support further studies on their involvement in magnetic reconnection at the magnetopause and in the magnetotail, their relationship to EMIC waves, and can also provide a more complete portrayal of these low-energy ions that fill the magnetosphere. Perhaps, those analyzing particle and magnetic field measurements by other spacecraft can leverage the methods and techniques I describe in this chapter to provide more properties of cold ions in such locations to refine the spatial resolution of their properties for application towards studying the above topics in the dynamic magnetospheric system.

CHAPTER 4

A review on the occurrence rates, properties, and transport of low-energy plasma populations near the Earth's equatorial magnetosphere

4.1 Introduction

Many low-energy plasma (LEP) populations exist near the Earth's equatorial magnetosphere. The solar and terrestrial sources of these populations are typically inferred from their properties (composition, densities, and temperatures). The observed compositional properties of LEP can also be used to infer a source's contribution to the total LEP population at various locations and enable studies of transport from that source throughout the magnetosphere.

Whether low-energy plasma is observed near the equatorial magnetosphere depends on many factors. The cusps and polar wind are consistent sources of LEP, and the extent to which their contributions recirculate in the magnetosphere is sensitive to the large-scale interplanetary magnetic field (IMF). In particular, polar wind outflow is active on lobe field lines at all times. It can be carried far into the magnetotail and lost to interplanetary space during northward IMF, and returned ($L<50\ R_E$) and recirculated in the magnetosphere during periods of southward IMF, increasing its transport to the equatorial plane, Figure 4.1 [e.g., *Haaland et al*., 2012]. During southward IMF the distance the polar wind is transported down the magnetotail before it is returned earthward depends on magnetotail reconnection and the strength of convection [*Haaland et al*., 2012, and references therein]. The distance the polar wind travels has also been described as being energy and mass dependent, with a tendency for heavier particles to fall back

at smaller geocentric distances [*Lockwood et al*., 1985; *Chappell et al*., 1987]. The IMF orientation also plays a role in population of the inner magnetosphere (L<15 R_E) with low-energy plasma. Periods of predominantly northward IMF can facilitate solar wind entry into the low-latitude boundary layer (LLBL) following lobe magnetic reconnection and at the same time waves excited at high latitudes can energize ionospheric plasma that can then be observed at dayside equatorial regions [e.g., *Fuselier et al*., 2012]. Periods of predominantly southward IMF can lead to a transition to terrestrial ionosphere sources providing the dominant supply of LEP to the inner magnetosphere. This change is due to recirculation of the lobe outflow in combination with increased electromagnetic energy input into the conjugate ionospheres from the magnetotail that can again energize the ionospheric plasma and drive nightside outflow that can feed back directly to the evening near-Earth plasma sheet and surrounding regions (|X-GSM|<15RE). Although the energy input that drives outflow from the nightside ionosphere is expected to increase with geomagnetic activity, it does not cease during quiet times. As *Angelopoulos et al*. [1994] showed, bursty bulk flows (BBFs) persist even during low AE (auroral electrojet) index, and dipolarization fronts embedded within BBFs have been shown to be capable of channeling a sizable portion of the cross-tail current into the nightside ionosphere [e.g., *Angelopoulos et al*., 2013; *Liu et al*., 2013]. This propagation of energy from the distant magnetotail, its buildup near Earth, its critical instability, and its explosive release manifest in the auroral substorm sequence captured using ground-based all-sky imagers. Such events, seen even in the largely quiet solar cycle 24 [e.g., *Nishimura et al*., 2010], suggest that energy input needed to drive outflow of low-energy plasma to the inner magnetosphere from the nightside ionosphere is available during all levels of geomagnetic activity. The nightside ionosphere is thus an additional terrestrial LEP source that should be considered in addition to the polar wind and cusp sources.

Although the above concepts for populating the equatorial magnetosphere with LEP are often discussed, it is difficult to determine the actual occurrence rates and properties of equatorial LEP because of common observational difficulties, such as spacecraft positive charging in sunlight. Positive charging often makes cold or low-energy ions invisible to particle instrumentation, and measurements of low-energy electrons can be hard to interpret due to difficulty in differentiating between ambient cold electrons and photoelectrons emitted by the spacecraft. Nonetheless, measuring LEP to facilitate understanding of the sequence of transport from their source regions—the terrestrial ionosphere in particular—and their subsequent observation in the equatorial magnetosphere, their circulation, and their participation in other phenomena occurring throughout the magnetosphere remains an active area of research. As will be seen, advances in satellite instruments and creativity in using their measurements has taken the idea of the terrestrial ionosphere being the dominant supplier of magnetospheric plasma from concept to fact. The topics discussed in this chapter are inspired by measurements made by recent Earth-orbiting satellite missions (Akebono, Geotail, Polar, Cluster II, and THEMIS) and the analyses and modeling studies that followed. References are also made to previous pathfinder missions.

4.2 Nightside

Between the Dynamics Explorer 1 (DE-1) mission (1981) and the Cluster II mission, launched in 2000 into a 4×19 R_E elliptical polar orbit, the fate of ionospheric outflow at the nightside equa-

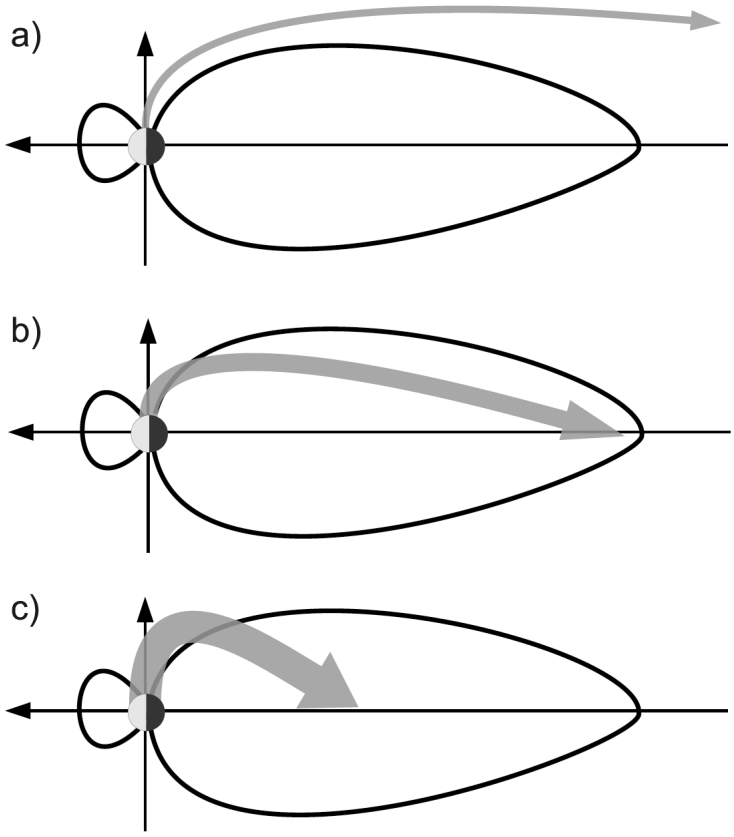

Figure 4.1: Depiction of lobe outflows and their transport tailward during (a) stagnant, (b) low to intermediate, and (c) strong convection by *Haaland et al*. [2012].

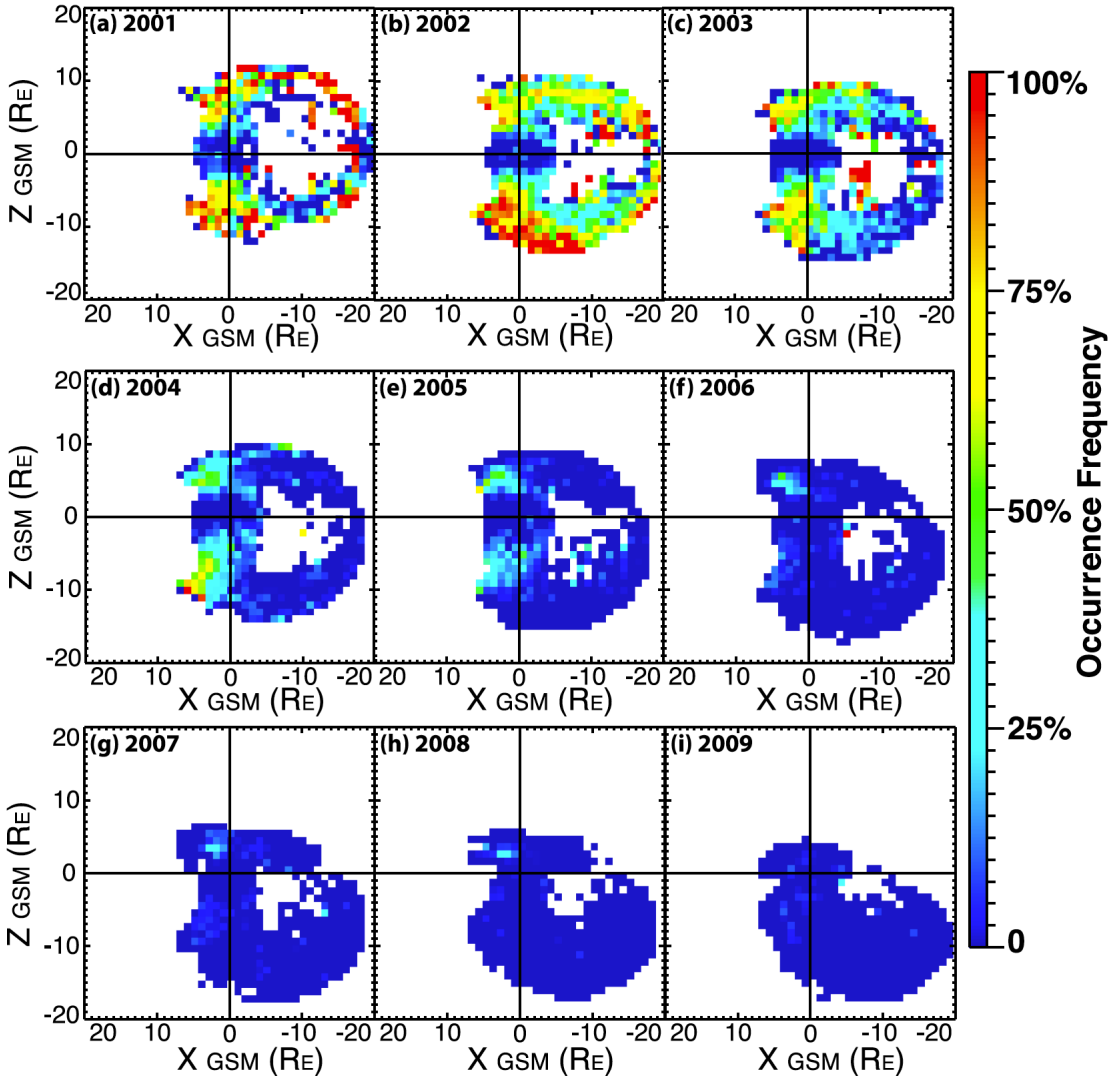

Figure 4.2: Streaming O^+ occurrence statistics and their solar cycle dependence as shown by *Liao et al*. [2012].

torial plane was studied using Akebono measurements in low-Earth orbit (LEO) [e.g., *Cully et al*., 2003a, 2003b], Polar measurements in highly elliptical orbit (HEO) (apogee ~9 R_E) [e.g., *Huddleston et al*., 2005], and particle trajectory modeling [e.g. *Delcourt et al*., 1989] to predict where the outflow observed by the spacecraft ended up. Modeling done using Akebono and Polar measurements showed the ionosphere to be capable of providing enough LEP to fill the

magnetosphere, lending support to an early prediction motivated by DE-1 observations [*Chappell et al*., 1987]. As Akebono and Polar surveyed the regions above the poles, the Geotail spacecraft, orbiting near the equatorial plane, made measurements at perigee (~9 R_E) of multiple cold ion species (H^+, He^+, and O^+) accelerated into the energy range of the particle instrument by Pc5 ULF (ultra-low frequency) waves [*Hirahara et al*., 2004]. According to these measurements, these cold ions were present 40 to 70% of the time the Pc5 waves were observed. Before these observations at perigee, Geotail had also measured cold ions hundreds of R_E in the magnetotail [*Hirahara et al*., 1996; *Seki et al*., 1999] that also supported predictions by *Chappell et al*. [1987]. The observations made by *Hirahara et al*. [2004] were strange, however, because the cold ions and an energetic ion component at the inner edge of the plasma sheet were observed simultaneously, showing that ionospheric LEP could cross the plasma sheet without being significantly energized [also see *Seki et al*., 2003]. Shown to have partial densities comparable to those of the energetic ion component, these cold ions were observed more frequently during the rising phase of the solar cycle. As a result, the authors suggested that the observations of terrestrial cold ion signatures were dependent on solar activity and implied that feeding of ionospheric outflow to the near-Earth plasma increases during more active times. *Liemohn et al*. [2005] performed a statistical survey of cold (from spacecraft potential energy, E_{SC}, to ~300 eV), streaming ions at similar local times when Polar precessed to the equatorial plane and showed that cold ion streams were common, occurring >70% of the time, and concluded that the ionosphere is directly linked to the near-Earth plasma sheet and could supply LEP to around the same locations where *Hirahara et al*. [2004] had observed multiple cold ion species. *Liemohn et al*. [2005] further suggested that this streaming ionospheric plasma could be pervasive on the nightside, though they noted a difference between occurrence frequency for bidirectional streams

(quiet times) and occurrence frequency for unidirectional streams (active times). These streaming cold ion populations were studied by *Chappell et al*. [2008], who noticed a similarity between their persistent occurrence in Polar observations and in a compilation of particle observations from multiple past satellite missions (ATS, ISEE, SCATHA, DE-1), leading them to infer the existence of a low-energy plasma population they called the warm plasma cloak. Named for its bidirectional streaming population of warm (~10 eV to few keV) plasma draped over the plasmasphere that was being blown sunwards by convection, the warm plasma cloak was predicted to eventually cross paths with energetic ring current ions on the dayside near noon. The authors also performed particle trajectory modeling to explain its formation. They showed that a centrifugally accelerated polar wind proton that crosses the plasma sheet at a smaller geocentric distance would pick up less energy and would not get deflected around dusk by magnetic drifts on earthward approach, but instead would flow around the dawnside due to combined convection and co-rotation drifts that transport it towards the dayside magnetopause. I will come back to the warm plasma cloak later.

More recent studies on the occurrence of magnetospheric low-energy plasma and its solar or terrestrial origin have drawn on enhanced observational capabilities provided by the four-satellite Cluster II mission and, beginning in 2007, the five-satellite THEMIS mission. The Cluster spacecraft orbits allow for sampling of LEP directly above the polar caps and also at larger geocentric distance in the tail lobes and plasma sheet. The instruments were also designed to observe the dominant ion species for studying sources and transport and could combat some difficulties of observing LEP because of their ability to actively control the spacecraft potential (ASPOC). Together, these capabilities enabled a cradle-to-grave inquiry into the transport of LEP (O^+ in particular) from the ionosphere into the magnetosphere and near the equatorial plane

as well as LEP energization [e.g., *Kistler et al*., 2005, 2010]. This inquiry motivated recent particle trajectory modeling studies [e.g., *Yau et al*., 2012] and are also the subject of many global magnetospheric simulations [*Lotko*, 2007; *Brambles et al*., 2011; *Yu and Ridley*, 2013]. Even so, spacecraft charging at higher altitudes could still render a significant LEP population invisible to the particle instruments most of the time, and that portion of LEP would remain unstudied.

Using the Cluster II dataset and a unique method that detected signatures of spacecraft electrostatic wake formation due to a supersonic flow of low-energy ions, *Engwall et al*. [2009] showed that the occurrence rate of ions too low in energy to be detected by standard particle instruments was >70% in the lobes out to X-GSM ~ −15 R_E. The ions' very low energy clearly identified them as ionospheric plasma and their high occurrence rate confirmed their prominence in the lobes. The *Engwall et al*. [2009] data also showed an occurrence rate decrease to <20% on approach to the plasma sheet (|Z-GSM| < 2 R_E). They suggested that the low occurrence rate at small Z-GSM distances was due to the low-energy ions being energized above tens of eV upon approach to and passage through the plasma sheet. They also noted, however, an observational limitation near the plasma sheet: the detection method required both a steady, strong magnetic field and the absence of ambient hot plasma. Therefore, LEP coexisting with hot plasma sheet particles [*Hirahara et al*., 2004, and *Liemohn et al*., 2005] was not observed in this study. But studies using direct measurements of the streaming O^+ lobe population revealed more characteristics of cold ions in the lobes and near the plasma sheet. *Liao et al*. [2010, 2012] also used Cluster ion measurements (>~40 eV) to show a positive correlation between solar activity and cold ion outflow; their study also showed a general decrease in streaming O^+ occurrence rate near the plasma sheet. Though the outflow occurrence rate decreased with lower solar activity,

outflows in the lobes still occurred between 0 and 25% of the time approaching solar minimum; cold ions below the instrument detection threshold were not accounted for. *Liao et al*. [2010, 2012] noted a seasonal as well as an orbital bias: the equatorial magnetosphere between 4 and 15 R_E was not often sampled due to the Cluster II orbit. Still, their results suggested that although ionospheric outflows contribute to the equatorial plasma content at all levels of solar activity, that this contribution should be greater near solar maximum (Figure 4.2).

As described in Chapter 3, I also sampled the nightside equatorial LEP out to ~13 R_E in the region deficient in the Cluster II dataset during predominantly quiet times (observation interval between 2008 and 2013). I used the THEMIS satellites to sample cold ions during intervals of enhanced bulk plasma flows (convection or ULF waves) that accelerated ambient cold ions above the spacecraft potential energy (E_{SC}) so the ions could be detected by the particle instruments carried by the three inner THEMIS spacecraft (low inclination, 1.5 × 13 R_E). I estimated the partial densities and temperatures of the three dominant ion species (H^+, He^+ and O^+) during such flow intervals and showed that all three species occurred around 1 to 20% of the time on the nightside and that the heavier ions were more abundant and warmer than the protons (H^+: few to 10 eV, He^+: 10s eV, O^+: 100s eV). These nightside equatorial observations support the interpretation by *Engwall et al*. [2009] that the outflowing LEP they saw with Cluster II was likely energized above the level needed to form a wake near the plasma sheet. I also used the heavy ion density ratios and higher temperatures on the nightside to infer a major ionospheric source of LEP at L<13 R_E. I noticed another trend: the median temperatures of all three species were quite warm (10–100s eV) and the trends in median temperature traced out a path from pre-midnight through the dawn side, consistent with particles in the warm plasma cloak. There was evidence of another path of nightside warm ions along the dusk side at larger geocentric

distances. The dawnside trend implied that the heavy ions that likely originate from the nightside ionosphere could reach the equator, gain moderate energy from injections or waves, and then become part of the cloak, as discussed but not directly observed by *Chappell et al*. [2008]. Taken together, the observations using Akebono, Polar, Geotail, Cluster, and THEMIS describe a consistent connection between LEP outflow to various geocentric distances on the nightside (including the plasma sheet) and LEP occurrence rates and properties, indicating that the ionospheric source can provide the primary plasma contribution to the nightside equatorial magnetosphere even during quiet times. These modern observations confirm clues picked up by earlier spacecraft suggesting the importance of the ionosphere in seeding the nightside magnetosphere [*Shelley et al*., 1972; *Lennartsson and Shelley*, 1986; *Chappell et al*., 1987].

4.3 Dayside

A mixture of solar and terrestrial plasma is known to exist at the dayside equatorial magnetosphere, and the typical dayside plasma number density is much higher than at the nightside. In particular, the terrestrial plasmasphere (and the trough region that is refilled with ionospheric material during quiet times) is a persistent and evolving LEP region. Although it has the highest concentration of cold particles at lower geocentric distance ($L<6$ R_E), it can nonetheless supply different parts of the dayside with cold particles during quiet and active times. During quiet times the boundary between the outer plasmasphere and the magnetosphere becomes diffuse, and cusp outflow and solar wind plasma entering the LLBL during northward IMF can mix with the diffuse dayside plasmasphere. Active-time features of the plasmasphere, specifically plumes that can extend from dusk and bring plasmasphere material around to the dawn side, are also important contributors to dayside LEP and fundamental for understanding

inner magnetosphere dynamics [e.g., *Moldwin et al*., 2004]. Such observations of the plasmasphere and its material made by various spacecraft provide a historical timeline that describes the increasing importance of the plasmasphere and its contributions to dayside magnetospheric topics such as reconnection and wave-particle interactions [*Chappell*, 1972; *Carpenter et al*., 1992; *Goldstein and Sandel*, 2005; *McFadden et al*., 2008; *Darrouzet et al*., 2009].

A series of Polar studies described measurements of LEP between 3 and ~9 R_E at the dayside equatorial magnetosphere and showed LEP to be common near the magnetopause; the observed LEP possessed properties consistent with the plasmasphere (>90% H^+, ~10% He^+, and trace O^+) [*Chandler and Moore*, 2003; *Chen and Moore*, 2004, 2006]. These authors identified the major ion species during plasma flows and studied the occurrence rate of LEP near the magnetopause around noon MLT, showing it to be near 50%. *André and Cully* [2012] conducted a similar study to determine the occurrence rate of LEP on the dayside using a combination of low-energy ion detection methods on Cluster II data from a sample of dayside magnetopause crossings. According to their statistics, low-energy ions were present 50–70% of the time. These occurrence rates, which emphasized the ions' importance for studies on dayside magnetic reconnection, were consistent with those presented in Chapter 3 using THEMIS data (dayside cold ion occurrence rates between 50 and 80% during bulk plasma flows). As shown in Chapter 3, I split the occurrence rates according to Kp condition (low or high) and showed that LEP occurrence was more frequent (>80%) along the entire dayside (including dawn) during low Kp conditions (with predominant northward IMF) than during higher Kp conditions (with predominant southward IMF), when I saw a decrease in occurrence to ~50% along dawn. During higher Kp conditions, I interpreted the frequent occurrence region concentrated more in

the late morning-to-afternoon sector as a loss of dayside cold ions that accumulated during northward IMF (solar wind entry and cusp sources combined with the diffuse plasmasphere) to the magnetopause during reconnection and enhanced sunward convection. This northward IMF orientation and its effect on dayside LEP sources has been discussed in the context of high-latitude reconnection [e.g., *Fuselier et al*., 2012]; the northward IMF orientation also has implications for transport of LEP from the dayside along the flanks to form a cold, dense plasma sheet [e.g., *Moore et al*., 1999]. *Fuselier et al*. [2012] described Cluster low-energy electron observations showing entry of solar wind electrons into the LLBL during northward IMF and related these observations to past observational work using AMPTE/CCE data which showed that direct injection of cusp O^+ beams into the LLBL during northward IMF could occur over a range of dayside MLT sectors [*Fuselier et al*., 1989, 1995]. These observations support the interpretation I gave in Chapter 3 that cold ions appear more frequently across the entire dayside during Kp≤1. When combined, the dayside observations show a mechanism for LEP buildup opposite that seen at the nightside during southward IMF and enhanced magnetotail reconnection. During northward IMF most of the low-energy plasma from the polar wind and nightside oval that are important for populating the plasma sheet are lost to interplanetary space along lobe field lines or do not outflow due to less electromagnetic energy input from the tail. LEP from the dayside cusps, solar wind, and expanding plasmasphere are then the primary sources that populate the magnetosphere. The compositional properties of magnetospheric low-energy plasma should also reflect this change in population of the magnetosphere by the different sources, with likely a greater concentration of H^+ at the dayside and changes in the transport mechanism of additional H^+ towards the nightside. Further study on this population and transport of the mixed

dayside LEP is needed to understand how this changing source contribution and composition affects other magnetospheric processes.

4.4 Deep inner magnetosphere

At least two inner magnetosphere LEP populations characterized by warmer temperatures (tens to hundreds eV) exist in addition to the cold plasmasphere at lower geocentric distances and have been observed by multiple spacecraft. Dynamics Explorer-1 observations described one such population as a region of warm plasma trapped near the equatorial magnetosphere with occurrence rates near 50% at dawn and approaching 100% near dusk [*Olsen et al*., 1987]. Although this population, mainly H^+ (n_{He+}/n_{H+} ~ 10%), was seen in a geocentric distance range similar to that of the plasmasphere (3–6 R_E) and had higher occurrence rate nearer the plasmapause, its temperature kept it from being a typical plasmasphere component. The peak occurrence rate along the dusk side suggested some involvement of energetic plasma sheet particles. Furthermore, the warm plasma was observed at the same time as equatorial noise (magnetosonic waves) excited by ring distributions [*Russell et al*., 1970]; these waves could have been a source of heating for originally cold plasmaspheric ions. EMIC waves were also considered to play a role in cold ion heating at this location. Using more recent measurements of this trapped warm plasma, *Yamauchi et al*. [2012] confirmed many of the results described by *Olsen et al*. [1987]. But further studies on the properties of this population, an explanation of its formation, and its dependence on geomagnetic activity remain to be done.

Another warm plasma population described as the oxygen torus has a nearly reversed spatial occurrence rate, with higher occurrence rates from pre-midnight to along the dawnside and lower occurrence rates near dusk and was also observed by Dynamics Explorer-1 [*Chappell*,

1982; *Roberts et al*., 1987]. Furthermore, its occurrence was independent of Kp and was observed even during low Kp. More recently, CRRES observations of the oxygen torus were made during quiet geomagnetic conditions following geomagnetic storms [*Nosé et al*., 2011]. Because of the spatial distribution of the torus and its presence during quiet times, it was suggested that it is a contributor to an O^+-rich ring current during geomagnetic storms due to near-Earth dipolarization and the torus being available for non-adiabatic acceleration [*Nosé et al*. 2010, 2011] (Figure 4.3). As described in the previous chapter, I also reported the existence of such a warm ion distribution in the deep inner magnetosphere but was unable to infer its composition due to the absence of plasma flows. The occurrence rate of this warm population was 40–60% in the evening and early dawn sectors and was consistent with previous occurrence statistics of the oxygen torus. The compositional properties of the oxygen torus and its location of peak occurrence imply that coupling between the magnetosphere and ionosphere is directly responsible for its formation. The fact that the torus is often observed following storms suggests it is an after-effect, likely a portion of outflow injected to a location nearer the Earth by the more dipolar geomagnetic field configuration following geomagnetic activity. This time sequence should be studied in greater detail, as the torus population has been found at the same geocentric distance where the greatest concentration of ring current particles are observed and has the potential to modify present simulation efforts to understand the effects of outflow contribution on the ring current [*Welling et al*., 2011]. The torus occurrence rate also peaks near the same local time and just within the geocentric distance range where I identified O^+ as the most abundant cold ion species at the nightside equatorial plane, suggesting gradual or diffusive

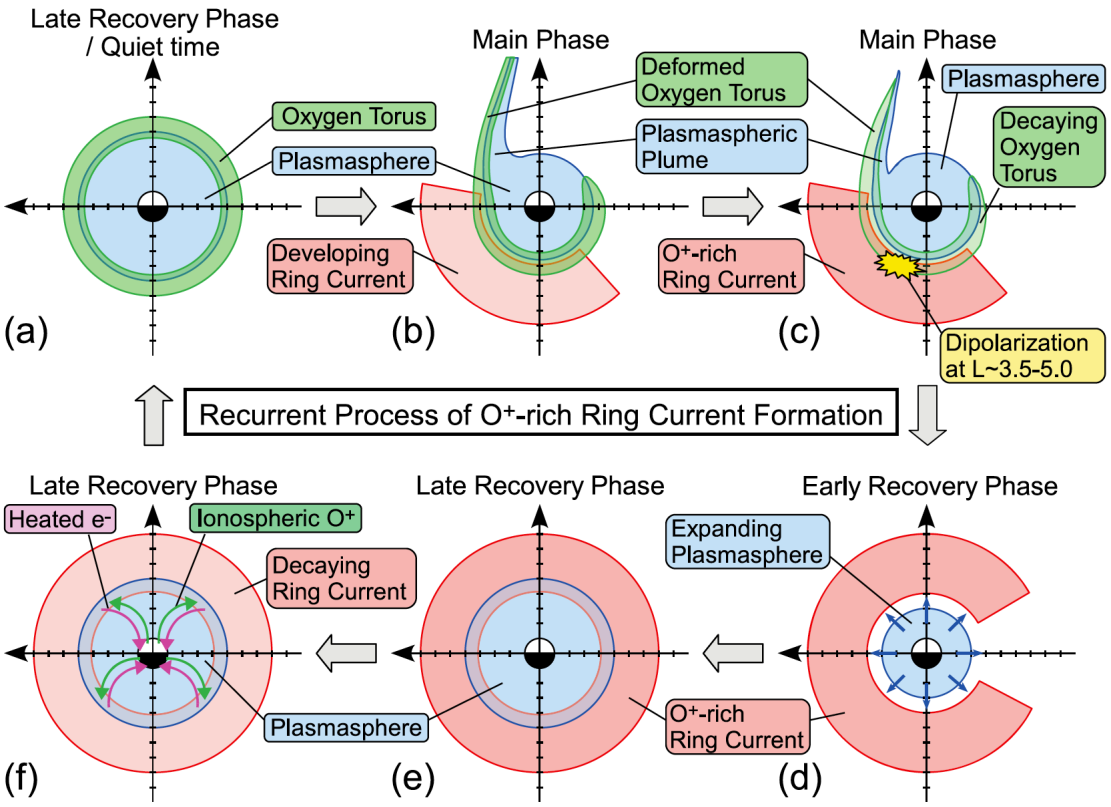

Figure 4.3: The oxygen torus and its participation in formation of an O^+-rich ring current as depicted by *Nosé et al*. [2011].

outflow of cold O^+ into the nightside. This diffusive outflow could be caused by energy input into the ionosphere that occurs over a spectrum. Combined observations from multiple polar-orbiting spacecraft inserted at different local times could facilitate confirmation of such a diffusive population of the nightside region between the oxygen torus and the plasma sheet populations.

4.5 Transport

Equatorial transport of LEP is to a large extent caused by E × B drift, including a contribution of co-rotation near the Earth. Early modeling showed the paths cold particles are expected to take through the equatorial magnetosphere [*Kavanagh et al*., 1968]. But there have been difficulties in

sampling the convective drift component of the cold plasma using spacecraft for comparison to this simple model.

IMAGE EUV observations have shown how the plasmasphere reacts to increases in geomagnetic activity and the evolution of the outer plasmasphere boundary [*Goldstein and Sandel*, 2005]. Although this boundary can be turbulent and have notable structure, it is in general consistent with co-rotating plasma within a closed drift path boundary at lower geocentric distance and sunward convective transport acting on its outer layer. Beyond this EUV imagery of the plasmasphere, direct measurements of the plasmaspheric particles to obtain the plasma moments and infer the convective and co-rotation drifts have been rare.

Until recently, inquiry into low-energy transport near and outside the plasmasphere boundary layer has been limited. *Dandouras et al*. [2005] described multiple cases and statistics of Cluster II observations near and within the plasmasphere during spacecraft perigee. Their studies of pitch-angle distributions of ions in the plasmasphere as well as near its outer edge and analysis of the ion distribution functions and moments showed that plasma was co-rotating within the plasmasphere and had a notable outward expansion velocity component outside it. Using Cluster II data obtained near the plasmasphere outer boundary during quiet times, *Dandouras* [2013] observed a constant outward leakage of plasmaspheric material that has been called the plasmaspheric wind [e.g., *Lemaire and Schunk*, 1992; *Yoshikawa et al*., 2003; *Tu et al*., 2007]. This wind, most pronounced at the magnetic equator due to imbalance between gravitational, centrifugal, and pressure gradient forces, has been predicted to be capable of contributing to the magnetospheric plasma independent of denser plumes that are observed extending towards the magnetopause during more active times on the afternoon side. The existence of such a wind provides an explanation for the observation of the plasmasphere being

diffuse on the entire dayside during prolonged periods of geomagnetic quiet and complements the opposition of convection and co-rotation drifts along dusk that result in the bulge along the dusk side.

Convection should still take over equatorial transport of LEP during moderate geomagnetic activity, however. *Yamauchi et al.* [2013] conceptualized the low-energy plasma and energetic ion transport paths and the expected magnitude of combined drifts in the inner magnetosphere. They suggested that plasma too low in energy to be affected by magnetic (gradient and curvature) drifts is transported by convective drift with an increasing contribution from co-rotation drift near the Earth that results in dominant low-energy plasma flow along the dawn side. Both the convective and magnetic drifts determine the transport of energetic plasma, with strongest energetic ion flow occurring along the dusk side and strongest energetic electron flow occurring along dawn. Although energetic plasma motion can be studied using measurements by existing satellite particle instruments, the low-energy plasma components remain difficult to measure due to positive spacecraft charging in sunlight. But by using periods of bulk plasma flow, I have obtained the inferred the flow pattern of cold ions by subtracting the energetic ion drift component estimated by a model diamagnetic drift. My result, which showed larger flows from pre-midnight along the dawn side with smaller flows along the dusk side, agrees with suggestions by *Yamauchi et al*. [2013] and the transport modeling performed by *Kavanagh et al*. [1968]. Using an inference from larger flow vectors (computed using the full ion moments) that penetrated to lower L globally during higher Kp, I also suggested that LEP flow due to increased convection should be faster and could occur at lower L during higher Kp. The cold particle transport results that I described in Chapter 3 are also consistent with the properties of the cold ion species I observed and showed that most cold/warm ions originating near pre-

midnight flow along the dawn side, and some flow along the dusk side beyond the plasmapause. The agreement in the temperature and the drift vectors is consistent with previous predictions on sunward convective transport of the warm plasma cloak as well as early modeling done by *Kavanagh et al*. [1968]. Even so, some trends, even at the larger spatial scale presented in Chapter 3 suggest significant inhomogeneity in the convection profile at the equatorial plane is not included in this simple model of LEP transport. For example, at pre-midnight (Figure 3.10c) there appears to be a region of flow shear that would be consistent with the Harang reversal observed in the ionosphere [*Zou et al*., 2011]. Better-coordinated studies on LEP transport are needed to better understand the LEP transport pattern and its variation with geomagnetic activity.

4.6 Future

In the decades following the first ISEE-1 observations showing a significant terrestrial heavy ion contribution to plasma sheet composition [*Shelley et al*., 1972], additional ionospheric LEP observations by instruments carried on the pathfinder DE-1 mission [*Chappell et al*., 1987], and descriptions of ionospheric particle transport trajectory to the plasma sheet [*Delcourt et al*., 1989] were performed. The wealth of spacecraft measurements and coordinated modeling studies discussed in this chapter that complement these groundbreaking studies define the methods needed for studying the plasma sources and magnetospheres of other planets. More research on the Earth's magnetosphere, however, is still needed.

Some concepts discussed here suggest a gradual, possibly diffusive population of the environment around Earth with terrestrial LEP driven by a spectrum of energy inputs. One such energy input that holds many clues about low-energy plasma populations is that associated with plasma waves. It has long been known that dispersive properties of plasma waves are defined by

multiple plasma components. For example, ion cyclotron waves display dispersive features in wave spectral data when multiple ion species are present in the surrounding plasma environment. These wave dispersive features have been shown to evolve in modeling and observations [e.g., Chapter 2] following heating of originally cold heavy ions. Detailed studies on plasma waves as a method for obtaining more low-energy particle characteristics may seed additional studies on low-energy plasma occurrence rates and properties as well as stepwise energization of the low-energy plasma to form hot plasma components. Such studies integrating wave and particle observations can be initiated now; existing datasets can provide terabytes of observational data for mining and analysis to test against theory and inform future developments.

More multi-spacecraft missions are required to study the energy input spectrum and its feedback on ionosphere-magnetosphere coupling and how this coupling varies on small temporal and spatial scales. For example, multiple polar-orbiting spacecraft that can sweep across many L-shells while being staggered in MLT can facilitate studies of this energy input and the LEP output cycle at the topside ionosphere and observe whether the energy input maps to a preferential location at the equatorial plane. Such multi-point observations are needed to constrain the modeling and simulation work being performed on magnetospheric topics. Many of the observational studies described here obtained LEP occurrence rates and properties projected onto 1×1 R_E or 2×2 R_E spatial resolution grids. Petascale kinetic plasma simulations are currently capable of exploring phenomena with much finer spatial structure (fractions of an Earth radius), and it is likely that variation in LEP occurrence and transport occurs on such small spatial scales. Multi-spacecraft missions are needed to obtain and supply the boundary conditions for such simulation work. Supplementing such missions with nanosatellite-scale observation networks can further refine the spatial resolution of the observations.

CHAPTER 5

Observations and modeling of electromagnetic ion cyclotron waves as function of local time in the presence of multiple ion species

5.1 Introduction

Electromagnetic ion cyclotron (EMIC) wave generation and propagation in Earth's magnetosphere depends on the readily measureable hot (a few to tens of keV) plasma sheet ions, the elusive plasmaspheric or ionospheric cold (sub-eV to a few eV) ion species, and the warmer ion species (tens to hundreds of eV) resulting from partial heating of the cold ones. Cold species are important for lowering the instability threshold and for multiple wave dispersion bands, but warm ions can suppress growth in one band and modify the propagation characteristics. I present analyses of four EMIC wave events typical of the four MLT sectors using measurements by multiple THEMIS spacecraft. The four prototypical EMIC wave intervals chosen have wave spectral properties similar to those found in the recent global survey of EMIC waves from THEMIS [*Min et al*., 2012]. Combining the in situ measured plasma conditions with knowledge of the typical cold/warm ion properties in those sectors gained from my results in Chapter 3, I interpret these wave observations in the context of linear theory. I find that, as expected from past studies, dusk EMIC waves grow because of the interaction of drifting hot anisotropic protons with cold plasmaspheric ions with a dominant cold proton component. Near midnight, EMIC waves are less common because warm heavy ions are more abundant there, suppressing wave growth, but the waves can grow when cold, plume-like or ionospheric outflow density

enhancements are present. Dawn EMIC waves, known for their peculiar properties, are generated away from the equator and attain their polarization due to propagation through the warm plasma cloak. Noon EMIC waves can also be generated non-locally and their properties modified during propagation by a plasmaspheric plume, combined with low-energy ions from solar and multiple terrestrial sources. Thus, accounting for multiple ion species in addition to the measured wave dispersion and propagation characteristics can explain previously elusive EMIC wave properties and is therefore also important for future studies of EMIC wave effects on energetic particle depletions.

5.2 Instruments and data

I use data from the following THEMIS instruments: the electron and ion electrostatic analyzers (ESA) [*McFadden et al*., 2008] providing measurements of the lower energy plasma without mass discrimination (~7 eV to 30 keV for electrons; ~6 eV to 25 keV for ions); the fluxgate magnetometer (FGM) [*Auster et al*., 2008] measuring the magnetic field from DC to 64 Hz; the electric field instrument (EFI) [*Bonnell et al*., 2008] measuring the three components of the electric field from DC to 16kHz and the spacecraft potential, a proxy of total plasma density (N_SCpot) when used in combination with the electron temperature from the ESA electron instrument; and the electron and ion solid state telescopes (SST) [cf. *Ni et al*., 2011], providing measurements of the high-energy portions of the electron and ion distributions (> 30 keV), are not analyzed in detail but are nonetheless included in the energy-time spectrograms to help identify the magnetospheric region of the event of interest. Following *Lee and Angelopoulos* [2014] (subsequently referred to as *LA2014*), I use the plasma convection velocity, common between multiple species, when it is sufficient to bring the cold ions above a minimum energy

threshold to be fully observed by the ESA instrument as a species discriminator: individual peaks in velocity space, one per ion species, correspond to different ion energies arranged by their mass, given their common convection speed, that then enables me to determine species density and temperature. The threshold for detection of such cold ions (E_{min} =0.5mv_{min}^2 = eΦ_{SC} + $IESA_{min}$ ≈ 5 to 10s eV + 6.5 eV) and the details of the method are explained in *LA2014*. Here I applied this technique for the wave event studied at dawn, but rely on statistical results on composition from *LA2014* for the other sectors. I use fast survey data products only (spin period, 3 s resolution samples for particle measurements; 4 Samples/s data for FGM measurements, and 8 Samples/s data for EFI measurements). Processing steps applied to these measurements are described in detail for the first event of my study and are the same for all subsequent events. Measurements from the three inner THEMIS spacecraft (TH-A, TH-D, and TH-E) are selected and have been analyzed from 6 years of operation; due to the similarly low inclinations and orbits, and the sufficient separation of the satellites along their orbits there has been no observational preference for a particular satellite.

5.3 Linear Theory

Similar to what was described in Chapter 2, I use the full dispersion relation for parallel propagating electromagnetic waves for all modeling performed in this chapter [e.g., *Gary*, 1993, chapter 7]. The use of the *LA2014* dataset provides the typical cold ion composition at all MLT sectors beyond about 7 R_E. I do not test linear theory proxies based on geosynchronous spacecraft observations of hot proton anisotropy and cold plasma density in this chapter [e.g., *Blum et al*., 2009, 2012]. Measurements by the Van Allen Probes may enable further tests of such a proxy for EMIC wave occurrence in the deep inner magnetosphere. In this chapter I

concentrate on using the full range of observations available to me and perform a more detailed test of local linear wave growth at larger geocentric distances. I will discuss why my results may also be applicable at smaller distances. In all cases I define a cold (immeasurable) electron component as having a temperature of 1 eV and a number density that is needed to maintain charge neutrality for the model environment.

Numerical solutions of the parallel (or anti-parallel) propagating cases are useful for establishing the conditions for wave growth since the maximum growth of the EMIC instability occurs for parallel (anti-parallel) propagating waves [e.g., *Gary et al*., 2012]. Use of the hot plasma dispersion relation is critical, as it avoids pitfalls inherent to the cold plasma approximation such as overestimating the wave growth rate at larger wavenumbers and subsequent estimates on energetic electron scattering rates [e.g., *Chen et al*., 2013]. My recent statistics [*LA2014*] on magnetospheric low energy ions (< 1 keV) also show that typical heavy ion temperatures (at tens of eV and above) differ significantly from the simplified cold plasma assumption made in most previous studies, resulting in a significant effect on EMIC wave growth, dispersion, and propagation [e.g., *Lee et al.,* 2012]. I use the following colors to represent each of the wave frequency bands: black for the O^+ band, red for the He^+ band, and green for the H^+ band. Numerical solution of the right-handed, circularly-polarized whistler mode (blue) is also included in the modeling for a straightforward visualization of the approximate crossover frequencies in the relevant EMIC wave frequency bands. These crossover frequencies become important after waves propagate away from their source. Depending on the strength and curvature of the magnetic field, the waves disperse and the wave normal angle becomes oblique; waves may then encounter the local crossover frequency and undergo mode-conversion or experience partial or full wave reflection prior to crossing over [e.g., *Thorne et al*.,

2006]. EMIC wave spectra suggest that such mode conversion and wave reflection is, in fact, common.

5.4 Event Selection and Analysis Methods

Selection of the four events presented (one per MLT sector: dusk, night, dawn and day) was motivated by my knowledge on wave properties acquired from previous, published statistical results [*Min et al*., 2012; *Anderson et al*., 1992b; *Keika et al*., 2013] and my examination of dozens of individual cases of EMIC waves observed in my database with information extracted and plotted in a similar fashion to the plots shown in this chapter. All four events I selected, including the one at dawn that shows peculiar linear or right-hand polarization, exhibit properties (wave frequency, power, wave normal angle, and ellipticity) that are representative of waves in each local time sector, as described, e.g., in *Min et al*. [2012].

5.5 Dusk

5.5.1 Particles

The particle measurements and other plasma properties observed by TH-D on 18 October 2011 just beyond a geocentric distance of 9 R_E in the dusk sector are shown in Figure 5.1. Figures 5.1a and 5.1b show the energy-time spectrograms from the combined ESA and SST measurements for ions and electrons, respectively. The sum of the transverse components of the magnetic ($P_{B,perp}$; Figure 5.1c) and electric ($P_{E,tot}$; Figure 5.1d) field dynamic power spectral density are marked by solid lines denoting the local (black) and equatorial (magenta) ion gyrofrequencies (labeled f_{O+},

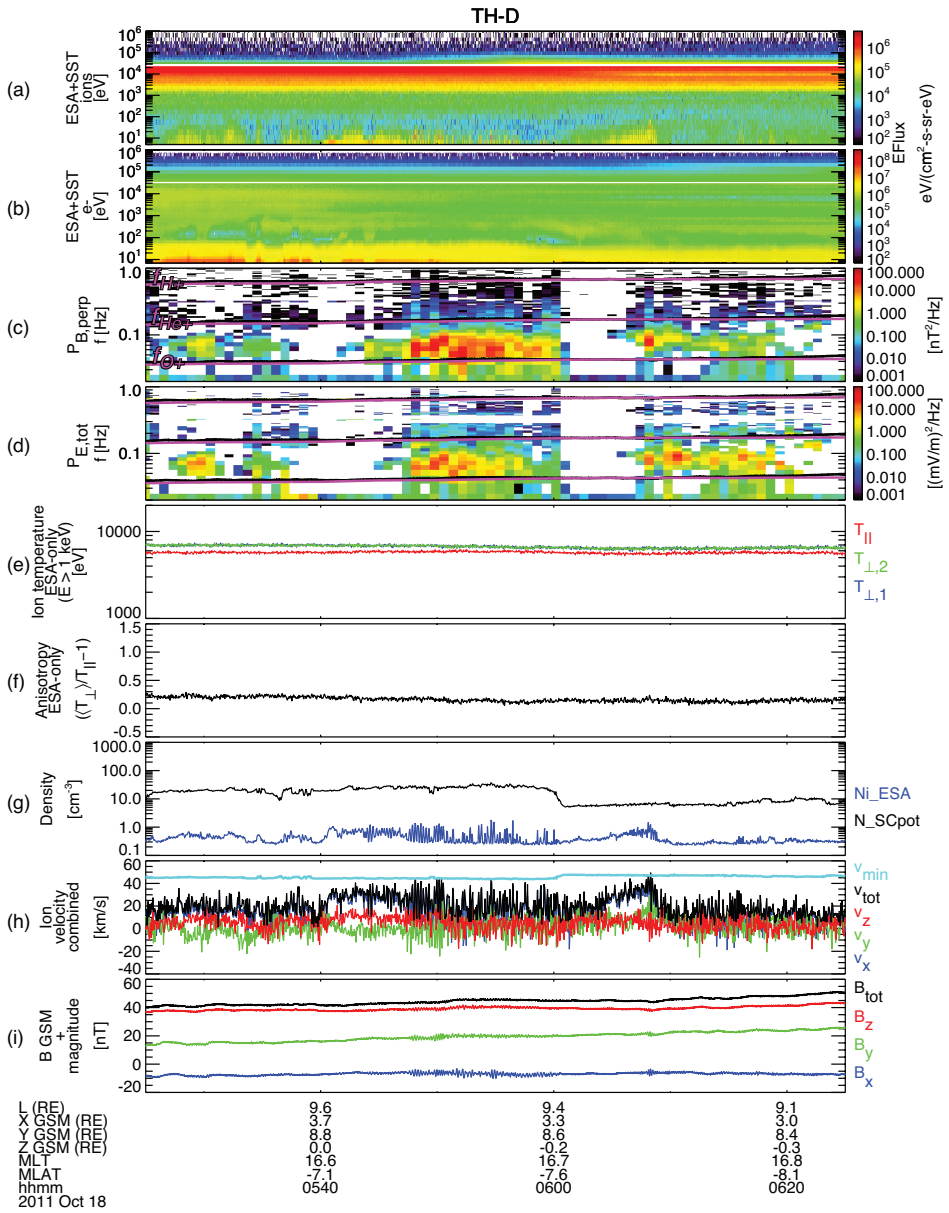

Figure 5.1: The particle, wave, and plasma properties observed on 18 October 2011 by TH-D. The panels are: (a) combined omnidirectional ion ESA and SST energy flux; (b) combined omnidirectional electron ESA and SST energy flux; (c) transverse magnetic field dynamic power spectrum; (d) total electric field dynamic power spectrum; (e) ion temperature computed from particle moments for energies above 1 keV; (f) estimated hot proton anisotropy computed from the ion temperature; (g) observed plasma density products: (black) the total plasma density inferred from the spacecraft potential, N_SCpot, and (blue) the ion density computed from the ion ESA measurements, Ni_ESA; (h) three components of the observed ion velocity in GSM coordinates, its magnitude, and the v_{min} threshold for cold ion detection; and (i) three components of the measured magnetic field in GSM coordinates and its magnitude.

f_{He+}, and f_{H+}). The equatorial ion gyrofrequencies are estimated using a magnetic field tracing routine based on the geomagnetic field model by *Tsyganenko* [2001], with IMF B_Y, IMF B_Z, solar wind dynamic pressure computed from the solar wind proton density and flow speed, and the Kyoto disturbance storm time (Dst) index as inputs. Figure 5.1e shows the ion temperature computed from the 2nd moments of the ESA distribution functions in the energy range 1 to ~25 keV (excludes contribution of the low energy ion components) and Figure 5.1f shows the temperature anisotropy computed using the mean perpendicular ion temperature and parallel ion temperature over the same (hot proton) energy range. I compared the temperature anisotropy computed from the moments (A_{mom}) to the anisotropy calculated from bi-Maxwellian fits (A_{fit}) (assuming protons) to the ion distribution function in the BV coordinate system (defined with B in the average magnetic field direction and V the average velocity vector perpendicular to the average field, e.g., *Lee et al*., [2012]); sample fits performed throughout the interval produced anisotropy estimates in good agreement with the moment-computed anisotropies shown in Figure 5.1f. The bi-Maxwellian fits also provide the estimate for the hot proton density and show agreement to within a factor of two of the measured ion density (~0.2–0.3 cm^{-3}) seen in Figure 5.1g when significant bulk plasma flows are absent; I use the estimate for hot proton density provided by the bi-Maxwellian fitting in the modeling since warmer ions with thermal energies above the spacecraft potential energy are included in the measured ion density provided by the ion ESA. Figure 5.1g shows the measured ion density from the ion ESA (blue; Ni_ESA), and the inferred total plasma density from the spacecraft potential (in black; N_SCpot); Figure 5.1h shows three components of the ion velocity moments in the GSM (geocentric solar magnetospheric) coordinate system, its magnitude (black), and the v_{min} threshold (cyan) for

detection of cold ions [*LA2014*]; and Figure 5.1i shows three components of the measured low-resolution magnetic field in the GSM coordinate system and its magnitude.

There is evidence of wave activity throughout the entire interval shown but I focus on the waves seen between 0545 and 0600 UT in Figures 5.1c and 5.1d. The hot proton temperature anisotropy computed from the moments (Figure 5.1f) remains steady (A ~ 0.3 to 0.4) during this interval and the inferred total plasma density of ~7–20 cm^{-3} (Figure 5.1g, black) suggests TH-D was passing through a high-density region consistent with previous descriptions of EMIC wave occurrence along the edge of an afternoon plasmaspheric plume. Some minor ion flows (Figure 5.1h) were also seen during this interval but due to the disagreement between Ni_ESA and N_SCpot, the flows were likely a combination of hot ion magnetic drifts and plasma convection; the majority of the cold ions were therefore not being measured by the ion ESA during this time. I note, however, that enhanced fluxes of low-energy (tens of eV) ions appear in the ion ESA spectra (Figure 5.1a) around the same times the wave power enhances in the magnetic and electric field dynamic power spectra. These low-energy ion flux enhancements (energy flux > 1e+5 eV/cm^2-s-sr-eV) could be related to resonant heating of the cold ions to thermal energies high enough to exceed the spacecraft potential energy [e.g., *Young et al.*, 1981]; I also see increases in the measured ion density during these flux enhancements. Aside from these flux enhancements, the ion fluxes below 1 keV lie in the 1e+3 to 1e+4 eV/cm^2-s-sr-eV range and the measured ion density is low (Ni_ESA ≈ 0.2 to 0.3 cm^{-3} during intervals without the enhancements). I will discuss the importance of the ambient energy flux level of low-energy ions and the measured ion density in the other MLT sectors.

The ambient magnetic field (Figure 5.1i) suggests TH-D is near but just below the magnetic equator ($B_y > 0$). Note also that the magnetic latitude (MLAT), estimated using the

spacecraft position data transformed into the SM (solar magnetospheric) coordinate system and shown for reference below Figure 5.1 (bottom), agrees with that interpretation (MLAT < 0). Shown also below the horizontal axis is the spacecraft geocentric distance (L, in R_E), the three position coordinates (also in R_E) in the GSM coordinate system, the magnetic local time (MLT) computed using the SM coordinate system, and Universal Time.

It is clear from the discussion above that although low-energy ions of significant density (approximately known from N_SCpot) were present, no information on partial density of heavy ions is available because the plasma was not flowing with sufficiently large convection velocity. I thus rely on statistical properties of low-energy ions derived in *LA2014* for further modeling, as described in section 5.5.3. To facilitate reproduction of the modeling results described within this chapter and to support future wave studies, I have transferred the dataset by *LA2014* into tabular and bar plot form in Appendix B (see Appendix B Tables B.1–B.4 and Figures B.1–B.4). The specific values of ion component relative abundances and temperatures taken from this larger dataset and used for modeling are presented as separate tables within the body of this chapter for each case examined. For example, for the dusk event, Tables 5.1a and 5.1b contain information read out from the material in Appendix B appropriate for this event.

5.5.2 Waves

Several processing steps are applied to the time series electric and magnetic field measurements. The fast-survey electric field data (8 S/s) are first interpolated to match the time resolution of the magnetic field data (4 S/s). Separate quantities for the DC electric field and magnetic field data

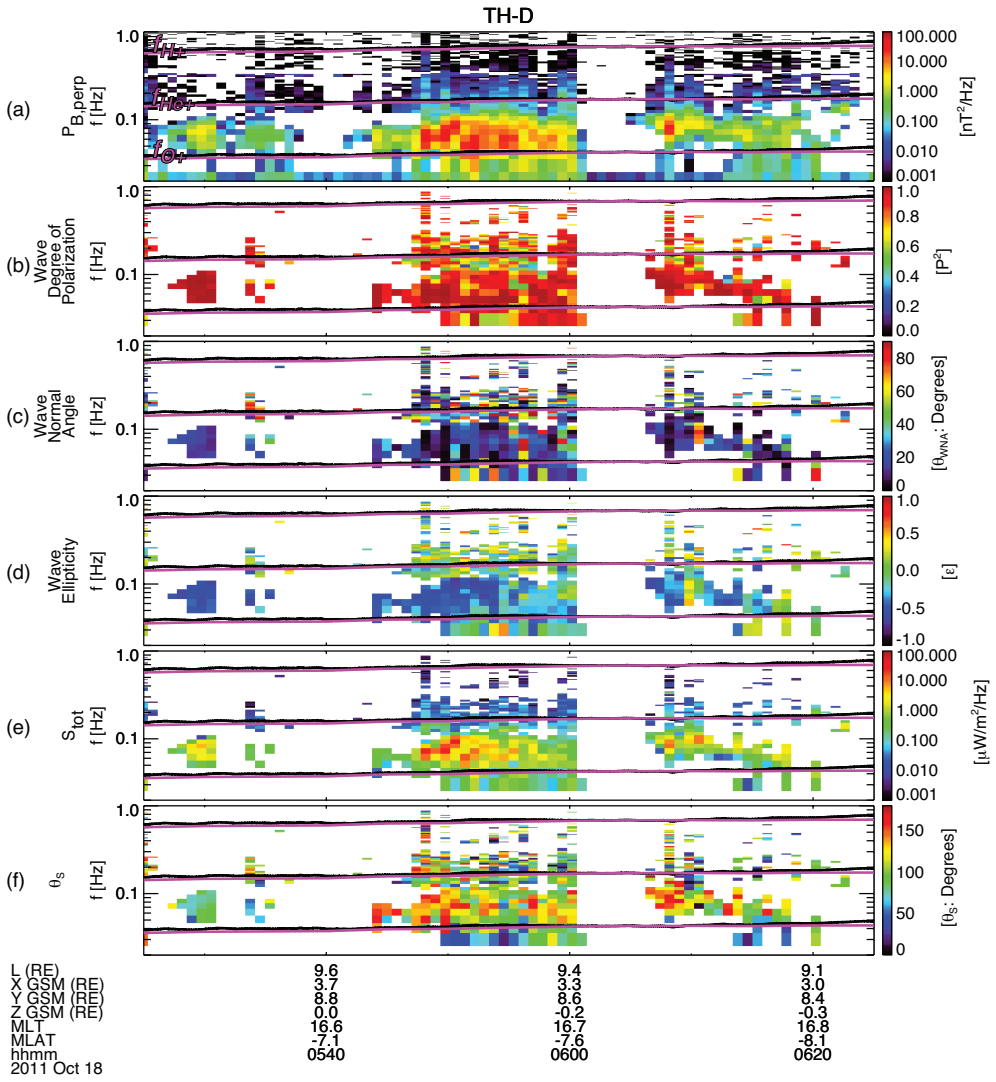

Figure 5.2: (a) Transverse magnetic field dynamic power spectrum, (b) wave degree of polarization, (c) wave normal angle computed from the magnetic field spectral matrix, (d) ellipticity, (e) total Poynting vector spectrum computed from the magnetic and electric field data, and (f) wave energy propagation angle computed from the three components of the Poynting vector. Further details about the spectral analysis are described in the text.

are then computed by first spin-averaging the fast-survey data to 3 s time resolutions and then subjecting the data to 161-sample sliding averages (~8 minutes). Both fast-survey datasets are then detrended using the respective DC data. The DC magnetic field data are then used to create a mean field-aligned coordinate matrix; the detrended fast-survey electric and magnetic field data are transformed into a mean field-aligned coordinate system using this field-aligned coordinate matrix (Z along the average ambient magnetic field, X normal to Z in the plane containing the Earthward direction, and Y completing the right-handed, orthogonal coordinate system, see e.g., *Lee et al*., [2012] and *LA2014*). The data in mean field-aligned coordinate (FAC) system are then fast Fourier transformed (FFT) into the frequency time domain and used to compute the magnetic and electric field dynamic power spectra. Further descriptions on the methods are provided in Appendix B.

The waves seen in Figures 5.1c and 5.1d display peak wave power below f_{He+} and emit over a broad frequency range beginning near and just below f_{O+}. A cut-off in spectral wave power appears below f_{He+}, consistent with previous descriptions of a stop band or spectral slot near one of the heavy ion gyrofrequencies that implies damping of the waves by one or more of the cold ion species. These waves undergo further processing to enable a detailed analysis of their properties, shown in Figure 5.2. All components of the magnetic field are used for wave polarization analysis (section 5.5.2.1). Poynting vector and its spectral data products following the methods described by *Loto'aniu et al*. [2005], *Li et al*. [2013], and *Santolik et al*. [2010] are also produced (section 5.5.2.2).

5.5.2.1 Polarization Analysis

The polarization properties of the observed waves are analyzed using the methods for polarization analysis described by *Samson and Olson* [1980] and *Means* [1972]; a more detailed description of these methods appears in Appendix A. A few methods for studying the polarization properties of waves centered on the FFT methodology exist and they perform similarly [cf. *Arthur et al*., 1976, for a comparison of methods]. The transverse magnetic field dynamic power spectrum has been transferred over from Figure 5.1c to Figure 5.2a for reference. Polarization analysis products are shown below it: Figure 5.2b shows the degree of polarization (P^2) that indicates the signal to noise ratio of the waves, in which values closer to 1.0 indicate a coherent wave; Figure 5.2c shows the wave normal angle (θ_{WNA}, from 0° and 90°) of the wave vector relative to the average magnetic field direction but does not provide the wave propagation direction; and Figure 5.2d shows the ellipticity data for the waves, with $\varepsilon = -1$ indicating a left-hand circular polarized wave, $\varepsilon = +1$ indicating a right-hand circular polarized wave, and $\varepsilon = 0$ indicating a wave with linear polarization. To resolve the ambiguity related to the absolute wave propagation direction I performed additional analysis of the spectral Poynting vector and computed the wave energy propagation angle, described in the next subsection—this also provides the sign of the wave propagation direction. In all events the ellipticity data prove useful for interpreting the wave properties when combined with the other polarization and Poynting vector data.

The time intervals and frequencies with the wave power enhancements in Figure 5.2a coincide well with large degree of polarization values ($P^2 > 0.8$) (Figure 5.2b). During those times the wave normal angle (Figure 5.2c) is low ($\theta_{WNA} < 20°$) and indicates near-parallel propagation. The ellipticity (Figure 5.2d) is left-handed ($\varepsilon \sim -0.5$) at most times but also

approaches 0 at certain times. I note there are at least two interpretations for the waves having ε ≈ 0: the waves may be linear polarized or there may be wave superposition that results in the ellipticity values being a median of superposed wave ellipticities (see *Denton et al*. [1996] and *Anderson et al*. [1996b]). Most signatures in the polarization analysis suggest the intervals of peak wave power are consistent with left-hand polarized EMIC waves growing below f_{He+} (He^+ band waves). Further analysis is needed to determine their propagation direction(s).

5.5.2.2 Poynting Vector

The propagation of EMIC wave energy has been described previously as being bi-directional within MLAT < |11°| and unidirectional away from the magnetic equator beyond that latitude range [*Loto'aniu et al.*, 2005]. The magnetic equator has thus been referred to as the source region for these waves. *Loto'aniu et al*. [2005] also described the methods for computing the Poynting vector of EMIC waves in the frequency-time domain to facilitate further analysis of Poynting flux in this format. The component of the Poynting vector spectral data along the ambient magnetic field (usually referred to as S_z) has been applied to studying the occurrence and propagation of EMIC waves at middle magnetic latitudes away from the equatorial source region [e.g., *Allen et al*., 2013]. But all three components can also be used to compute the dominant wave energy propagation angle, θ_S, also as a spectral data product. *Li et al*. [2013] applied such a combination of Poynting vector spectral data to studying the propagation direction of upper and lower band chorus waves (also see *Santolik et al*., [2010]). I use these two data products for studying EMIC wave energy and its propagation angle relative to the mean magnetic field direction for the cases in this chapter. A description of the methods for obtaining the Poynting vector data appears in Appendix A.

The combination of the Poynting vector spectral data with the polarization analysis data can eliminate the ambiguity of wave normal angle computed from only three components of the ambient magnetic field. Furthermore, θ_S can be combined with the polarization analysis data to detect multiple wave presence in the observations. The presence of more than one wave can affect the polarization analysis results since the results are obtained based on the single wave assumption. When more than one wave propagates towards the observer, wave superposition can affect the resulting data products [*Denton et al*., 1996]. For example, while the polarization data for 0528–0532 UT all suggest detection of a packet of parallel propagating left-handed EMIC waves, θ_S indicates a clear oblique energy propagation angle signature during that time ($\theta_S > 60°$). Wave packets propagating parallel and anti-parallel to the field passing by the observer at the same time (e.g., $\theta_{Wave1} = 0°$ and $\theta_{Wave2} = 180°$) result in an oblique median θ_S ($\theta_{med} = 90°$) and provides a straightforward explanation for this disagreement between θ_{WNA} and θ_S. Other than this interval, the θ_S signatures that coincide with the frequencies where peak wave and Poynting vector spectral power are seen indicate wave propagation in two opposing directions ($\theta_S < 50°$ or $\theta_S > 150°$) along and opposite the field, consistent with the bi-directionality of EMIC waves within the equatorial source region as described by *Loto'aniu et al*. [2005].

5.5.3 Modeling

The TH-D observations all suggest that the dusk waves are emitted in the He^+ band. *Min et al*. [2012] often observed such waves in the dusk sector with statistical properties consistent with those described above. They also noted much lower wave power and occurrence rates for waves in the H^+ band ($f_{wave} > f_{He+}$). Again consistent with their statistics, H^+ band waves are not seen

Table 5.1a. Dusk observed environment properties and low-energy ions inferred from statistics.

B (T)	N_{tot} (m^{-3})
4.50E-08	2.00E+07

Species	Hot Protons	Cold Protons	He^+	O^+	Cold e-
n_s (m^{-3})	1.8E+05	1.61E+07	2.43E+06	1.29E+06	2.00E+07
Tpar (eV)	6050	2.2	10.5	40.7	1
Tperp (eV)	8470	2.2	10.5	40.7	1

Normalized	Hot Protons	Cold Protons	He^+	O^+	Cold e-
ns	0.01	0.81	0.12	0.06	1
Tpar	1	3.62E-04	1.74E-03	6.73E-03	1.65E-04
Tperp/Tpar	1.4	1	1	1	1

Table 5.1b. Dusk observed environment properties and low-energy ions with O^+ component removed.

Species	Hot Protons	Cold Protons	He^+	Cold e-
n_s (m^{-3})	1.8E+05	1.722E+07	2.6E+06	2.00E+07
Tpar (eV)	6050	2.2	10.5	1
Tperp (eV)	8470	2.2	10.5	1

Normalized	Hot Protons	Cold Protons	He^+	Cold e-
n_s/N_{tot}	0.01	0.86	0.13	1
Tpar/Tpar,Hot	1	3.62E-04	1.74E-03	1.65E-04
Tperp/Tpar	1.4	1	1	1

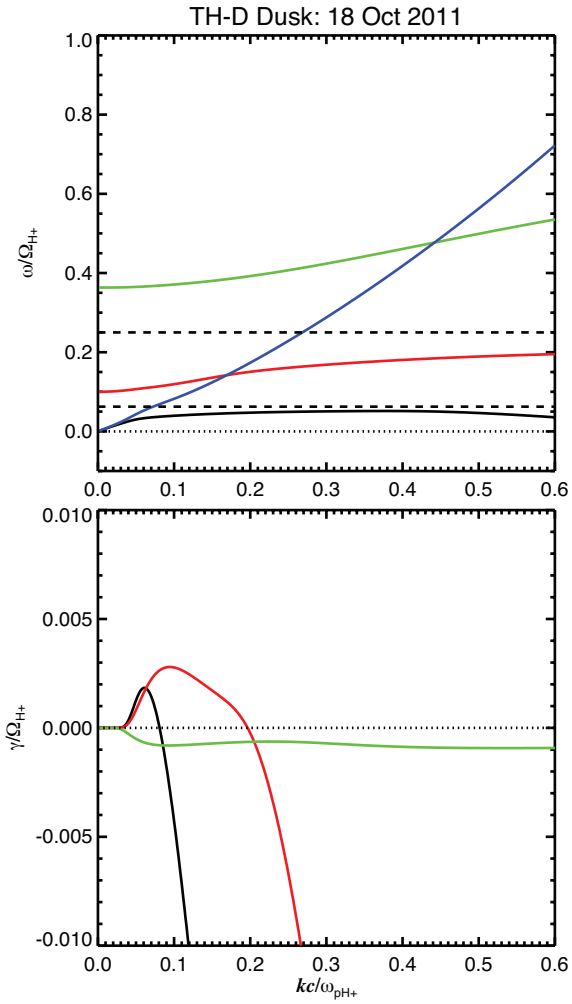

Figure 5.3: Numerical solutions to the full dispersion relation for waves in the (black) O^+ band, (red) He^+ band, (green) H^+ band, and (blue) the right-handed whistler using the parameters in Table 5.1a.

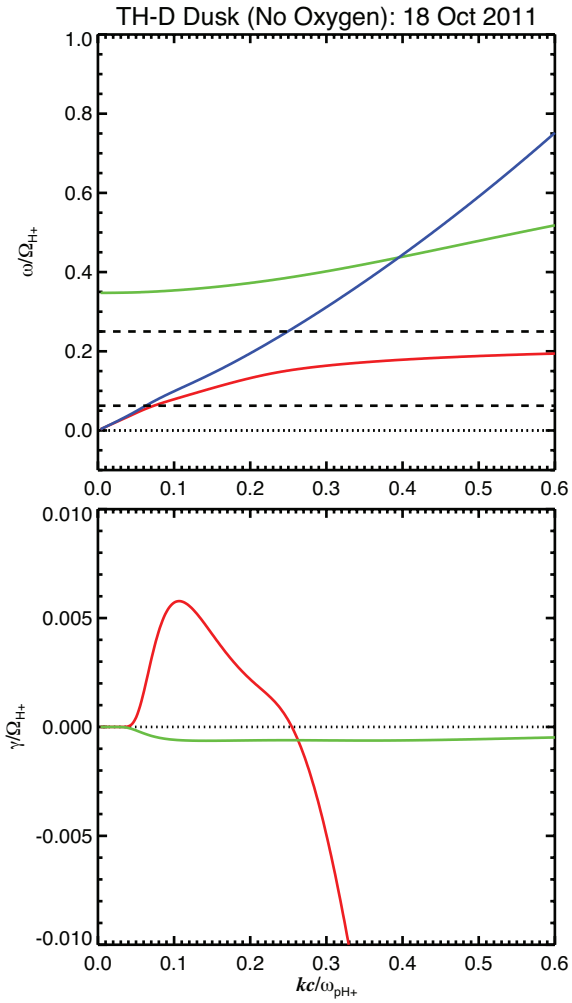

Figure 5.4: Numerical solution to the full dispersion relation for waves in the (red) He^+ band, (green) H^+ band, and (blue) the right-handed whistler using the parameters in Table 5.1b.

during the interval discussed here. In this section I use the local plasma conditions observed by the spacecraft in combination with typical low-energy ion composition properties [*LA2014*] and model the observed wave growth and spectral properties. The parameters used for the modeling appear in Tables 5.1a and 5.1b.

Figure 5.3 shows the numerical solutions to the dispersion relation for the O^+ (black), He^+ (red), H^+ (green), and right-hand whistler (blue) bands using the parameters of Table 5.1a. I note that the cold ion partial densities seen in Table 5.1a are also consistent with previous descriptions of plasmaspheric ion composition: ~90% cold H^+, several to ~10% He^+, and up to a few percent cold O^+ [e.g., *Comfort et al*., 1988]. Modeling with these parameters shows peak growth rate in the He^+ band near ~0.5 Ω_{He+} and damping at higher wavenumbers, as Ω_{He+} is approached; there is little to no growth in the O^+ and H^+ bands. Although the damping of the He^+ band near Ω_{He+} is consistent with the observations, the dispersion characteristics near Ω_{O+} for both He^+ and O^+ band waves, and in particular the prediction of a stop band, do not match observations that show wave presence there. I interpret this as evidence for the absence of cold O^+ during this time and perform modeling without a cold O^+ component (parameters in Table 5.1b). I note that an absence of a spectral stop band near f_{O+} could also be due to the presence of O^+ that is sufficiently warm. I note that tests were performed to determine whether O^+ that is warm (400 eV) or hot (1000 eV) could lead to a vanishing O^+ stop band for the same partial density shown in Table 5.1a and I observed increased damping of both He^+ and O^+ band waves as the O^+ temperature was increased. I therefore suggest that the absence of cold O^+ is a better explanation for this case, which is supported by previous findings that the typical temperature of cold O^+ is also not that warm in the afternoon sector [*LA2014*].

Figure 5.4 shows the wave solutions without a cold O^+ component. They indeed show better agreement with observations: the He^+ band is now unstable over a broad range of normalized frequency including across Ω_{O+} (still damped on approach to Ω_{He+}) consistent with the broad wave power signatures in the observations.

5.5.4 Discussion

The above dusk event analysis demonstrates the process I adopted in performing multi-instrument observations of EMIC wave properties. It also shows how I used wave spectral information and linear theory to refine the properties of the multiple ion species present, by adjusting the plasma parameters in my model to match wave observations assuming some initial knowledge based on my previous statistics [*LA2014*], even when direct low-energy plasma measurements were not available. I note that one variable that I do constrain from measurements is the hot proton anisotropy.

The linear growth rate in the two cases, with and without O^+, can be used to compute the maximum path-integrated wave gain [e.g., *Chen et al*., 2010] and can provide additional information on whether local wave growth occurs. Though the frequency range over which the growth rate is positive (Figure 5.4) agrees with observations (Figures 5.1c or 5.2a), I found that the maximum wave gain is below 10 dB (a reasonable threshold for above-noise wave power detection based on past practices [e.g., *Horne and Thorne*, 1993; *Chen et al*., 2010]) for both cases (Figures 5.3 and 5.4), suggesting that either the distributions are in marginal stability or that the waves were generated elsewhere and propagate to that location. Multi-spacecraft observations are needed to further examine such propagation effects. But an increase of the measured hot proton anisotropy (0.4) by a factor of two (to 0.8) indeed resulted in larger growth rate (predominantly in the He^+ band) as well as a significant increase in the calculated wave gain (to > 10 dB), supporting the marginal stability hypothesis.

Although the occurrence of EMIC waves at small (< 7 R_E) geocentric distances at all MLT sectors have thus far been rare in recent datasets, likely due to the drawn out solar minimum, their occurrence at the dusk sector has strong correlation with storms in datasets from

previous solar cycles (e.g., *Keika et al*. [2013]). Such dusk, low L-shell waves could be important for depletion of radiation belt electrons [*Thorne and Kennel*, 1971; *Ukhorskiy et al*., 2010]. Low-energy ion composition and properties need to be carefully considered for such storm-associated EMIC waves. In addition to the plume and the injected (hot) plasma sheet ions, warmer ions convecting from the nightside just outside the plasmapause boundary could also be present at dusk [*LA2014*]. Even in cases of poor knowledge of the cold and warm plasma populations, parametric studies of the kinetic dispersion relation as shown in this section, could help refine our knowledge on the plasma conditions that would be consistent with the wave observations, and in addition characterize the wave effects on energetic electron scattering.

5.6 Midnight

5.6.1 Particles

On 17 April 2010 TH-E passed through the midnight sector within a few degrees of the magnetic equator and near a geocentric distance of 9 R_E. A comparison between the low-energy ion fluxes in the dusk case (Figure 1a) to this case (Figure 5a) shows about an order of magnitude higher low-energy ion fluxes for this case (dusk: 1e+3 to 1e+4, midnight: 1e+4 to 1e+5). This suggests more ions with total energies above the spacecraft potential energy are present during this interval and are being measured by the particle instrument, consistent with the presence of warmer ions. This is also seen by comparing the measured ion densities at the two locations: Ni_ESA ≈ 0.6 to 0.7 cm^{-3} (Figure 5g, blue) in this midnight case versus Ni_ESA ≈ 0.2 to 0.3 cm^{-3} in the dusk case. The total plasma density inferred from the spacecraft potential is greater than a few cm^{-3} (Figure 5g, black), higher than values typically seen at this region of space (median N_SCpot < 1 cm^{-3} during Kp ≤ 1 and Kp > 1 in *LA2014*) and is suggestive of the

presence of a cold, plume-like feature or ionospheric outflow. Ni_ESA is a fraction of N_SCpot during this time, suggesting that the density enhancement during the interval of wave activity is due to particles too cold (~1 eV) to be measured by the ion ESA. I assume for simplicity that this cold density feature consists of cold protons and discuss the implications of this cold proton component on wave growth in section 4.3. The anisotropy of the energetic protons is significant but steady: Figure 5j (an insert in Figure 5) is a 2-D cut of the ion distribution function during the time of peak wave power, in which significant anisotropy is evident at intermediate ion energies (400 km/s < V_V < 1500 km/s or ~1 keV < E_V < ~10 keV). The associated temperature anisotropy is not captured well by the moment computation method even after limiting the energy range for the computation from 1 to 12 keV (A_{mom} ~ 0.6) and disagrees with the anisotropy provided by the bi-Maxwellian fitting (A_{fit} ~ 1.0 to 2.0) by about a factor of 2 to 3. This disagreement in anisotropy can be attributed to the increased density of warm ions that cannot be discriminated for when computing the moments but can be avoided when performing fits to 2-D cuts of the ion distribution function.

5.6.2 Waves

TH-E observed an interval of EMIC wave emissions just after midnight MLT (01–02 MLT) between 1250 and 1320 UT (Figure 5.5c, 5.5d, and 5.6a). The waves start to intensify just along the edge of the plasmaspheric density enhancement beginning around 1245 UT in Figure 5g. These midnight waves show peak wave power in the He^+ band but near f_{He+} with some wave power even crossing over f_{He+} into the H^+ band. Without further analysis and modeling, it is not clear what causes this spectral feature. One possibility is the presence of a low-density component of warm He^+ in the presence of hot proton anisotropy and a high-density cold proton

component as discussed in *Lee et al*. [2012] for an event in the pre-midnight sector. Another is minimal He^+ density and cold plasma consistent with the cold plasma approximation (waves un-damped at large *k*).

5.6.2.1 Polarization Analysis

The waves are coherent (Figure 6b) near the frequencies of peak wave power just below f_{He+} (Figure 6a), as well as at the weaker wave region just above f_{He+}. Wave normal angles (Figure 6c) are mostly low (especially during peak power) but become more oblique ($\theta_{WNA} \geq 60°$) at 1250–1255 UT. During this same interval the ellipticity becomes more right-handed ($\varepsilon \approx +0.4$) and consistent with previous work describing polarization change of waves following propagation [e.g., *Young et al*., 1981, and *Thorne et al*., 2006]. The ellipticity is mixed throughout the interval except during peak wave power (1258–1302 UT), when $\varepsilon \approx -0.5$. The mixed ellipticity signatures are in contrast to those seen in the dusk case. Inspection of certain intervals suggest some wave superposition effects are present and could be affecting the analysis, especially at times when $\theta_{WNA} \approx 0$ and $\varepsilon \approx 0$ such as between 1310 and 1320 UT. Further information needed to check for this hypothesis is obtained below.

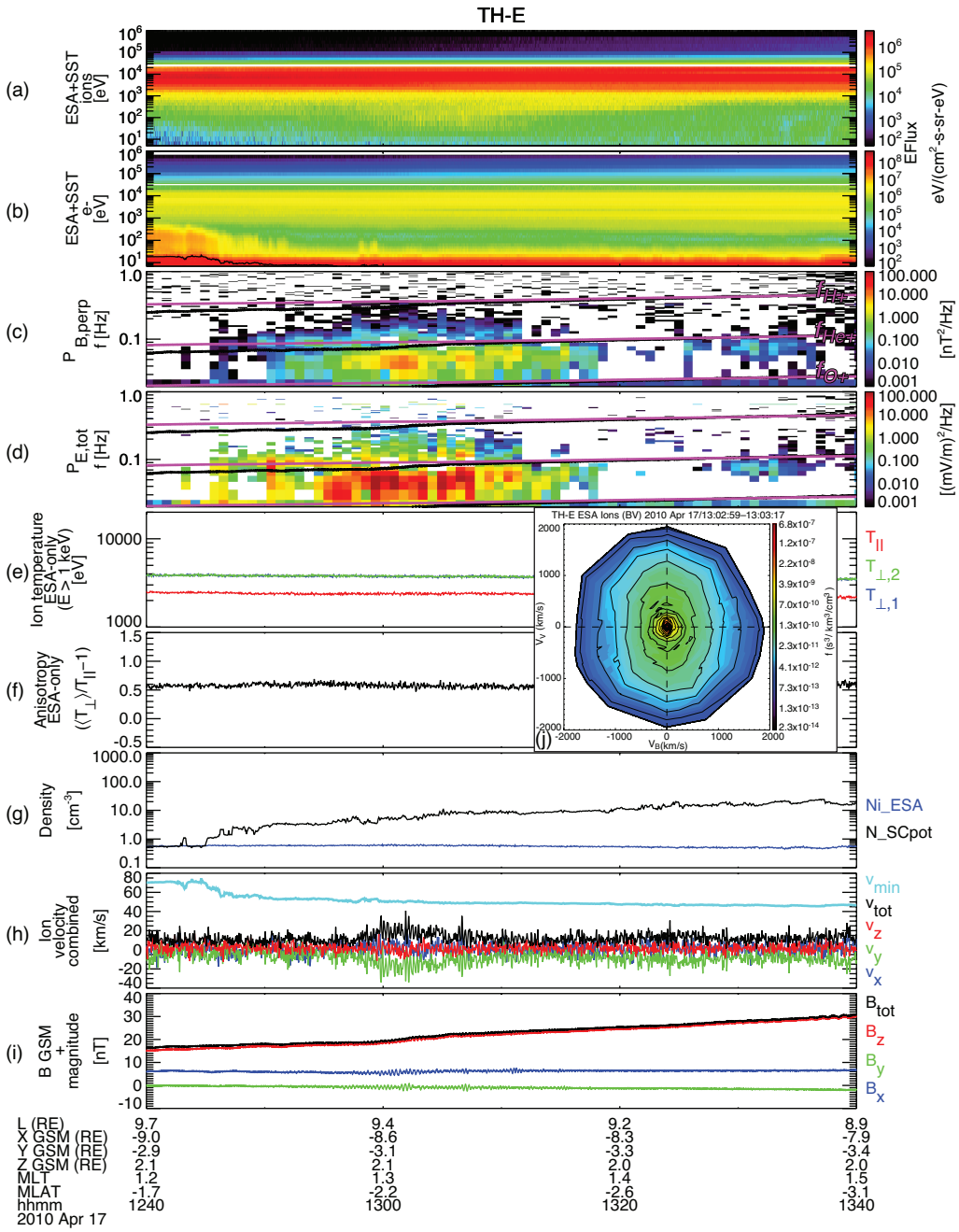

Figure 5.5: The particle, wave, and plasma properties observed on 17 April 2010 by TH-E.

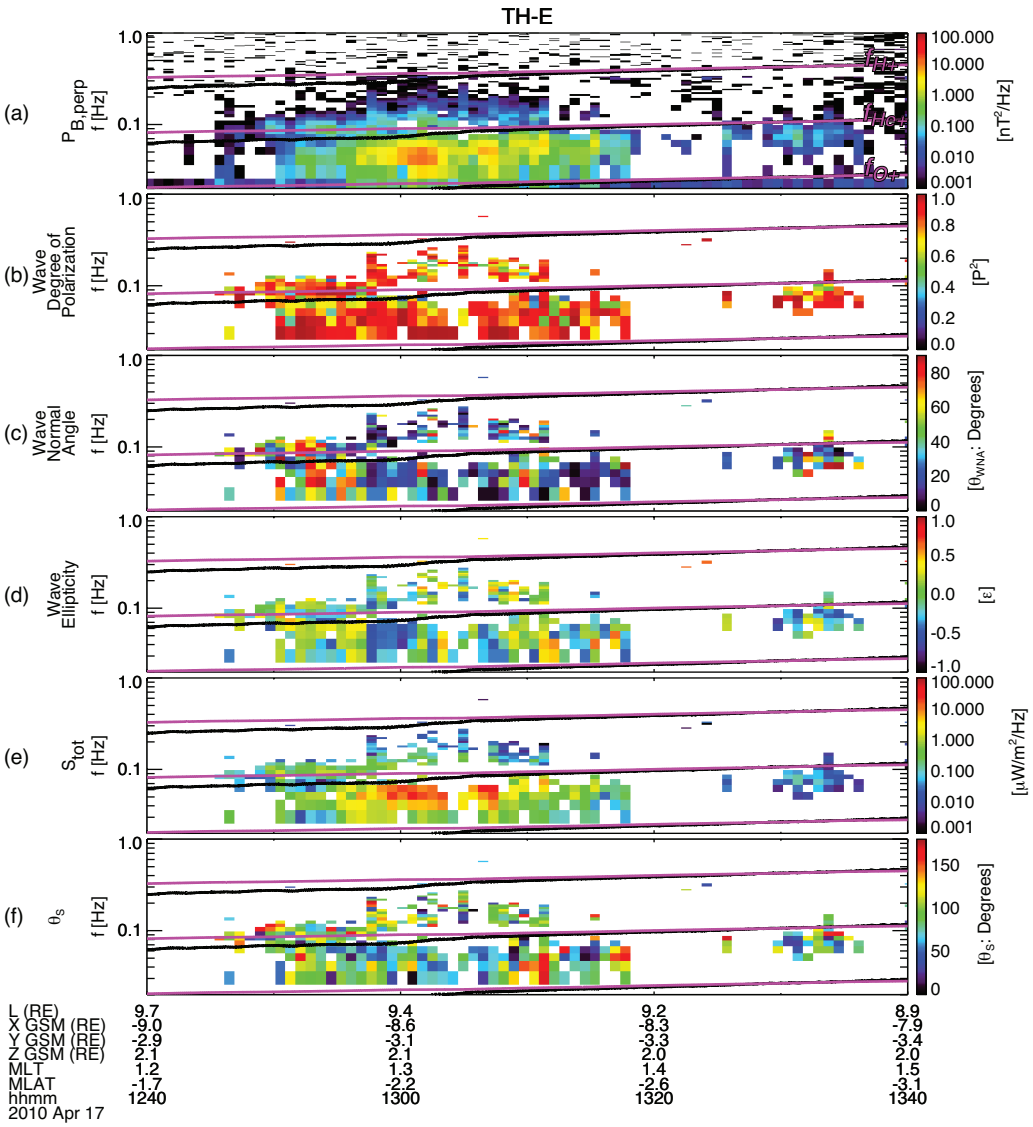

Figure 5.6: Wave polarization and Poynting vector spectral properties.

5.6.2.2 Poynting Vector

Peaks in Poynting vector spectral power are seen at the same frequencies where the wave power peaks (Figure 5.6e). The wave energy propagation angles, however, are mainly oblique and a consistent propagation direction is hard to infer for many time intervals. These signatures support the hypothesis of multiple waves suggested by the mixed polarization data. In particular, between 1310 and 1320 UT, when the wave normal angle was low (Figure 5.6c) and the ellipticity linear (Figure 5.6d), we can see strong intermittent signatures of mostly anti-parallel ($\theta_S \approx 180°$) followed by mostly parallel ($\theta_S \approx 0°$) wave energy propagation (Figure 5.6f). Two counter-propagating wave packets are expected to result in linear polarization in FFT analysis [*Denton et al*., 1996]. I therefore suggest that at least two and maybe more wave packets are passing by TH-E throughout the time interval shown. I next test whether the observed conditions indeed support local growth of left-handed waves.

5.6.3 Modeling

I look to the observations to define the parameters for the modeling. Since the inferred total plasma density (Figure 5.5g) is much larger than the median densities for the individual low-energy ion species as well as the total plasma density seen by *LA2014*, I define two parameter sets. For the first set the low-energy ion components are obtained by subtracting the fitted hot proton density ($N_{hot} \approx 0.3$ to 0.4 cm^{-3}) from the total plasma density (5 cm^{-3}) and computing the number densities for the low-energy ions using the partial density ratios described by *LA2014* (Table 5.2a). For the second set I assume nightside warm ions are present and use their median densities and temperatures described by *LA2014* and then fill the remaining plasma

Table 5.2a. Midnight observed environment properties and low-energy ions from statistics.

B (T)	N_{tot} (m^{-3})
2.00E-08	5.00E+06

Species	Hot Protons	Protons	He^+	O^+	Cold e-
n_s (m^{-3})	3.8E+05	9.7E+05	1.53E+06	2.12E+06	5.00E+06
Tpar (eV)	2100	8.8	51.9	179.5	1
Tperp (eV)	4200	8.8	51.9	179.5	1

Normalized	Hot Protons	Protons	He^+	O^+	Cold e-
n_s/N_{tot}	0.076	0.194	0.306	0.424	1
Tpar/Tpar,Hot	1	4.19E-03	2.47E-02	8.55E-02	4.76E-04
Tperp/Tpar	2	1	1	1	1

Table 5.2b. Midnight observed environment properties, low-energy ions from statistics, and an additional cold plume component.

Species	Hot Protons	Protons	He^+	O^+	Cold e-	Plume H^+
n_s (m^{-3})	3.8E+05	6.0E+04	9.5E+04	1.32E+05	5.00E+06	4.333E+06
Tpar (eV)	2100	8.8	51.9	179.5	1	1
Tperp (eV)	4200	8.8	51.9	179.5	1	1

Normalized	Hot Protons	Protons	He^+	O^+	Cold e-	Plume H^+
n_s/N_{tot}	0.076	0.012	0.019	0.026	1.00	0.867
Tpar/Tpar,Hot	1	4.19E-03	2.47E-02	8.55E-02	4.76E-04	4.76E-04
Tperp/Tpar	2	1	1	1	1	1

density with an additional colder (1 eV) proton component that represents the density enhancement inferred from the spacecraft potential (Figure 5.5g, black) (Table 5.2b). I note that summing the warm (> few eV) ion component densities in Table 5.2b produces a combined ion density consistent with the measured ion density during this interval (Ni_ESA ≈ 0.6 to 0.7 cm^{-3}).

As shown in Figure 5.7, the numerical solutions using the first parameter set predict wave dispersion and growth that do not match the observations: a large stop band is seen around Ω_{He+} and with the exception of negligible growth in the He^+ band at small wave number all the wave bands are strongly damped.

The second parameter set (solutions plotted in Figure 5.8), however, reveals that addition of a dense, cold proton component ($N_{plume} \approx 4.33$ cm^{-3}; $T_{plume} = 1$ eV) strongly affects the wave growth. The He^+ band waves are now unstable over a frequency range including across Ω_{He+} [e.g., *Chen et al*., 2011; *Lee et al*., 2012] and in good agreement with the observations. The maximum path-integrated wave gain exceeds 50 dB and supports our inference of local wave generation from the bi-directional propagation signatures seen in the observations.

I obtained a similar result regarding growth and path-integrated gain using the moment-computed hot proton anisotropy though positive growth did not fully extend across the stop band due to the lower anisotropy; I believe the fitting results better approximate the gradient in phase space density near the resonant energy than the 2^{nd} order moments of the entire measured ion distribution. I conclude that a combination of a modest increase in cold plasma density in the presence of the warmer ions, typical of the nightside, and hot proton anisotropy adequately explain generation of the observed waves at TH-E. Such a combination of multiple ion species

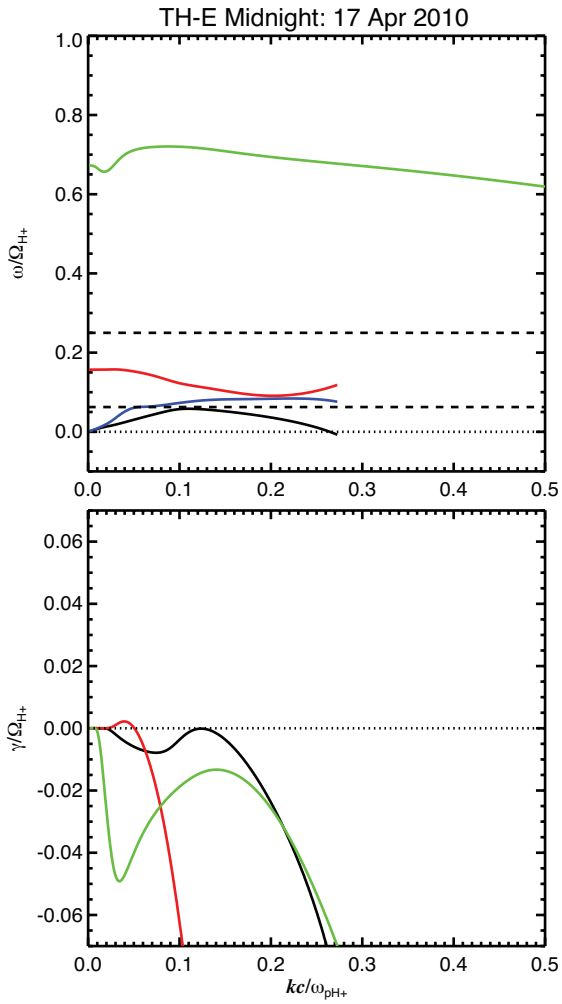

Figure 5.7: Numerical solutions to the full dispersion relation for the midnight waves using the parameters in Table 5.2a.

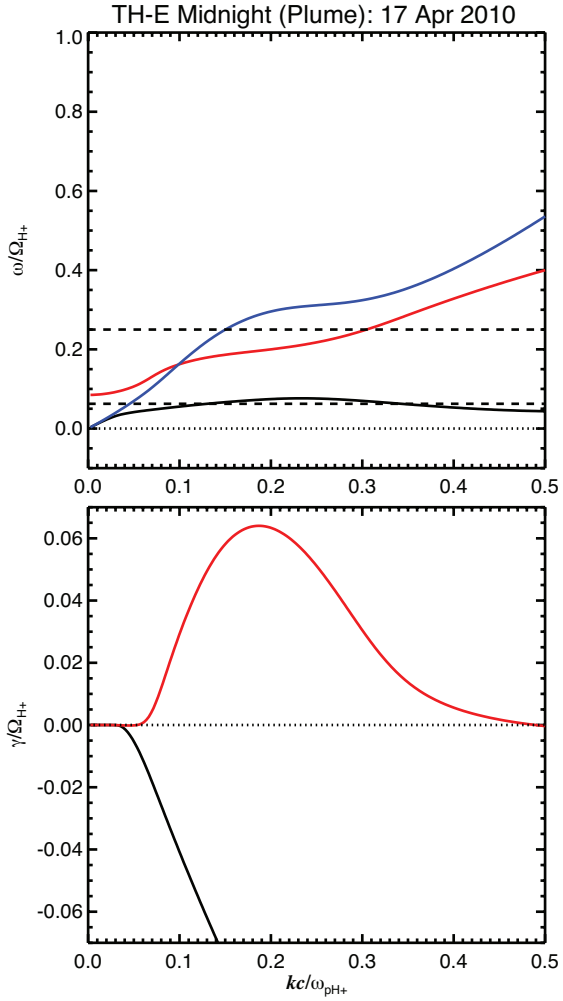

Figure 5.8: Numerical solutions to the full dispersion relation for the midnight waves using the parameters in Table 5.2b with anisotropy obtained through bi-Maxwellian fitting.

prone to generation of EMIC waves near midnight may not be restricted to large geocentric distances. *Fraser et al*. [2012], using multiple GOES spacecraft at geosynchronous orbit, also described an indistinct spectral slot (stop band) near f_{He+} in the midnight sector (0–6 MLT). They suggested it could be warmer He^+ or low He^+ abundance that may have contributed to this spectral feature [e.g., *Chen et al*., 2011], and concluded that the low He^+ abundance explanation

was more likely. Our results demonstrate how a warmer He^+ temperature could also apply to the GOES observations since populations of warm ions have been shown to exist near geosynchronous orbit [*Nosé et al*., 2011; *LA2014*].

5.6.4 Discussion

Locations near midnight were shown to have low EMIC wave occurrence rates in recent THEMIS statistics [*Min et al*., 2012; *Usanova et al*., 2012]. By performing modeling using the typical environment properties that describe the nightside low-energy ions' temperatures as being much warmer and the heavy ions being more abundant than protons, I have shown why wave growth can be suppressed around midnight during typical conditions. I also showed how the waves become unstable simply due to a local cold plasma density increase and the presence of moderate hot proton temperature anisotropy [e.g., *Cornwall*, 1965].

I have also used the polarization and Poynting vector spectral data to show that propagation effects on EMIC wave properties are evident near the magnetic equator and can be observed even when ambient conditions are also favorable for local wave generation. Waves generated near the magnetic equator in the presence of high heavy ion relative abundance were previously shown to be reflected or damped closer to the equator [*Omidi et al*., 2013] and are known to change polarization from left-handed to right-handed also due to the presence of the heavy ions [*Young et al*., 1981; *Mauk and McPherron*, 1980]. Such propagation effects could be more sensitive to the presence of heavy ions than previously thought and may occur soon after the waves are generated in any location where low-energy heavy ions are present. Future studies can provide better understanding on the contribution of multiple heavy ion species to such wave reflection and propagation effects.

5.7 Dawn

5.7.1 Particles

On 6 March 2012 all three THEMIS spacecraft (L ~ 11 R_E) passed through the outer dawn magnetosphere. During this time the particle measurements and other plasma properties were similar at each spacecraft. The ion fluxes below 1 keV are lower than seen earlier at midnight but still higher than at dusk and indicate the presence of warmer ions. The measured ion density provides similar information about the ambient ions (dawn: Ni_ESA ≈ 0.4 to 0.6 cm^{-3}; midnight: Ni_ESA ≈ 0.6 to 0.7 cm^{-3}; dusk: Ni_ESA ≈ 0.2 to 0.3 cm^{-3}). The inferred total plasma density (Figure 5.9g) is much lower (~0.6 cm^{-3}) in this case in comparison to the midnight (~5 cm^{-3}) and dusk cases (~20 cm^{-3}) but is consistent with the median total plasma density along dawn during quiet and more active times [*LA2014*]. In addition, the approximate agreement between Ni_ESA and N_SCpot suggests most of the ions have total energies high enough to be measured during this interval. The hot proton temperature anisotropy (Figure 5.9f) fluctuates between 0.4 and ~0.7 during this interval and could be related to anisotropy enhancements caused by upstream solar wind ULF dynamic pressure fluctuations. ULF fluctuations are indeed seen in both the ion velocity and magnetic field measurements with periods ranging from fractions of to a few minutes (consistent with Pc4–5 ULF activity). Present in Figure 5.9h between 1820–1830 UT (also at 1810 UT) are several instances of enhanced plasma flows, also consistent with ULF activity, that are large enough so that multiple ion species appear at separate energies in the ion flux data (Figure 5.9a). I use the method of *LA2014* to infer composition during the plasma flows and thus obtain estimates of the ion species partial densities and temperatures during these times for modeling. Selected low-energy ion parameters as deduced using the multi-component fitting method and comparison plots showing the model and data are presented in Appendix B. A

comparison to other low-energy ion compositional properties as determined on previous spacecraft with composition instrumentation (e.g., AMPTE/CCE) also appears in this appendix.

Because the flows allowed for sampling of the ambient ion species and the fact that the inferred total plasma density is similar to nominal conditions encourages a comparison of modeling results using the in situ ion composition to those obtained using the statistical composition described by *LA2014*. This modeling comparison is described in section 5.7.3.

5.7.2 Waves

During this orbit all three THEMIS spacecraft also observed similar, coherent EMIC wave emissions above f_{He+} in the proton band (f_{wave}/f_{H+} ~ 0.4 to 0.7) over a range of MLTs (~6 to 8 MLT) for several hours (~1800 to 2300 UT). Only the waves observed by TH-E between 1748 and 1856 UT are described here (and are shown Figure 5.9). The patchy emissions in Figures 5.9c and 5.9d (can be tracked by the peak wave power, often exceeding 1 nT^2/Hz) recur on approximately ULF wave periods and is evidence of magnetospheric compressions driven by solar wind ULF-driven local magnetic pressure enhancements, increases in hot proton anisotropy, and subsequent wave generation [*Anderson and Hamilton*, 1993]. It has also been suggested, based on linear theory, that a larger temperature anisotropy in the hot proton distribution drives wave generation at higher frequencies [e.g., *Kennel and Petschek*, 1966; *Horne and Thorne*, 1994]. I will explore whether the observed temperature anisotropy is consistent with wave generation at the observed band in section 5.7.3.

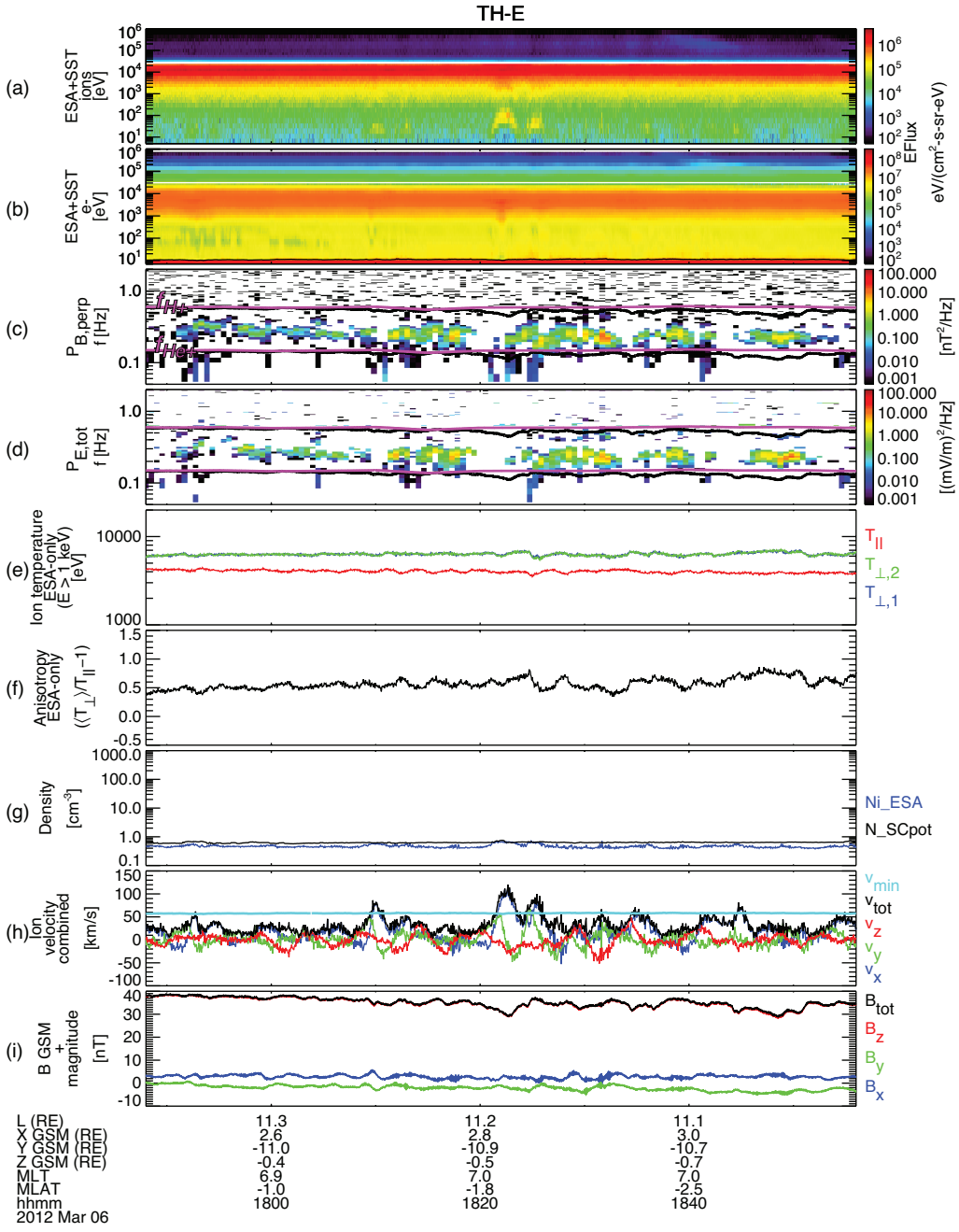

Figure 5.9: The particle, wave, and plasma properties observed on 6 March 2012 by TH-E.

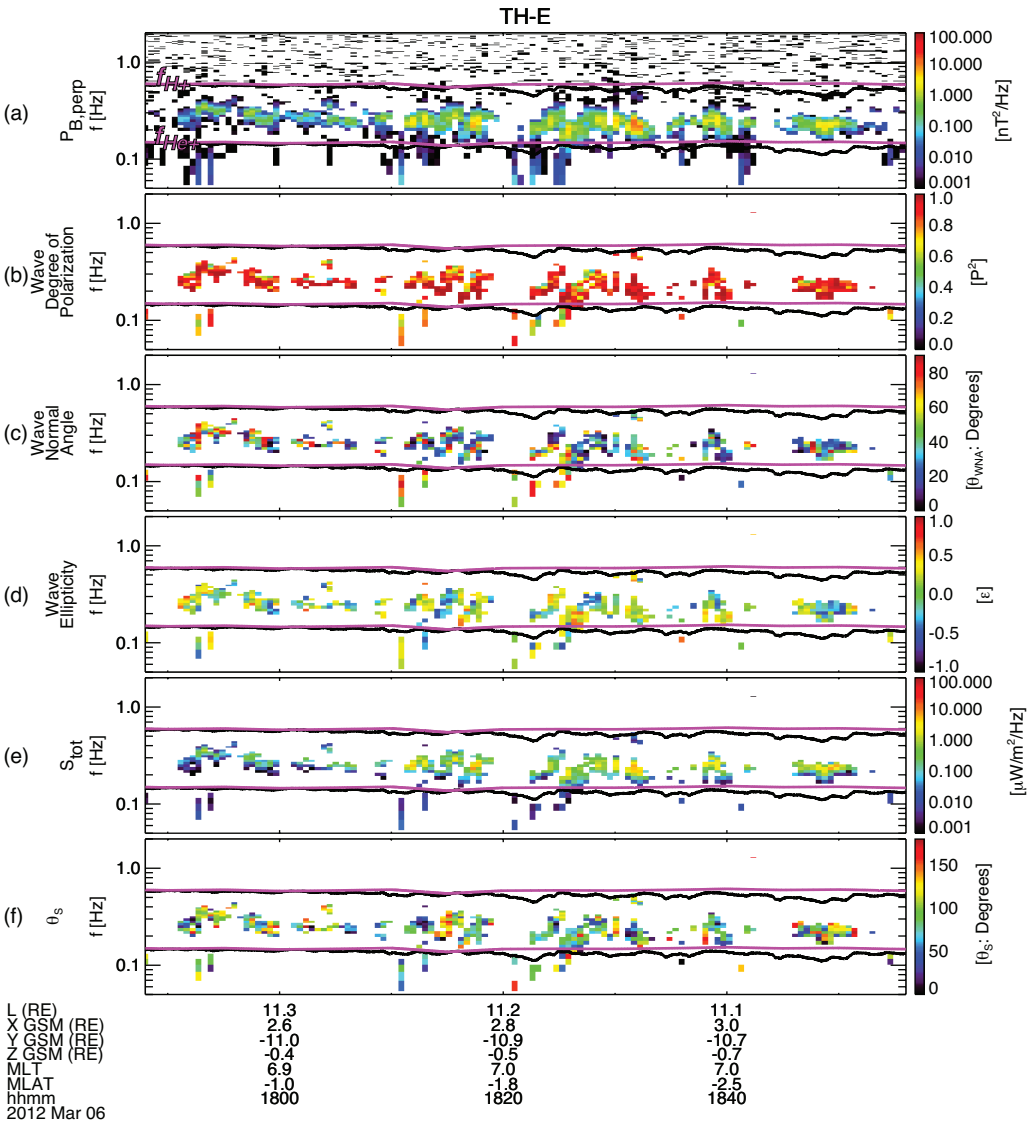

Figure 5.10: Wave polarization and Poynting vector spectral properties.

5.7.2.1 Polarization Analysis

Polarization analysis data are shown in Figure 5.10. The waves are coherent ($P^2 > 0.8$) (Figure 5.10b) at the same frequencies where the peak wave power emissions (Figure 5.10a) are seen. The remaining polarization data are variable and again appear in short duration patches. The wave normal angles (Figure 5.10c) are mixed: a combination of field-aligned ($\theta_{WNA} \leq 20°$) and oblique waves ($\theta_{WNA} \geq 60°$) are interspersed in both time and frequency. The ellipticity (Figure 5.10d) varies between linear and elliptically polarized and a dominant polarization sense for the waves is not obvious (though the median and average of ε is above zero). For example, during 1824–1828UT, the peak power waves (~0.3 Hz) start out with low wave normal angles but are right-hand polarized ($\varepsilon \approx +0.5$) at lower frequencies (0.2 Hz). Towards the end of that interval the waves have low wave normal angles at all frequencies of significant wave power (>0.1 nT^2/Hz) but become more left-handed ($\varepsilon \approx -0.5$) at higher frequencies and linearly polarized at lower frequencies. The evolving polarization of the waves suggests the influence of wave propagation on the polarization properties despite the waves being observed near the magnetic equator. I will reexamine this behavior with the help of Poynting vector spectral data.

5.7.2.2 Poynting Vector

The Poynting vector can be at times parallel or anti-parallel (interspersed $\theta_S \leq 20°$ and $\theta_S \geq 160°$ intervals, Figure 5.10f) and at times quite oblique ($\theta_S \geq 90°$) when wave normal angle (Figure 5.10c) is low (this happens often between 1810–1840 UT). Parallel/anti-parallel Poynting vectors imply counter-streaming (bi-directional) wave propagation. Oblique ($\theta_S \sim 90°$) Poynting vectors during low wave normal angles are consistent with that interpretation, arising from averaging of counter-streaming waves. Clear left-handed ($\varepsilon \leq -0.5$) signatures, however, are not observed at

the same time as oblique ($\theta_S \sim 90°$, wave superposition effect) or parallel/anti-parallel ($\theta_S \sim 0°$ or 180°) Poynting vectors. This suggests that "classic" left-handed waves (unaffected by propagation effects) were not being generated at the time of observation. The observed waves could have been generated sometime before and be propagating as well as reflecting (and subsequently developing oblique θ_{WNA}, θ_S, and $\varepsilon \geq 0$) between locations above or below our equatorially situated spacecraft. I next perform modeling to determine the conditions for growth.

5.7.3 Modeling

Linear theory using the locally observed (e.g., Figure 9a) and statistical (in *LA2014*) low-energy ion properties can facilitate a determination of the conditions supporting wave generation. The model parameters used for linear theory are shown in Tables 5.3a (observed, derived by the same methods as in *LA2014*) and 5.3b (statistical, from *LA2014*). Again, the summed ion component densities in both tables are in approximate agreement with the range of Ni_ESA and N_SCpot values seen in the observations. I note that the low-energy protons have the lowest temperature in both the observed and statistical parameter sets. This results in the dominant wave dispersion characteristics, which are propagating wave solutions above f_{He+} as seen in the observations as well as the statistical wave properties by *Min et al*. [2012]. This connection of low-energy proton temperature to preferential wave propagation in this (H^+) band is consistent with previous modeling [*Gomberoff et al*., 1996].

As seen in both low-energy parameter sets, however, the waves are actually damped in the H^+ band, even though there is some wave growth in the He^+ band for the statistical low-energy ion parameter set (Figure 5.11b). So, for the observed low-energy ion properties and hot anisotropy, there is no wave growth expected, despite what is observed in the wave power. While

Table 5.3a. Dawn observed environment properties and low-energy ions sampled during the bulk plasma flows.

B_o (T)	N_{tot} (m^{-3})
3.50E-08	6.11E+05

Species	Hot Protons	Protons	He^+	O^+	Cold e-
n_s (m^{-3})	2.50E+05	1.68E+05	3.6E+04	1.57E+05	6.11E+05
Tpar (eV)	4000	4.35	11.6	152.1	1
Tperp (eV)	6800	4.35	11.6	152.1	1

Normalized	Hot Protons	Protons	He^+	O^+	Cold e-
n_s/N_{tot}	0.409	0.275	0.059	0.257	1
Tpar/Tpar,Hot	1	1.09E-03	2.89E-03	3.80E-02	2.50E-04
Tperp/Tpar	1.7	1	1	1	1

Table 5.3b. Dawn observed environment properties and low-energy ions from statistics.

B_o (T)	N_{tot} (m^{-3})
3.50E-08	5.74E+05

Species	Hot Protons	Protons	He^+	O^+	Cold e-
n_s (m^{-3})	2.50E+05	1.54E+05	7.9E+04	9.1E+04	5.74E+05
Tpar (eV)	4000	9.4	31.9	139.9	1
Tperp (eV)	6800	9.4	31.9	139.9	1

Normalized	Hot Protons	Protons	He^+	O^+	Cold e-
n_s/N_{tot}	0.436	0.268	0.137	0.159	1
Tpar/Tpar,Hot	1	2.35E-03	7.98E-03	3.50E-02	2.50E-04
Tperp/Tpar	1.7	1	1	1	1

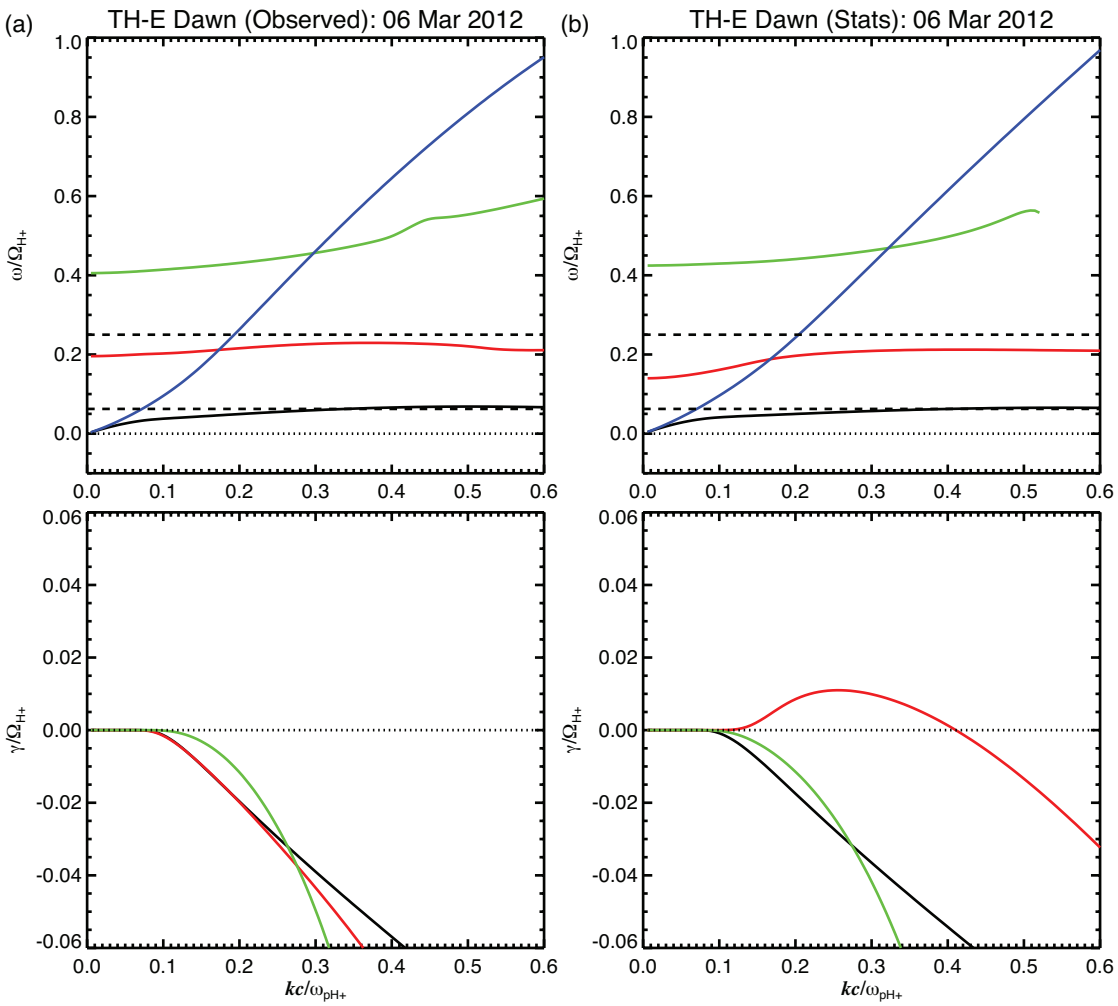

Figure 5.11: Numerical solutions to the full dispersion relation using the (a) observed parameters in Table 5.3a and (b) statistical parameters in Table 5.3b.

a marginal stability scenario, similar to the dusk case, could be used to explain away the lack of linear wave growth (observed anisotropy quenched below threshold), our aforementioned observations of mixed polarization and Poynting vector spectral data (sections 5.7.2.1, 5.7.2.2) do not favor this scenario. I therefore explore, using linear theory, the anisotropy conditions needed for growth of H^+ band waves that could occur away from the equator (though equatorial generation is not ruled out) and whether typical temperatures of the low-energy ion species are consistent with growth in the observed frequency range [*Gomberoff et al*., 1996].

Kennel and Petschek [1966] showed that proton cyclotron waves are marginally stable above a critical frequency, f_c, that depends on hot proton anisotropy, i.e., $f_c = f_{H+}[A/(A + 1)]$. From the observations of normalized wave frequency (f_{wave}/f_{H+} ranges from near 0.4 and up to 0.7) and this equation, I estimate an expected anisotropy range of 1.0–2.3. This is clearly above the locally observed hot proton anisotropy (the observations show 0.4 to ~0.7). Using A = 1.2, corresponding to the lower end of the unstable EMIC waves in the proton band, I indeed obtain H^+ band growth at frequencies that agree well with observations. A calculation of the wave gain produces values above 70 dB and suggests such anisotropy would indeed be sufficient for growth. This is true either using the observed (Figure 5.12a) or the statistical low-energy ion parameters (Figure 5.12b); peak growth rates and unstable wave ranges are consistent between the two parameter sets and support the observations of predominant wave emissions above f_{He+} in this case study as well as EMIC wave statistics [*Min et al*., 2012]. Note that although the local ion measurements do not support wave growth in the He^+ band (Figure 5.12a), small positive growth is seen in that band in the statistical low-energy ion parameter case (Figure 5.12b). The latter is indeed consistent with the *Min et al*. [2012] statistics along dawn, where the authors showed He^+ band waves do occur along dawn, but with occurrence rates and wave power lower than the H^+ band waves.

Although my observations show that locally the ion anisotropy is below critical for wave growth at the time of observation, an additional possibility is that the perpendicular phase space gradient could be higher slightly off the equator due to the evolution of pitch angles in higher magnetic field regions by conservation of the first adiabatic invariant. Thus, conditions for growth could be present on the same field lines but away from the magnetic equator. The warm

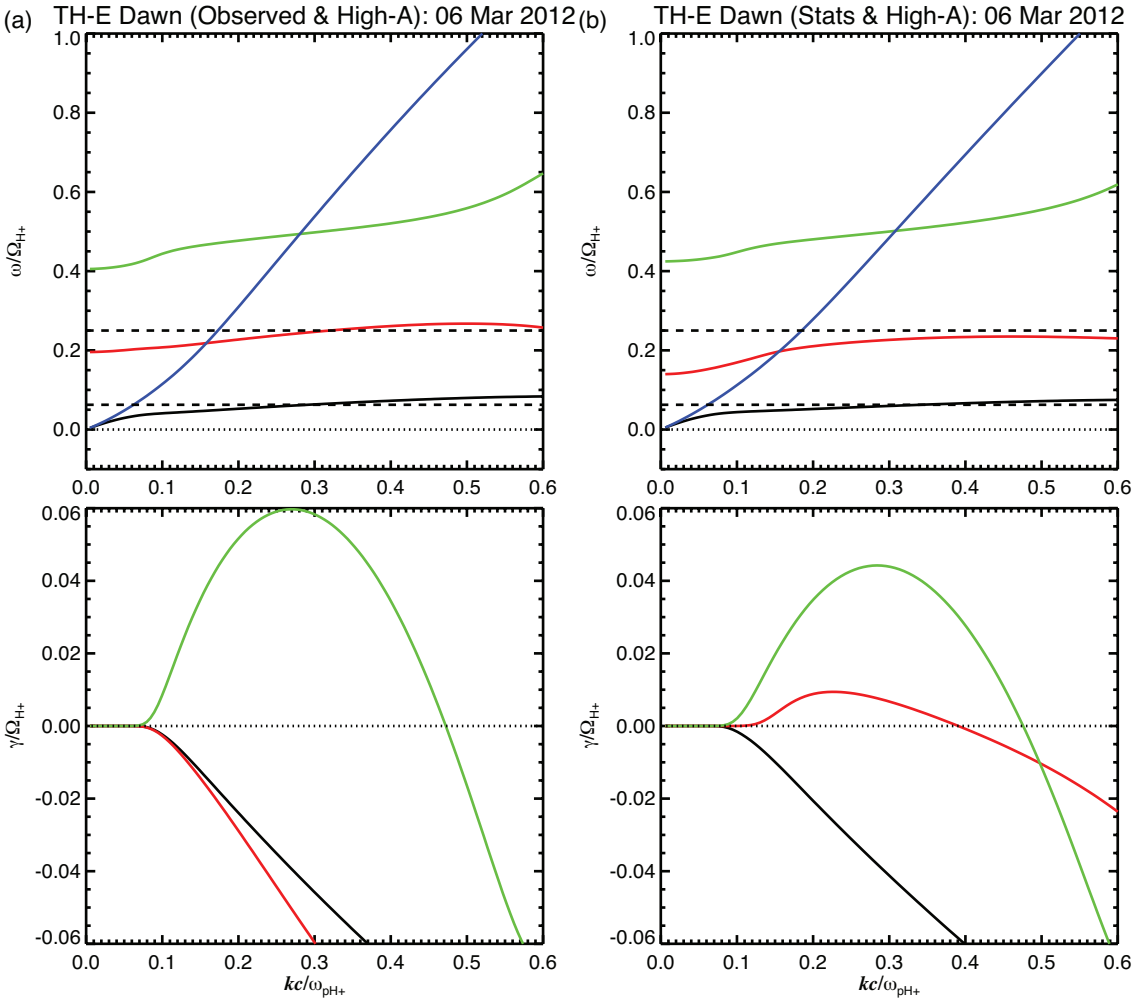

Figure 5.12: Numerical solutions to the full dispersion relation using the (a) observed parameters in Table 5.3a and (b) statistical parameters in Table 5.3b with increased temperature anisotropy of the hot protons.

plasma cloak was also shown to be pervasive along the dawn side [e.g., *Chappell et al.*, 2008]. Furthermore, this cloak has been shown to contain heavy ion species with warmer temperatures (~10 eV and above) [*LA2014*]. Thus, the modeling results using the properties for the low-energy ions sampled near the equatorial magnetosphere likely also hold at off-equator magnetic latitudes

and at other local times, where recent studies have also suggested EMIC wave generation could occur [*Liu et al*., 2012; *Allen et al*., 2013].

5.7.4 Discussion

The observations and modeling of the dawn EMIC waves suggest that off-equatorial wave generation could occur in addition to the "classical" expectation of equatorial wave generation and that the peculiar polarization properties are consistent with propagation effects occurring after generation. Armed with improved knowledge of the low-energy ion properties, the linear theory results described here provide an explanation of the statistical results by *Min et al*., [2012] and *Anderson et al*. [1992b], and an improvement to the modeling by *Horne and Thorne* [1994], in which they described dawn EMIC wave spectral properties and polarization characteristics as due to increased hot proton anisotropy (above what is typically observed), much lower low-energy plasma density than typically observed, and wave propagation and reflection within the growth region.

Simultaneous multi-spacecraft studies of dawn EMIC waves over an angular range of magnetic latitudes are needed to further validate the explanations given within this section and characterize more accurately, with local measurements from the source region, wave generation and propagation. In addition to multi-point observations, ray-tracing simulations can help explain the wave reflection and mode conversion effects that are implied herein. Observational studies and modeling of the free energy source are also needed to validate our expectation on the preferred wave source region(s) in this sector.

5.8 Noon

As shown in *LA2014*, the median temperature of the low-energy ion species evolves quickly from warmer near dawn to cooler near noon. This temperature azimuthal gradient is consistent with the large-scale transition from a warm plasma cloak at dawn to cooler plasmaspheric or ionospheric outflow material near noon and post-noon. I also expect that the magnetic field configuration strongly deviates from dipolar near noon, due to the proximity to the magnetopause (as well as dynamic effects from solar dynamic pressure variations and diurnal variations of the Earth dipole affecting the location of minimum B regions along the field line). These factors influence EMIC wave activity in ways that have been introduced in preceding sections: wave properties can evolve from the "classical" dusk picture due to mixing of low-energy ions of varying temperatures from multiple sources, free energy enhancements modulated solar wind-driven ULF waves, and wave generation could occur both at as well as off the magnetic equator due to the location of free energy. I consider these factors in my analysis of this event.

5.8.1 Particles

The particle measurements and other plasma properties obtained by TH-A at a geocentric distance of 9 R_E near the noon sector (~11 MLT) on 2 January 2013 are shown in Figure 5.13. The spacecraft is located (see Figure 5.13, bottom) beyond the equatorial source region for EMIC waves described by *Loto'aniu et al*. [2005], i.e., |MLAT| > 11° (I will come back to the importance of the spacecraft location when I analyze the wave observations). Transient enhancements in low-energy ion fluxes are seen during this interval at times of flows (Figures

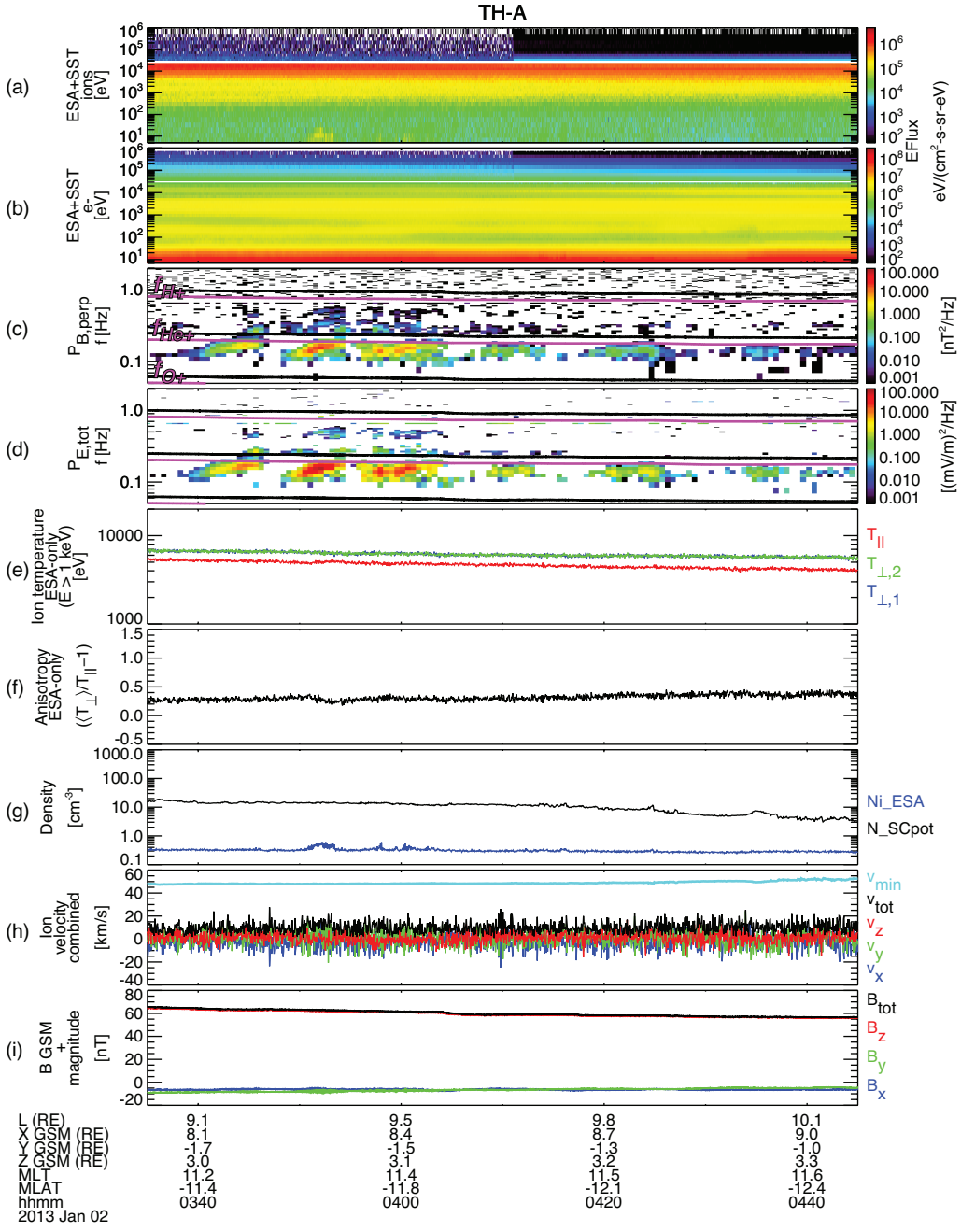

Figure 5.13: The particle, wave, and plasma properties observed on 2 January 2013 by TH-A.

5.13a, 5.13h) like in other sectors, consistent with the inference from N_SCpot (Figure 5.13g) of persistent cold, low-energy ions of significant density. I also note that the electron flux signatures imply the presence of at least three and possibly four electron populations that again suggest particles from different sources are present at this location. The temperature anisotropy of the hot protons (Figure 5.13f) is moderate during the entire interval (~0.3–0.4). The total plasma density (~10–15 cm^{-3}) in this noon case is higher than for the dawn and midnight cases and similar to that at dusk. Also similar to dusk is most of these ions have energies below E_{min} (Ni_ESA and N_SCpot traces in Figure 5.13g disagree). But contrary to dusk, the measured low-energy (< 1 keV) ion flux spectra reveal the presence of significant fluxes of warm ions, at levels a factor of ten larger than at dusk (noon: 1e+4 to 1e+5 eV/cm^2-s-sr-eV; dusk: 1e+3 to 1e+4 eV/cm^2-s-sr-eV). This, again, implies that multiple ion populations are present, some with suprathermal tails that extend above the spacecraft potential energy (although most of their density is still invisible to the ESA detector). Their significance will be apparent in the modeling section.

5.8.2 Waves

The waves are observed in several discrete bursts that occur on a 5−10 minute cadence. Such bursts could again be related to ULF wave modulations of the hot proton anisotropy that occur on a Pc5 wave period, though such modulations in the particle observations are not seen at TH-A.

5.8.2.1 Polarization Analysis

The waves are close to the local f_{He+} with some wave power crossing over f_{He+} at ~345 UT and

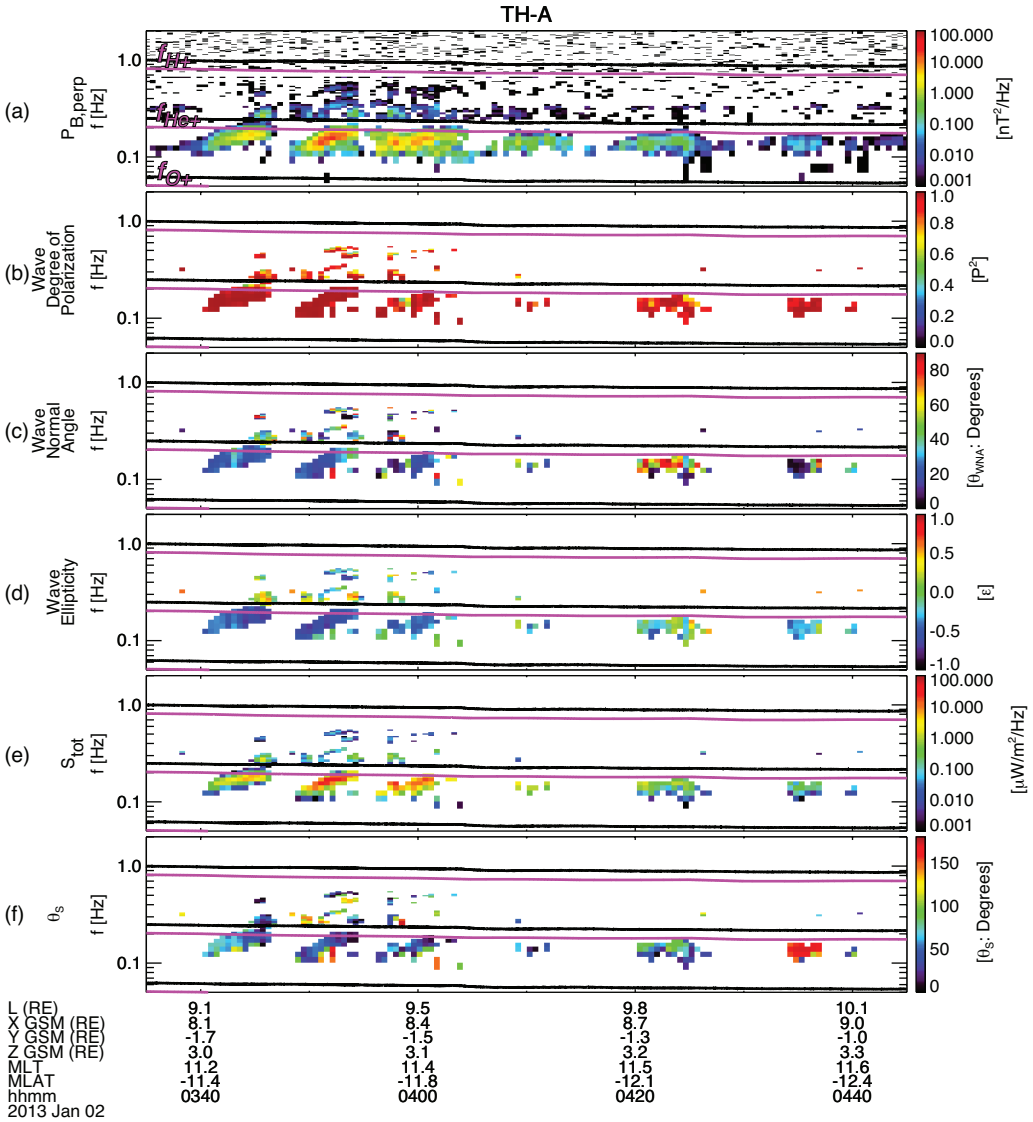

Figure 5.14: Wave polarization and Poynting vector spectral properties.

~354 UT (Figure 5.14a). These signatures are similar to those seen at midnight; here, too, they suggest warm heavy ion effects on wave growth, and are consistent with my inference of the presence of warm ions at the spacecraft location. Wave coherence (Figure 5.14b) is high (P^2 >

0.8) during the most intense wave power signatures. The wave normal angle (Figure 5.14c) and ellipticity (Figure 5.14d) data show the waves are nearly field-aligned and have clear left-handed polarization. When combined, the wave properties are consistent with local generation and based on the spacecraft location and previous work [*Loto'aniu et al*., 2005], I expect these waves to be propagating anti-field-aligned (away) from the nominal equator. I next check whether the Poynting vector spectral data confirm my expectation.

5.8.2.2 Poynting Vector

The wave energy propagation angle data (Figure 5.14f) show the waves have clear field-aligned signatures. From the spacecraft location that is below the magnetic equator (Figures 5.13 or 5.14, bottom), the field-aligned wave energy propagation angle ($\theta_S \leq 10°$) implies that most of the observed waves are actually propagating towards the magnetic equator and contradict what I expected. Instead, the θ_S data suggest that the waves were generated at non-equatorial magnetic latitudes and are retaining a propagation angle mostly along the field as they propagate from their source region towards the equator. The last burst of wave activity just before 440 UT shows energy propagation in the anti-parallel direction ($\theta_S \approx 180°$), consistent with propagation away from the nominal equator, and is either a result of reflection or of wave generation at northern magnetic latitudes.

5.8.3 Modeling

To confirm whether I am indeed observing waves generated away from their source region, I follow the same procedure as described for the midnight modeling. I first use the low-energy ion

Table 5.4a. Noon observed environment properties and low-energy ions from statistics.

B_o (T)	N_{tot} (m^{-3})
6.00E-08	1.50E+07

Species	Hot Protons	Protons	He^+	O^+	Cold e-
n_s (m^{-3})	2.2E+05	9.35E+06	3.09E+06	2.34E+06	1.50E+07
Tpar (eV)	3700	5.0	20.3	109.5	1
Tperp (eV)	5200	5.0	20.3	109.5	1

Normalized	Hot Protons	Protons	He^+	O^+	Cold e-
n_s/N_{tot}	0.015	0.623	0.206	0.156	1.000
Tpar/Tpar,Hot	1	1.34E-03	5.49E-03	2.96E-02	2.70E-04
Tperp/Tpar	1.4	1	1	1	1

Table 5.4b. Noon observed environment properties, low-energy ions from statistics, and an additional cold plume component.

B_o (T)	N_{tot} (m^{-3})
6.00E-08	1.50E+07

Species	Hot Protons	Protons	He^+	O^+	Cold e-	Plume H^+
n_s (m^{-3})	2.20E+05	4.0E+05	1.3E+05	1.0E+05	1.50E+07	1.415E+07
Tpar (eV)	3700	5.0	20.3	109.5	1	1
Tperp (eV)	5200	5.0	20.3	109.5	1	1

Normalized	Hot Protons	Protons	He^+	O^+	Cold e-	Plume H^+
n_s/N_{tot}	0.015	0.026	0.009	0.007	1.000	0.943
Tpar/Tpar,Hot	1	1.34E-03	5.49E-03	2.96E-02	2.70E-04	2.70E-04
Tperp/Tpar	1.4	1	1	1	1	1

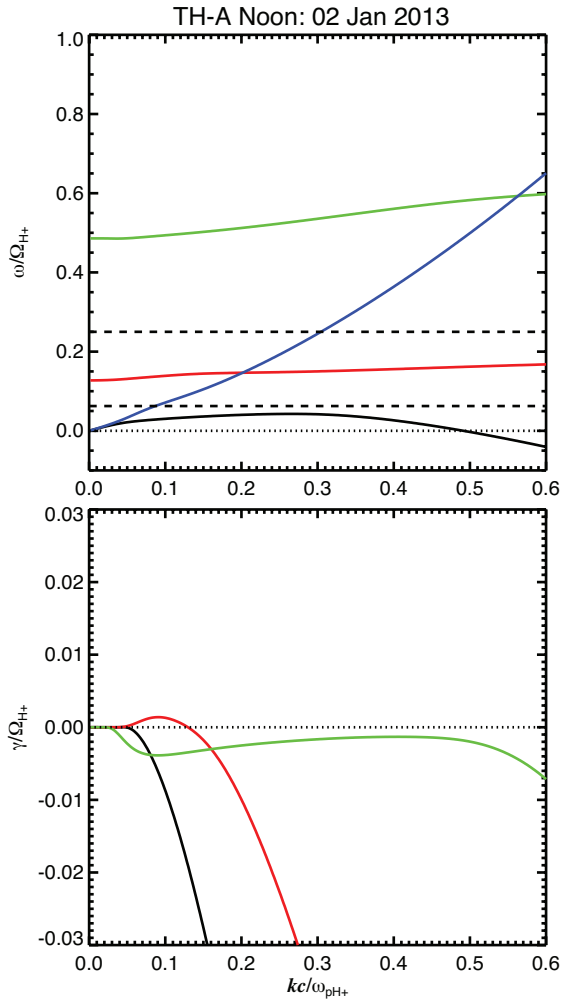

Figure 5.15: Numerical solutions to the full dispersion relation for the noon waves using the parameters in Table 5.4a.

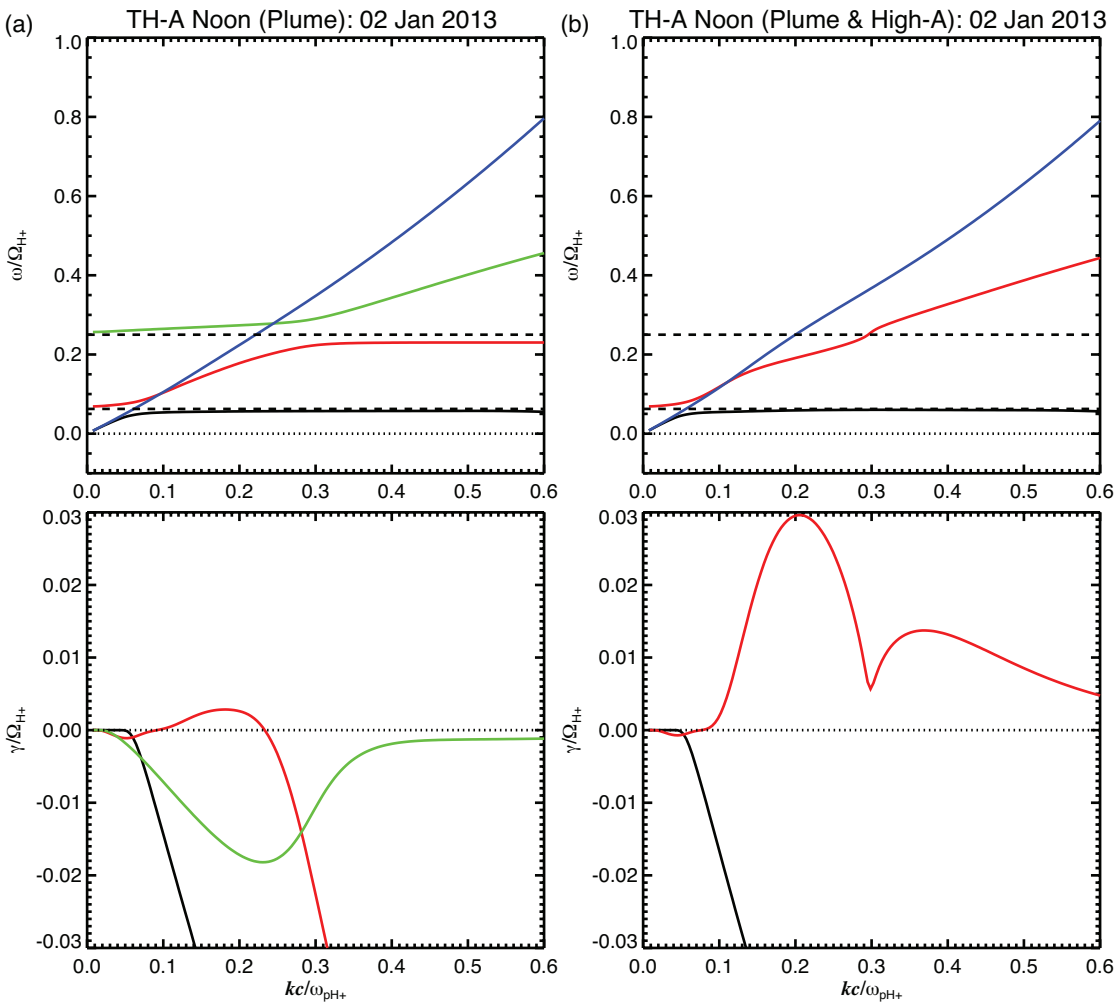

Figure 5.16: (a) Numerical solutions to the full dispersion relation for the noon waves using the parameters in Table 5.4b and (b) the solutions after increasing the hot proton anisotropy to ~2.5.

partial density ratios and median temperatures provided by *LA2014* to determine the densities and temperatures of the low-energy ion components for the modeling, summarized in Table 5.4a, and obtain solutions that do not agree with what was observed; Figure 5.15 shows that a large stop band is present near Ω_{He+} while the He^+ band has negligible growth. The entire He^+ band branch does not match the observations.

Based on the observation of larger N_SCpot and the disagreement between Ni_ESA and N_SCpot, I add a cold (1 eV) proton component and use only the median densities and

temperatures to define the other low-energy ion components, as summarized in Table 5.4b. Such an assumption has also been made in the past because the particle energy is below the spacecraft potential [*Anderson et al*., 1996a]. As seen in Figure 5.16a, the modeling results using these parameters show better agreement with the observations, with a well-defined He^+ band branch and a positive growth rate on the rising frequency portion of this branch. The calculated wave gain, however, is below 10 dB and too low for local wave growth when local hot proton anisotropy measurements are used (A ~ 0.4). Wave growth across Ω_{He+} is also not seen. As I have done in the dawn case, after increasing the hot proton anisotropy to the level needed (A ~ 2.5) for local growth and for full agreement with the wave spectral signatures seen in the observations I obtain Figure 5.16b. In particular, I am able to reproduce linear wave growth that would explain the wave power signatures near and across f_{He+}.

5.8.4 Discussion

Even though the noon waves showed polarization characteristics consistent with locally-generated, left-handed EMIC waves, the Poynting vector angle data showed that most of the waves were instead propagating into the equatorial region from a non-equatorial magnetic latitude. The magnetospheric regions of minimum in total magnetic field located off the magnetic equator [e.g., *McCollough et al*., 2010, 2012] has been previously proposed as the source of unstable EMIC waves observed at high magnetic latitudes [*Liu et al*., 2012]. The minimum B regions have magnetic field values below that at the equator. By comparing the local (black) to the equatorial (magenta) ion gyrofrequencies in any of the panels in Figure 5.14 (as estimated by the *Tsyganenko* [2001] model), I see that the local magnetic field strength is greater locally, at MLAT = −11° to −12°, than at the equator and therefore it is expected to be also

higher than at the minimum B region. The stop band observed for our waves, however, is consistent with wave generation at only slightly reduced fields relative to the local field, above equatorial values and certainly above the minimum B value. Based on this and the wave propagation properties (from high to low latitudes) I suggest that the source region is at intermediate latitudes between the spacecraft and a minimum B location. *Le et al*. [2001], using Polar data, found that EMIC waves were a permanent feature (>90% occurrence rate) in the high-altitude cusp region; these waves could be rendered unstable due to ion ring distributions formed by solar wind ions charge-exchanging with the Earth's exosphere [*C. T. Russell*, personal communication, May 13, 2014]. Once generated these cusp EMIC waves could propagate down the field towards the ionosphere but also potentially up the field line into multiple magnetospheric locations. More recently, *Allen et al*. [2013] showed EMIC waves observed by Cluster II at dayside middle (MLAT > 30°) magnetic latitudes were bi-directional and consistent with a local, or nearby source. My results are consistent with these past observations. Once the waves are generated at off-equator latitudes, guiding of the waves along the edges of enhanced cold plasma density outward gradients [e.g., *de Soria-Santacruz et al*., 2013] could explain how the Poynting vector angle remained nearly along the field for all wave bursts seen during my event.

5.9 Summary and conclusions

I analyzed EMIC wave cases as a function of local time near the equatorial magnetosphere. Both the particle and wave observations were discussed in this multi-case analysis and then applied to modeling of local linear wave growth. As I stepped through each local time sector I discussed how the low-energy ion properties that vary as functions of local time and geocentric distance

[*Lee and Angelopoulos*, 2014] manifest themselves in the multi-instrument observations and how the wave observations provide a further diagnostic on the presence and properties of these low-energy ions during the wave activity. I have shown that the locally measured, inferred or statistically constrained [*LA2014*] low-energy ion properties influence greatly wave generation and properties and suggest that these low-energy ion properties are critical to include in future studies of the waves and their interactions with radiation belt particles. My main points are listed by local time sector below.

1. At the dusk side, consistent with previous studies, the cooler, plasmaspheric ions dominated by cold protons contribute significantly to a reduction of the critical anisotropy for local wave growth. Given the natural drift path of injected hot plasma sheet ions into this sector, ample free energy is frequently available for wave growth even under conditions of moderate geomagnetic activity.
2. At the night side, the heavy ions are typically warmer and more abundant than at dusk and tend to suppress EMIC wave activity. Plume-like cold plasma density increases, as inferred from the observations, can lower the instability threshold needed for wave growth and can explain the infrequent but finite EMIC wave observations there as due to local wave generation. Once generated, the waves may grow across the He^+ stop band due to the critical presence and/or further heating of low-energy He^+ at moderate densities and already elevated temperature. Due to such heated heavy ions, wave polarization can evolve rapidly even after only limited propagation, consistent with prior observations in that sector.
3. At the dawn side, the total plasma density is typically much lower than at dusk (or in plasmaspheric plumes) and the low-energy ion species have a lower relative

abundance of cold protons. When free energy becomes available (due to injections of hot ions or magnetospheric compressions) in the presence of these dawn ion species, the waves experience strongest growth in the proton band due to the already heated heavy ions; waves in the other EMIC bands (if those exist at all) have either smaller growth rates or are fully damped for the same reason. In the event shown (and as others have analyzed), all three THEMIS satellites, situated near the magnetic equator, did not measure the required free energy for the observed proton band wave growth. Moreover, consistent with previous statistical studies of the waves, mixed wave polarizations were observed, contradicting previous expectations for classical left-handed EMIC waves generated near the equator. My combined observations and modeling showed that the waves could be generated both locally and non-locally, at higher latitudes, and their propagation through the warm plasma cloak is consistent with the mixed polarizations observed.

4. At the dayside, a combination of effects involving multiple low-energy particle populations, non-equatorial free energy sources, and the large-scale ambient magnetic field configuration affects the generation and properties of the waves. A plume-like cold plasma density increase is important for defining the dispersion bands of the waves but is insufficient on its own to explain the observed wave properties. The large hot proton anisotropy required to explain wave growth consistent with the wave observations was not measured, so non-local growth was inferred. The predominantly field-aligned Poynting vectors propagating toward the equator from a southern beyond the location of the spacecraft, and the presence of a distinct, though shallow, stop band in the data at fields comparable to but lower than that measured locally are

both in agreement with the non-local source hypothesis and suggest a source at intermediate latitudes between the spacecraft and an additional low B region. The inclusion of low-energy He^+, again with critical density and temperature, allowed for this wave growth to occur over an observed frequency range including across the shallow He^+ stop band.

Future investigations of EMIC waves and the free energy sources needed to drive their instability are necessary. Use of multiple satellites is critical for determining the extent of the wave generation regions and for the correlation of wave amplitudes and properties (emission frequencies, polarization, propagation angles, wave energy, and directions of propagation) with recent results on observed abundance and properties of low-energy ions. Such studies are needed to verify my picture of non-equatorial wave generation and the effects of low-energy heavy ions in both wave growth and propagation effects. Additional studies of wave propagation using multi-spacecraft observations together with ray tracing and hybrid simulations as a function of local time can also improve our current understanding of these effects. Lastly, more inquiry into the contribution of EMIC waves to scattering of radiation belt particles remains to be done but should be done with the knowledge that low-energy ions are pervasive in the Earth's magnetosphere. In particular, warm ions from the plasma torus and the plasma cloak surround the cold plasmasphere along both the dawn and dusk sides. The presence of these warm ions could be another reason why recent EMIC wave activity [*Turner et al*., 2014; *Usanova et al*., 2014] occurring near the edge of the plasmasphere in association with moderate-to-strong geomagnetic storms appeared to only scatter electrons in the >2 MeV energy range.

CHAPTER 6

Conclusions and future work

6.1 Conclusions

Electromagnetic ion cyclotron waves are strongly influenced by the presence and properties of multiple ion species and are often observed at many locations in Earth's magnetosphere. The Earth's magnetosphere is a large plasma physics laboratory where experimental measurements can be obtained by spacecraft and then tested to theory. By leveraging the multi-instrument measurements made by the multiple THEMIS spacecraft near Earth's equatorial magnetosphere and applying the measurements to linear theory of electromagnetic waves, I have shown how EMIC wave growth and properties evolve in a way that is fully consistent with effects determined by the compositional properties of the multiple ion species. In particular, I have described how the warm plasma effects on EMIC waves are strongly dependent on both the densities and temperatures of the low-energy heavy ion species and how these effects are likely pervasive in the Earth's magnetosphere. I have accomplished this task by conducting the focused studies below.

1. My first study described observations of multiple ion species and concurrent EMIC wave activity that contradicted expectations based on linear cold plasma theory. Observations of the multiple ion species during the time interval of wave activity motivated detailed modeling of the observations in the context of linear warm plasma theory. The modeling with warm plasma theory was consistent with the observations

and showed that EMIC wave properties evolve following marginal heating of a low-density and low-energy He^+ component in the presence of a high-density, cold proton component and the low-density hot proton free energy needed to drive the waves. This result then motivated a parametric study of the effects of low-energy He^+ density and temperature on the growth and dispersion of magnetospheric EMIC waves. The results of this parametric study suggested a range of He^+ densities and temperatures could support the evolution of warm plasma EMIC waves throughout the Earth's magnetosphere provided that the necessary hot proton free energy and cold, dense protons are also present.

2. Motivated by the results and implications of the parametric study on low-energy He^+, I designed and conducted a statistical study to explore the typical properties of low-energy plasma ion populations that are useful to determine where such ions could influence magnetospheric EMIC waves due to warm plasma effects. In the study I revealed the spatial distributions of occurrence rates, abundance, and temperatures of the dominant cold and warm ions (H^+, He^+, and O^+) near the Earth's equatorial magnetosphere, and obtained insights into the sources and transport pathways of those ions. I also showed that the temperatures of the low-energy (< 1 keV) ions were warmest at pre-midnight, and all three species' partial densities and temperatures varied significantly with geocentric distance and magnetic local time.
3. I then reviewed other spacecraft observations of the occurrence rates, properties, and transport of low-energy plasma populations near the equator in light of the results of my study on low-energy ions. Through this review, I found that the combined observations from THEMIS and other missions imply that, likely due to a spectrum of

low frequency electromagnetic energy inputs at the dayside and nightside, a diffusion of ions emanating from both the ionosphere and the solar wind results in the equatorial low-energy plasma. Future multi-spacecraft missions are needed to characterize this electromagnetic energy input and its effects on plasma sources and mixing. Even with existing missions, however, significant knowledge on the low-energy plasma populations can be gained by multi-instrument measurements of both the particles and waves, since together with linear theory even limited particle observations can be used to infer particle composition.

4. Armed with the knowledge from the results of my preceding studies, I revisited critical EMIC wave questions raised in previous studies, such as their source location, mode, and propagation, and conducted case studies of representative waves in each MLT sector. I included composition either measured in situ, or inferred from my statistical study on low-energy ions, and modeling using the full dispersion relation for parallel-propagating EMIC waves. Four prototypical EMIC wave intervals were chosen based on their similarity in wave spectral properties to those found in a recent global survey of such waves from THEMIS [*Min et al*., 2012]. I then explained the MLT-dependence of EMIC wave properties and the peculiar wave characteristics noted in the past as entirely due to the compositional properties of the background plasma, and identified their source locations. The success of this investigation leads me to believe that similar tools can be used hand-in-hand with statistical studies to examine the wave sources as well as the properties of the background low-energy ions as function of MLT and geomagnetic activity level.

6.2 Future work

6.2.1 Improved global study of magnetospheric EMIC waves

A global study of EMIC wave properties using a combination of waves and particles as demonstrated in this dissertation is necessary to properly characterize magnetospheric EMIC waves during quiet and active times. Use of multiple satellites can determine the extent of the wave generation regions and a correlation of typical wave amplitudes and properties (emission frequencies, polarization, propagation angles, wave energy, and directions of propagation) with my results on abundance and properties of low-energy ions can then inform further studies on the waves' interactions with energetic particles.

6.2.2 Observations and modeling of the free energy source

My results suggest that many magnetospheric regions could have the necessary free energy to generate EMIC waves. Observations and modeling of the hot proton free energy that drives EMIC waves unstable are needed to characterize such regions. Global multi-spacecraft case and statistical studies of the hot protons as function of energy can provide spatial distributions of peak anisotropy, occurrence rates, and also reveal their latitudinal dependence. Further binning of the statistical data as functions of solar wind and geomagnetic activity indices can enable more inquiry into the relationship of free energy enhancements due to solar wind compressions or geomagnetic activity (injections). These trends can then be combined with similar trends from global statistics of EMIC waves and their properties for implementation into global dynamic magnetosphere simulations.

Particle tracing can be performed independent of a multi-spacecraft study and be used to predict the asymmetric orbits of injected hot plasma sheet ions in a realistic geomagnetic field as function of pitch-angle. This modeling can reveal where additional non-equatorial EMIC wave source regions could be and potentially look for those anisotropies in current or historical spacecraft data at those regions. Such studies on the hot proton free energy are needed to further test the picture I have suggested of non-equatorial wave generation in addition to the classical equatorial source and for further understanding on the participation of low-energy heavy ions in both wave growth and propagation effects.

6.2.3 EMIC wave propagation

Wave propagation and the evolution of wave properties during propagation can be investigated using multi-spacecraft observations, ray tracing, parametric studies of the linear dispersion relation at oblique wave normal angles, and hybrid simulations. For example, orbits when multiple spacecraft are distributed in magnetic latitude could provide opportunities to observe propagating EMIC waves by all spacecraft at the same time. During such times analysis of the measurements may reveal different polarization and Poynting vector spectral signatures at each spacecraft that can then be interpreted and explored by ray tracing and linear theory of oblique waves. These studies can be performed as function of local time to determine how a background plasma with composition that is also variable in local time affects wave propagation. The typical properties of the low-energy ions described in this dissertation can facilitate definition of the background plasma for such studies on wave propagation.

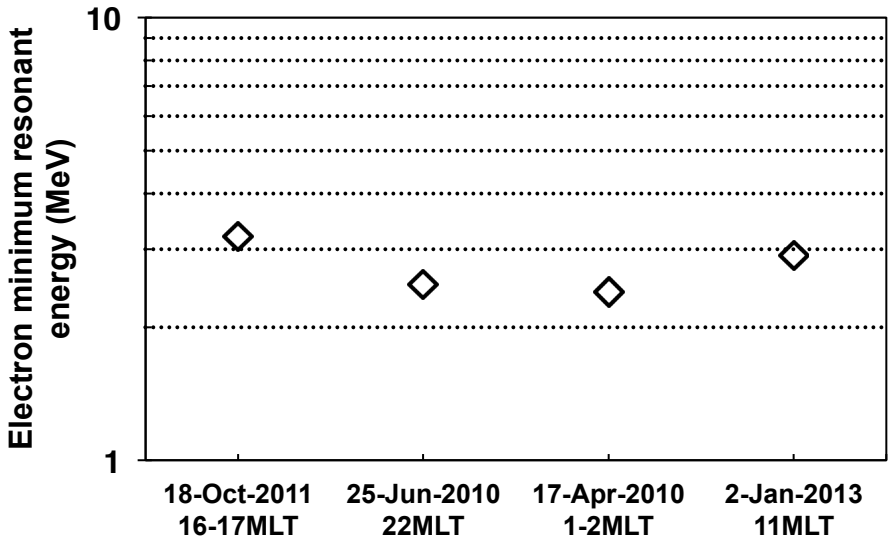

Figure 6.1: The predicted minimum resonant energies for relativistic electron interaction with the modeled EMIC wave cases. The resonant energies were calculated using $k_{||}$ values obtained from numerical solutions to the warm plasma or full dispersion relations.

6.2.3 Scattering of radiation belt particles by EMIC waves

Lastly, more research into how effective EMIC waves are in scattering of radiation belt particles remains to be done but should be done with the knowledge that low-energy ions are pervasive in the Earth's magnetosphere and affect wave dispersion and wave-particle interactions. In particular, warm ions from the plasma torus and the plasma cloak surround the cold plasmasphere along both the dawn and dusk sides. During times of increased geomagnetic activity and coincident intensifications in convection electric field strength, these warm ion populations can be expected to penetrate to small geocentric distances and be present near the outer plasmasphere boundary layer. The warm ions would then also be in the direct pathway of injected ring current ions.

Taking some of the waves that I presented within this dissertation to show how the inclusion of warm ions affects the minimum resonant energy of relativistic electrons, I again use the equation

$$\boldsymbol{E^{e}_{res\|} = \left(\left[\frac{\Omega_e^2}{c^2 k_\|^2} + 1 \right]^{1/2} - 1 \right) E_o},$$

where the $k_{||}$ values I use here are the approximate maximum $k_{||}$ at which the waves remained undamped as obtained from the modeling (using the numerical solutions where the unstable wave number range and path-integrated gain were consistent with explaining the observed waves). It is apparent that the electron resonant energy is predicted to be >2 MeV for each of these cases, Figure 6.1.

The presence of warm ions at small geocentric distances could be another reason why recent EMIC wave activity occurring near the edge of the plasmasphere in association with moderate-to-strong geomagnetic storms appeared to only scatter radiation belt electrons also in this >2 MeV energy range [*Turner et al*., 2014; *Usanova et al*., 2014]. Thus, it is critical that efforts are made to obtain detailed in situ knowledge or use the statistical low-energy ion properties I have supplied within this dissertation when performing analysis and modeling of future intervals of storm-related EMIC wave activity. Signatures of warm plasma effects in wave spectral data as I have analyzed within also need to be considered. Such an approach is essential to accurately determine how effective EMIC waves are in scattering of radiation belt particles.

APPENDIX A

Instruments and Methods

A.1 Introduction

In this section the THEMIS spacecraft orbits and three of its instruments (ion electrostatic analyzer, fluxgate magnetometer, and electric field instrument) and their measurements are discussed. This discussion is followed by a more specific description on the data processing steps applied to those measurements and also their analysis. Further details on the instrument electronics and calibration are described in the respective references [ESA: *McFadden et al*., 2008a; FGM: *Auster et al*., 2008; EFI: *Bonnell et al*., 2008] and are not the subject of this supplemental chapter. The analysis procedures are accompanied by selected demonstrations on actual measurements obtained by one or more of the THEMIS spacecraft, and are directly from observation time intervals presented in the various chapters in this thesis.

A.2 Overview of THEMIS spacecraft orbits and instruments

The THEMIS spacecraft orbits have evolved over the time period from orbit insertion to present. The original five-spacecraft mission, first launched 17 February 2007 into identical low-inclination "coasting" orbits at ~1 × 15.4 R_E, have been repositioned into numerous configurations since then and two of the outer most spacecraft have been inserted into lunar orbit. The remaining three Earth-orbiting spacecraft continue to add to a large database of multi-satellite plasmas and fields measurements at various locations in the Earth's equatorial

magnetosphere; the space-based observations are complemented by ground-based observations with large networks of all sky imagers and fluxgate magnetometers. Each satellite carries identical instrumentation and their orbits continue to be reconfigured for coordinated temporal and spatial scale studies, in particular supporting conjunctive studies with the recently launched Van Allen Probes mission. As of this writing, the state of health of all THEMIS satellites remains nominal and they continue to obtain measurements and return data via downlink on a regular cadence.

The measurements made by the "inner" THEMIS spacecraft (TH-A, TH-D, and TH-E) are analyzed and presented in this thesis. The inner spacecraft have perigees near 1.5 R_E and apogees that range from 10 to ~13 R_E. The apogees rotate around the Earth so that each spacecraft performs a full MLT clock rotation approximately once every 12 months. The rotation of the apogees support science investigations at each MLT sector (since the apogees gradually rotate into the next MLT sector every ~3 to 4 months) and are referred to as phases (e.g., tail science phase, dawn phase, etc.). The greatest dwell times of the spacecraft occur at geocentric distances beyond 6 R_E (e.g., Figure 3.4b, where each "event" is a single 3 s fast survey interval).

A.2.1 Ion electrostatic analyzer (IESA)

The ion ESA [*McFadden et al*., 2008a] measures energy per charge without mass discrimination via microchannel plate (MCP) detectors. Charge (current) pulses generated by particle kinetic energy deposited into the detectors are amplified and events exceeding a pulse threshold are recorded via counters during each spin. The particle counts are read out 1024 times per spacecraft spin (3 ms). The particle count rate divided by the geometric factor (at each energy) produces the differential particle energy flux. The energy range of the IESA generally ranges

from 25 keV down to ~6 eV, split into 24 or 31 energy bins; as noted within this thesis, the actual minimum energy for detection of low-energy ions of ~6 eV is offset by the spacecraft floating potential that is often positive (few to tens of Volts) during sunlit portions of each orbit and ions of a few to tens of eV cannot be detected. Sweeps through this energy range are performed from high to low energy (i.e., voltage). The "reduced packets" obtained during fast-survey intervals (spin-period time resolution of 3 s) consist of 24 energy bins and 50 solid angles, sufficient for moment computations [*McFadden et al*., 2008a], and are the primary data product utilized for the statistical study on low-energy ion properties described in Chapter 3. The "burst-mode packets" are utilized in Chapter 2, which provide increased energy (32 energy bins) and angle (88 solid angles) resolution at spin-period time resolution. Because of limitations on telemetry, burst-mode is operated for only short duration intervals each orbit. The ion ESA instruments on each spacecraft are cross-calibrated so that complementary (as well as comparison) studies can be performed.

A.2.2 Fluxgate magnetometer (FGM)

The fluxgate magnetometer on each THEMIS spacecraft [*Auster et al*., 2008] has flight heritage from magnetometers on board other spacecraft missions. As described by *Auster et al*. [2008], the science objectives and spacecraft obits required that the instrument obtain measurements of the magnitude of the magnetic field over a wide range (0.1 to ~25,000 nT); the instrument should also support rapid time sampling in order to capture sudden reconfigurations of the magnetic field in association with substorms that occur on ~10 Hz time scales (or faster). During these magnetic field reconfigurations the change in field can be as small as 1 nT and therefore the ability to resolve these changes on a 0.1 nT scale or better was also needed. The instrument was

therefore designed to operate over a ±25,000 nT range, with 3 pT resolution, and with low noise (10 pT/(Hz)$^{1/2}$ at 1 Hz). Because of the requirements imposed on the instrument performance by the core science objectives, the THEMIS FGM is also well suited for studying the properties of plasma waves.

The FGM samples the ambient field in three basic modes. During fast-survey intervals the sensor measures three dimensions of the ambient magnetic field in low-resolution (4 S/s or FGL) mode; these are the measurements that were processed, applied to performing coordinate transformation, and further analyzed for wave activity in this thesis. The FGM can also be operated in a "burst" high-resolution mode, in which the sampling rate is increased to 128 S/s (FGH) to meet and exceed the measurement requirements discussed above. There is also an additional mode operated only near perigee for attitude control purposes at 8 S/s (FGE).

A.2.3 Electric field instrument (EFI)

The electric field instrument consists of three pairs of probes (each measuring voltage) that are separated along three orthogonal axes (two pairs of spherical probes, 1&2 "X" and 3&4 "Y", are extended along booms in the radial axes and a single pair of cylindrical probes, 5&6 "Z", are extended along booms in the axial direction); estimation of three dimensions of the ambient electric field can be determined by measuring the potential difference between these three probe pairs [*Bonnell et al*., 2008, and references therein]. The measurements are obtained over a range of sampling frequencies from 1 S/spin (~0.33 S/s) to 8192 S/s (and up to ~16 kS/s for AC sampling). The electric field measurement resolution for the radial probes is near 10 μV/m and is ~80 μV/m for the axial probes. The primary data products utilized in this thesis are the spacecraft potential (3 s) and EFF (fast-survey electric field, 8 S/s). There are also two additional "burst"

modes of instrument operation; during particle burst mode (EFP) the sampling rate is 128 S/s and during wave burst mode (EFW) the sampling rate is 8192 S/s.

A.3 Analysis methods for particle and fields data

A.3.1 On the methods for determining low-energy ion presence and properties

Additional aspects of the techniques for inferring the presence and properties of low-energy ions that were not described in detail in Chapter 3 are discussed here. Specifically, the steps leading up to the multi-component fit to the subtracted ion flux data are discussed with examples.

A.3.1.1 Low-energy ion presence

As described in Chapter 3, enhanced fluxes of low-energy ions can be detected by comparing the observed fluxes in the ~5 to 120 eV energy range to a background threshold over that same range that is determined by computing the 10^{th} percentile of the observed ion fluxes over a sliding interval. Figure A.1 shows such a comparison between the observed (black crosses) and 10^{th} percentile background ion fluxes (green solid line). If the background flux is exceeded and enhanced flows ($v_{i,perp} > v_{min}$) occur at the same time, such as during the interval shown in Figure A.1, the observed fluxes are passed into an automated fitting routine.

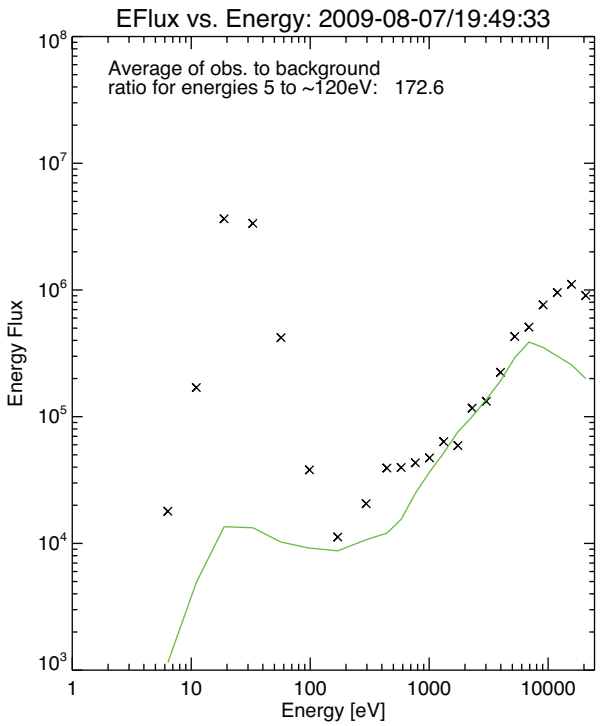

Figure A.1: A comparison between the observed (black crosses) and background ion fluxes (green solid line) to determine if low-energy ion fluxes are present during the interval.

A.3.1.2 Flowing Maxwellian fits to the ion energy flux data

The fitting routine that was developed for the research presented in Chapter 3 and also applied to deduce the low-energy ion composition for one of the wave cases discussed in Chapter 5 first fits the IESA energetic (E > 1 keV) ion flux component using a single flowing Maxwellian energy flux model. This model is obtained by beginning with the directional differential energy flux [*L. Chen*, personal communication, January 27, 2013]

$$\frac{dQ}{dEd\Omega} = 2\left(\frac{E_i}{m_i}\right)^2 f_i \hat{v},$$

where E_i is the particle kinetic energy, m_i is the ion mass, f_i is the Maxwellian phase space density, $\hat{v}$ is the unit vector that provides the direction, and the subscript i indicates the ion

species. Note that E_i corresponds to the energy bins over which the energy flux is obtained (~6 eV to 25 keV). The omnidirectional energy flux is then

$$\frac{1}{4\pi}\int_{4\pi}\frac{dQ}{dEd\Omega}d\Omega$$

and

$$\left\langle\frac{dQ}{dEd\Omega}\right\rangle\equiv\frac{1}{4\pi}\int_0^{2\pi}\int_0^{\pi}\sin\theta\,d\theta\,d\phi 2\left(\frac{E_i}{m_i}\right)^2 f_i,$$

where the phase space density f_i that includes the bulk flow velocity term is

$$f_i=\frac{N_i}{\pi^{3/2}\alpha^3}e^{-\left(\frac{v_z-v_d}{\alpha}\right)^2}e^{-v_x^2/\alpha^2}e^{-v_y^2/\alpha^2},$$

with α being the thermal velocity of the energetic protons and v_d being the bulk flow velocity, both in m/s. We can rewrite f_i in terms of v and v_d in a few steps

$$f_i=\frac{N_i}{\pi^{3/2}\alpha^3}e^{-\left(\frac{v\cos\theta-v_d}{\alpha}\right)^2}e^{-v^2\sin^2\theta/\alpha^2}$$

$$f_i=\frac{N_i}{\pi^{3/2}\alpha^3}e^{-\left(\frac{v^2+v_d^2}{\alpha}\right)}e^{2vv_d\cos\theta/\alpha^2}.$$

If we then substitute f_i into the equation for omnidirectional energy flux above and perform the integration we obtain

$$\left\langle\frac{dQ}{dEd\Omega}\right\rangle=\left(\frac{E_i}{m_i}\right)^2\frac{N_i}{2\pi^{3/2}\alpha v_d\sqrt{2E_i/m_i}}e^{-\left(\frac{2E_i}{m_i}+v_d^2\right)\Big/\alpha^2}\left(e^{\frac{2v_d}{\alpha^2}\sqrt{\frac{2E_i}{m_i}}}-e^{-\left(\frac{2v_d}{\alpha^2}\sqrt{\frac{2E_i}{m_i}}\right)}\right),$$

which has units of eV/m^2-s-sr-eV and $m_i = m_p$ (1.673e−27 kg) and v_d is the bulk flow velocity during the interval. To match the units of the IESA energy flux data (eV/cm^2-s-sr-eV) we need to multiply the model flux by 1e−4.

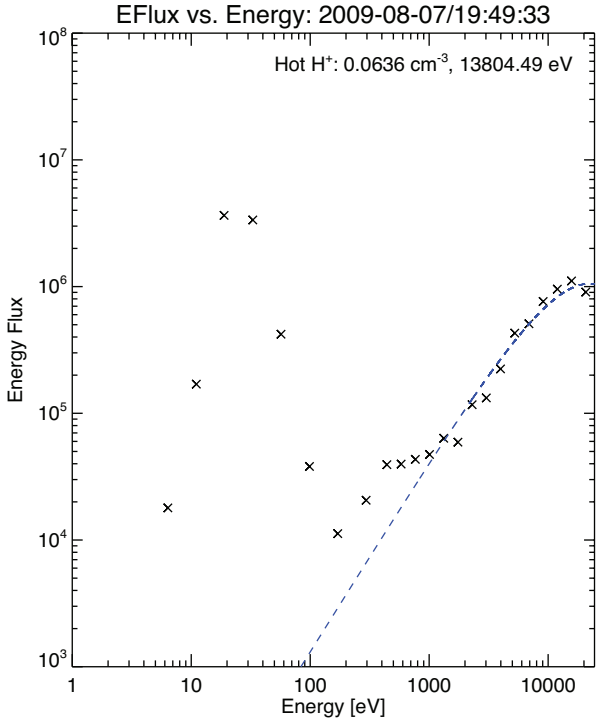

Figure A.2: A single flowing Maxwellian fit (dashed blue line) to the > 1 keV ion energy fluxes (black crosses).

The routine then fits the data in the energy range above 1 keV with the model using an initial guess T_i = 3000 eV (which is converted to thermal velocity) and N_i = 0.2 cm^{-3} until the routine converges (successfully minimizes the sum of the squares deviations) on a best fit density and temperature parameter set for the hot ion component (assumed protons), as shown in Figure A.2, where the dashed blue line indicates the model fit. Note that if this initial fit to the hot ion flux data does not converge successfully, the routine skips to the next interval that the energy flux and flow criteria are satisfied and proceeds to fit the hot proton component in this next interval.

Following subtraction of the model energetic hot proton component from the data, the remainder low-energy ion flux data in the energy range between 0 and 4000 eV are fitted with

another model that is the sum of three flowing Maxwellian energy flux distributions (assuming protons, He^+, and O^+), i.e.,

$$\left\langle \frac{dQ}{dEd\Omega} \right\rangle_{low} = \left(\frac{E_i}{m_p} \right)^2 \frac{N_p}{2\pi^{3/2}\alpha_p v_d \sqrt{2E_i/m_p}} e^{-\left(\frac{2E_i}{m_p}+v_d^2\right)\Big/\alpha_p^2} \left(e^{\frac{2v_d}{\alpha_p^2}\sqrt{\frac{2E_i}{m_p}}} - e^{-\left(\frac{2v_d}{\alpha_p^2}\sqrt{\frac{2E_i}{m_p}}\right)}\right)$$

$$+ \left(\frac{E_i}{4m_p} \right)^2 \frac{N_{He+}}{2\pi^{3/2}\alpha_{He+} v_d \sqrt{2E_i/4m_p}} e^{-\left(\frac{2E_i}{4m_p}+v_d^2\right)\Big/\alpha_{He+}^2} \left(e^{\frac{2v_d}{\alpha_{He+}^2}\sqrt{\frac{2E_i}{4m_p}}} - e^{-\left(\frac{2v_d}{\alpha_{He+}^2}\sqrt{\frac{2E_i}{4m_p}}\right)}\right)$$

$$+ \left(\frac{E_i}{16m_p} \right)^2 \frac{N_{O+}}{2\pi^{3/2}\alpha_{O+} v_d \sqrt{2E_i/16m_p}} e^{-\left(\frac{2E_i}{16m_p}+v_d^2\right)\Big/\alpha_{O+}^2} \left(e^{\frac{2v_d}{\alpha_{O+}^2}\sqrt{\frac{2E_i}{16m_p}}} - e^{-\left(\frac{2v_d}{\alpha_{O+}^2}\sqrt{\frac{2E_i}{16m_p}}\right)}\right),$$

where there are now 6 α and N_i variables. The routine that performs this multi-component fit of the low-energy ions differs slightly from the routine that fitted the hot protons. In the hot proton case the routine allows the Levenberg-Marquardt algorithm to perform least squares minimization based on the same initial guess every time. The multi-component fitting routine allows the guesses to evolve after each fit. Specifically, the guesses start out with a default parameter set of {[T_{H+} = 1 eV, N_{H+} = 10 cm^{-3}], [T_{He+} = 10 eV, N_{He+} = 0.1 cm^{-3}], and [T_{O+} = 10 eV, N_{O+} = 0.1 cm^{-3}]} and a new parameter set is adopted if the fitting converges and if the sum of the squares deviations are sufficiently low. This allows the guesses to evolve with use and ideally improve over time provided that the plasma properties are similar enough during times of flows at each magnetospheric location. If the deviations become too large, the routine resets and subsequent fits start out with the default guesses again. A comparison plot of the model (red dashed line) to the observations (red asterisks) and the low-energy ion parameter set deduced

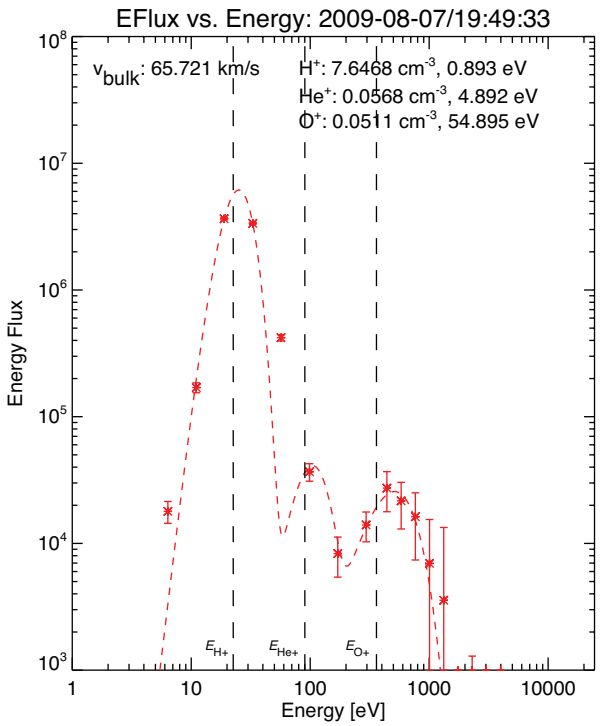

Figure A.3: The multi-component fit to the remaining low-energy ion flux data following subtraction of the hot proton component.

from the multi-component fit is shown in Figure A.3. Note that though the prediction is that peaks in energy flux should be seen at approximate multiples of the observed bulk flow velocity (converted to particle kinetic energy), the fitting routine is only guided by this prediction and proceeds to obtain the best model parameter set resulting in the smallest deviations; this is evident in Figure A.3 in which the model flux peaks are offset slightly from the kinetic energies calculated from the bulk flow velocity.

A.3.1.3 Additional multi-component fits to the low-energy ion fluxes

This section describes additional multi-component fits to the low-energy ion flux data and other related discussions. Fits obtained during two events are discussed in particular: the convection flow that accelerated the H^+ and He^+ so they could be detected around the time of EMIC wave

activity described in Chapter 2 and the ULF waves that modulated the ion fluxes so that low-energy ion properties could be deduced at the same time as the dawn EMIC waves described in Chapter 5.

A comparison of the low-energy ion parameters as deduced from the fitting is made for the convection flow case described in Chapter 2; as noted in this chapter, the low-energy ion properties were estimated from individual Maxwellian fits to 1-d cuts of the 18 s averaged ion distribution function transformed into the BV coordinate system. Examples of multi-component fits obtained from 3 s samples during the 11:00–11:03 UT interval are shown in Figure A.4. The low-energy H^+ and He^+ parameters from these and additional multi-component fits are summarized alongside the parameters described in Chapter 2 in Table A.1. It is evident that the low-energy ion properties deduced from the two fitting methods are comparable.

Figures A.5, A.6, and A.7 show example fits to the ion flux data from TH-A, TH-D, and TH-E, respectively, during the ULF wave activity occurring during the Chapter 5 dawn wave case. Recall that all three THEMIS spacecraft observed the EMIC waves as well as the ULF wave activity; the plasma properties were also similar at each spacecraft location. A collection of additional low-energy ion parameters determined from the fitting is shown in Table A.2.

Table A.1: The properties of low-energy protons and He^+ deduced from multi-component fits to the TH-A low-energy ion energy flux data on 25 June 2010 and the parameter set shown in Chapter 2.

	Cold protons		Helium ions	
	n_s (cm^{-3})	T_s (eV)	n_s (cm^{-3})	T_s (eV)
Chapter 2	20.4	2.2	0.16	30.0
Multi-fit 1	15.0	0.7	0.32	15.4
Multi-fit 2	34.6	0.9	0.22	16.1
Multi-fit 3	47.0	1.0	0.51	16.2
Multi-fit 4	26.2	1.3	0.46	10.1
Multi-fit 5	14.1	0.8	0.34	19.8
Multi-fit 6	35.5	0.7	0.61	19.0

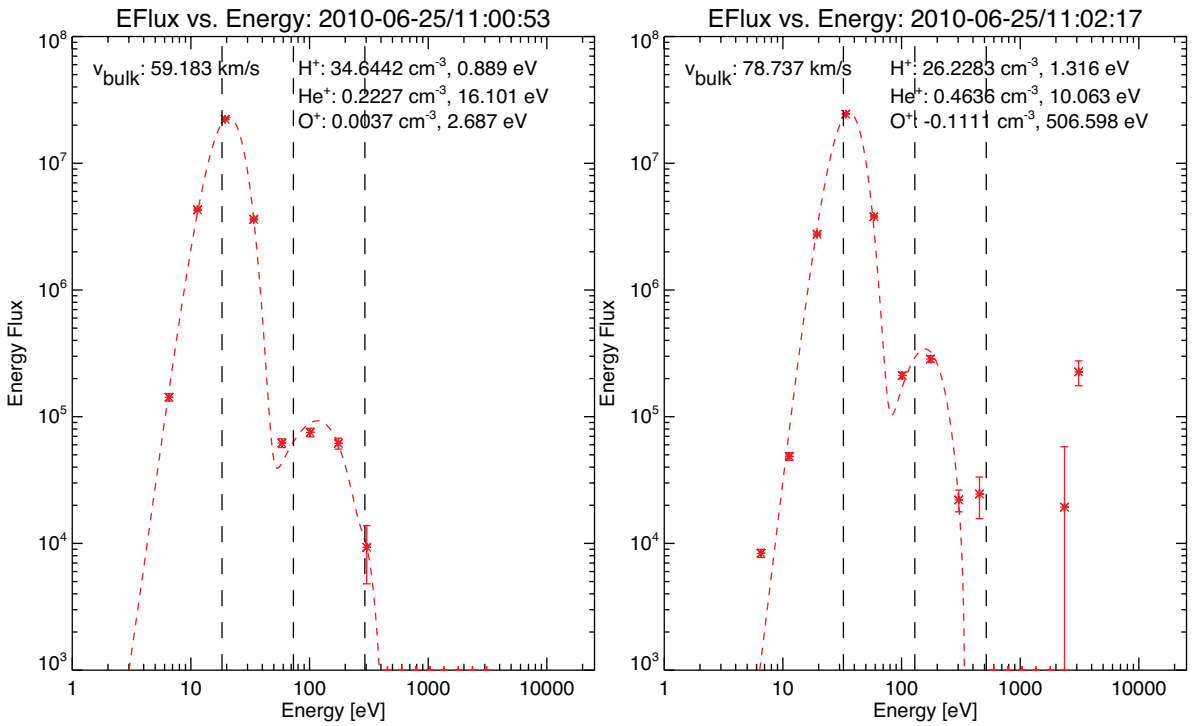

Figure A.4: Example fits obtained using the multi-component fitting method during the EMIC wave event on 25 June 2010 described in Chapter 2.

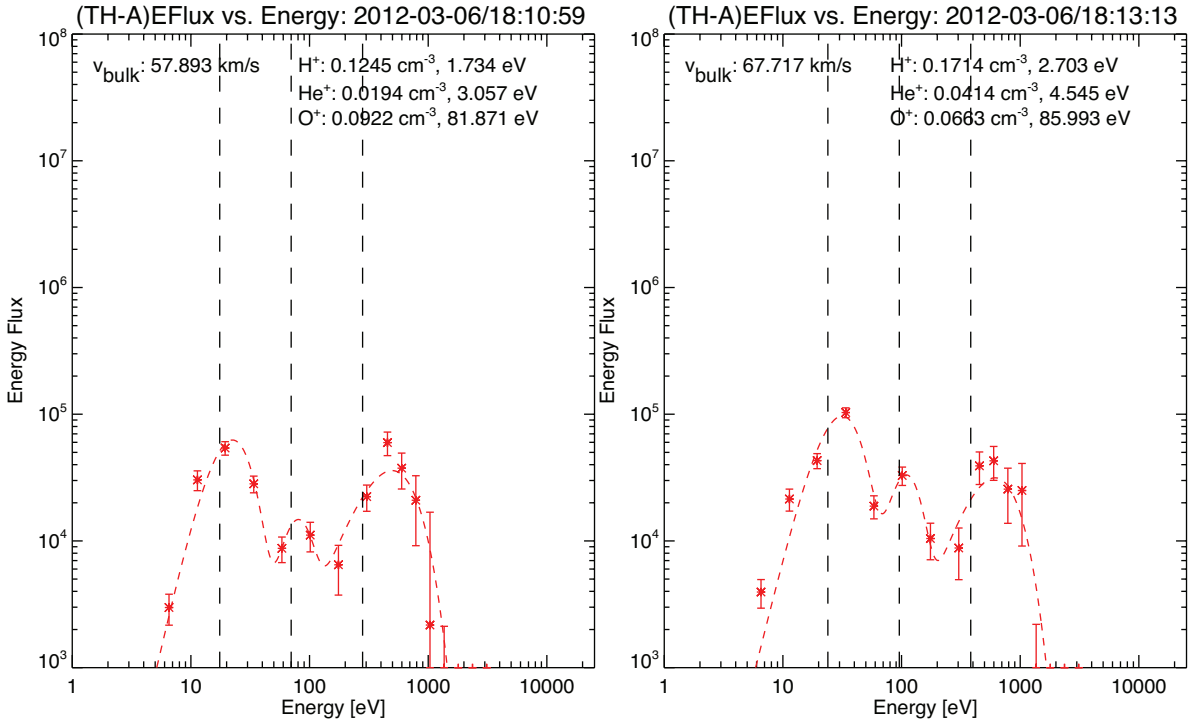

Figure A.5: Selected fits to TH-A low-energy ion flux data observed on 6 March 2012.

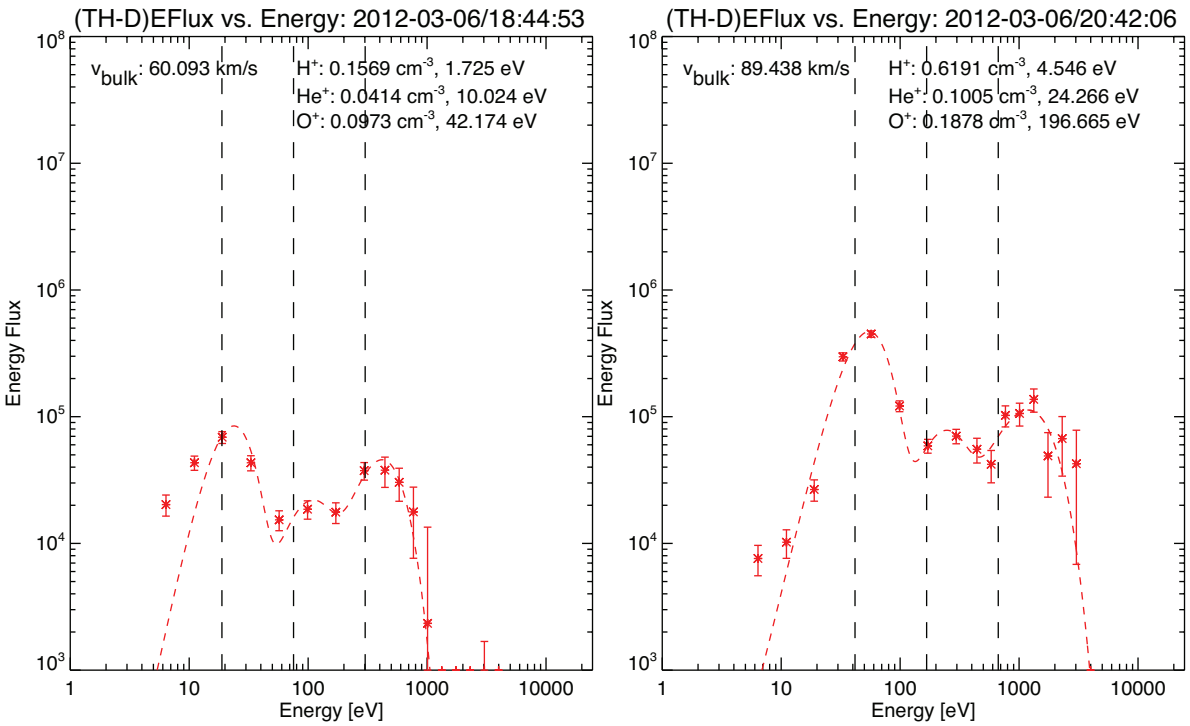

Figure A.6: Selected fits to TH-D low-energy ion flux data observed on 6 March 2012.

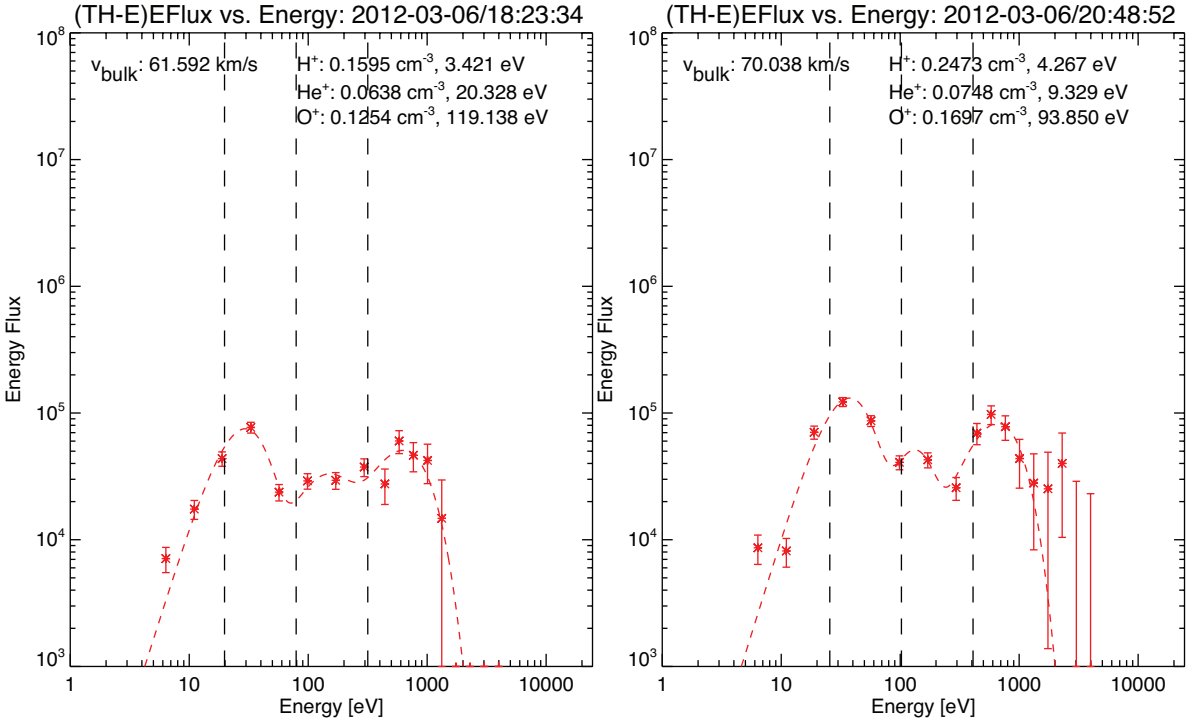

Figure A.7: Selected fits to TH-E low-energy ion flux data observed on 6 March 2012.

Table A.2: Collection of low-energy ion parameters obtained throughout the extended interval of dawn EMIC wave activity described in Chapter 5.

	Cold protons		Helium ions		Oxygen ions	
	n_s (cm^{-3})	T_s (eV)	n_s (cm^{-3})	T_s (eV)	n_s (cm^{-3})	T_s (eV)
A: Multi-fit 1	0.12	1.7	0.02	3.1	0.09	81.9
A: Multi-fit 2	0.17	2.7	0.04	4.5	0.07	86.0
A: Multi-fit 3	0.17	4.3	0.04	11.6	0.16	152.1
D: Multi-fit 1	0.22	6.1	0.04	15.0	0.11	128.6
D: Multi-fit 2	0.16	1.7	0.04	10.0	0.10	42.2
D: Multi-fit 3	0.62	4.5	0.10	24.3	0.19	196.7
E: Multi-fit 1	0.16	3.4	0.06	20.3	0.13	119.1
E: Multi-fit 2	0.13	2.7	0.09	18.1	0.19	266.7
E: Multi-fit 3	0.25	4.3	0.07	9.3	0.17	93.9

A.3.2 Wave analysis

The FGM (and EFI) data are subjected to several basic processing steps prior to performing wave analysis to study further properties of the waves through the power spectral density, wave normal angle, polarization, and Poynting vector data. The techniques for obtaining these additional wave properties are performed using the procedures described by *Samson and Olson* [1980], *Means* [1972], *Loto'aniu et al*. [2005], and *Santolik et al*. [2010] (also *Li et al*. [2013]).

A.3.2.1 Processing of the time series data

The fast-survey EFI data (8 S/s) are first interpolated to match the time resolution of the fast-survey FGM data (4 S/s). The fields data are then prepared for transformation into the mean field-aligned coordinate (FAC) system. This is achieved by taking the fast-survey FGM data in the GSM (Geocentric Solar Magnetospheric) coordinate system (Figure A.8) and computing the DC magnetic field by spin-averaging (~3 s) the fast-survey data followed by taking a sliding average of the data using a time interval significantly longer than the perturbations being studied (e.g., 161 points of the 3 s data ~ 8 minutes >> Pc 1–2 wave periods); a similar process is applied to determine the DC electric field that is later used to detrend the interpolated fast-survey EFI data. The DC magnetic field data (Figure A.9) are passed through a coordinate transform routine to determine the dominant magnetic field component (Z) and the X and Y components transverse to Z (X containing the earthward direction and Y completing the right-handed orthogonal system); this routine produces the mean FAC matrix. Since we would like to study the

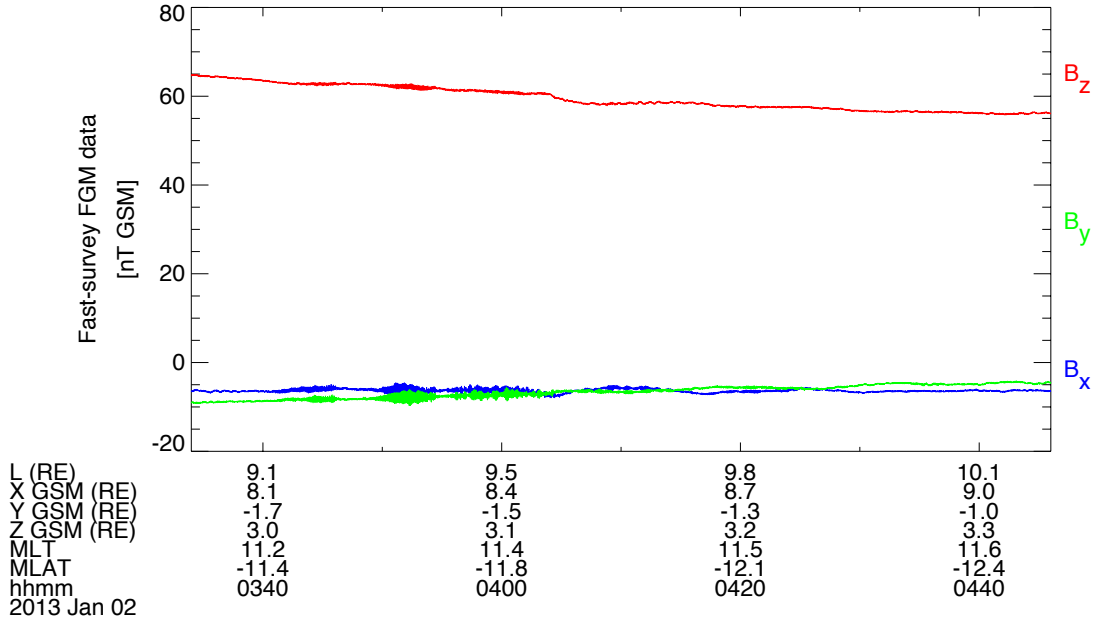

Figure A.8: The fast-survey magnetic field data in GSM coordinates.

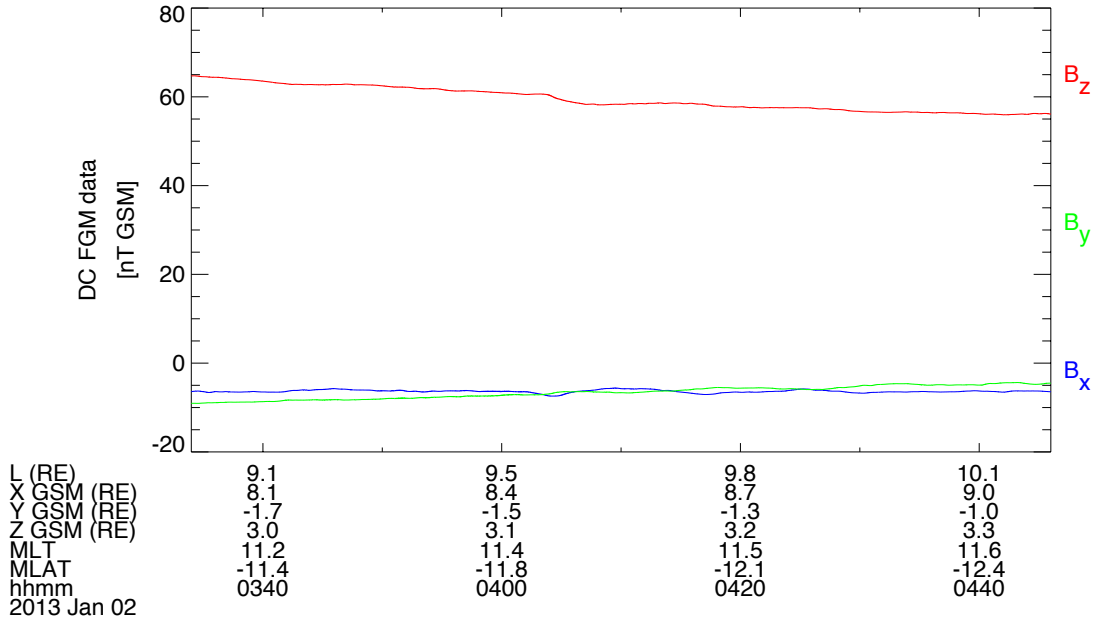

Figure A.9: The DC magnetic field data.

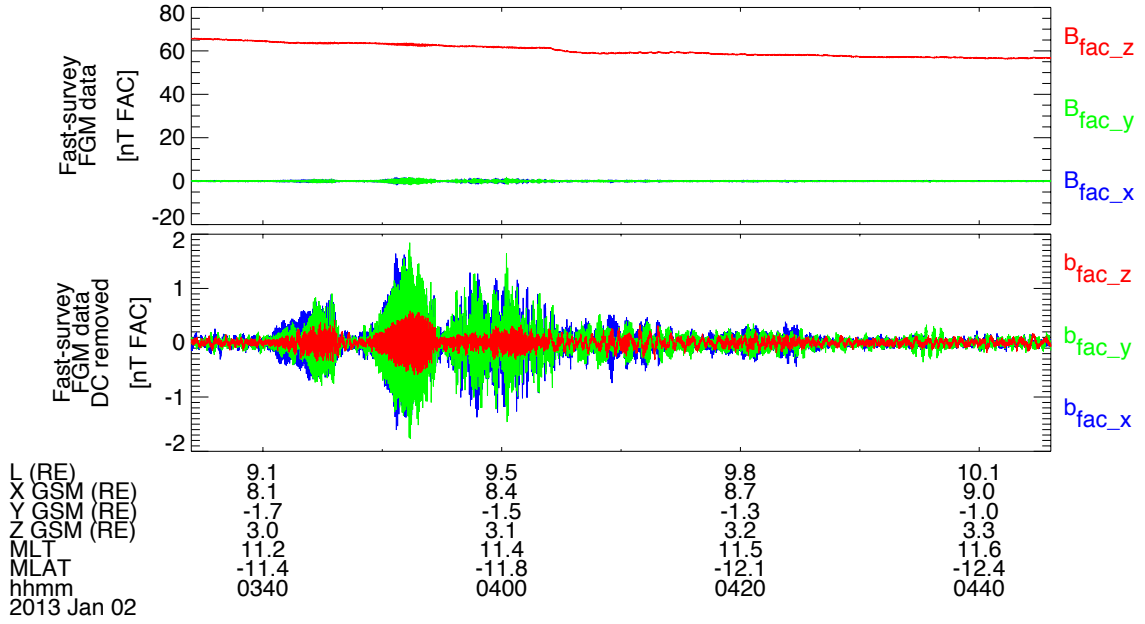

Figure A.10: (top) The fast-survey FGM data transformed into the mean FAC system and (bottom) just the perturbation magnetic field transformed into the mean FAC system.

perturbation fields only, it is useful to remove the DC fields and produce additional times series that contain only the perturbation fields that are then transformed into the mean FAC system using the mean FAC matrix (Figure A.10 shows the (top) fast-survey FGM data transformed into the mean FAC system and (bottom) the three components of the perturbation magnetic field transformed into the mean FAC system). The removal of the DC fields is particularly relevant and often required for analysis of EFI data, since nonphysical, instrumental offsets and noise often exist in this data. The DC electric fields are removed by detrending the fast-survey fields data from their respective DC data. Wave analysis is performed following transformation of the perturbation fields into the mean FAC system.

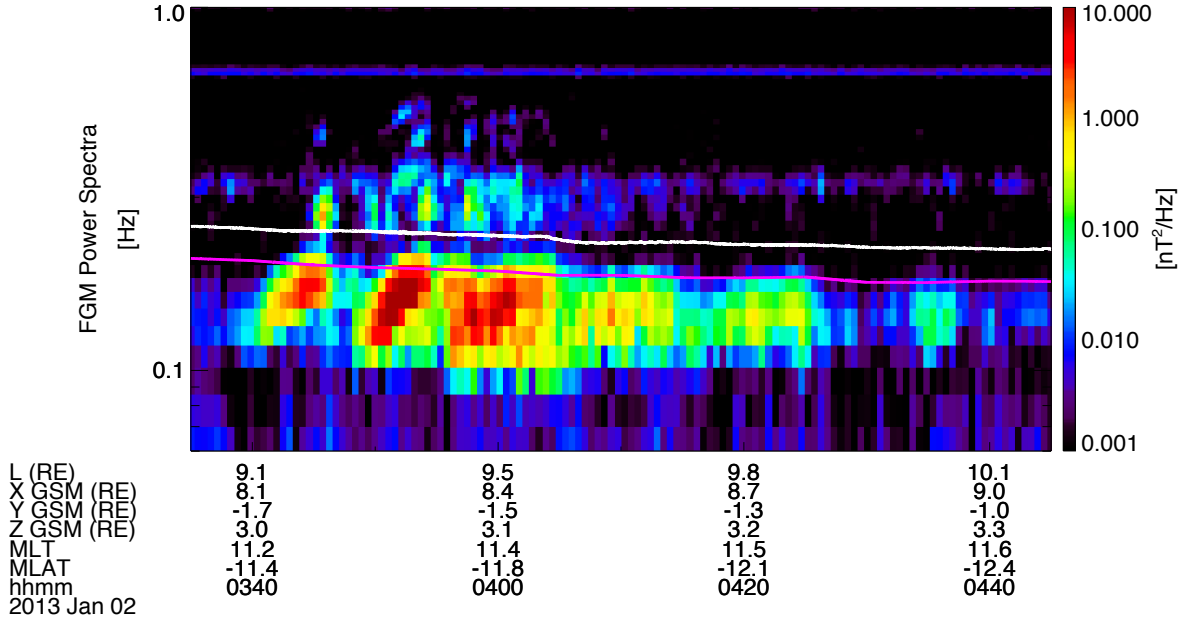

Figure A.11: The total magnetic field dynamic power spectra computed from the real portion of the spectral matrices. Local (white) and equatorial (magenta) f_{He+} has been plotted on the power spectra.

A.3.2.2 Wave power spectra

The fast-survey FGM data in the mean FAC system is fast Fourier transformed (FFT) into series of amplitudes of cosines and sines. The $f \geq 0$ portion of the Fourier spectra is used to compute the spectral matrix that has both real and imaginary portions (when dealing with both the real and imaginary portions of this matrix, i.e., the full spectral matrix, we will refer to it as F and will further discuss analysis of F later); smoothing based on the Hann function [e.g., *Blackman and Tukey*, 1958] is then applied to this spectral matrix. A basic quantity that can be computed from the real portion of the smoothed spectral matrix, denoted S, is the power spectrum, which is the trace (sum of the diagonal elements) of S. The real portion of the smoothed spectral matrix can be represented as follows [adapted from *C. T. Russell*, unpublished manuscript, 1994], with c terms corresponding to amplitudes of cosines, s terms corresponding to

amplitudes of sines, and *i* indicating a specific frequency in the range between 0 and 2 Hz (the Nyquist frequency of the 4 S/s fast-survey FGM data):

$$S_i = \begin{pmatrix} (c_{ix}^2 + s_{ix}^2) & (c_{ix}c_{iy} + s_{ix}s_{iy}) & (c_{ix}c_{iz} + s_{ix}s_{iz}) \\ (c_{ix}c_{iy} + s_{ix}s_{iy}) & (c_{iy}^2 + s_{iy}^2) & (c_{iy}c_{iz} + s_{iy}s_{iz}) \\ (c_{ix}c_{iy} + s_{ix}s_{iy}) & (c_{iy}c_{iz} + s_{iy}s_{iz}) & (c_{iz}^2 + s_{iz}^2) \end{pmatrix}.$$

For simplicity in referring to *S* later in this section, the above elements are rewritten in the form

$$S_i = \begin{pmatrix} S_{11} & S_{12} & S_{13} \\ S_{21} & S_{22} & S_{23} \\ S_{31} & S_{32} & S_{33} \end{pmatrix},$$

where the subscripts refer to the position of the element in *S* at some frequency. For plotting and visualization of wave power spectra, it may sometimes be useful to also perform a comparison to computed "background" power spectra; this background can be determined by taking the 10^{th} percentile of the power spectra over a sliding interval, similar to the procedure that was performed on the ion flux data. Then, if one subtracts the background spectra from the actual wave power spectra, only the frequencies with wave power significantly above the background remain; this is the process that was taken to obtain the wave spectra presented in Chapter 5 (e.g., Figure 5.1c and 5.2a). This is primarily to aid visualization and not a requirement for performing wave analysis, though this background removal could facilitate more straightforward wave detection for statistical studies.

A.3.2.3 Wave Analysis

Numerous techniques for wave analysis described by *Samson and Olson* [1980] and *Means* [1972] can be applied to the spectral matrix computed from Fourier spectra of magnetic field

time series data; these techniques were previously coded (wavpol.pro) and are included in the THEMIS data analysis software (TDAS) package. TDAS is freely available for download from the THEMIS website (http://themis.ssl.berkeley.edu/software.shtml). This section describes how the combined techniques have been adapted for use in analyses of EMIC wave spectra as presented in this thesis. I note that the computation of degree of polarization and wave ellipticity in wavpol.pro come from *Samson and Olson* [1980] whereas the methods for obtaining wave normal angle and the handedness of the wave come from *Means* [1972].

Following *Samson and Olson* [1980] (hereafter referred to as *SO1980*), an important first step for wave analysis is to compute the degree of polarization, which is similar to coherence in that both degree of polarization (P^2) and coherence provide an indicator of basically the same thing: signal to noise ratio; P^2 values close to 1 are generally preferable. As described by *SO1980*, $P^2 = 1$ indicates that the wave is a "pure state" or a "purely polarized wave" and can be computed by again using only the real portion of the smoothed spectral matrix and the equation

$$P^2 = \frac{n(tr\ S)^2 - (tr\ S^2)}{(n-1)(tr\ S)^2},$$

in which *tr* indicates the trace and $n = 3$ for our case. P^2 can be used as a screening tool to determine the frequencies where the wave power spectra have poor signal to noise ratio and deviate significantly from the purely polarized wave assumption; removal or masking of frequencies with low P^2 (noise) can again aid in the visualization and interpretation of wave spectra. Such masking (e.g., by using NaN flags) has been applied to the plots of P^2 seen in Chapters 2 and 5 (e.g., Figure 5.2b). Once the criterion for masking (e.g., $P^2 < 0.6$) has been determined, the frequencies with low P^2 can also be masked in subsequent wave analysis (wave normal angle, ellipticity, Poynting vector). This procedure for masking of the wave analysis products has also been applied in Chapters 2 and 5 and retains data only for the frequencies with

high P^2 (e.g., Figures 5.2c and 5.2d). Again, this masking can be applied to aid in automated wave detection algorithms, in particular when performing statistical studies of wave phenomena.

The method for estimating the wave normal angle comes from *Means* [1972] and is performed using the information contained in the imaginary part of the smoothed spectral matrix, denoted *I*. The imaginary part of the spectral matrix can also be calculated at each frequency [again adapted from *C. T. Russell*, unpublished manuscript, 1994]

$$I_i = \begin{pmatrix} 0 & (s_{ix}c_{iy} - s_{iy}c_{ix}) & (s_{ix}c_{iz} - s_{iz}c_{ix}) \\ -(s_{ix}c_{iy} - s_{iy}c_{ix}) & 0 & (s_{iy}c_{iz} - s_{iz}c_{iy}) \\ -(s_{ix}c_{iz} - s_{iz}c_{ix}) & -(s_{iy}c_{iz} - s_{iz}c_{iy}) & 0 \end{pmatrix}.$$

Means [1972] showed that the imaginary part of the spectral matrix can be rotated to another coordinate system by similarity transformation and that elements of this rotated matrix can then be used to determine the components of the wave normal vector *k*. Similar to how we have rewritten *S* in simplified form for straightforward referencing to its elements in the calculations for ellipticity shown later, we can also rewrite the imaginary part of the smoothed spectral matrix as

$$I_i = \begin{pmatrix} I_{11} & I_{12} & I_{13} \\ I_{21} & I_{22} & I_{23} \\ I_{31} & I_{32} & I_{33} \end{pmatrix}.$$

Means [1972] described that the components of the wave normal vector can be obtained directly from *I* by using

$$k_x^2 + k_y^2 + k_z^2 = 1,$$
$$\sqrt{I_{12}^2 + I_{13}^2 + I_{23}^2} = ab,$$

and

$$k_x = \frac{I_{23}}{ab} \qquad k_y = \frac{-I_{13}}{ab} \qquad k_z = \frac{I_{12}}{ab}.$$

The wave normal angle can then be calculated from

$$\theta_{WNA} = \arctan\left(\frac{\sqrt{k_x^2 + k_y^2}}{|k_z|}\right),$$

where θ_{WNA} ranges between 0° and 90°.

To obtain an estimate for the wave ellipticity we return to techniques described by *SO1980*. *SO1980* discussed that both the real and imaginary portions of the smoothed spectral matrix (F) can be represented in terms of eigenvalues (λ) and eigenvectors ($\underline{u}$) and that by solving for those eigenvalues and eigenvectors, one can characterize the properties of the wave. For the 3-dimensional data we are concerned with here, the full spectral matrix F can be expanded in the form below, where n = 3 and the * indicates the Hermitian adjoint (or the complex conjugate):

$$F = \sum_{j=1}^{n} \lambda_j \underline{u}_j \underline{u}_j^*.$$

There would then be a series of three vectors in the form $\lambda_j^{1/2}\underline{u}_j$ that represent the information contained in F; the authors referred to these vectors as the state-vectors of F. For a purely polarized wave, a single solution to the first state-vector $\lambda_1^{1/2}\underline{u}_1$ (by obtaining solutions to 5 independent equations, below) would be needed to characterize the wave. The authors described that the solution to the state-vectors can be obtained from the real and imaginary elements of F and put into a standard form ($\lambda_1^{1/2}\underline{u}_1 = \underline{r}_1 + i\underline{r}_2$) to describe the directions and magnitudes of the major ($\underline{r}_1$) and minor ($\underline{r}_2$) axes of the wave polarization ellipse; the magnitudes of $\underline{r}_1$ and $\underline{r}_2$ can then be used to determine the ellipticity of the wave ($\varepsilon = r_2/r_1$). The 5 independent equations for $\lambda_1^{1/2}\underline{u}_1$ are:

$$a_1 = S_{11}^{1/2}$$
$$a_2 \cos\phi_2 = S_{12} / S_{11}^{1/2}$$
$$a_2 \sin\phi_2 = -I_{12} / S_{11}^{1/2}$$
$$a_3 \cos\phi_3 = S_{13} / S_{11}^{1/2}$$
$$a_3 \cos\phi_3 = -I_{13} / S_{11}^{1/2},$$

where the subscripts to S and I are again indicating the elements of the real and imaginary portions of F as simplified above, respectively. The solutions can be rewritten in the form

$$\lambda_1^{1/2} \underline{u}_1^T = [a_1, a_2 \cos\phi_2, a_3 \cos\phi_3] + i[0, a_2 \sin\phi_2, a_3 \sin\phi_3],$$

where ^{T} indicates the transpose. This equation is multiplied by a phase factor (i.e., equations 3 and 4 in *SO1980*) to obtain the solution to $\lambda_1^{1/2}\underline{u}_1$ in the standard form and the ellipticity of a purely polarized wave can then be computed. Because the field fluctuations captured by the THEMIS FGM include a finite amount of noise (P^2 values can be high, e.g., >~0.7 to 0.8, but still deviate from 1), the waves are not purely polarized and therefore solutions to the additional two state-vectors $\lambda_2^{1/2}\underline{u}_2$ and $\lambda_3^{1/2}\underline{u}_3$ (by solving 2 additional sets of 5 independent equations, below) are computed following the procedure above, producing two additional sets of $\underline{r}_1$ and $\underline{r}_2$ that are used to obtain two additional estimates for ellipticity. Note that ` symbols have been added to subscripts of the α and ϕ terms below to differentiate them from the set of 5 equations described above.

$$a_{1`} = S_{22}^{1/2}$$
$$a_{2`} \cos\phi_{2`} = S_{21} / S_{22}^{1/2}$$
$$a_{2`} \sin\phi_{2`} = -I_{21} / S_{22}^{1/2}$$
$$a_{3`} \cos\phi_{3`} = S_{23} / S_{22}^{1/2}$$
$$a_{3`} \cos\phi_{3`} = -I_{23} / S_{22}^{1/2}$$

$$a_{1``} = S_{33}^{1/2}$$
$$a_{2``}\cos\phi_{2``} = S_{31} / S_{33}^{1/2}$$
$$a_{2``}\sin\phi_{2``} = -I_{31} / S_{33}^{1/2}$$
$$a_{3``}\cos\phi_{3``} = S_{32} / S_{33}^{1/2}$$
$$a_{3``}\cos\phi_{3``} = -I_{32} / S_{33}^{1/2}$$

All three estimated ellipticities are computed in wavpol.pro and are averaged to obtain the estimate for ellipticity. This value for ellipticity only tells us whether the wave is elliptically polarized (or linear) but does not give us the handedness of the wave. A couple last steps are required to determine the handedness that comes from $\hat{k}\cdot\hat{B}$ [*Means*, 1972]. By using the relation between the wave vector and the imaginary portion of the spectral matrix, we can determine the perturbation unit vector by

$$\frac{k_z \sin\theta_{WNA}}{\left|k_z \sin\theta_{WNA}\right|},$$

which gives us the sign needed to determine rotation sense so that +1 (−1) indicates right-hand (left-hand) polarization. Lastly, because a polarized wave propagating to the observer is seen by the observer as having a rotation sense opposite to the actual rotation occurring in the frame of the wave, this sign needs to be multiplied by −1 so that we are characterizing the wave's rotation in its own frame. This final value for ellipticity is what is used for all wave cases described within this thesis.

A.3.2.4 Poynting vector spectra

Viewing the Poynting vector spectra alongside the other wave analysis data can provide further information on the wave activity and are particularly relevant for studying the absolute propagation directions of wave energy. The methods described by *Loto'aniu et al*. [2005],

Santolik et al. [2010], and *Li et al*. [2013] have been adapted for describing the waves and their properties in Chapter 5; specific intervals of interest were discussed within Chapter 5. Fourier spectra of the fast-survey FGM and EFI data are used to compute the average Poynting vector as expressed in the equation

$$S_{av} = \frac{1}{4\mu_o}(\delta E^* \times \delta B + \delta E \times \delta B^*),$$

where δE and δB are the real portions of the Fourier electric and magnetic field spectra and * indicates the complex conjugate [after *Loto'aniu et al*., 2005]. *Loto'aniu et al*. [2005] specifically studied the field-aligned component of the Poynting vector (S_z) and noted that S_z was both positive and negative within the EMIC wave source region (MLAT < |11°|).

Three components of the Poynting vector spectra are applied to wave analysis in Chapter 5 because together they provide the total wave energy as well as its dominant propagation angle and direction relative to the mean field, described below. The calculation is performed following the procedures described by *Santolik et al*. [2010] (also see *Li et al*. [2013]) and have been adapted to match the format (same frequency and time resolution) of data output from wavpol.pro so that all the wave properties are presented in the same format. The three components and total Poynting vector spectra are calculated from

$$S_x = \frac{1}{\mu_o}(\delta E_y \times \delta B_z^* - \delta E_z \times \delta B_y^*)$$

$$S_y = -\frac{1}{\mu_o}(\delta E_x \times \delta B_z^* - \delta E_z \times \delta B_x^*)$$

$$S_z = \frac{1}{\mu_o}(\delta E_x \times \delta B_y^* - \delta E_y \times \delta B_x^*)$$

$$S_{tot} = \sqrt{S_x^2 + S_y^2 + S_z^2},$$

and the wave energy propagation angle (θ_S) is calculated from

$$\theta_S = \arctan\left(\frac{\sqrt{S_x^2 + S_y^2}}{S_z}\right),$$

where θ_S ranges between 0° and 180° [after *Santolik et al*., 2010]. An example of the calculation of the Poynting vector from Fourier electric and magnetic field spectra is present in the TDAS crib thm_crib_poynting_flux.pro following procedures similar to those described by *Santolik et al*. [2010]. I have also prepared a version of the code that incorporates all the above wave analysis methods into a single routine. This routine will be considered for inclusion in future releases of the TDAS package.

APPENDIX B

Supplemental material on low-energy ion compositional properties

B.1 Recompilation of low-energy ion properties for wave applications

As noted in Chapter 5, the low-energy ion densities and temperatures data products that were obtained from the global multi-spacecraft study on low-energy ion species (Chapter 3) were recompiled into tabular (Tables B.1–B.4), bar plot (Figures B.1–B.4), and have also been re-plotted in modified spatial distribution formats (Figures B.5–B.14) to facilitate their application to the work presented in Chapter 5 and to future wave studies.

Table B.1: Median low-energy ion density (cm^{-3}).

		L: 7–9 R_E	L: 9–11 R_E	L: 11–13 R_E
Protons	00 - 03 MLT	0.07	0.06	0.09
	03 - 06 MLT	0.15	0.14	0.12
	06 - 09 MLT	0.28	0.19	0.13
	09 - 12 MLT	0.99	0.40	0.26
	12 - 15 MLT	1.91	1.08	0.94
	15 - 18 MLT	1.88	0.77	0.50
	18 - 21 MLT	0.19	0.13	0.13
	21 - 24 MLT	0.08	0.07	0.07
Helium ions	00 - 03 MLT	0.10	0.10	0.10
	03 - 06 MLT	0.13	0.08	0.09
	06 - 09 MLT	0.23	0.10	0.09
	09 - 12 MLT	0.30	0.13	0.10
	12 - 15 MLT	0.24	0.12	0.11
	15 - 18 MLT	0.18	0.12	0.09
	18 - 21 MLT	0.10	0.07	0.07
	21 - 24 MLT	0.11	0.08	0.08
Oxygen ions	00 - 03 MLT	0.17	0.14	0.10
	03 - 06 MLT	0.18	0.07	0.10
	06 - 09 MLT	0.33	0.11	0.08
	09 - 12 MLT	0.33	0.10	0.08
	12 - 15 MLT	0.13	0.05	0.05
	15 - 18 MLT	0.13	0.06	0.06
	18 - 21 MLT	0.10	0.09	0.11
	21 - 24 MLT	0.14	0.12	0.11

Table B.2: Median low-energy ion temperature (eV).

		L: 7–9 R_E	L: 9–11 R_E	L: 11–13 R_E
Protons	00 - 03 MLT	7.5	8.8	8.7
	03 - 06 MLT	5.3	7.6	10.1
	06 - 09 MLT	8.2	9.4	12.3
	09 - 12 MLT	4.7	5.0	7.0
	12 - 15 MLT	1.7	1.9	2.3
	15 - 18 MLT	1.1	2.2	3.2
	18 - 21 MLT	3.4	4.7	4.7
	21 - 24 MLT	6.0	5.6	5.7
Helium ions	00 - 03 MLT	42.9	51.8	40.2
	03 - 06 MLT	21.1	21.5	32.7
	06 - 09 MLT	53.4	32.1	35.9
	09 - 12 MLT	19.8	20.2	24.9
	12 - 15 MLT	9.9	9.4	10.2
	15 - 18 MLT	10.0	10.4	12.7
	18 - 21 MLT	18.4	21.9	18.2
	21 - 24 MLT	50.2	43.5	47.2
Oxygen ions	00 - 03 MLT	169.3	178.6	144.4
	03 - 06 MLT	121.2	51.7	49.7
	06 - 09 MLT	292.8	139.6	82.0
	09 - 12 MLT	249.5	109.3	116.8
	12 - 15 MLT	82.4	32.2	38.0
	15 - 18 MLT	40.4	40.7	65.5
	18 - 21 MLT	91.7	104.8	136.3
	21 - 24 MLT	200.0	194.4	194.3

Table B.3: Median low-energy heavy ion density ratios (n_s/n_{H+}).

		L: 7–9 R_E	L: 9–11 R_E	L: 11–13 R_E
Helium ions	00 - 03 MLT	1.39	1.58	1.16
	03 - 06 MLT	0.87	0.57	0.72
	06 - 09 MLT	0.81	0.51	0.67
	09 - 12 MLT	0.30	0.33	0.39
	12 - 15 MLT	0.13	0.11	0.12
	15 - 18 MLT	0.09	0.15	0.19
	18 - 21 MLT	0.53	0.52	0.57
	21 - 24 MLT	1.27	1.15	1.24
Oxygen ions	00 - 03 MLT	2.33	2.20	1.15
	03 - 06 MLT	1.19	0.51	0.80
	06 - 09 MLT	1.17	0.59	0.65
	09 - 12 MLT	0.33	0.25	0.30
	12 - 15 MLT	0.07	0.05	0.05
	15 - 18 MLT	0.07	0.08	0.12
	18 - 21 MLT	0.53	0.70	0.81
	21 - 24 MLT	1.71	1.59	1.62

Table B.4: Median low-energy heavy ion temperature ratios (T_s/T_{H+}).

		L: 7–9 R_E	L: 9–11 R_E	L: 11–13 R_E
Helium ions	00 - 03 MLT	5.7	5.9	4.6
	03 - 06 MLT	4.0	2.8	3.2
	06 - 09 MLT	6.5	3.4	2.9
	09 - 12 MLT	4.2	4.1	3.5
	12 - 15 MLT	5.7	4.9	4.4
	15 - 18 MLT	9.5	4.8	4.0
	18 - 21 MLT	5.4	4.7	3.8
	21 - 24 MLT	8.4	7.7	8.3
Oxygen ions	00 - 03 MLT	22.5	20.4	16.6
	03 - 06 MLT	23.0	6.8	4.9
	06 - 09 MLT	35.8	14.9	6.6
	09 - 12 MLT	53.4	22.1	16.6
	12 - 15 MLT	47.4	16.7	16.4
	15 - 18 MLT	38.3	18.6	20.7
	18 - 21 MLT	26.7	22.4	28.8
	21 - 24 MLT	33.6	34.5	34.1

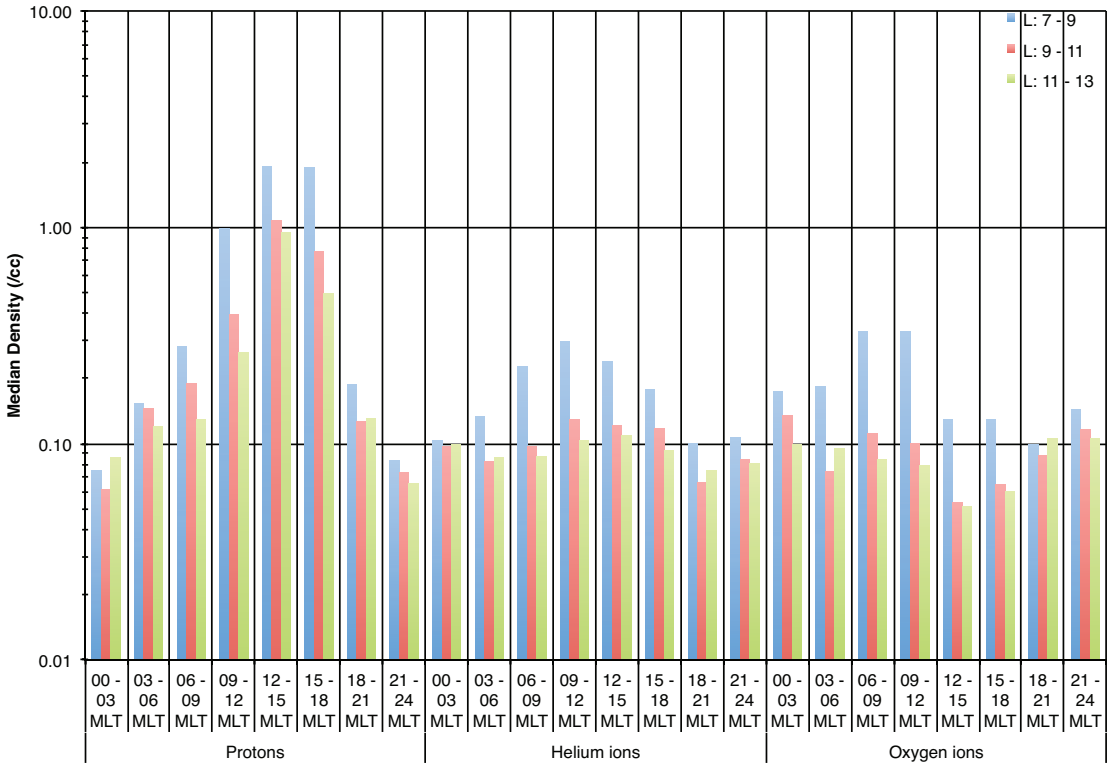

Figure B.1: Median low-energy ion density (cm^{-3}).

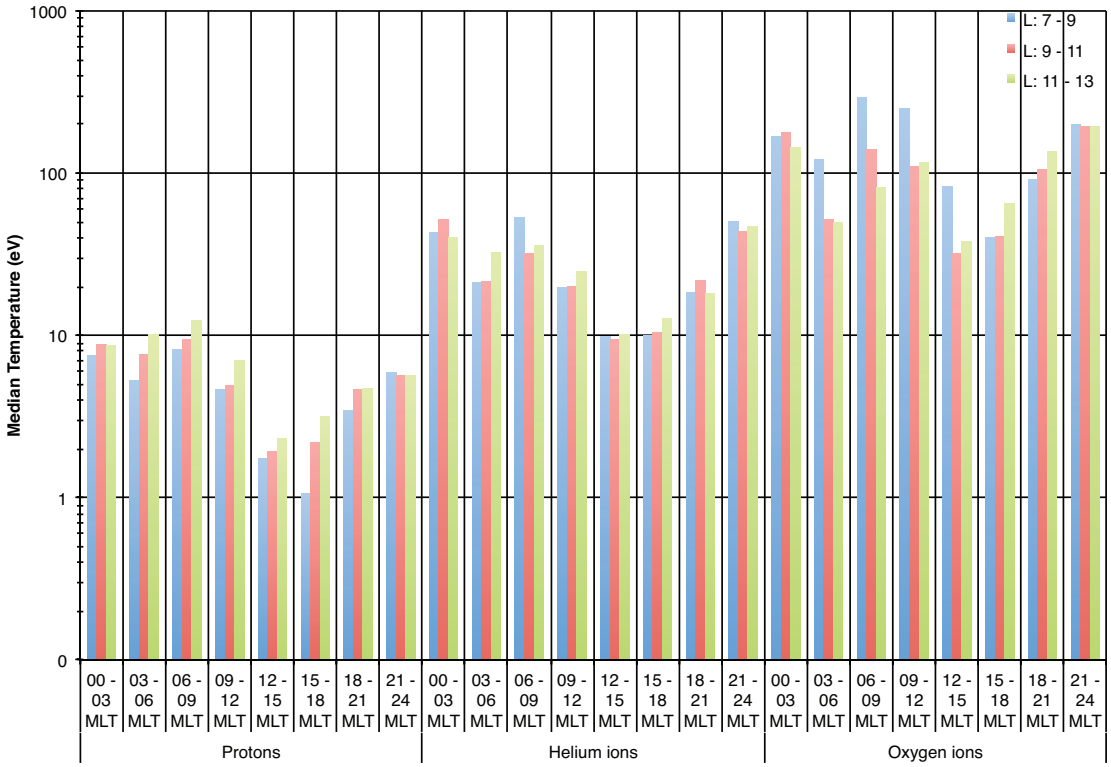

Figure B.2: Median low-energy ion temperature (eV).

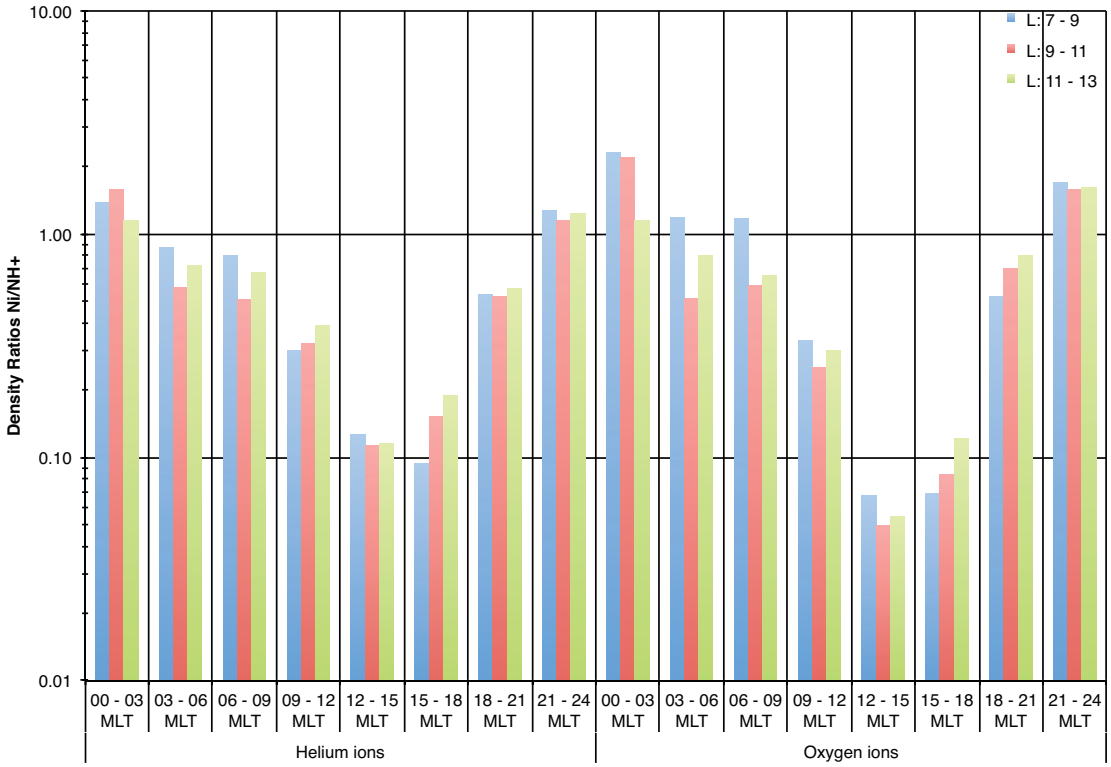

Figure B.3: Median low-energy heavy ion density ratios (n_s/n_{H+}).

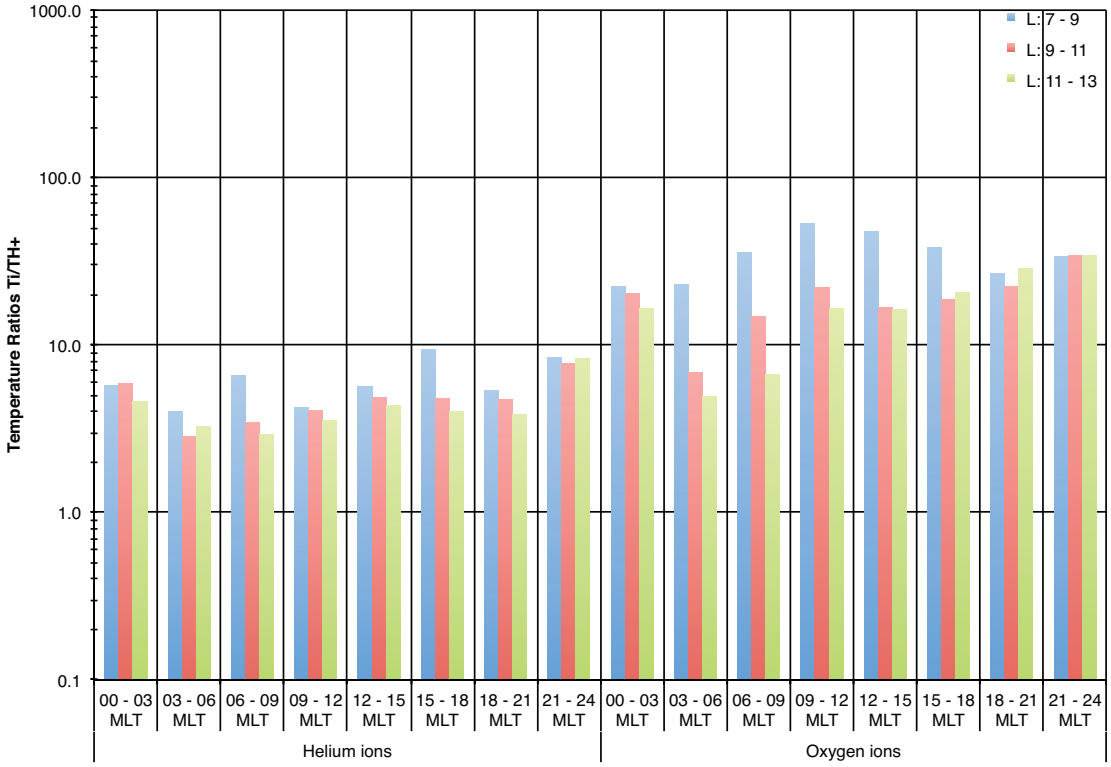

Figure B.4: Median low-energy heavy ion temperature ratios (T_s/T_{H+}).

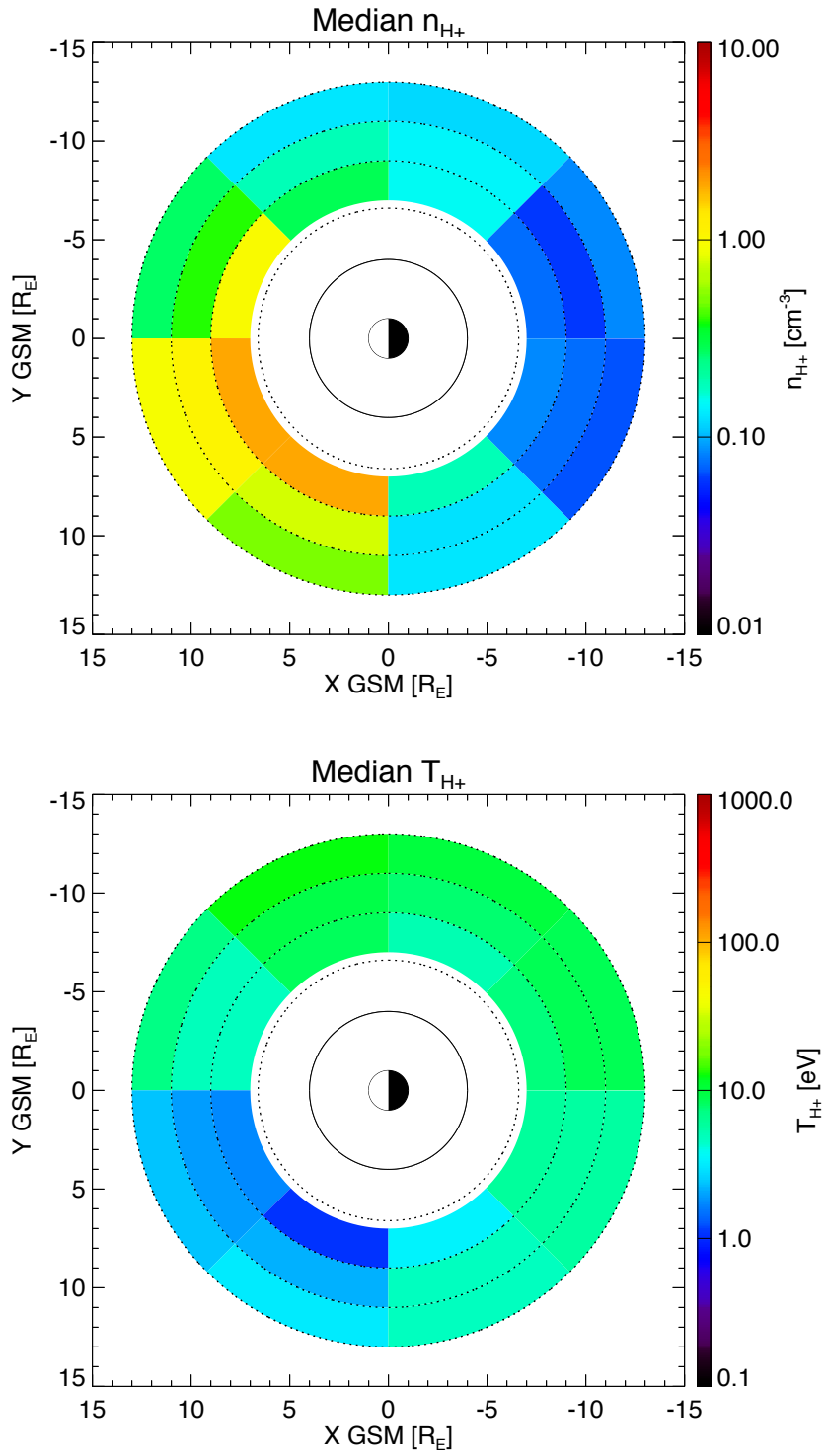

Figure B.5: Median H^+ density and temperature. The properties are plotted over the radial distance range 7–13 R_E and have been binned into 2 R_E by 3 hr MLT bins. The innermost dotted circle is geosynchronous distance (6.6 R_E).

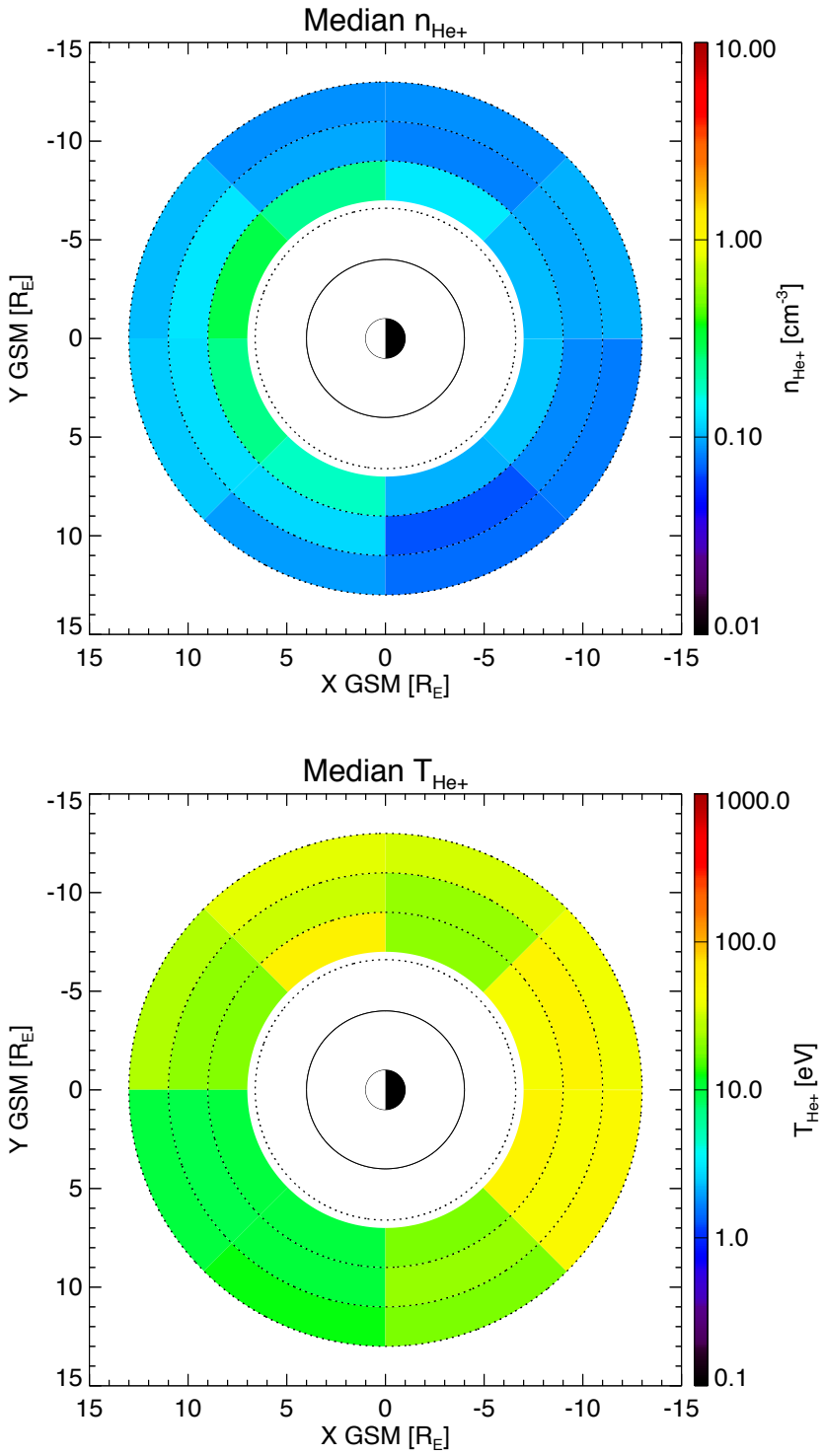

Figure B.6: Median He^+ density and temperature.

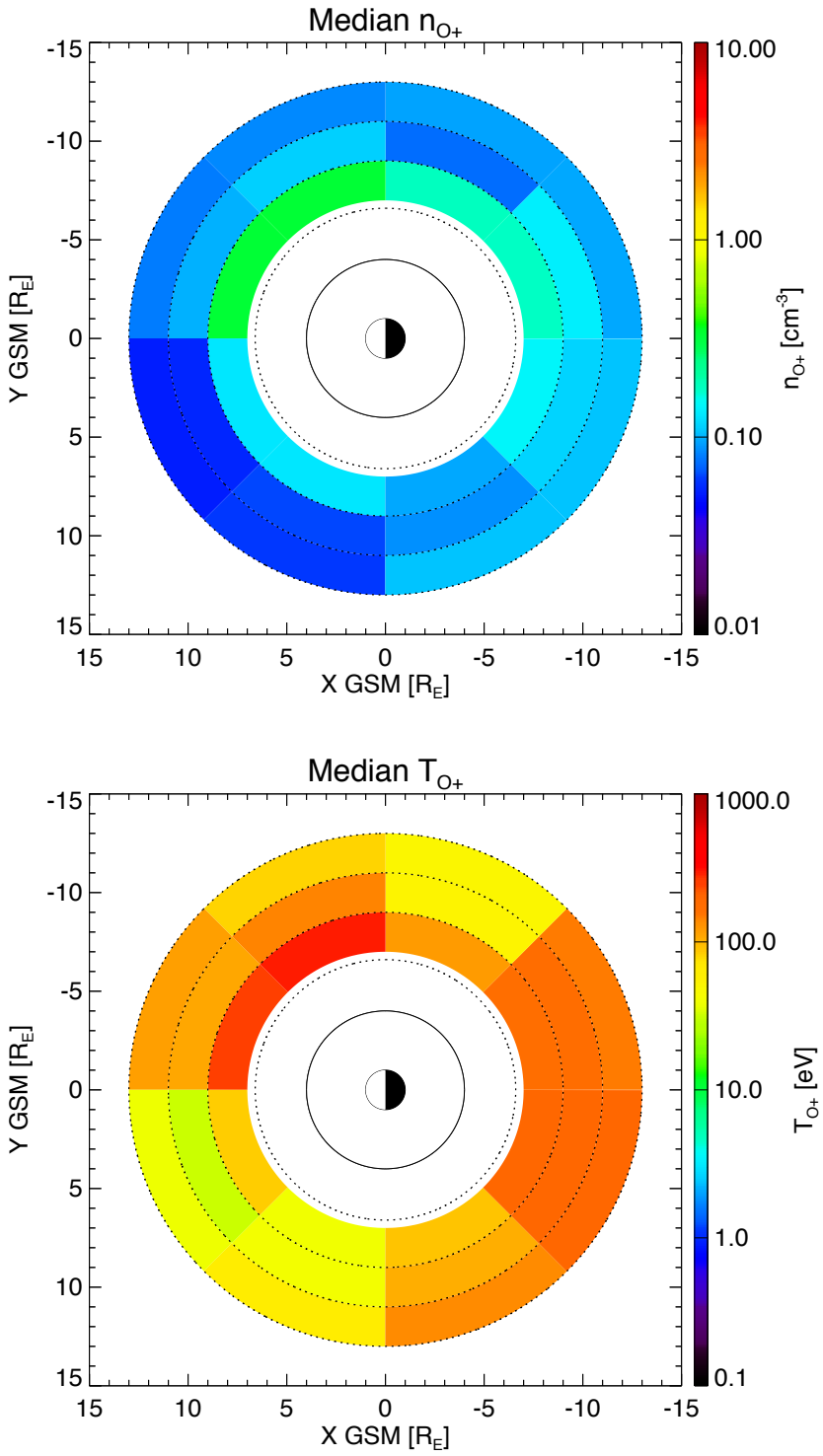

Figure B.7: Median O^+ density and temperature.

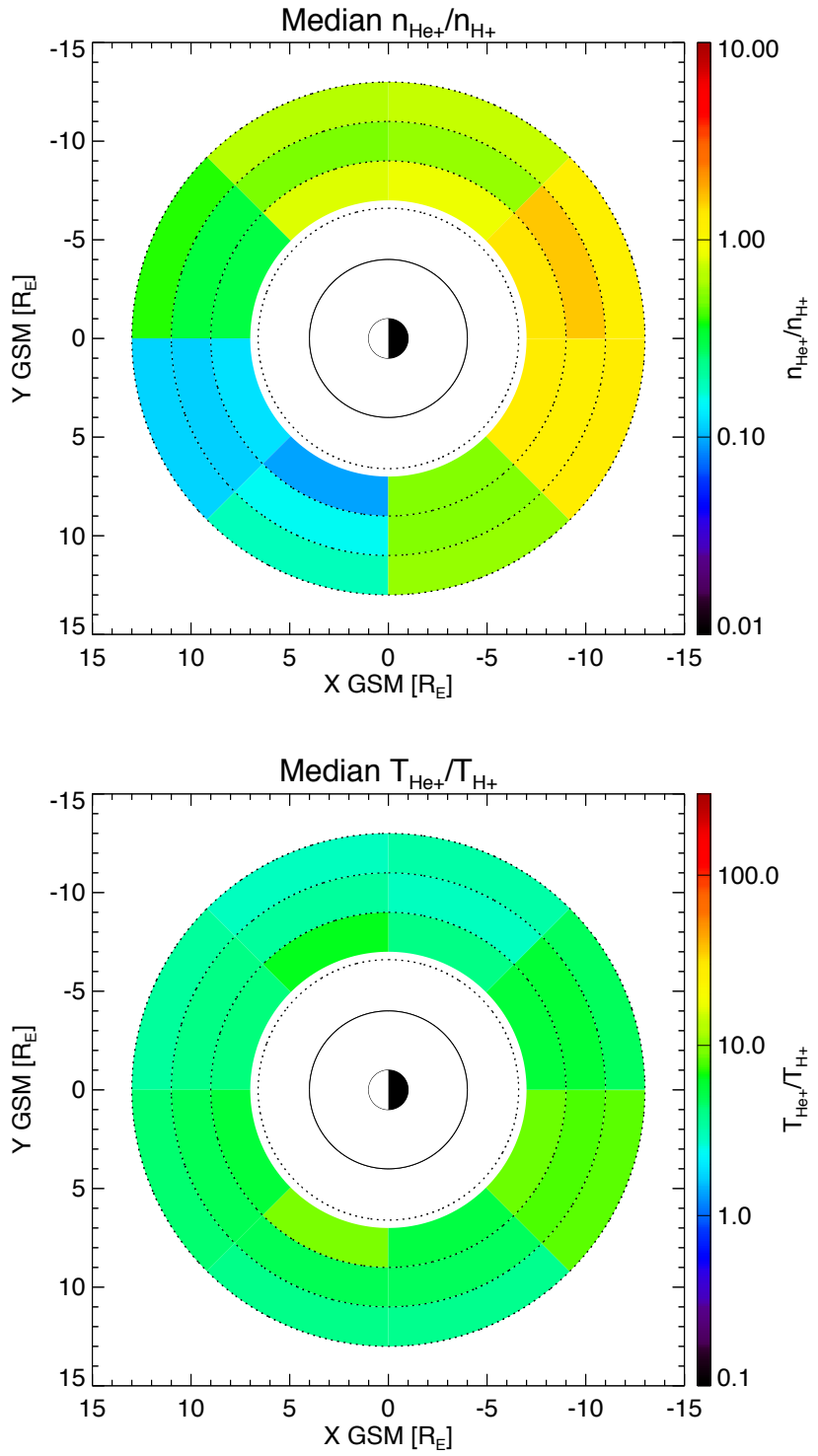

Figure B.8: Median n_{He+}/n_{H+} density ratio and T_{He+}/T_{H+} temperature ratio.

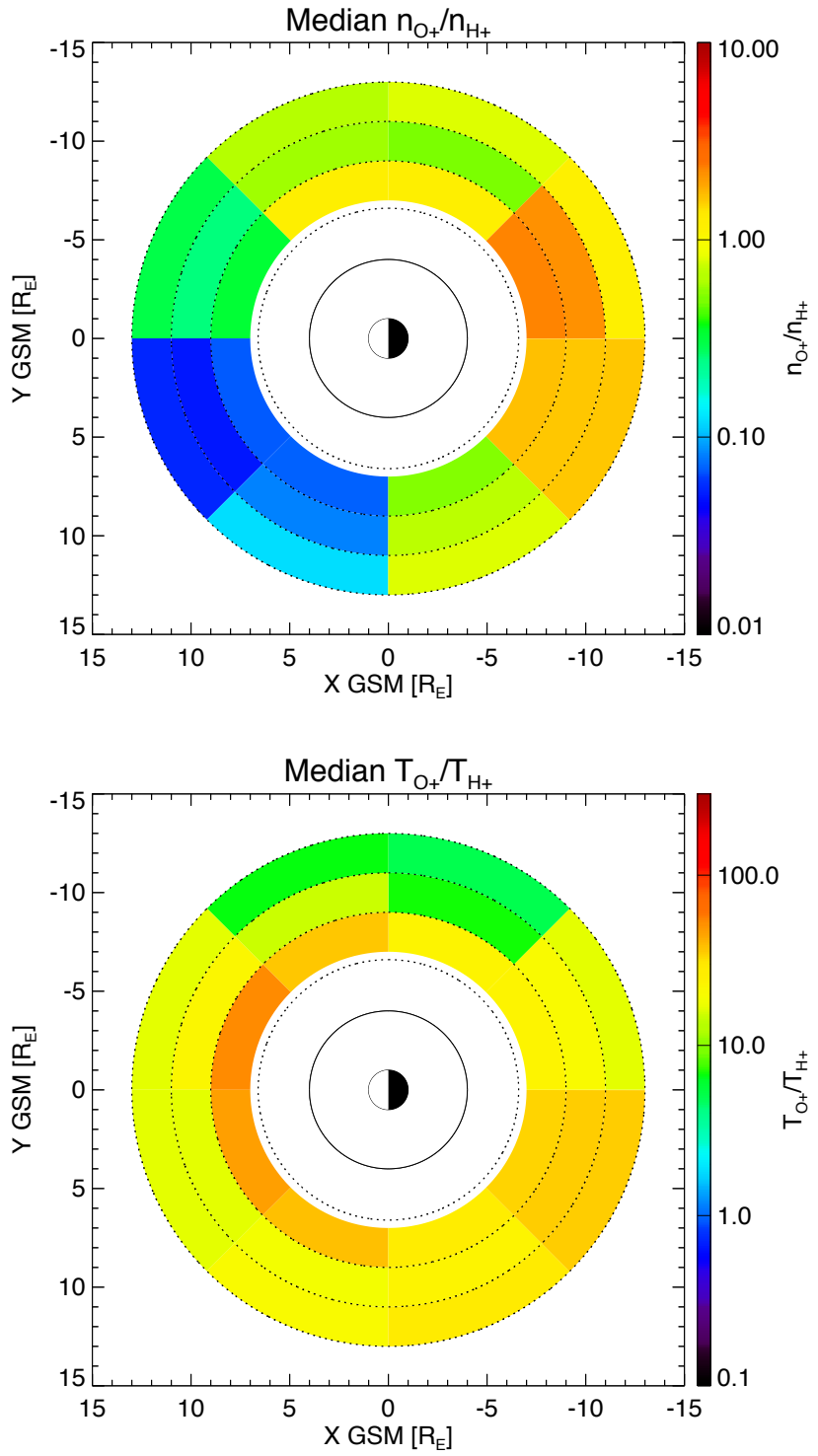

Figure B.9: Median n_{O+}/n_{H+} density ratio and T_{O+}/T_{H+} temperature ratio.

B.2 Comparison of statistical low-energy ion properties to previous observations

Table B.5 shows the compositional properties of low-energy ions at geocentric distances greater than ~7 R_E as presented in previous studies is included for comparison to the properties deduced using the multi-component fitting method; in some previous studies both the parallel and perpendicular temperatures are given and the temperature shown in the table is computed from $T_s = (2/3)T_{perp} + (1/3)T_{par}$. I note that Table B.5 is likely not exhaustive. An effort was made to search for additional sources for comparison and those that were found are shown.

In most cases the composition was inferred through some model fit made to the data. *Anderson and Fuselier* [1994] (in fig. 8) presented multiple samples of He^+ compositional properties obtained during "quiet" and "active" EMIC wave events; a few of these were selected and input into Table B.5 to represent the range of values that were inferred through the CCE retarding potential analyzer; the values for n_{He+}/n_{H+} and T_{He+}/T_{H+} in Table B.5 are approximate and obtained by reading the values directly off the figure presented in *Anderson and Fuselier* [1994]. The exclamation marker superscript indicates the He^+ properties that were inferred during an active EMIC wave event. The asterisks in the table (i.e., *Anderson et al*., [1996]) indicate when values were below the detection threshold of the instrument and values appearing in parentheses (i.e., *Chen and Moore*, [2004]) indicate an average value. In some cases only the proton properties were presented.

A spread of values is seen in the He^+ concentration. At times the He^+ concentration is indeed low and indicates that He^+ is a minority ion component. But high concentrations were also seen and in a few cases this concentration exceeded 1.0.

Table B.5: Values for low-energy ion composition determined by previous spacecraft missions at L > 7 R_E.

				Protons		Helium ions	
	Spacecraft	L	MLT	n_{H+} (cm^{-3})	T_{H+} (eV)	n_{He+}/n_{H+}	T_{He+}/T_{H+}
Anderson and Fuselier [1994]	AMPTE/CCE	>7 R_E	13	--	6.1!	--	21.2!
		~9 R_E	8	--	4.9	--	0.3
		>7 R_E	Dayside	--	--	0.01	0.1
				--	--	0.01!	0.2!
				--	--	0.03	0.3
				--	--	0.02!	0.6!
				--	--	0.06	0.9
				--	--	0.25!	0.9!
				--	--	2.33	6.0
				--	--	1.50!	10.0!
Anderson et al. [1996]	AMPTE/CCE	8.6 R_E	12.6	0.05	--	1.29	--
		8.1 R_E	12.4	0.02	--	0.17	--
		8.9 R_E	6.6	0.11	--	<0.002*	--
		9.0 R_E	7	0.56	--	<0.002*	--
Seki et al. [2003]	Geotail	~9 R_E	Nightside	~0.2	--	--	--
Chandler and Moore [2003]	Polar	~9 R_E	Dayside	24.0	0.3	--	--
				68.0	0.5	--	--
				14.0	0.3	--	--
				2.8	1.1	--	--
				0.1	2.3	--	--
				24.0	0.2	--	--
				16.0	1.5	--	--
Chen and Moore [2004]	Polar	~9 R_E	Dayside	1.4−102 (7.8)	0.6−2.5 (1.3)	0−0.125 (0.011)	--
				1.9	0.9	0.52	--
				24.0	1.0	0.34	--

B.3 Supporting statistical information

The last collection of figures in this section are multiple sets of the spatial distribution plots presented side-by-side to provide a comparison of the low-energy properties obtained for different X^2 thresholds (using the X^2 values obtained following each multi-component fit) and also additional figures of the low-energy ion parameters that have been binned into additional distributions to facilitate further interpretation of the statistics.

B.3.1 Spatial distributions

Sets of the spatial distributions of low-energy ion density and temperature (Figures B.10–B.19) produced from the parameters deduced from fits with low X^2 (<100) are compared alongside the spatial distributions produced including the fits with higher X^2 (<10000), where the X^2 value is obtained through the fitting routine following minimization of the deviations between the multi-component Maxwellian energy flux fit and the data (in units of energy flux, eV/cm^2-s-sr-eV). The MLT bin size has been further reduced (to 1.5 hr bins) to better show any differences between the properties at different X^2 thresholds. The statistical low-energy ion properties presented in Chapter 3 were determined using the properties inferred from all fits that successfully converged; there was no discrimination for low or high X^2 since high X^2 could be observed if, for example, the assumed H^+ and He^+ components could be fitted to the data but the fit to fluxes at higher energies (assumed to be O^+) was not successful. By comparing the low and high X^2 distributions it is evident that the trends remain similar. The low X^2 spatial distributions tend to show slightly lower densities and higher temperatures in comparison to the higher X^2 distributions.

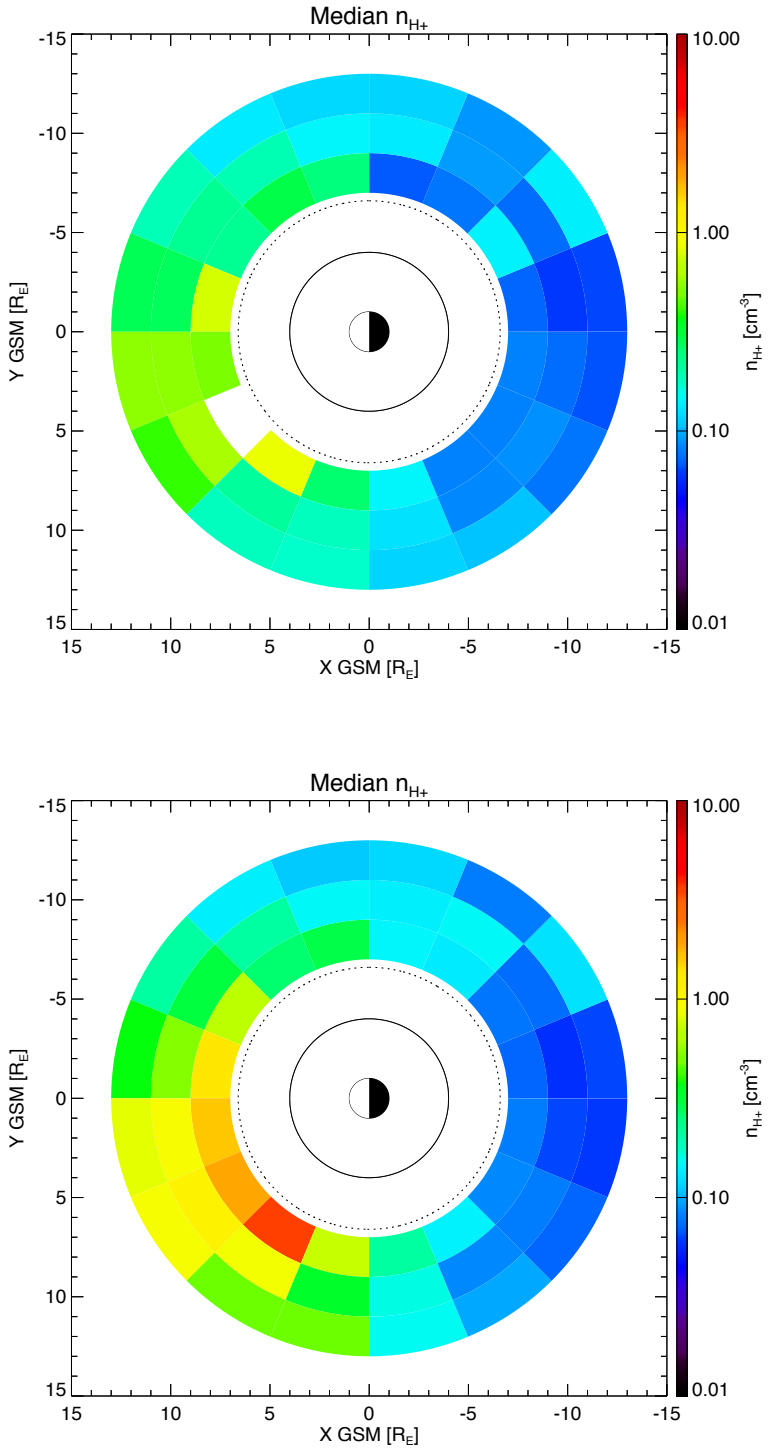

Figure B.10: Spatial distributions of median H^+ density for (top) low X^2 and (bottom) high X^2.

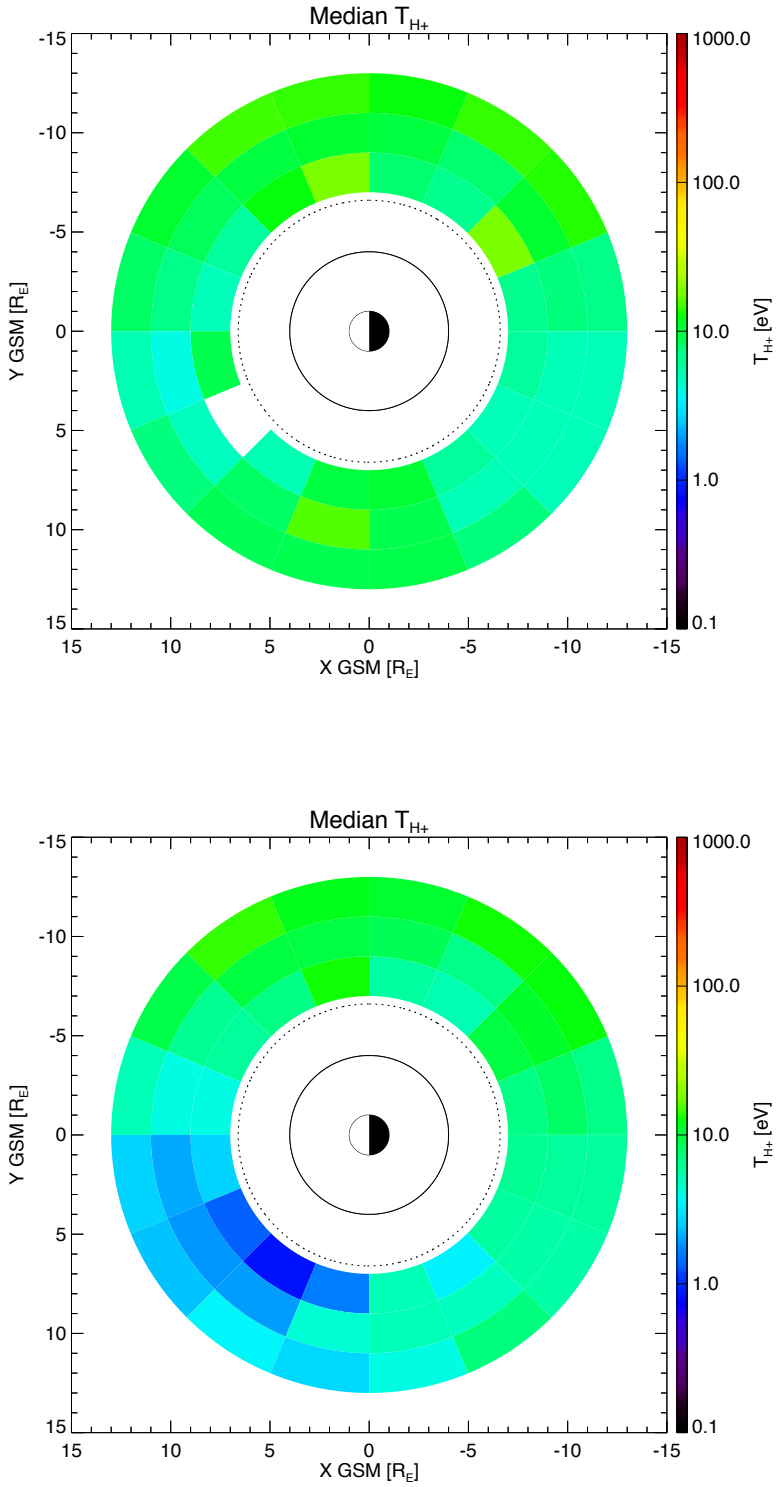

Figure B.11: Spatial distributions of median H^+ temperature for (top) low X^2 and (bottom) high X^2.

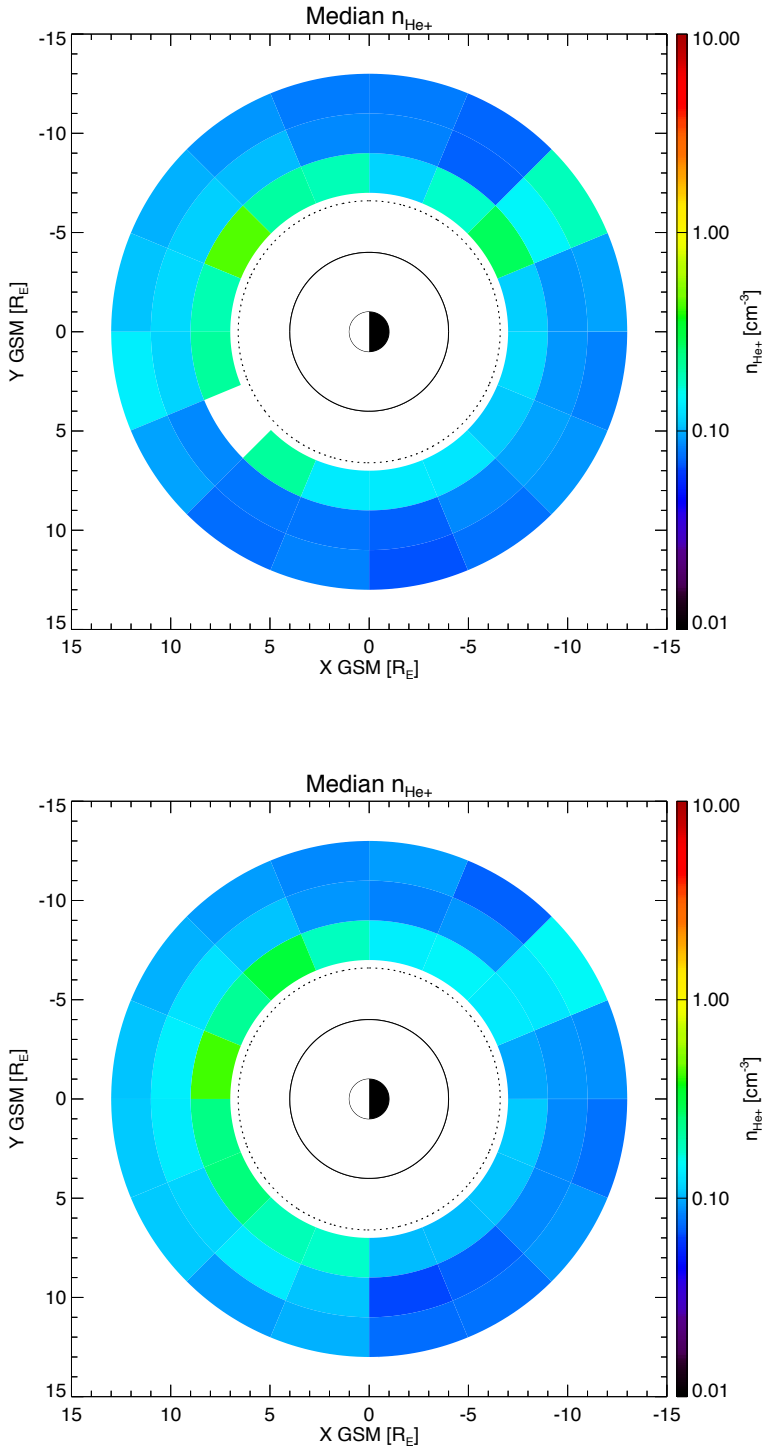

Figure B.12: Spatial distributions of median He^+ density for (top) low X^2 and (bottom) high X^2.

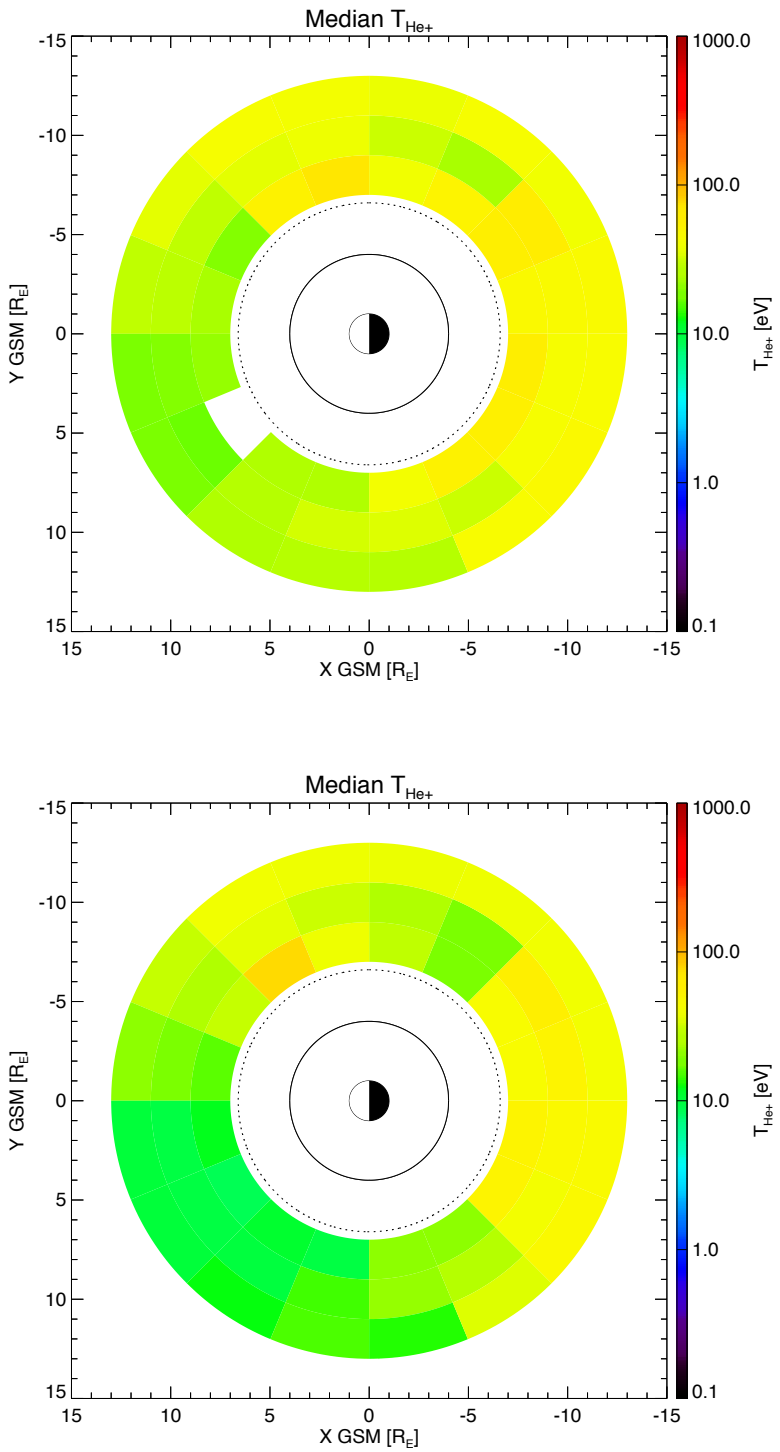

Figure B.13: Spatial distributions of median He^+ temperature for (top) low X^2 and (bottom) high X^2.

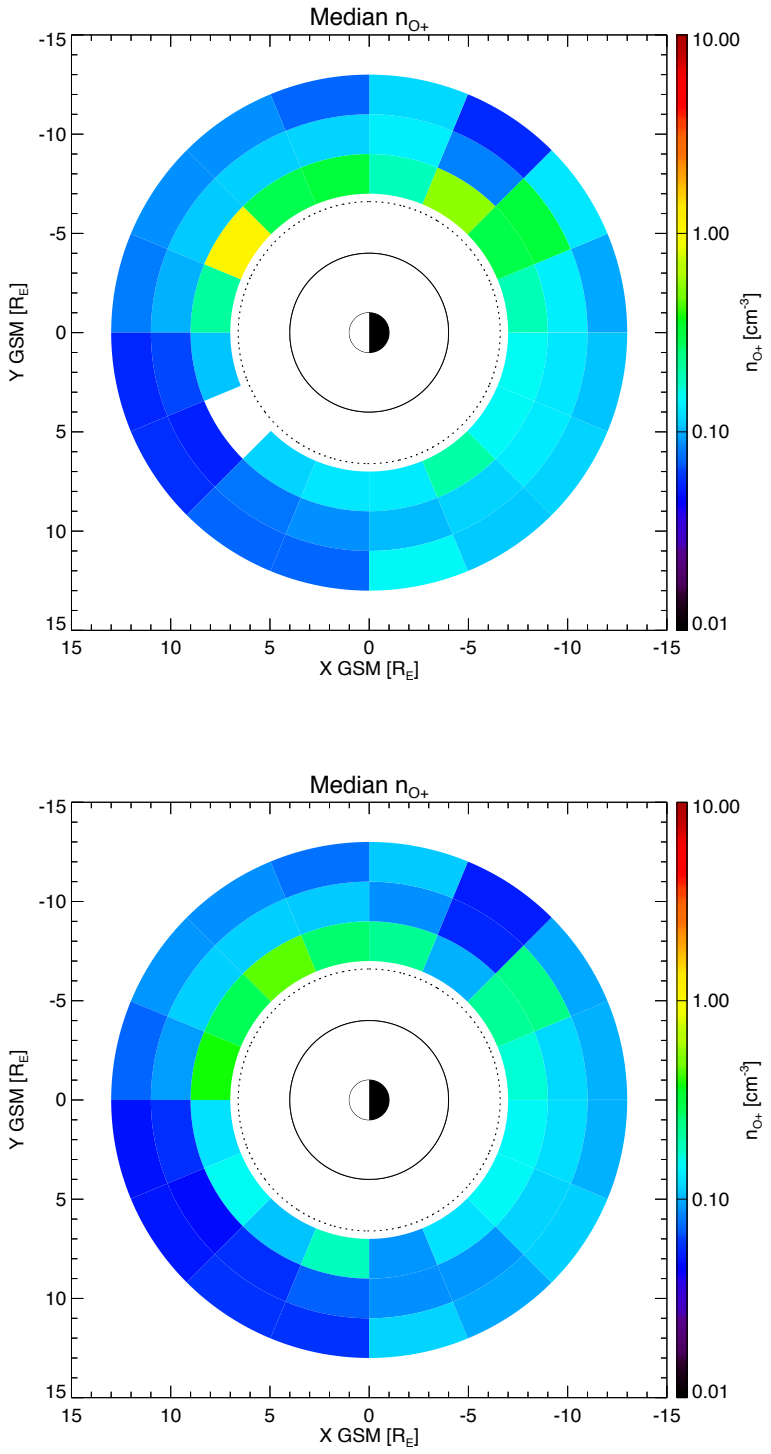

Figure B.14: Spatial distributions of median O^+ density for (top) low X^2 and (bottom) high X^2.

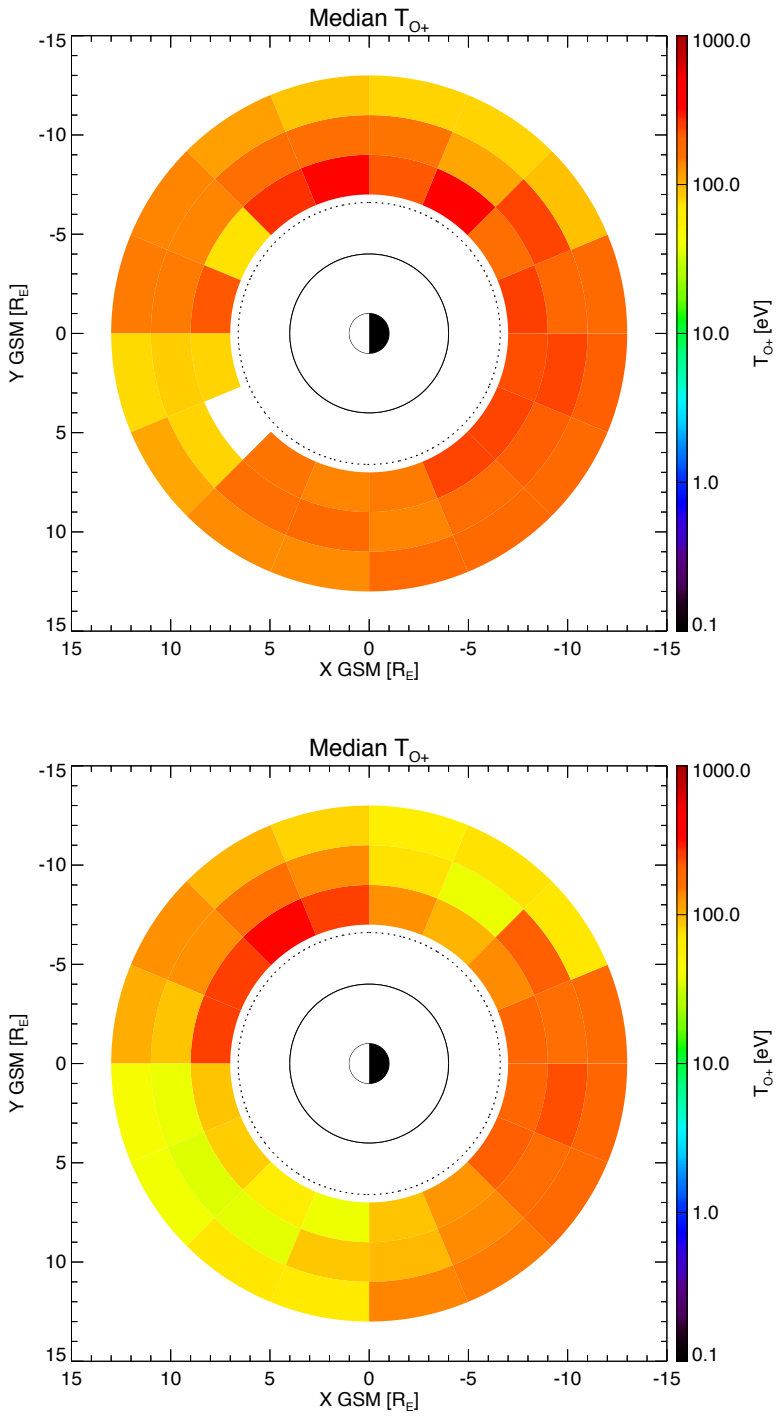

Figure B.15: Spatial distributions of median O^+ temperature for (top) low X^2 and (bottom) high X^2.

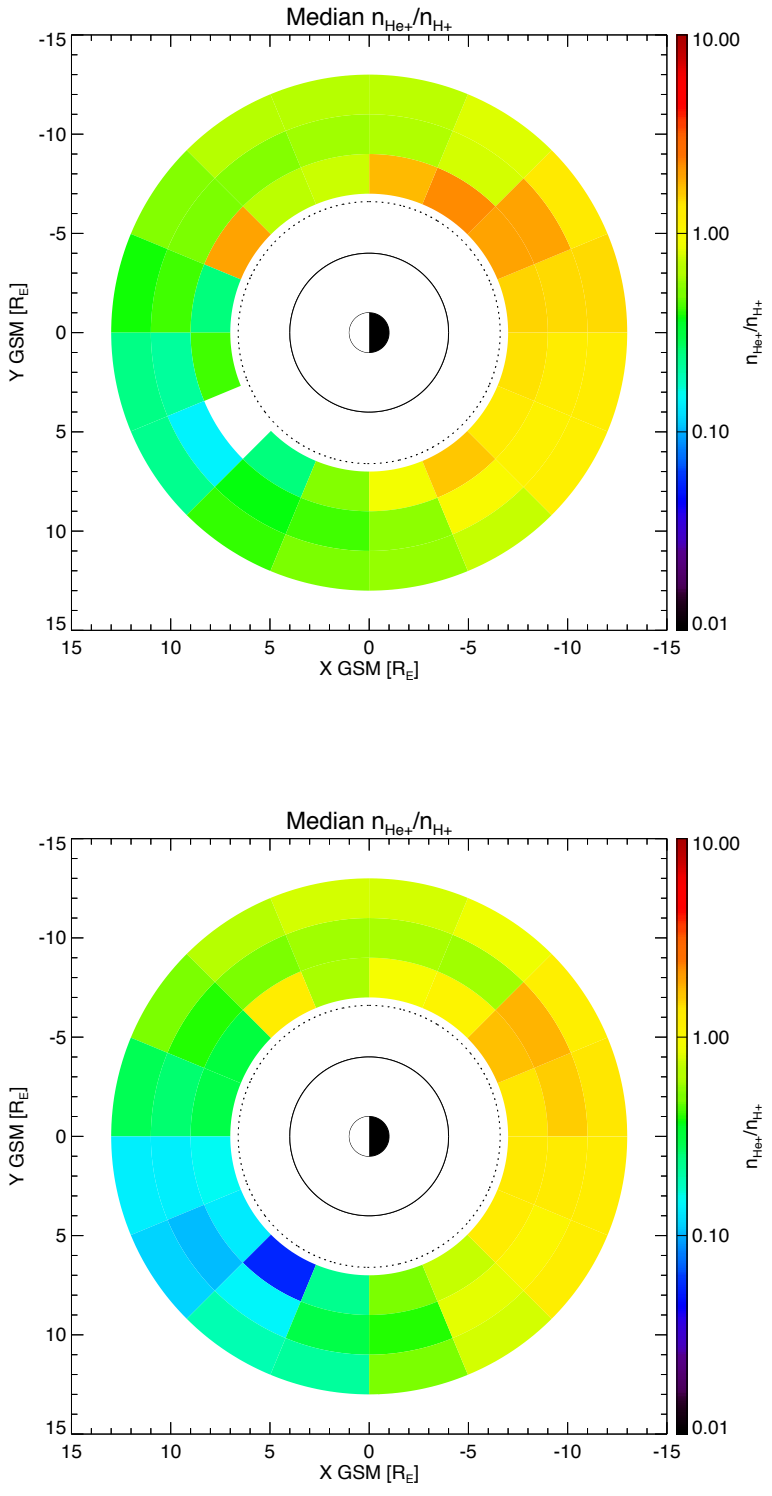

Figure B.16: Spatial distributions of median He^+ to H^+ density ratios for (top) low X^2 and (bottom) high X^2.

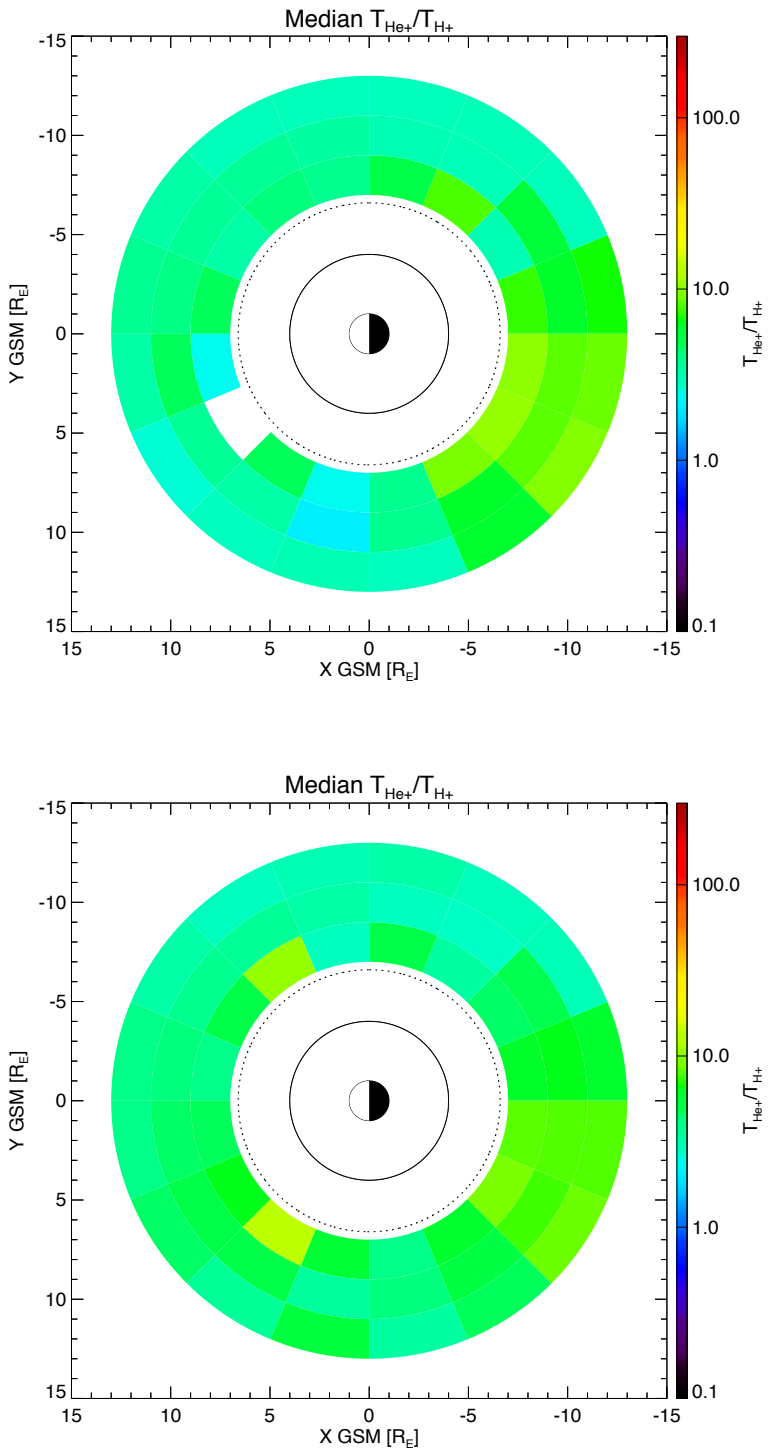

Figure B.17: Spatial distributions of median He^+ to H^+ temperature ratios for (top) low X^2 and (bottom) high X^2.

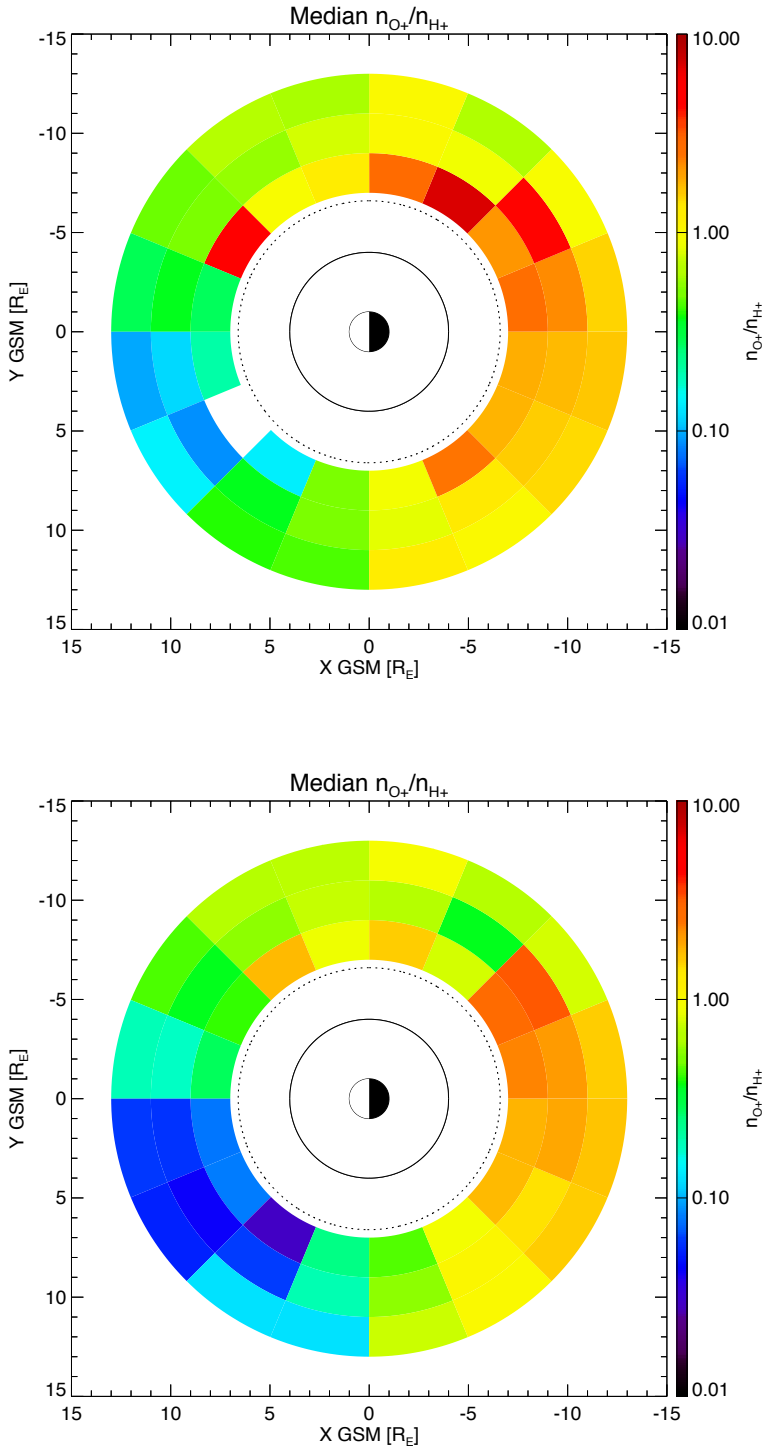

Figure B.18: Spatial distributions of median O^+ to H^+ density ratios for (top) low X^2 and (bottom) high X^2.

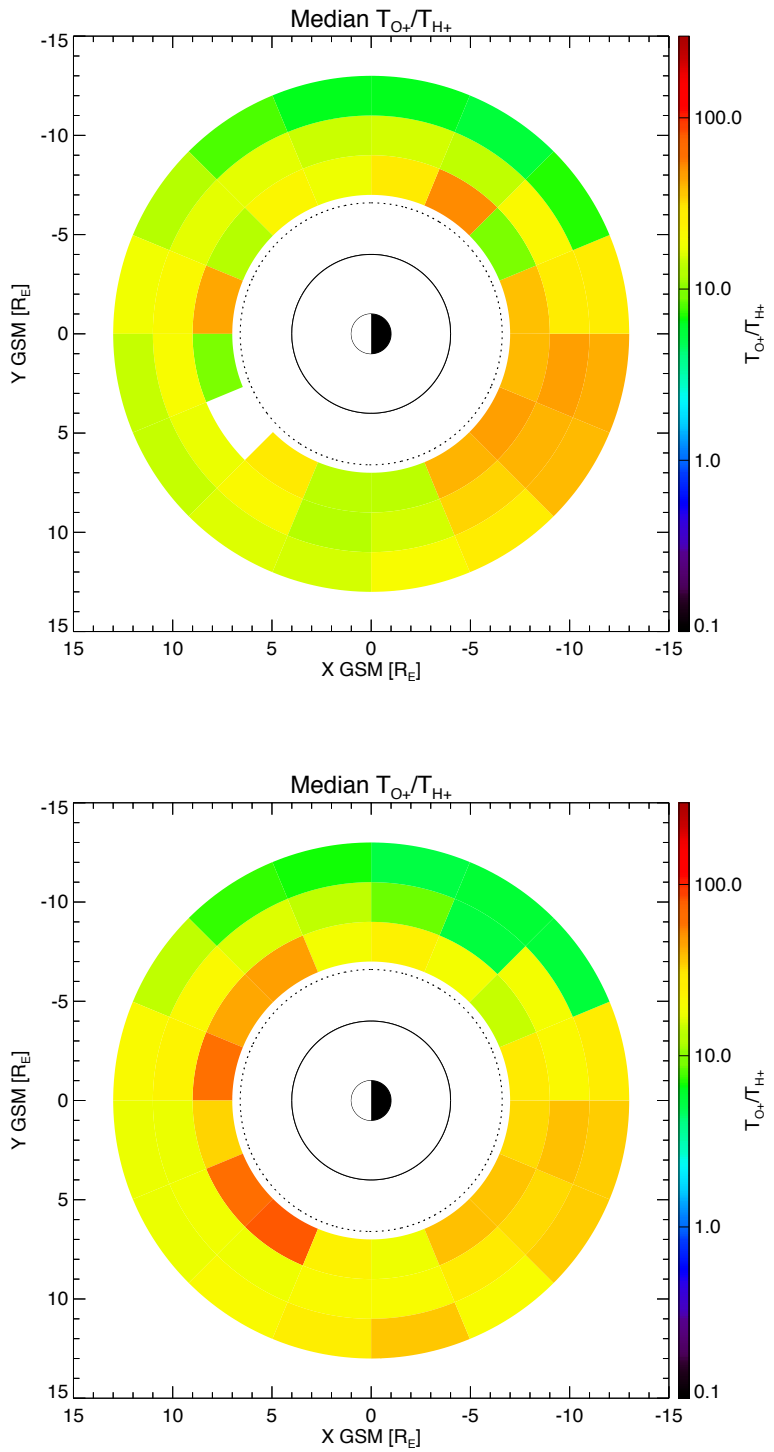

Figure B.19: Spatial distributions of median O^+ to H^+ temperature ratios for (top) low X^2 and (bottom) high X^2.

B.3.2 Binning of separate quantities

Some additional comparisons were performed to observe whether the ion properties, when viewed in different formats, showed more obvious dependencies. A comparison was made between the ion temperatures to determine whether temperature was directly proportional to mass number. Because the fits were obtained during bulk plasma flows, the ion temperatures were binned with respect to flow velocity. The low-energy ion temperatures were binned into velocity bins at 5 km/s increments over the velocity range 10 to 400 km/s and then the means, medians, and standard deviations of the means were computed; only the bins with more than 10 samples are plotted, where a sample is one temperature value deduced from a successful fit. Figure B.20 shows the number of ion temperature samples within each velocity bin. The ion temperature ratios were investigated by taking the ratios of the medians and averages of one ion's temperatures with respect to another ion's, as shown in Figures B.21–B.23. Although O^+ temperatures were generally the warmest of the three ion species, its temperature ratio with respect to the other ions was not directly proportional to mass number, i.e., $\langle T_{O^+} \rangle / \langle T_{He^+} \rangle \neq A_{O^+}(16)/A_{He^+}(4)$; the mass number ratio of 4 is indicated with the horizontal dashed line in Figure B.21. Further comparisons between O^+ and H^+ (ratio of 16) as well as He^+ and H^+ (ratio of 4) are shown in Figures B.22 and B.23, respectively. A temperature ratio near but below 4 is seen for median T_{He^+}/T_{H^+} in the flow velocity range between ~75 and 110 km/s.

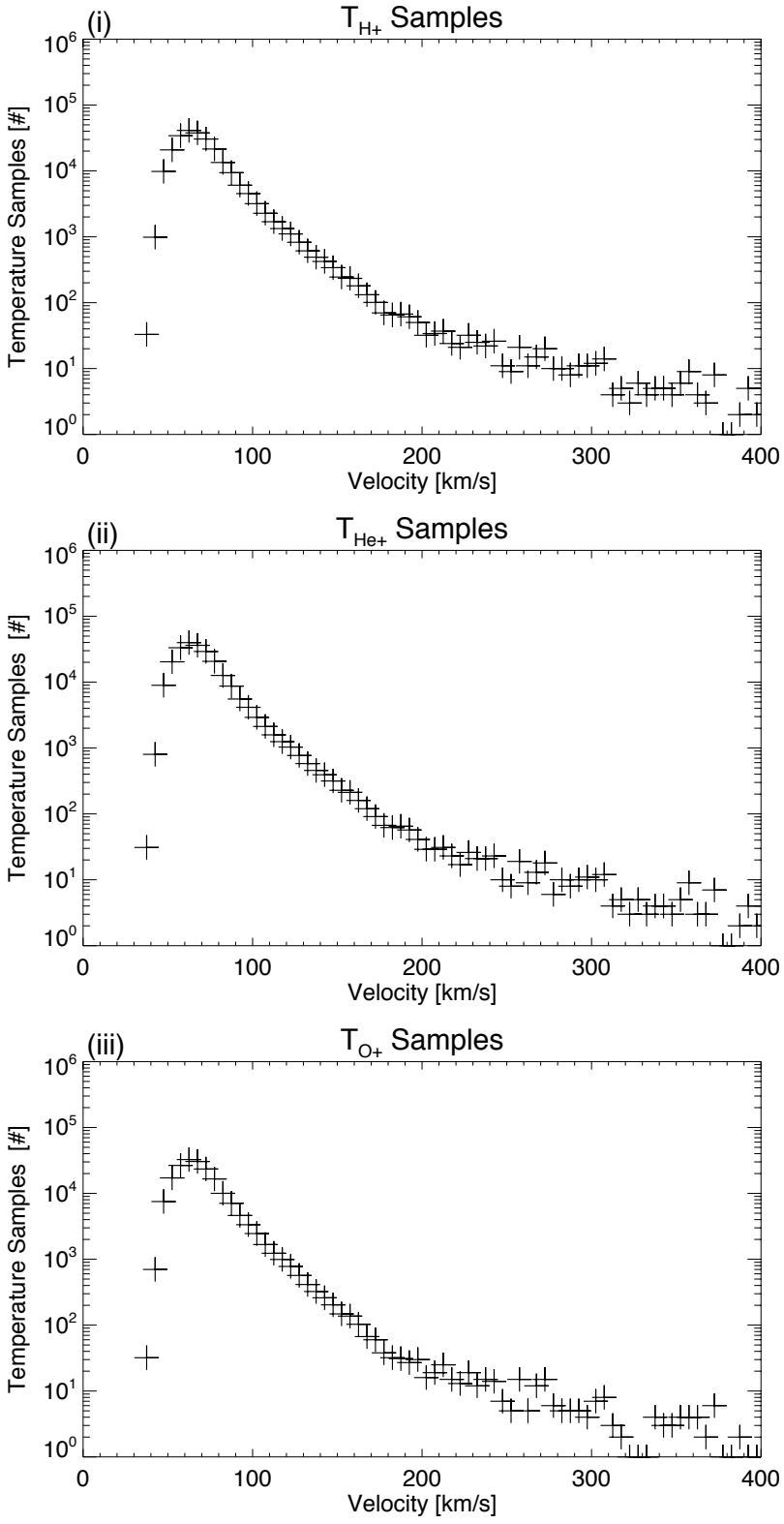

Figure B.20: Number of temperature samples in each 5 km/s velocity bin.

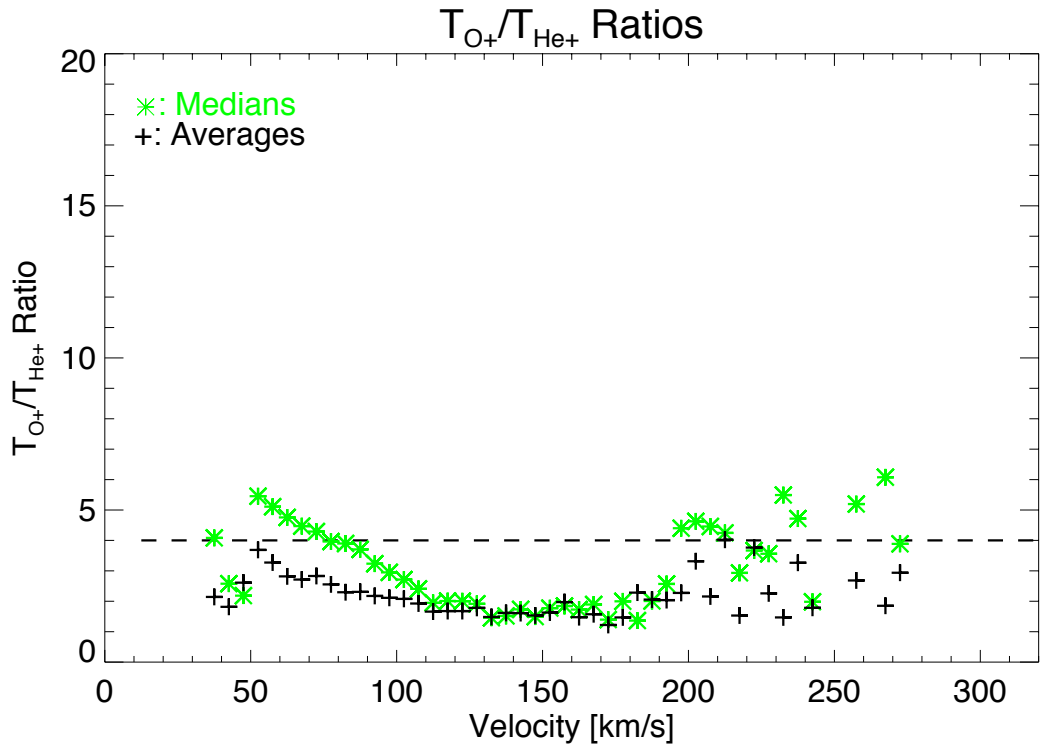

Figure B.21: Ratio of O^+ to He^+ temperature. The horizontal dashed line is at 4.

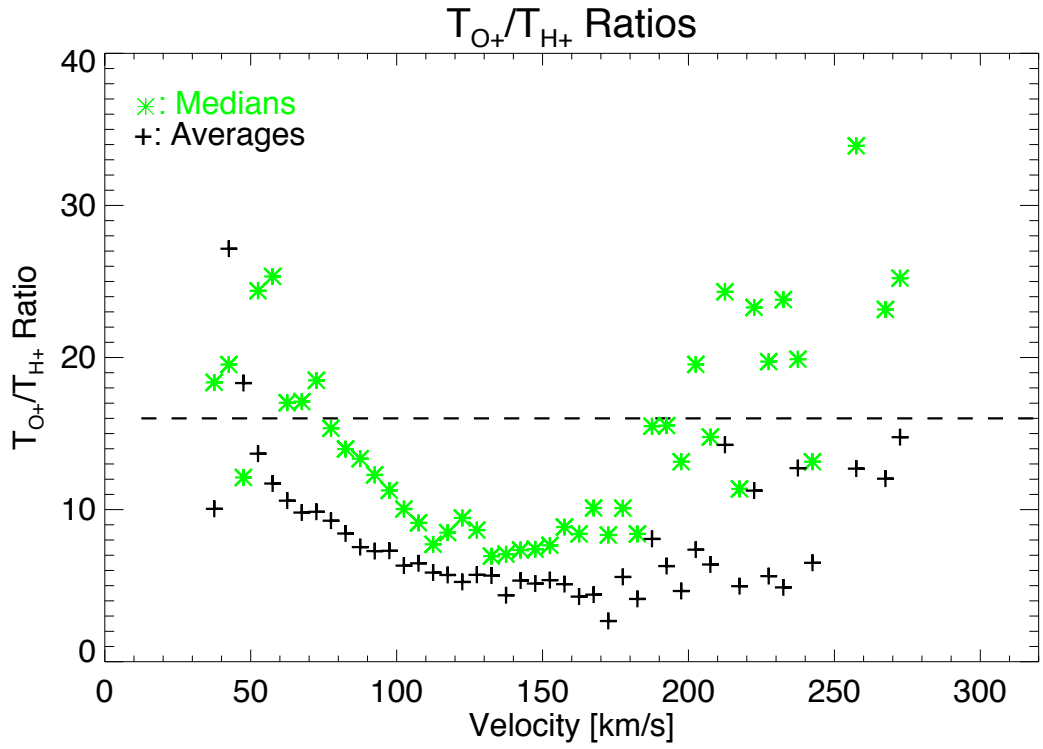

Figure B.22: Ratio of O^+ to H^+ temperature. The horizontal dashed line is at 16.

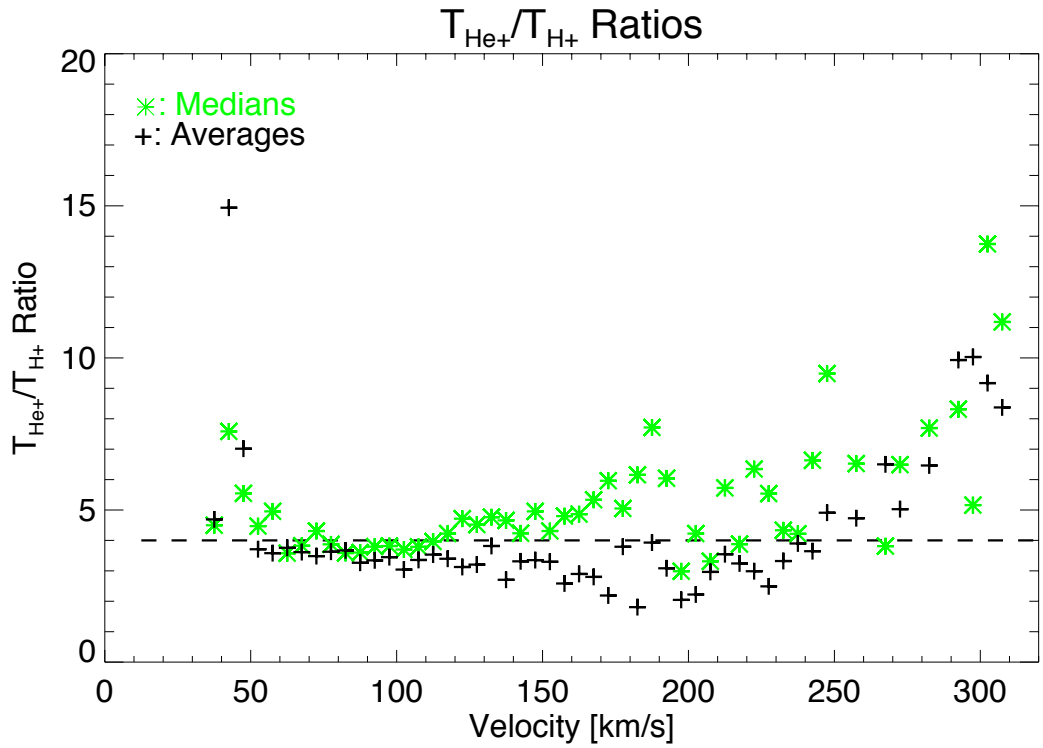

Figure B.23: Ratio of He^+ to H^+ temperature. The horizontal dashed line is at 4.

Another test was performed to check on the ion temperatures deduced from fits that successfully converged at low ion densities (as noted in Chapter 3, the lowest density that was considered valid was 0.01 cm^{-3}). The test was performed after binning the ion temperatures with respect to density for density increments of 0.05 cm^{-3} over the density range 0.01 to 10 cm^{-3}; note that there were density values above 10 cm^{-3} in the statistical database but this test was primarily to check for the temperature statistics at low densities. The means, medians, and standard deviations of the means were then computed from the temperature values within each density bin. Figure B.24 shows the number of temperature samples within each density bin for each ion species. In viewing the distribution of the temperatures versus densities, Figures B.25–B.27 (with each figure showing a reduced range for density on the x-axis), it is evident that the standard deviations are larger at low density (n_s < 1 cm^{-3}) for all three ion species but in particular for O^+. Recall that in the plots of the spatial distributions of median O^+ density and

temperature (Figures 3.8a and 3.8b), the local time where the lowest median densities appeared was the afternoon (plume region) as well as another low density region near pre-dawn at geocentric distances beyond 8 R_E. Median T_{O+} was also lowest in these two regions. If we consider the similarities of median and mean T_{O+} at all $n_{O+} > \sim 0.2$ cm^{-3} in Figure B.27 (showing the density range between 0 and 1 cm^{-3}), this suggests typical T_{O+} could actually be warmer than portrayed in the afternoon and pre-dawn locations and the apparent drop in temperature for $n_{O+} < \sim 0.2$ cm^{-3} could be a result of the temperatures not being resolved well at the low end of the densities considered. Such a correlation between low density and low temperature is not seen for H^+ and He^+.

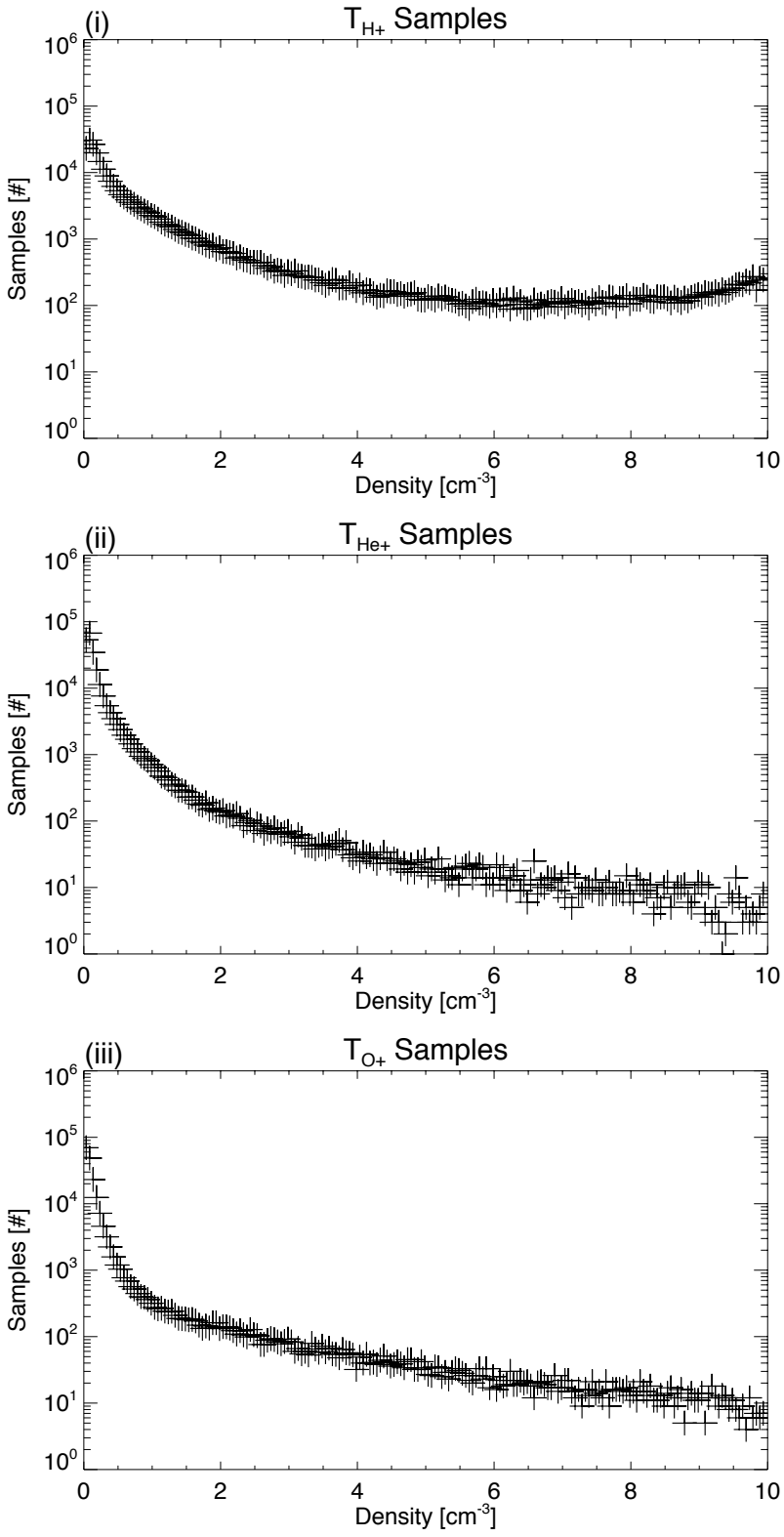

Figure B.24: The number of temperature samples within each 0.05 cm^{-3} bin.

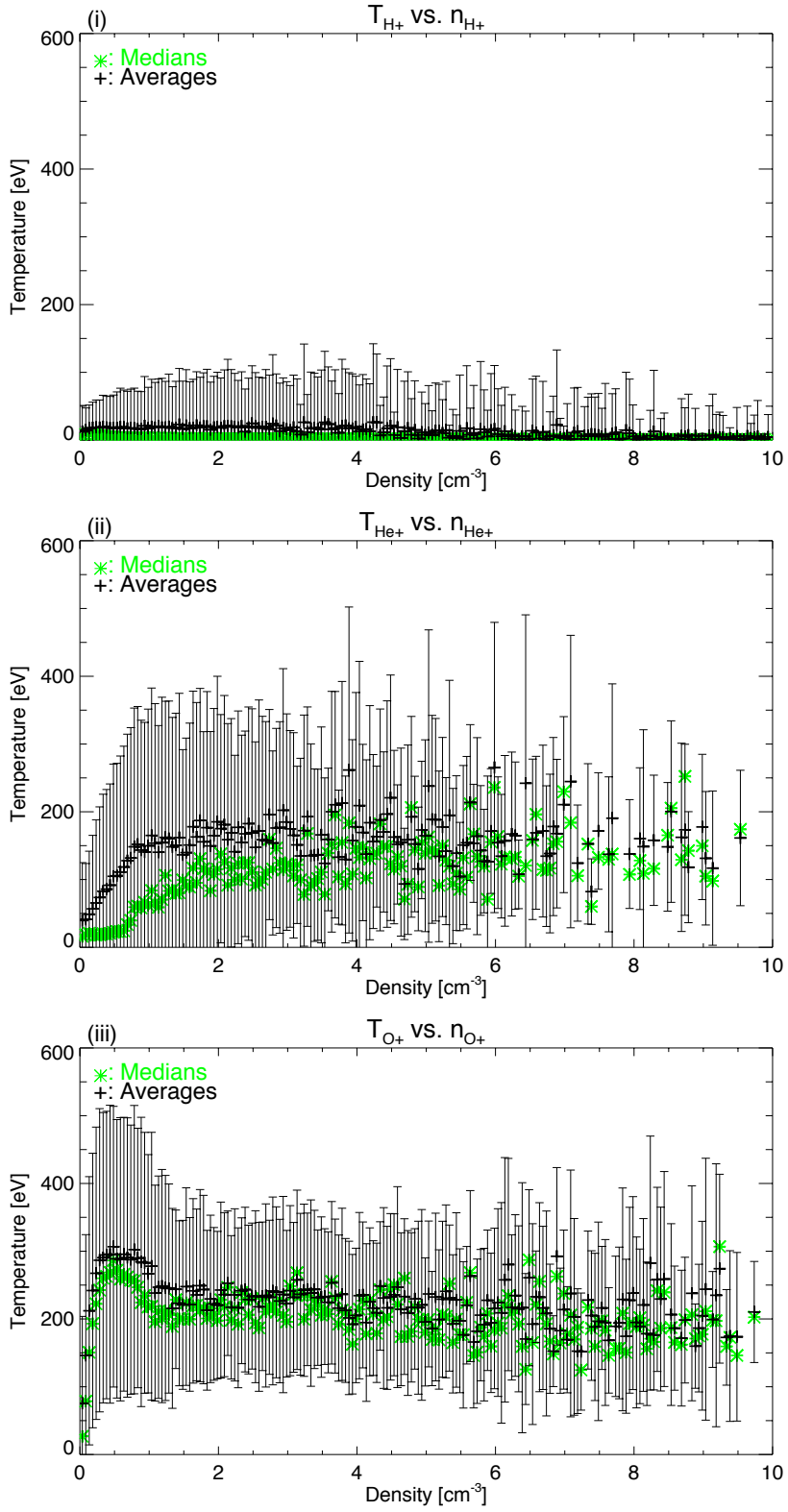

Figure B.25: The distribution of ion temperatures over the 0–10 cm^{-3} range for (i) H^+, (ii) He^+, and (iii) O^+.

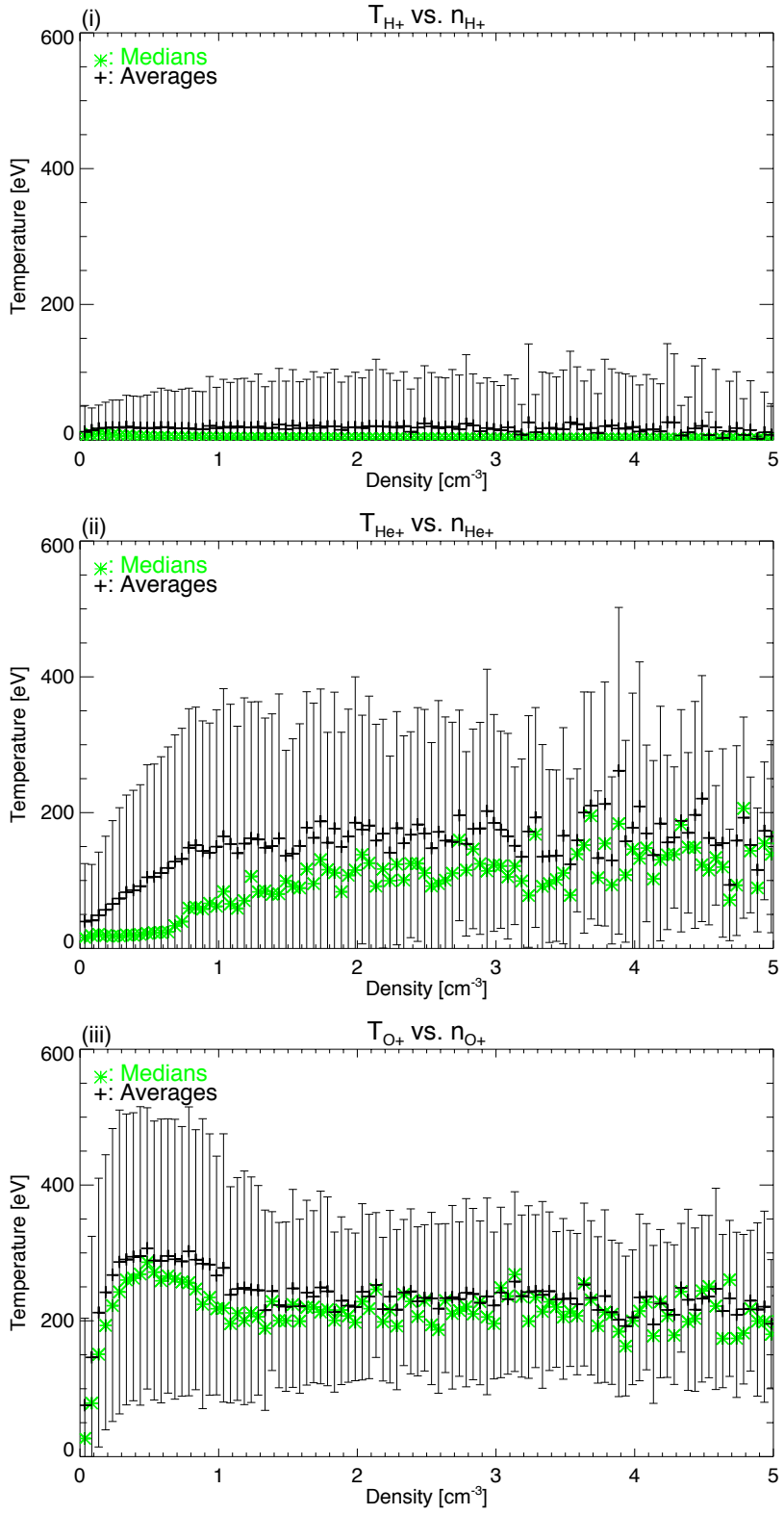

Figure B.26: Same as Figure B.25 except only plotting the 0–5 cm^{-3} range.

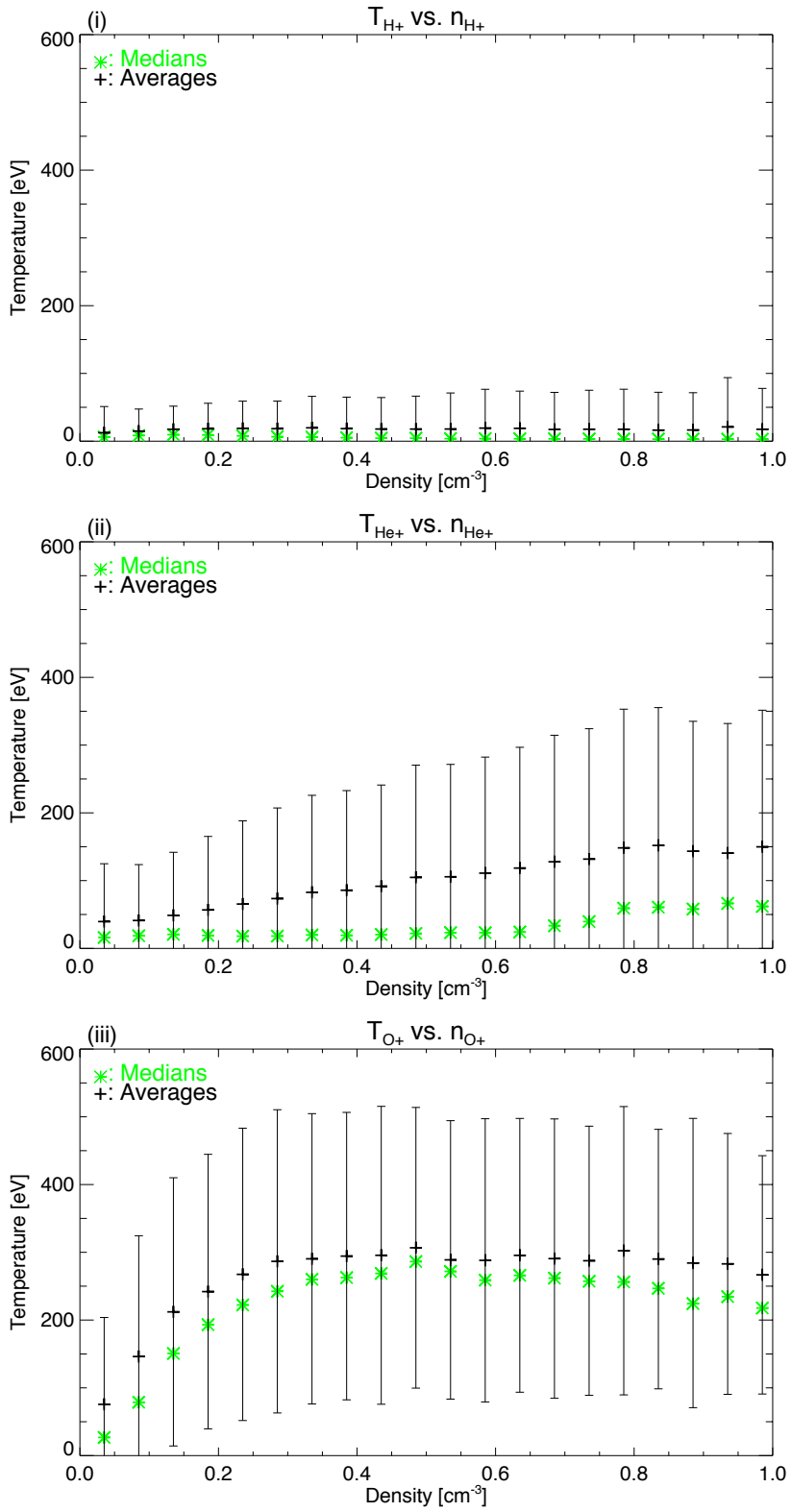

Figure B.27: Same as Figure B.25 except only plotting the 0–1 cm^{-3} range.

BIBLIOGRAPHY

Allen, R. C., J.-C. Zhang, L. M. Kistler, H. E. Spence, R.-L. Lin, M. W. Dunlop, and M. André (2013), Multiple bidirectional EMIC waves observed by Cluster at middle magnetic latitudes in the dayside magnetosphere, *J. Geophys. Res. Space Physics*, *118*, 6266–6278, doi:10.1002/jgra.50600.

Anderson, B. J., M. J. Engebretson, S. P. Rounds, L. J. Zanetti, T. A. Potemra (1990), A statistical study of Pc 3–5 pulsations observed by the AMPTE CCE Magnetic Fields Experiment, 1. Occurrence distributions, *J. Geophys. Res*., *95*, 10495–10523, doi:10.1029/JA095iA07p10495.

Anderson, B. J., R. E. Erlandson, and L. J. Zanetti (1992a), A statistical study of Pc 1–2 magnetic pulsations in the equatorial magnetosphere: 1. Equatorial occurrence distributions, *J. Geophys. Res*., *97*(A3), 3075–3088, doi:10.1029/91JA02706.

Anderson, B. J., R. E. Erlandson, and L. J. Zanetti (1992b), A statistical study of Pc 1–2 magnetic pulsations in the equatorial magnetosphere: 2. Wave properties, *J. Geophys. Res*., *97*(A3), 3089–3101, doi:10.1029/91JA02697.

Anderson, B. J., and D. C. Hamilton (1993), Electromagnetic ion cyclotron waves stimulated by modest magnetospheric compressions*, J. Geophys. Res*., *98*(A7), 11369–11382.

Anderson, B. J., R. E. Denton, G. Ho, D. C. Hamilton, S. A. Fuselier, and R. J. Strangeway (1996a), Observational test of proton cyclotron instability in the Earth's magnetosphere, J. *Geophys. Res*., 101(A10), 21527–21543, doi:10.1029/96JA01251.

Anderson, B. J., R. E. Denton, and S. A. Fuselier (1996b), On determining polarization characteristics of ion cyclotron wave magnetic field fluctuations, *J. Geophys. Res*., *101*(A6), 13195–13213, doi:10.1029/96JA00633.

Anderson, B. J., and S. A. Fuselier (1994), Response of thermal ions to electromagnetic ion cyclotron waves, *J. Geophys. Res*., *99*(A10), 19413–19425, doi:10.1029/94JA01235.

André, M. and C. M. Cully (2012), Low-energy ions: A previously hidden solar system particle population, *Geophys. Res. Lett*., *39*, L03101, doi:10.1029/2011GL050242.

Angelopoulos, V. (2008), The THEMIS Mission, *Space Sci. Rev*., doi:10.1007/s11214-008-9336-1.

Angelopoulos, V., A. Runov, X.-Z. Zhou, D. L. Turner, S. A. Kiehas, S.-S. Li, I. Shinohara (2013), Electromagnetic energy conversion at reconnection fronts, *Science*, *341*(6153), 1478–1482, doi:10.1126/science.1236992.

Angelopoulos, V., C. F. Kennel, F. V. Coroniti, R. Pellat, M. G. Kivelson, R. J. Walker, W. Baumjohann, W. C. Feldman, J. T. Gosling, and C. T. Russell (1993), Characteristics of ion flow in the quiet state of the inner plasma sheet, *Geophys. Res. Lett*., *20*(16): 1711–1714.

Angelopoulos, V., C. F. Kennel, F. V. Coroniti, R. Pellat, M. G. Kivelson, R. J. Walker, C. T. Russell, W. Baumjohann, W. C. Feldman, and J. T. Gosling (1994), Statistical characteristics of bursty bulk flow events, *J. Geophys. Res*., *99*(A11), 21257–21280, doi:10.1029/94JA01263.

Arthur, C. W., R. L. McPherron, and J. D. Means (1976), A comparative study of three techniques for using the spectral matrix in wave analysis, *Radio Sci*., *11*(10), 833–845, doi:10.1029/RS011i010p00833.

Auster, H. U., et al. (2008), The THEMIS Fluxgate Magnetometer, *Space Sci. Rev*., *141*(1–4), 235–264, doi:10.1007/s11214-008-9365-9.

Barfield, J. N., and P. J. Coleman Jr. (1970), Storm-related wave phenomena observed at the synchronous, equatorial orbit, *J. Geophys. Res*., *75*(10), 1943–1946, doi:10.1029/JA075i010p01943.

Barfield, J. N., and R. L. McPherron (1972), Investigation of interaction between Pc 1 and 2 and Pc 5 micropulsations at the synchronous orbit during magnetic storms, *J. Geophys. Res*., *77*(25), 4707–4719, doi:10.1029/JA077i025p04707.

Blackman, R. B., and Tukey, J. W. (1958), The Measurement of Power Spectra, From the Point of View of Communications Engineering–Part II. Bell System Technical Journal, 37: 485–569, doi:10.1002/j.1538-7305.1958.tb01530.x.

Blum, L. W., E. A. MacDonald, S. P. Gary, M. F. Thomsen, and H. E. Spence (2009), Ion observations from geosynchronous orbit as a proxy for ion cyclotron wave growth during storm times, *J. Geophys. Res*., *114*, A10214, doi:10.1029/2009JA014396.

Blum, L. W., E. A. MacDonald, L. B. N. Clausen, and X. Li (2012), A comparison of magnetic field measurements and a plasma-based proxy to infer EMIC wave distributions at geosynchronous orbit, *J. Geophys. Res*., *117*, A05220, doi:10.1029/2011JA017474.

Bonnell, J. W., et al. (2008), The Electric Field Instrument (EFI) for THEMIS, *Space Sci. Rev*., *141*, 303–341, doi:10.1007/s11214-008-9469-2.

Borovsky, J. E. and M. H. Denton (2008), A statistical look at plasmaspheric drainage plumes, *J. Geophys. Res*., *113*, A09221, doi:10.1029/2007JA012994.

Brambles, O. J., W. Lotko, B. Zhang, M. Wiltberger, J. Lyon, and R. J. Strangeway (2011), Magnetosphere sawtooth oscillations induced by ionospheric outflow, *Science*, *332*(6034), 1183–1186, doi:10.1126/science.1202869.

Brice, N. (1974), Wave-wave coupling in multiple-ion plasmas, *J. Geophys. Res*., *79*(16), 2519–2520, doi:10.1029/JA079i016p02519.

Brice, N., and C. Lucas (1975), Interaction between heavier ions and ring current protons, *J. Geophys. Res*., *80*(7), 936–942, doi:10.1029/JA080i007p00936.

Carpenter, D. L. (1963), Whistler evidence of a 'knee' in the magnetospheric ionization density profile, *J. Geophys. Res*., *68*(6), 1675–1682, doi:10.1029/JZ068i006p01675.

Carpenter, D. L., A. J. Smith, B. L. Giles, C. R. Chappell, and P. M. E. Décréau (1992), A case study of plasma structure in the dusk sector associated with enhanced magnetospheric convection, *J. Geophys. Res*., *97*(A2), 1157–1166, doi:10.1029/91JA01546.

Carpenter, D. L., B. L. Giles, C. R. Chappell, P. M. E. Décréau, R. R. Anderson, A. M. Persoon, A. J. Smith, Y. Corcuff, and P. Canu (1993), Plasmasphere dynamics in the duskside bulge region: A new look at an old topic, *J. Geophys. Res*., *98*(A11), 19243–19271, doi:10.1029/93JA00922.

Chappell, C. R., K. K. Harris, and G. W. Sharp (1970), The morphology of the bulge region of the plasmasphere, *J. Geophys. Res*., *75*(19), 3848–3861, doi:10.1029/JA075i019p03848.

Chappell, C. R. (1972), Recent satellite measurements of the morphology and dynamics of the plasmasphere, *Rev. Geophys*., *10*(4), 951–979, doi:10.1029/RG010i004p00951.

Chappell, C. R. (1974), Detached plasma regions in the magnetosphere, *J. Geophys. Res*., *79*(13), 1861–1870, doi:10.1029/JA079i013p01861.

Chappell, C. R. (1982), Initial observations of thermal plasma composition and energetics from Dynamics Explorer-1, *Geophys. Res. Lett.*, *9*, 929–932, doi:10.1029/GL009i009p00929.

Chappell, C. R., K. K. Harris, and G. W. Sharp (1970), The morphology of the bulge region of the plasmasphere, *J. Geophys. Res.*, *75*(19), 3848–3861, doi:10.1029/JA075i019p03848.

Chappell, C. R., M. M. Huddleston, T. E. Moore, B. L. Giles, and D. C. Delcourt (2008), Observations of the warm plasma cloak and an explanation of its formation in the magnetosphere, *J. Geophys. Res.*, *113*, A09206, doi:10.1029/2007JA012945.

Chappell, C. R., T. E. Moore, and J. H. Waite Jr. (1987), The ionosphere as a fully adequate source of plasma for the Earth's magnetosphere, *J. Geophys. Res.*, *92*(A6), 5896–5910, doi:10.1029/JA092iA06p05896.

Chandler, M. O., and T. E. Moore (2003), Observations of the geopause at the equatorial magnetopause: Density and temperature, *Geophys. Res. Lett.*, *30*(16), 1869, doi:10.1029/2003GL017611.

Chen, F. F. (1984), *Introduction to Plasma Physics and Controlled Fusion*, Plenum Press, New York.

Chen, L., R. M. Thorne, and J. Bortnik (2011), The controlling effect of ion temperature on EMIC wave excitation and scattering, *Geophys. Res. Lett.*, *38*, L16109, doi:10.1029/2011GL048653.

Chen, L., R. M. Thorne, and R. B. Horne (2009), Simulation of EMIC wave excitation in a model magnetosphere including structured high-density plumes, *J. Geophys. Res.*, *114*, A07221, doi:10.1029/2009JA014204.

Chen, L., R. M. Thorne, V. K. Jordanova, C.-P. Wang, M. Gkioulidou, L. Lyons, and R. B. Horne (2010), Global simulation of EMIC wave excitation during the 21 April 2001 storm from coupled RCM-RAM-HOTRAY modeling, *J. Geophys. Res*., *115*, A07209, doi:10.1029/2009JA015075.

Chen, L., R. M. Thorne, V. K. Jordanova, C.-P. Wang, M. Gkioulidou, L. Lyons, and R. B. Horne (2010), Global simulation of EMIC wave excitation during the 21 April 2001 storm from coupled RCM-RAM-HOTRAY modeling, *J. Geophys. Res*., *115*, A07209, doi:10.1029/2009JA015075.

Chen, L., R. M. Thorne, Y. Shprits, and B. Ni (2013), An improved dispersion relation for parallel propagating electromagnetic waves in warm plasmas: Application to electron scattering, *J. Geophys. Res*., doi:10.1002/jgra.50260.

Chen, S.-H., and T. E. Moore (2004), Dayside flow bursts in the Earth's outer magnetosphere, *J. Geophys. Res*., *109*, A03215, doi:10.1029/2003JA010007.

Chen, S.-H., and T. E. Moore (2006), Magnetospheric convection and thermal ions in the dayside outer magnetosphere, *J. Geophys. Res*., *111*, A03215, doi:10.1029/2005JA011084.

Comfort, R. H., Newberry, I. T. and Chappell, C. R. (1988) Preliminary Statistical Survey of Plasmaspheric Ion Properties from Observations by DE-1/RIMS, in *Modeling Magnetospheric Plasma* (edited by T. E. Moore, J. H. Waite, T. W. Moorehead and W. B. Hanson), American Geophysical Union, Washington, D. C.. doi: 10.1029/GM044p0107.

Cornwall, J. M. (1965), Cyclotron instabilities and electromagnetic emission in the ultra low frequency and very low frequency ranges, *J. Geophys. Res*., *70*(1), 61–69, doi:10.1029/JZ070i001p00061.

Cornwall, J. M., and M. Schulz (1971), Electromagnetic ion-cyclotron instabilities in multicomponent magnetospheric plasmas, *J. Geophys. Res*., *76*(31), 7791–7796, doi:10.1029/JA076i031p07791.

Cully, C. M., E. F. Donovan, A. W. Yau, and G. G. Arkos (2003a), Akebono/Suprathermal Mass Spectrometer observations of low-energy ion outflow: Dependence on magnetic activity and solar wind conditions, *J. Geophys. Res*., *108*(A2), 1093, doi:10.1029/2001JA009200.

Cully, C. M., E. F. Donovan, A. W. Yau, and H. J. Opgenoorth (2003b), Supply of thermal ionospheric ions to the central plasma sheet, *J. Geophys. Res*., *108*(A2), 1092, doi:10.1029/2002JA009457.

Dandouras, I. (2013), Detection of a plasmaspheric wind in the Earth's magnetosphere by the Cluster spacecraft, *Ann. Geophys*., *31*, 1143–1153, doi:10.5194/angeo-31-1143-2013.

Dandouras, I., V. Pierrard, J. Goldstein, C. Vallat, G. K. Parks, H. Rème, C. Gouillart, F. Sevestre, M. Mccarthy, L. M. Kistler, B. Klecker, A. Korth, M. B. Bavassano-Cattaneo, P. Escoubet, and A. Masson (2005), Multipoint Observations of Ionic Structures in the Plasmasphere by CLUSTER—CIS and Comparisons with IMAGE-EUV Observations and with Model Simulations, in *Inner Magnetosphere Interactions: New Perspectives from Imaging* (edited by J. Burch, M. Schulz and H. Spence), American Geophysical Union, Washington, D. C.. doi: 10.1029/159GM03.

Darrouzet, F., J. De Keyser, P. M. E. Décréau, F. El Lemdani-Mazouz, and X. Vallières (2008), Statistical analysis of plasmaspheric plumes with Cluster/WHISPER observations, *Ann. Geophys*., *26*, 2403-2417, doi:10.5194/angeo-26-2403-2008.

Darrouzet, F., et al. (2009), Plasmaspheric density structures and dynamics: Properties observed by the CLUSTER and IMAGE missions, *Space Sci. Rev*., 145, 55–106, doi:10.1007/s11214-008-9438-9.

Delcourt, D. C., C. R. Chappell, T. E. Moore, and J. H. Waite Jr. (1989), A three-dimensional numerical model of ionospheric plasma in the magnetosphere, *J. Geophys. Res*., *94*, 11, 893, doi:10.1029/JA094iA09p11893.

de Soria-Santacruz, M., M. Spasojevic, and L. Chen (2013), EMIC waves growth and guiding in the presence of cold plasma density irregularities, *Geophys. Res. Lett*., *40*, 1940–1944, doi:10.1002/grl.50484.

Denton, R. E., M. K. Hudson, and I. Roth (1992), Loss-cone-driven ion cyclotron waves in the magnetosphere, *J. Geophys. Res*., *97*(A8), 12093–12103, doi:10.1029/92JA00954.

Denton, R. E., B. J. Anderson, G. Ho, and D. C. Hamilton (1996), Effects of wave superposition on the polarization of electromagnetic ion cyclotron waves, *J. Geophys. Res*., *101*(A11), 24869–24885, doi:10.1029/96JA02251.

Engebretson, M. J., L. J. Cahill Jr., R. L. Arnoldy, B. J. Anderson, T. J. Rosenberg, D. L. Carpenter, U. S. Inan, and R. H. Eather (1991), The role of the ionosphere in coupling upstream ULF wave power into the dayside magnetosphere, *J. Geophys. Res*., *96*(A2), 1527–1542, doi:10.1029/90JA01767.

Engwall, E., A. I. Eriksson, C. M. Cully, M. André, P. A. Puhl-Quinn, H. Vaith, and R. Torbert (2009), Survey of cold ionospheric outflows in the magnetotail, *Ann. Geophys*., *27*, 3185–3201, doi:10.5194/angeo-27-3185-2009.

Fraser, B. J., and R. L. McPherron (1982), Pc 1–2 magnetic pulsation spectra and heavy ion effects at synchronous orbit: ATS 6 results, *J. Geophys. Res*., *87*(A6), 4560–4566, doi:10.1029/JA087iA06p04560.

Fraser, B. J., R. S. Grew, S. K. Morley, J. C. Green, H. J. Singer, T. M. Loto'aniu, and M. F. Thomsen (2010), Storm time observations of electromagnetic ion cyclotron waves at geosynchronous orbit: GOES results, *J. Geophys. Res*., *115*, A05208, doi:10.1029/2009JA014516.

Fraser, B. J., S. K. Morley, R. S. Grew, and H. J. Singer (2012), Classification of Pc1−2 Electromagnetic Ion Cyclotron Waves at Geosynchronous Orbit, in *Dynamics of the Earth's Radiation Belts and Inner Magnetosphere* (edited by D. Summers, I. R. Mann, D. N. Baker and M. Schulz), American Geophysical Union, Washington, D. C., doi:10.1029/2012GM001353.

Fried, B. D., and S. D. Conte (1961), *The Plasma Dispersion Function*, Academic, New York.

Fuselier, S. A., B. J. Anderson, and T. G. Onsager (1995), Particle signatures of magnetic topology at the magnetopause: AMPTE/CCE observations, *J. Geophys. Res*., *100*, 11,805.

Fuselier, S. A., D. M. Klumpar, W. K. Peterson, and E. G. Shelley (1989), Direct injection of ionospheric O^+ into the dayside low latitude boundary layer, *Geophys. Res. Lett*., *16*, 1121.

Fuselier, S. A., K. J. Trattner, S. M. Petrinec, and B. Lavraud (2012), Dayside magnetic topology at the Earth's magnetopause for northward IMF, *J. Geophys. Res*., *117*, A08235, doi:10.1029/2012JA017852.

Fuselier, S. A., W. K. Peterson, D. M. Klumpar, and E. G. Shelley (1989), Entry and acceleration of He^+ in the low latitude boundary layer, *Geophys. Res. Lett*., *16*(7), 751–754.

Gary, S. P. (1993), *Theory of Space Plasma Microinstabilities*, Cambridge Univ. Press, New York, doi:10.1017/CBO9780511551512.

Gary, S. P., K. Liu, and L. Chen (2012), Alfvén-cyclotron instability with singly ionized helium: Linear theory, *J. Geophys. Res.*, *117*, A08201, doi:10.1029/2012JA017740.

Gendrin, R. (1968), Pitch angle diffusion of low energy protons due to gyroresonant interaction with hydromagnetic waves, *J. Atmos. Terr. Phys.*, *30*, 1313–1330, doi:10.1016/S0021-9169(68)91158-6.

Gendrin, R., and A. Roux (1980), Energization of helium ions by proton-induced hydromagnetic waves, *J. Geophys. Res.*, *85*(A9), 4577–4586, doi:10.1029/JA085iA09p04577.

Goldstein, J., and B. R. Sandel (2005), The global pattern of evolution of plasmaspheric drainage plumes, in *Inner Magnetosphere Interactions: New Perspectives from Imaging*, edited by J. L. Burch, M. Schulz, and H. Spence, p. 1, American Geophysical Union, Washington, D. C., doi:10.1029/159GM01.

Gomberoff, L., F. T. Gratton, and G. Gnavi (1996), Acceleration and heating of heavy ions by circularly polarized Alfvén waves, *J. Geophys. Res.*, *101*(A7), 15661–15665, doi:10.1029/96JA00684.

Gomberoff, L., and R. Neira (1983), Convective growth rate of ion cyclotron waves in a H^+–He^+ and H^+–He^+–O^+ plasma, *J. Geophys. Res.*, *88*(A3), 2170–2174, doi:10.1029/JA088iA03p02170.

Gomberoff, L., and S. Cuperman (1982), Combined effect of cold H^+ and He^+ ions on the proton cyclotron electromagnetic instability, *J. Geophys. Res.*, *87*(A1), 95–100, doi:10.1029/JA087iA01p00095.

Gurnett, D. A., and U. S. Inan (1988), Plasma wave observations with the Dynamics Explorer 1 spacecraft, *Rev. Geophys*., *26*(2), 285–316, doi:10.1029/RG026i002p00285.

Haaland, S., et al. (2012), Estimating the capture and loss of cold plasma from ionospheric outflow, *J. Geophys. Res.*, *117*, A07311, doi:10.1029/2012JA017679.

Hirahara, M., K. Seki, Y. Saito, and T. Mukai (2004), Periodic emergence of multicomposition cold ions modulated by geomagnetic field line oscillations in the near-Earth magnetosphere, *J. Geophys. Res.*, *109*, A03211, doi:10.1029/2003JA010141.

Hirahara, M., T. Mukai, S. Machida, T. Terasawa, Y. Saito, T. Yamamoto, and S. Kokubun (1996), Cold dense ion flows with multiple components observed in the distant tail lobe by geotail, *J. Geophys. Res*., *101*, 7769– 7784.

Horne, R. B., and R. M. Thorne (1993), On the preferred source location for convective amplification of ion cyclotron waves, *J. Geophys. Res*., *98*(A6), 9233–9247, doi:10.1029/92JA02972.

Horne, R. B., and R. M. Thorne (1994), Convective instabilities of electromagnetic ion cyclotron waves in the outer magnetosphere, *J. Geophys. Res*., *99*(A9), 17259–17273, doi:10.1029/94JA01259.

Horne, R. B., and R. M. Thorne (1997), Wave heating of He^+ by electromagnetic ion cyclotron waves in the magnetosphere: Heating near the H^+–He^+ bi-ion resonance frequency, *J. Geophys. Res*., *102*(A6), 11457–11471, doi:10.1029/97JA00749.

Horwitz, J. L., R. H. Comfort, and C. R. Chappell (1984), Thermal ion composition measurements of the formation of the new outer plasmasphere and double plasmapause

during storm recovery phase, *Geophys. Res. Lett.*, *11*, 701–704, doi:10.1029/GL011i008p00701.

Huddleston, M. M., C. R. Chappell, D. C. Delcourt, T. E. Moore, B. L. Giles, and M. O. Chandler (2005), An examination of the process and magnitude of ionospheric plasma supply to the magnetosphere, *J. Geophys. Res.*, *110*, A12202, doi:10.1029/2004JA010401.

Kavanagh Jr., L. D., J. W. Freeman Jr., and A. J. Chen (1968), Plasma flow in the magnetosphere, *J. Geophys. Res.*, *73*(17), 5511–5519, doi:10.1029/JA073i017p05511.

Keika, K., L. M. Kistler, and P. C. Brandt (2013a), Energization of O^+ ions in the Earth's inner magnetosphere and the effects on ring current buildup: A review of previous observations and possible mechanisms, J. *Geophys. Res. Space Physics*, *118*, doi:10.1002/jgra.50371.

Keika, K., K. Takahashi, A. Y. Ukhorskiy, and Y. Miyoshi (2013b), Global characteristics of electromagnetic ion cyclotron waves: Occurrence rate and its storm dependence, *J. Geophys. Res. Space Physics*, doi:10.1002/jgra.50385.

Kennel, C. F., and H. E. Petschek (1966), Limit on stably trapped particle fluxes, *J. Geophys. Res.*, *71*(1), 1–28, doi:10.1029/JZ071i001p00001.

Kistler, L. M., et al. (2005), Contribution of nonadiabatic ions to the cross-tail current in an O^+ dominated thin current sheet, *J. Geophys. Res.*, *110*, A06213, doi:10.1029/2004JA010653.

Kistler, L. M., C. G. Mouikis, B. Klecker, and I. Dandouras (2010), Cusp as a source for oxygen in the plasma sheet during geomagnetic storms, *J. Geophys. Res.*, *115*, A03209, doi:10.1029/2009JA014838.

Klumpar, D. M., S. A. Fuselier, and E. G. Shelley (1990), Ion composition measurements within magnetospheric flux transfer events, *Geophys. Res. Lett.*, *17*(12), 2305–2308.

Kokubun, D., M. G. Kivelson, R. L. McPherron, C. T. Russell, and H. I. West Jr. (1977), Ogo 5 observations of Pc 5 waves: Particle flux modulations, *J. Geophys. Res*., *82*(19), 2774–2786, doi:10.1029/JA082i019p02774.

Kozyra, J. U., T. E. Cravens, A. F. Nagy, E. G. Fontheim, and R. S. B. Ong (1984), Effects of energetic heavy ions on electromagnetic ion cyclotron wave generation in the plasmapause region, *J. Geophys. Res*., *89*(A4), 2217–2233, doi:10.1029/JA089iA04p02217.

Le, G., X. Blano-Cano, C. T. Russell, X.-W. Zhou, F. Mozer, K. J. Trattner, S. A. Fuselier, and B. J. Anderson (2001), Electromagnetic ion cyclotron waves in the high-altitude cusp: Polar observations, *J. Geophys. Res*., *106*(A9), 19067–19079, doi:10.1029/2000JA900163.

Lee, J. H., L. Chen, V. Angelopoulos, and R. M. Thorne (2012), THEMIS observations and modeling of multiple ion species and EMIC waves: Implications for a vanishing He^+ stop band, *J. Geophys. Res*., *117*, A06204, doi:10.1029/2012JA017539.

Lee, J. H., and V. Angelopoulos (2014), On the presence and properties of cold ions near Earth's equatorial magnetosphere, *J. Geophys. Res. Space Physics*, *119*, 1749–1770, doi:10.1002/2013JA019305.

Lemaire, J. F. and Schunk, R. W.: Plasmaspheric wind, *J. Atmos. Terr. Phys*., *54*, 467–477, 1992.

Lennartsson, W., and E. G. Shelley (1986), Survey of 0.1- to 16-keV/e plasma sheet ion composition*, J. Geophys. Res*., *91*(A3), 3061–3076, doi:10.1029/JA091iA03p03061.

Li, W. et al. (2010), THEMIS analysis of observed equatorial electron distributions responsible for the chorus excitation, *J. Geophys. Res*., 115, A00F11, doi:10.1029/2009JA014845.

Li, W., J. Bortnik, R. M. Thorne, C. M. Cully, L. Chen, V. Angelopoulos, Y. Nishimura, J. B. Tao, J. W. Bonnell, and O. LeContel (2013), Characteristics of the Poynting flux and wave

normal vectors of whistler-mode waves observed on THEMIS, *J. Geophys. Res. Space Physics*, *118*, 1461–1471, doi:10.1002/jgra.50176.

Li, W., J. Raeder, M. Øieroset, and T. D. Phan (2009), Cold dense magnetopause boundary layer under northward IMF: Results from THEMIS and MHD simulations, *J. Geophys. Res*., *114*, A00C15, doi:10.1029/2008JA013497.

Liao, J., L. M. Kistler, C. G. Mouikis, B. Klecker, I. Dandouras, and J.-C. Zhang (2010), Statistical study of O^+ transport from the cusp to the lobes with Cluster CODIF data, *J. Geophys. Res*., *115*, A00J15, doi:10.1029/2010JA015613.

Liao, J., L. M. Kistler, C. G. Mouikis, B. Klecker, and I. Dandouras (2012), Solar cycle dependence of the cusp O^+ access to the near-Earth magnetotail, *J. Geophys. Res*., *117*, A10220, doi:10.1029/2012JA017819.

Liemohn, M. W., T. E. Moore, P. D. Craven, W. Maddox, A. F. Nagy, and J. U. Kozyra (2005), Occurrence statistics of cold, streaming ions in the near-Earth magnetotail: Survey of Polar-TIDE observations, *J. Geophys. Res*., *110*, A07211, doi:10.1029/2004JA010801.

Liu, J., V. Angelopoulos, A. Runov, and X.-Z. Zhou (2013), On the current sheets surrounding dipolarizing flux bundles in the magnetotail: The case for wedgelets, *J. Geophys. Res. Space Physics*, *118*, 2000–2020, doi:10.1002/jgra.50092.

Liu, Y. H., B. J. Fraser, and F. W. Menk (2012), Pc2 EMIC waves generated high off the equator in the dayside outer magnetosphere, *Geophys. Res. Lett*., *39*, L17102, doi:10.1029/2012GL053082.

Lockwood, M., T. E. Moore, J. H. Waite Jr., C. R. Chappell, J. L. Horwitz, and R. A. Heelis (1985), The geomagnetic mass spectrometer – mass and energy dispersions of ionospheric ion flows into the magnetosphere, *Nature*, *316*, 612 – 613, doi:10.1038/316612a0.

Lotko, W. (2007), The magnetosphere–ionosphere system from the perspective of plasma circulation: A tutorial, *J. Atmos. Sol. Terr. Phys*., *69*, 191–211, doi:10.1016/j.jastp.2006.08.011.

Loto'aniu, T. M., B. J. Fraser, and C. L. Waters (2005), Propagation of electromagnetic ion cyclotron wave energy in the magnetosphere, *J. Geophys. Res*., *110*, A07214, doi:10.1029/2004JA010816.

Markwardt, C. B. (2009), Non-Linear Least Squares Fitting in IDL with MPFIT, in *Proceedings Astronomical Data Analysis Software and Systems XVIII, Quebec, Canada*, ASP Conference Series, Vol. 411, eds. D. Bohlender, P. Dowler and D. Durand (Astronomical Society of the Pacific: San Francisco), p. 251-253 (ISBN: 978-1-58381-702-5).

Mauk, B. H. (2013), Analysis of EMIC-wave-moderated flux limitation of measured energetic ion spectra in multispecies magnetospheric plasmas, *Geophys. Res. Lett*., *40*, 3804–3808, doi:10.1002/grl.50789.

Mauk, B. H., R. L. McPherron (1980), An experimental test of the electromagnetic ion cyclotron instability within the earth's magnetosphere, *Phys. Fluids*, *23*, 2111.

McCollough, J. P., S. R. Elkington, M. E. Usanova, I. R. Mann, D. N. Baker, and Z. C. Kale (2010), Physical mechanisms of compressional EMIC wave growth, *J. Geophys. Res*., *115*, A10214, doi:10.1029/2010JA015393.

McCollough, J. P., S. R. Elkington, and D. N. Baker (2012), The role of Shabansky orbits in compression-related electromagnetic ion cyclotron wave growth, *J. Geophys. Res.*, *117*, A01208, doi:10.1029/2011JA016948.

McFadden, J. P., et al. (2008a), The THEMIS ESA Plasma Instrument and In-flight Calibration, *Space Sci. Rev.*, doi:10.1007/s11214-008-9440-2.

McFadden, J. P., C. W. Carlson, D. Larson, J. Bonnell, F. S. Mozer, V. Angelopoulos, K.-H. Glassmeier, and U. Auster (2008b), Structure of plasmaspheric plumes and their participation in magnetopause reconnection: First results from THEMIS, *Geophys. Res. Lett.*, *35*, L17S10, doi:10.1029/2008GL033677.

Means, J. D. (1972), Use of the three-dimensional covariance matrix in analyzing the polarization properties of plane waves, *J. Geophys. Res.*, *77*(28), 5551–5559, doi:10.1029/JA077i028p05551.

Meredith, N. P., R. M. Thorne, R. B. Horne, D. Summers, B. J. Fraser, and R. R. Anderson (2003), Statistical analysis of relativistic electron energies for cyclotron resonance with EMIC waves observed on CRRES, *J. Geophys. Res.*, *108*(A6), 1250, doi:10.1029/2002JA009700.

Min, K., J. Lee, K. Keika, and W. Li (2012), Global distribution of EMIC waves derived from THEMIS observations, *J. Geophys. Res.*, *117*, A05219, doi:10.1029/2012JA017515.

Moldwin, M. B., J. Howard, J. Sanny, J. D. Bocchicchio, H. K. Rassoul, and R. R. Anderson (2004), Plasmaspheric plumes: CRRES observations of enhanced density beyond the plasmapause, *J. Geophys. Res.*, *109*, A05202, doi:10.1029/2003JA010320.

Moore, T. E., C. J. Pollock, R. L. Arnoldy, and P. M. Kintner (1986), Preferential O^+ heating in

the topside ionosphere, *Geophys. Res. Lett*., *13*, 901–904.

Moore, T. E., et al. (1995), The Thermal Ion Dynamics Experiment and Plasma Source Instrument, *Space Sci. Rev*., *71*, 409.

Moore, T. E., Chandler, M. O., Chappell, C. R., Comfort, R. H., Craven, P. D., Delcourt, D. C., Elliott, H. A., Giles, B. L., Horwitz, J. L., Pollock, C. J. and Su, Y.-J. (1999) Polar/TIDE Results on Polar Ion Outflows, in *Sun-Earth Plasma Connections* (eds J. L. Burch, R. L. Carovillano and S. K. Antiochos), American Geophysical Union, Washington, D. C.. doi:10.1029/GM109p0087.

Moré, J. (1978), The Levenberg-Marquardt Algorithm: Implementation and Theory, in *Numerical Analysis*, vol. 630, edited by G. A. Watson, pp. 105–116, Springer-Verlag, Berlin, Germany, doi:10.1007/BFb0067690.

Mozer, F. S. (1973), Analysis of techniques for measuring DC and AC electric fields in the magnetosphere, *Space Sci. Rev*., *14*(2), 272–313, doi:10.1007/BF02432099.

Ni, B., Y. Shprits, M. Hartinger, V. Angelopoulos, X. Gu and D. Larson (2011), Analysis of radiation belt electron phase space density using THEMIS SST measurements: Cross-satellite calibration and a case study, *J. Geophys. Res*., *116*, A03208, doi:10.1029/2010JA016104.

Nishimura, Y., L. Lyons, S. Zou, V. Angelopoulos, and S. Mende (2010), Substorm triggering by new plasma intrusion: THEMIS all‐sky imager observations, *J. Geophys. Res*., *115*, A07222, doi:10.1029/2009JA015166.

Nosé, M., H. Koshiishi, H. Matsumoto, P. Brandt, K. Keika, K. Koga, T. Goka, and T. Obara (2010), Magnetic field dipolarization in the deep inner magnetosphere and its role in

development of O^+-rich ring current, *J. Geophys. Res*., *115*, A00J03, doi:10.1029/2010JA015321.

Nosé, M., K. Takahashi, R. R. Anderson, and H. J. Singer (2011), Oxygen torus in the deep inner magnetosphere and its contribution to recurrent process of O^+-rich ring current formation, *J. Geophys. Res*., *116*, A10224, doi:10.1029/2011JA016651.

Øieroset, M., T. D. Phan, V. Angelopoulos, J. P. Eastwood, J. McFadden, D. Larson, C. W. Carlson, K.-H. Glassmeier, M. Fujimoto, and J. Raeder (2008), THEMIS multi-spacecraft observations of magnetosheath plasma penetration deep into the dayside low-latitude magnetosphere for northward and strong B_y IMF, *Geophys. Res. Lett*., *35*, L17S11, doi:10.1029/2008GL033661.

Olsen, R. C. (1982), The hidden ion population of the magnetosphere, *J. Geophys. Res*., *87*(A5), 3481–3488, doi:10.1029/JA87iA05p03481.

Olsen, R. C., S. D. Shawhan, D. L. Gallagher, J. L. Green, C. R. Chappell, and R. R. Anderson (1987), Plasma Observations at the Earth's Magnetic Equator*, J. Geophys. Res*., *92*(A3), 2385–2407, doi:10.1029/JA092iA03p02385.

Omidi, N., J. Bortnik, R. Thorne, and L. Chen (2013), Impact of cold O^+ ions on the generation and evolution of EMIC waves, *J. Geophys. Res. Space Physics*, *118*, 434–445, doi:10.1029/2012JA018319.

Otto, A. and Nykyri, K. (2003) Kelvin-Helmholtz Instability and Magnetic Reconnection: Mass Transport at the LLBL, in *Earth's Low-Latitude Boundary Layer* (eds. P. T. Newell and T. Onsager), American Geophysical Union, Washington, D. C., doi:10.1029/133GM05.

Pedersen, A., F. Mozer, and G. Gustafsson (1998), Electric field measurements in a tenuous

plasma with spherical double probes, in *Measurement Techniques in Space Plasmas: Fields*, Geophys. Monogr. Ser., vol. 103, edited by J. Borovsky, R. Pfaff, and A. Young, pp. 1–12, AGU, Washington, D.C.

Pedersen, A., et al. (2008), Electron density estimations derived from spacecraft potential measurements on Cluster in tenuous plasma regions, *J. Geophys. Res*., *113*, A07S33, doi:10.1029/2007JA012636.

Petrinec, S. M., and C. T. Russell (1993), Factors which control the size of the magnetosphere, in *Solar Terrestrial Predictions IV*, vol. 2, edited by J. Hruska, M. A. Shea, D. F. Smart, and G. Heckman, pp. 627–625, Natl. Oceanic, and Atmos. Admin., Environ. Res. Lab., Boulder, Colorado.

Petrinec, S. M., P. Song, and C. T. Russell (1991), Solar cycle variations in the size and shape of the magnetopause, *J. Geophys. Res., 96*, 7893–7896.

Phan, T. D., G. Paschmann, J. T. Gosling, M. Oieroset, M. Fujimoto, J. F. Drake, and V. Angelopoulos (2013), The dependence of magnetic reconnection on plasma β and magnetic shear: Evidence from magnetopause observations, *Geophys. Res. Lett*., *40*, 11–16, doi:10.1029/2012GL054528.

Roberts, W. T., Jr., J. L. Horwitz, R. H. Comfort, C. R. Chappell, J. H. Waite Jr., and J. L. Green (1987), Heavy ion density enhancements in the outer plasmasphere, *J. Geophys. Res*., *92*(A12), 13499–13512, doi:10.1029/JA092iA12p13499.

Roux, A., S. Perraut, J. L. Rauch, C. de Villedary, G. Kremser, A. Korth, and D. T. Young (1982), Wave-particle interactions near Ω_{He+} observed on board GEOS 1 and 2: 2.

Generation of ion cyclotron waves and heating of He^+ ions, *J. Geophys. Res*., *87*, 8174-8190, doi:10.1029/HA087iA10p08174.

Russell, C. T. (1994), *Appendix 4: Time Series Analysis Techniques*, unpublished manuscript.

Russell, C. T., R. Holzer, and E. Smith (1970), OGO 3 observations of ELF noise in the magnetosphere, 2: The nature of the equatorial noise, *J. Geophys. Res*., *75*(4), 755–768.

Russell, C. T., and R. M. Thorne (1970), On the structure of the inner magnetosphere, *Cosmic Electrodynamics*, *1*, 67–89.

Samson, J. C. and Olson, J. V. (1980), Some comments on the descriptions of the polarization states of waves, *Geophys. J. R. Astron. Soc.*, *61*, 115–129, doi:10.1111/j.1365-246X.1980.tb04308.x.

Santolík, O., J. S. Pickett, D. A. Gurnett, J. D. Menietti, B. T. Tsurutani, and O. Verkhoglyadova (2010), Survey of Poynting flux of whistler mode chorus in the outer zone, *J. Geophys. Res*., *115*, A00F13, doi:10.1029/2009JA014925.

Seki, K., M. Hirahara, T. Terasawa, T. Mukai, and S. Kokubun (1999), Properties of He^+ Beams Observed by Geotail in the Lobe/Mantle Regions: Comparison with O^+ Beams, *J. Geophys. Res*., *104*, 6973– 6985.

Seki, K., M. Hirahara, M. Hoshino, T. Terasawa, Y. Saito, T. Mukai, and H. Hayakawa (2003), Hidden cold ions in the hot plasma sheet of Earth's magnetotail, Nature, 422, 589–592.

Sheeley, B. W., M. B. Moldwin, H. K. Rassoul, and R. R. Anderson (2001), An empirical plasmasphere and trough density model: CRRES observations, *J. Geophys. Res*., *106*(A11), 25631–25641.

Shelley, E. G., R. G. Johnson, and R. D. Sharp (1972), Satellite observations of energetic heavy ions during a geomagnetic storm, *J. Geophys. Res*., *77*(31), 6104–6110, doi:10.1029/JA077i031p06104.

Shoji, M. and Y. Omura (2011), Simulation of electromagnetic ion cyclotron triggered emissions in the Earth's inner magnetosphere, *J. Geophys. Res*., *116*, A05212, doi:10.1029/2010JA016351.

Shoji, M., Y. Omura, B. Grison, J. Pickett, I. Dandouras, and M. Engebretson (2011), Electromagnetic ion cyclotron waves in the helium branch induced by multiple electromagnetic ion cyclotron triggered emissions, *Geophys. Res. Lett*., *38*, L17102, doi:10.1029/2011GL048427.

Silin, I., I. R. Mann, R. D. Sydora, D. Summers, and R. L. Mac (2011), Warm plasma effects on electromagnetic ion cyclotron wave MeV electron interactions in the magnetosphere, *J. Geophys. Res*., *116*, A05215, doi:10.1029/2010JA016398.

Smith, R. L., and N. Brice (1964), Propagation in multicomponent plasmas, *J. Geophys. Res*., *69*(23), 5029–5040, doi:10.1029/JZ069i023p05029.

Swanson, D. G. (1989), *Plasma Waves*, Academic, Boston, Mass., doi:10.1887/075030927X.

Thorne, R. M., and C. F. Kennel (1971), Relativistic electron precipitation during magnetic storm main phase, *J. Geophys. Res*., *76*(19), 4446–4453, doi:10.1029/JA076i019p04446.

Thorne, R. M., Horne, R. B., Jordanova, V. K., Bortnik, J. and Glauert, S. (2006), Interaction of EMIC Waves With Thermal Plasma and Radiation Belt Particles, in *Magnetospheric ULF Waves: Synthesis and New Directions* (eds K. Takahashi, P. J. Chi, R. E. Denton and R. L. Lysak), American Geophysical Union, Washington, D. C., doi:10.1029/169GM14.

Tsyganenko, N. A. (1989), A Magnetospheric Magnetic Field Model with a Warped Tail Current Sheet, *Planet. Space Sci*., *37*, 5–20.

Tsyganenko, N. A. (2001), Empirical Magnetic Field Models for the Space Weather Program, in *Space Weather* (eds P. Song, H. J. Singer and G. L. Siscoe), American Geophysical Union, Washington, D. C., doi:10.1029/GM125p0273.

Tu, J., P. Song, B. W. Reinisch, and J. L. Green (2007), Smooth electron density transition from plasmasphere to the subauroral region, *J. Geophys. Res*., *112*, A05227, doi:10.1029/2007JA012298.

Turner, D. L., et al. (2014), Competing source and loss mechanisms due to wave-particle interactions in Earth's outer radiation belt during the 30 September to 3 October 2012 geomagnetic storm, *J. Geophys. Res. Space Physics*, *119*, 1960–1979, doi:10.1002/2014JA019770.

Ukhorskiy, A. Y., Y. Y. Shprits, B. J. Anderson, K. Takahashi, and R. M. Thorne (2010), Rapid scattering of radiation belt electrons by storm-time EMIC waves, *Geophys. Res. Lett*., *37*, L09101, doi:10.1029/2010GL042906.

Usanova, M. E., et al. (2010), Conjugate ground and multisatellite observations of compression-related EMIC Pc1 waves and associated proton precipitation, *J. Geophys. Res*., *115*, A07208, doi:10.1029/2009JA014935.

Usanova, M. E., I. R. Mann, J. Bortnik, L. Shao, and V. Angelopoulos (2012), THEMIS observations of electromagnetic ion cyclotron wave occurrence: Dependence on AE, SYMH, and solar wind dynamic pressure, *J. Geophys. Res*., *117*, A10218, doi:10.1029/2012JA018049.

Usanova, M. E., F. Darrouzet, I. R. Mann, and J. Bortnik (2013), Statistical analysis of EMIC waves in plasmaspheric plumes from Cluster observations, *J. Geophys. Res. Space Physics*, *118*, 4946–4951, doi:10.1002/jgra.50464.

Usanova, M. E., et al. (2014), Effect of EMIC waves on relativistic and ultrarelativistic electron populations: Ground-based and Van Allen Probes observations, *Geophys. Res. Lett.*, *41*, 1375–1381, doi:10.1002/2013GL059024.

Walsh, B. M., D. G. Sibeck, Y. Nishimura, and V. Angelopoulos (2013), Statistical analysis of the plasmaspheric plume at the magnetopause, *J. Geophys. Res. Space Physics*, *118*, doi:10.1002/jgra.50458.

Welling, D. T., V. K. Jordanova, S. G. Zaharia, A. Glocer, and G. Toth (2011), The effects of dynamic ionospheric outflow on the ring current, *J. Geophys. Res.*, *116*, A00J19, doi:10.1029/2010JA015642.

Yamauchi, M., I. Dandouras, H. Rème, and F. El-Lemdani Mazouz (2012), Equatorially confined warm trapped ions at around 100 eV near the plasmapause, *Geophys. Res. Lett.*, *39*, L15101, doi:10.1029/2012GL052366.

Yamauchi, M., I. Dandouras, H. Rème, R. Lundin, and L. M. Kistler (2013), Cluster observation of few-hour-scale evolution of structured plasma in the inner magnetosphere, *Ann. Geophys.*, *31*, 1569-1578, doi:10.5194/angeo-31-1569-2013.

Yau, A. W., A. Howarth, W. K. Peterson, and T. Abe (2012), Transport of thermal-energy ionospheric oxygen (O^+) ions between the ionosphere and the plasma sheet and ring current at quiet times preceding magnetic storms, *J. Geophys. Res.*, *117*, A07215, doi:10.1029/2012JA017803.

Yoshikawa, I., A. Yamazaki, K. Yamashita, Y. Takizawa, and M. Nakamura (2003), Which is a significant contributor for outside of the plasmapause, an ionospheric filling or a leakage of plasmaspheric materials?: Comparison of He II (304Å) images, *J. Geophys. Res*., *108*, 1080, doi:10.1029/2002JA009578.

Young, D. T., J. Geiss, H. Balsiger, P. Eberhardt, A. Ghielmetti, and H. Rosebauer (1977), Discovery of He^{2+} and O^{2+} ions of terrestrial origin in the outer magnetosphere. *Geophys. Res. Lett.*, *4*, 561–564. doi:10.1029/GL004i012p00561.

Young, D. T., S. Perraut, A. Roux, C. deVilledary, R. Gendrin, A. Korth, G. Kremser, and D. Jones (1981), Wave-particle interactions near Ω_{He+} observed on GEOS 1 and 2 1. Propagation of ion cyclotron waves in He^{+}-rich plasma, *J. Geophys. Res*., *86*(A8), 6755–6772, doi:10.1029/JA086iA08p06755.

Yu, Y., and A. J. Ridley (2013), Exploring the influence of ionospheric O^{+} outflow on magnetospheric dynamics: dependence on the source location, *J. Geophys. Res*., *118*, doi:10.1029/2012JA018411.

Yu, Y., and A. J. Ridley (2013), Exploring the influence of ionospheric O^{+} outflow on magnetospheric dynamics: dependence on the source location, *J. Geophys. Res. Space Physics*, *118*, 1711–1722, doi:10.1029/2012JA018411.

Zhang, J. C., L. M. Kistler, C. G. Mouikis, M. W. Dunlop, B. Klecker, and J. A. Sauvaud (2010), A case study of EMIC wave-associated He^{+} energization in the outer magnetosphere: Cluster and Double Star 1 observations, *J. Geophys. Res*., *115*, A06212, doi:10.1029/2009JA014784.

Zhang, J. C., L. M. Kistler, C. G. Mouikis, B. Klecker, J. A. Sauvaud, and M. W. Dunlop (2011), A statistical study of EMIC wave-associated He^{+} energization in the outer magnetosphere:

Cluster/CODIF observations, *J. Geophys. Res*., *116*, A11201, doi:10.1029/2011JA016690.

Zou, S., L. R. Lyons, and Y. Nishimura (2011), Mutual Evolution of Aurora and Ionospheric Electrodynamic Features Near the Harang Reversal During Substorms, in *Auroral Phenomenology and Magnetospheric Processes: Earth And Other Planets* (edited by A. Keiling, E. Donovan, F. Bagenal and T. Karlsson), American Geophysical Union, Washington, D. C., doi:10.1029/2011GM001163.